Porous Carbon Based Solid Adsorbents for Carbon Dioxide Capture

Will Travis

Centre for Materials Chemistry

Department of Chemistry,

University College London

London, August 2014

A Thesis Submitted for the Degree of Doctor of Philosophy

I, Will Travis confirm that the work presented in this thesis is my own. Where information has been derived from other sources, I confirm that this has been indicated in the thesis.

……..……

Acknowledgments

I would like to give the greatest thanks to my supervisor, Prof Zheng Xiao Guo for his continued support and advice. I would also like to thank Dr Srinivas Gadipelli, for his guidance, tuition and friendship which has been invaluable.

Furthermore, Prof Julian Evans has helped me immeasurably throughout this PhD and without his very kind, unselfish and wonderful help I would have toiled a great deal more. I would also like to thank Prof Jim Anderson for his knowledge and eagerness to advise, from which I have greatly benefited. To Prof Stephen GeorgeYeates I am also greatly indebted for his passionate support, kindness and the belief in which he installed in me.

I would also like to thank several others to whom I am deeply grateful, in no particular order: Steve Firth, Joe Nolan, Liz Read, Mary Lou Jabore, Dave Ladd, Jawwad Darr, Isaac Sugden and Helen Grounds.

Lastly I would like to thank my parents and family, whom I love dearly.

Abstract

The aim of this project is the design, synthesis and characterisation of porous carbon structures capable of the selective capture of carbon dioxide (CO_2) from the exhaust gases of coal and gas post-combustion power stations. In such systems, the fossil fuel is burnt in an air environment producing CO_2 as just one of a multi-component flue gas. This flue gas is expected to contain nitrogen and water among other constituents. It is at ambient pressures and temperatures of ≥323 K.

Successful capture materials should have highly microporous structures, rapid sorption kinetics and be capable of repeated sorption/desorption cycles. To develop highly microporous carbon sorbents a range of porous materials have been synthesised using chemical and physical activation of precursors obtained through top down and bottom up approaches. Porosity has also been achieved in precursors through the controlled use of graphene exfoliation, melamine-formaldehyde resin aerogel formation, soft templates, controlled carbonisation and synthesis of microporous organic polymers. The role of nitrogen dopants (N-dopants) within the CO_2 sorbent materials has also been investigated. To increase understanding and tune the sorbents performance, porous carbon structures have been synthesized containing: pyridine, pyrrole, quaternary and triazine nitrogen groups.

Characterisation was achieved using Fourier transform infrared spectroscopy, X-ray photoelectron spectroscopy, nuclear magnetic resonance spectroscopy, transmission electron microscopy X-ray diffraction, thermogravimetric analysis and nitrogen (N_2) isotherms at 77 K. CO_2 sorption analysis was carried out using volumetric and gravimetric analysis. The influence of N-dopants on the adsorbate-adsorbent interaction is characterised using CO_2 volumetric isotherms, isosteric heats of adsorption and CO_2/N_2 selectivity analysis.

Contents

List of Tables

List of Figures

Objectives

The scientific objectives of this thesis are to:

1. Research and analyse existing methods utilised and factors instrumental in the synthesis of successful porous carbon based solids for CO_2 separation and storage.
2. Discuss the role nitrogen dopants play in the adsorbent-CO_2 interaction and further mechanistic understanding through the synthesis of nitrogen functionalities in a range of carbon matrices.
3. Discuss the role pore size plays in the CO_2 adsorption behaviour of porous carbon solids and provide further evidence for the discussion.
4. Achieve a performance increase of 30–50% compared with current amine solvent systems, i.e. synthesise materials capable of ~3 mmol/g CO_2 uptake at 323 K.
5. Investigate, synthesise and analyse novel nitrogen-rich microporous organic polymers for the separation and storage of CO_2.
6. Investigate, synthesise and analyse porous N-doped exfoliated graphene materials for the separation and storage of CO_2.
7. Experiment with a range of activated carbon precursors to develop highly microporous carbons, assaying their potential as CO_2 sorbents.
8. Utilise various nitrogen-rich precursors to nitrogen-doped porous carbon, affording materials with ranging porosities and nitrogen dopants. Therefore developing an understanding of the most suitable precursors for future study.
9. Determine the potential for porosity inducing techniques common in the synthesis of porous carbon to be applied to carbon nitride. Indeed can a microporous carbon nitride be synthesised.

1. Introduction

This thesis outlines the design, synthesis and analysis of carbon based adsorbents for the selective capture of carbon dioxide from industrial point sources, such as coal and gas power stations. In this introduction, the global requirement for the capture of carbon dioxide is presented. This is followed by an explanation of how capture may be achieved and a brief discussion of current and potential technologies. The salient features of these technologies are then used to guide design and synthesis of a range of new materials.

1.1 Measuring Carbon Dioxide and Temperature Levels

From the coal-powered steam trains, furnaces and industry of the nineteenth century, to the oil-powered combustion and jet engine transport systems and gas or coal powered generators of the twentieth, the advancement in global technologies and infrastructure seen over the last 200 years has been built around and made possible by fossil fuels. The term fossil fuel refers mainly to the use of coal, oil and natural gas as sources of energy through their combustion. Fossil fuels are formed by the anaerobic decomposition of organisms that were alive predominately during the Carboniferous Period, between 360 and 286 million years ago. They are predominately carbon based and through combustion in oxygen, carbon dioxide (CO_2) is produced. However, in recent times the scientific community has linked rising levels of anthropogenic CO_2 with increasing global temperatures [IPCC (2001)-(2013)].

Measurements taken from firn data and ice cores show that over the industrial advancement of the last two hundred years, the concentration of atmospheric CO_2 has increased from 280–391.6 ppm, 1800–2012 [Trans *et al.* (1959 – current)] (Figure 1.1 (a)). In 2010 global CO_2 emissions from fossil-fuel combustion and cement production grew 5.9%, surpassing 9 Pg of anthropogenic carbon released per annum for the first time [Peters *et al.* (2012)]. Also over the last two hundred years a period of global warming has been observed [IPCC (2001) pp. 3], with temperature rising considerably (Figure 1.1 (b)). The recorded increase is dependant on data source: 0.911 ± 0.042 °C based on 2011 levels since the 1950s as reported by the Berkeley Earth Surface Temperature project [Witze *et al.* (2012)] and 0.74 °C (0.56 to 0.92 °C) over the 100 year period from 1906–2005 as reported by the Intergovernmental Panel on Climate Change (IPCC) [IPCC (2007) pp. 5]. These measurements have been carried out using thermometers, tree rings, corals, ice cores and historical records.

1.2 The Greenhouse Effect

Rising global temperature is linked to a rise in the 'greenhouse gas' carbon dioxide due to the 'greenhouse effect' [IPCC (2001) pp. 3, Tyndall (1860)]. Sunlight is broadly made up of the entire electromagnetic spectrum, and each year any typical location on the earth's surface adsorbs on average 235 $W.m^{-2}$ of radiation, limited by geometric effects and reflection [Karl *et al.* (2003)]. This radiation is converted into heat causing the emission of long wavelength infrared (IR) (0.74-1000 μm) radiation back into the atmosphere. If this were all radiated back into space the average temperature of the earth would be 33 °C lower [Karl *et al.* (2003)]. However, the atmosphere recycles much of the radiation released from the earth surface delivering an additional 324 $W.m^{-2}$ [Lashof (1989)]. This mechanism of recycling is carried out by greenhouse gases that adsorb thermal infrared radiation due to dipole fluctuations interacting with the electromagnetic oscillations of IR radiation. If the frequencies match then radiation is adsorbed causing a change in vibrational, rotational, stretching or bending states. There main greenhouse gases are: water vapour, CO_2, nitrous oxide and methane. It has been calculated that a doubling of CO_2 concentration would lead to an increase in 4 $W.m^{-2}$ downward energy flux [Lashof (1989)]. As early as 1860 CO_2 was shown to be able to adsorb and emit radiation within the infrared range [Tyndall (1860)].

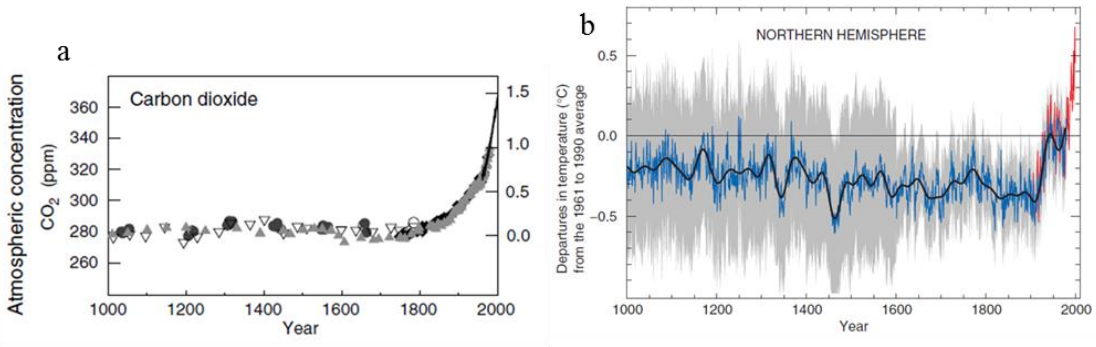

Figure 1.1. (a) Carbon dioxide (from ice core and firn data) fluctuations and (b) temperature (recorded using thermometers, tree rings, corals, ice cores and historical records) over the last 1000 years [IPCC (2001) pp. 6 and 134)]. The polar firn is the intermediate product between ice and snow that covers the Antarctic ice sheet.

1.3 Projections of Future Scenarios

This large body of evidence has led to the belief that dangerous anthropogenic interference in the world's climate is possible due to anthropogenically released CO_2 [Hansen *et al.* (2006), Oreskes (2004)]. IPCC special reports on emission scenario projections, leading from current and projected use of fossil fuels, forecasts a variety of possible future temperature change [IPCC

(2007) and (2013)]. The models vary in response to different economic, population and technological changes. An average 0.2 °C warming per decade is projected over the next two decades for a range of IPCC special report emissions scenarios (SRES). Even if greenhouse gas and aerosol concentrations are kept constant at year 2000 levels, a further warming of about 0.1 °C per decade would be expected. The most reserved scenario's best estimate projects an increase of 0.4 to 1.6 °C relative to 1950 levels, within a likely mean increase of 1.3-14 °C by 2050 (Figure 1.2(a)). Under all projections, snow and ice cap coverage will retract and sea levels will rise (Figure 1.2(b)). It is also likely that hot extremes, heat waves and heavy precipitation events will become more frequent. Tropical cyclones (hurricanes and typhoons) may also become more intense and extratropical storm tracks will move towards the poles. The distribution of precipitation patterns is also likely to change with increases towards the poles and reductions around the equator [IPCC (2007) pp. 7].

a

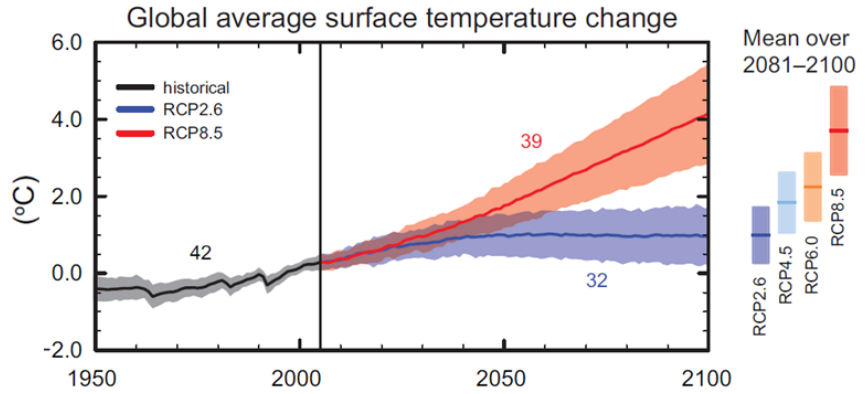

b

		2046–2065		2081–2100	
	Scenario	Mean	*Likely* range[c]	Mean	*Likely* range[c]
Global Mean Surface Temperature Change (°C)[a]	RCP2.6	1.0	0.4 to 1.6	1.0	0.3 to 1.7
	RCP4.5	1.4	0.9 to 2.0	1.8	1.1 to 2.6
	RCP6.0	1.3	0.8 to 1.8	2.2	1.4 to 3.1
	RCP8.5	2.0	1.4 to 2.6	3.7	2.6 to 4.8
	Scenario	**Mean**	***Likely* range[d]**	**Mean**	***Likely* range[d]**
Global Mean Sea Level Rise (m)[b]	RCP2.6	0.24	0.17 to 0.32	0.40	0.26 to 0.55
	RCP4.5	0.26	0.19 to 0.33	0.47	0.32 to 0.63
	RCP6.0	0.25	0.18 to 0.32	0.48	0.33 to 0.63
	RCP8.5	0.30	0.22 to 0.38	0.63	0.45 to 0.82

Figure 1.2. (a) CMIP5 multi-model simulated time series from 1950 to 2100 for the change in global annual mean surface temperature relative to 1986–2005 (b) Projected change in global mean surface air temperature and global mean sea level rise for the mid- and late 21st century relative to the reference period of 1986–2005 [IPCC (2013) pp. 21 and 23].

1.4 Political Response

In the face of such warnings, governments have acted in response. In 1997, the Kyoto Protocol was drawn up and has since been ratified by all major polluting countries except the United States of America. The Protocol legally bound participating member states to reduce CO_2 emission by 5 % in the period 2007 – 2012 against 1990 levels [United Nation (1998)]. But despite this, during the period 1997 – 2012 global greenhouse-gas emissions still went up by up 25% [Diringer (2011)]. The Copenhagen Accord follows on from where the Kyoto Protocol finished. It underlines the fact that climate change is one of the greatest challenges of our time and emphases a strong political desire to tackle the problem [United Nations Framework Convention on Climate Change (2009)]. It also recognises the scientific view that the increase in global temperature should be kept below 2° C. The accord is, however, not legally binding and asks for member states to pledge their own emissions reduction targets. Compared to 1990 levels the EU has pledged a 30% reduction, Japan 25 % and Russia a reduction of 15 – 25%. The US has pledged a reduction of 17% against 2005 levels while China a reduction in carbon intensity of 40 – 45% from 2005 levels [Mitigation pledges can be found at http://unfccc.int].

1.5 The Supply and Demand of Energy

Current primary energy supply is dominated by fossil fuels. The global primary energy supply in 2008 was 492 EJ, oil contributed 34.6%, coal 28.4% and gas 22.1%. 12.9% came from renewable energies, with 10.2% of that coming from biomass [IPCC (2011) pp. 10]. Hydropower contributed 2.1% while solar and wind produced 0.1% and 0.2% respectively. Nuclear power supplied 2.0%. Studies into technical potentials of possible energy supply from renewable fuels indicate that current energy requirements can be readily met using renewable sources [de Vries *et al.* (2007), Krewitt *et al.* (2009)]. Of these, solar photovoltaic (PV) has the greatest potential to be a leading contributor alongside wind and biomass [OECD/IEA (2011)].

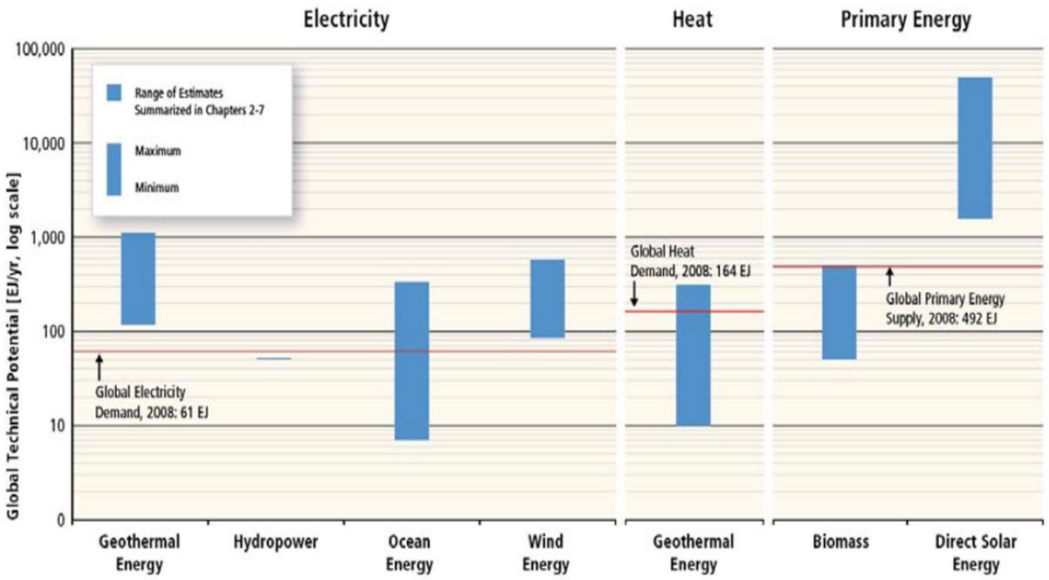

Figure 1.3. Ranges of global technical potentials of renewable energy sources [IPCC (2011) pp. 12].

1.5.1 Renewable Energy Sources

To avoid detrimental effects from climate change, a structural shift from an energy system based on fossil fuels to one based on renewable sources is required within several decades [Davis *et al*. (2010)]. Previous energy transitions, e.g. from wood to coal and from coal to oil were slow and primarily triggered by improved power density and economic benefits [Kerr (2010)]. A transition to renewable fuels, however, may not be a transition to a better fuel in terms of power density and economic benefits. While shortage of global and domestic energy supplies may encourage a transition to renewable energy sources, governmental influence on markets will likely be a major force driving any change. The cost of supply for renewables has fallen in recent years: cost of globally produced PV modules has fallen from 65 USD/W in 1976 to 1.4 USD/W in 2011 and onshore wind power in the US has fallen in cost from 4.3 to 1.9 USD/W from 1984 to 2011 [IPCC (2011) pp. 381]. Increasing costs of oil and coal, and benefits from economies of scale are making renewable technologies economically more attractive. It is important to note that the reductions in the cost of a technology per unit capacity understate the actual reduction in the levelised cost of the technology when improvements in performance occur. The levelised cost takes the high initial cost of renewable energy sources and accounts for the many years of energy that will be produced; i.e. levelised cost = net cost to install a renewable energy system divided by its expected life-time energy output (Figure 1.4).

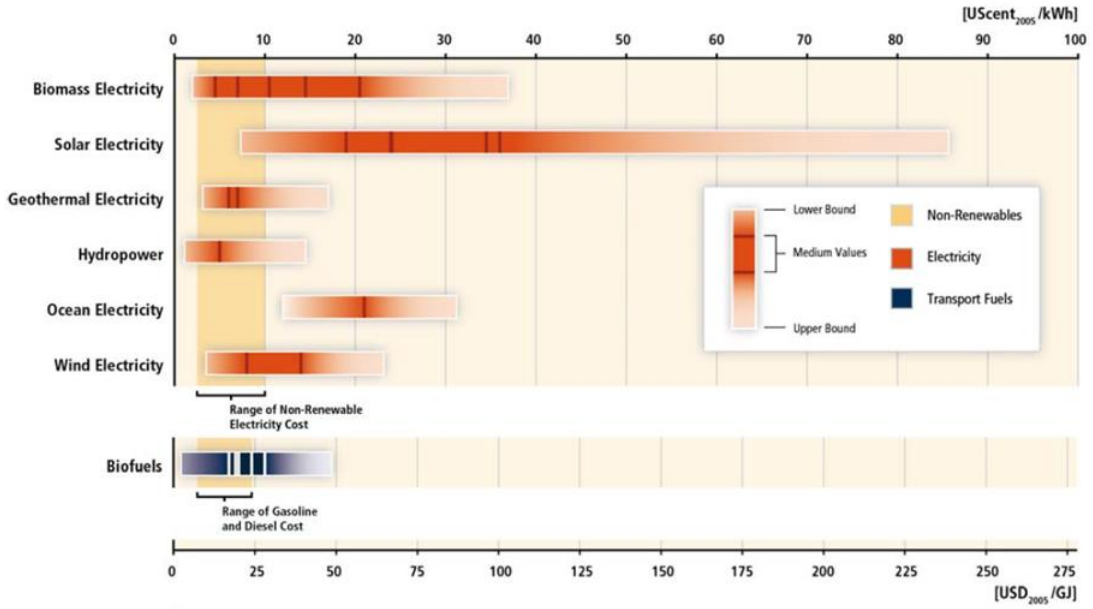

Figure 1.4. The levelised cost of energy for selected renewable technologies compared to recent non-renewable sources [IPCC (2011) pp. 42].

However, difficulties in infrastructure alterations and potential profits that can be made from oil, coal and gas mean these fossil fuels will continue to be attractive. In response to this, governments are looking for a way of mitigating the contribution of fossil fuel emissions to global warming. One way to do this is to trap and store the CO_2 as it is released from industrial point sources such as coal and gas power stations; this has become known as carbon capture and storage or carbon capture and sequestration (CCS).

1.6 Carbon Capture and Storage

A carbon capture and storage (CCS) process would consist of the separation and capture of CO_2 at large point sources. The CO_2 would then be compressed and transported to a long-term storage location where it can be isolated from the atmosphere. Other approaches to mitigating climate change rely on increasing energy efficiency and the use of renewable energy sources or nuclear power. Because CCS removes CO_2 from the atmosphere it can allow the continued combustion of fossils fuels facilitating, in terms of time and cost, the transition from non-renewable to renewable technologies. Currently available technology captures 85–95% of CO_2 processed at a capture plant. Compared to a site without CCS a plant equipped with CCS would require 10–40% more energy for operation [Chapel *et al.* (1999)]. It is estimated that application of CCS to energy production would increase electricity costs by 0.01–0.05 US dollars per kilowatt hour (US$/kWh), based on 2002 data [IPCC (2005) pp. 10]. Of the predicted overall cost for CCS $40-80/t$CO_2$, the cost typically includes $30-50/tCO2 for capture, $5-20/t$CO_2$ for

onshore/offshore pipeline transport (100-200 km) and \$5-10/tCO_2 for storage , dependent on combustion and storage type, some 40 % of the transport costs will be associated with CO_2 compression into a supercritical fluid [IEA (2008)].

An alternative to long term storage is the utilization of CO_2 as a feedstock for the manufacture of fuel, chemicals and materials, this is a process that has become known as Carbon Capture and Utilization (CCU) [Styring *et al.* (2011)]. For example, using photoelectrochemical systems with electrocatalysts CO_2 may be reduced to synthesize chemicals like methanol useful as fuels [Barton Cole *et al.* (2010)]. Alternatively the requirement of CO_2 for organic matter growth is useful, such as in Bio CCS Algal Synthesis. Here CO_2 is injected into membranes containing select strains of algae that grow rapidly forming a very oil-rich biomass that can be used as a fuel [Savage *et al.* (2011)]. The main barrier to the success of CCU is the high stability of the CO_2 molecule. So far the methods of CO_2 utilization are not suitable to handle the quantities of gas produced by industrial point sources. Therefore, while their implementation may be useful, some CO_2 will likely need to be stored elsewhere.

1.6.1 Storage of CO_2

1.6.1.1 Underground Geological Storage of CO_2

CO_2 deposits are naturally found within geological formations underground [Pearce *et al.* (1996)]. The formation of CO_2 reservoirs in similar geologic formations may be one way to store CO_2 and this process has become known as underground geological storage. A large number of existing enhanced oil recovery schemes, where CO_2 is injected into existing oil fields to increase the amount of oil extracted, have shown that the storage of CO_2 in geological formations is feasible [Gale *et al.* (2003)], notable are projects in Sleipner, Weyburn and In Salah [IEA (2013)]. Industrial underground natural gas storage and acid gas injection have also shown that CO_2 can be stored and monitored safely. It is expected that 99% of the CO_2 injected into storage sites will be retained for 1000 years [IPCC (2005) pp. 14]. Suitable sites for storage are depleted oil and gas reserves, coal formations and saline formations (deep underground porous rocks saturated with brackish water or brine). At depths of 800-1000 m underground CO_2 is supercritical and liquid-like, making storage in porous sedimentary rock possible. Other mechanisms of storage are also apparent, such as trapping below an impermeable confining rock layer [Stefan *et al.* (2008)].

Ramifications from public fears regarding onshore geological storage of CO_2 mean that geological storage will likely occur offshore, with test-plants such as the North Sea's Sleipner gas field proving successful [Gale *et al.* (2003)]. Economic gains from increased oil and gas production at depleted oil and gas reservoirs may also offset the cost of the capture process and is very promising due to the currently existing infrastructure; such reserves have estimated capacity of 675-900 $GtCO_2$ while storage in porous sedimentary rock may be at least 1000 $GtCO_2$ [IPCC (2005) pp. 34].

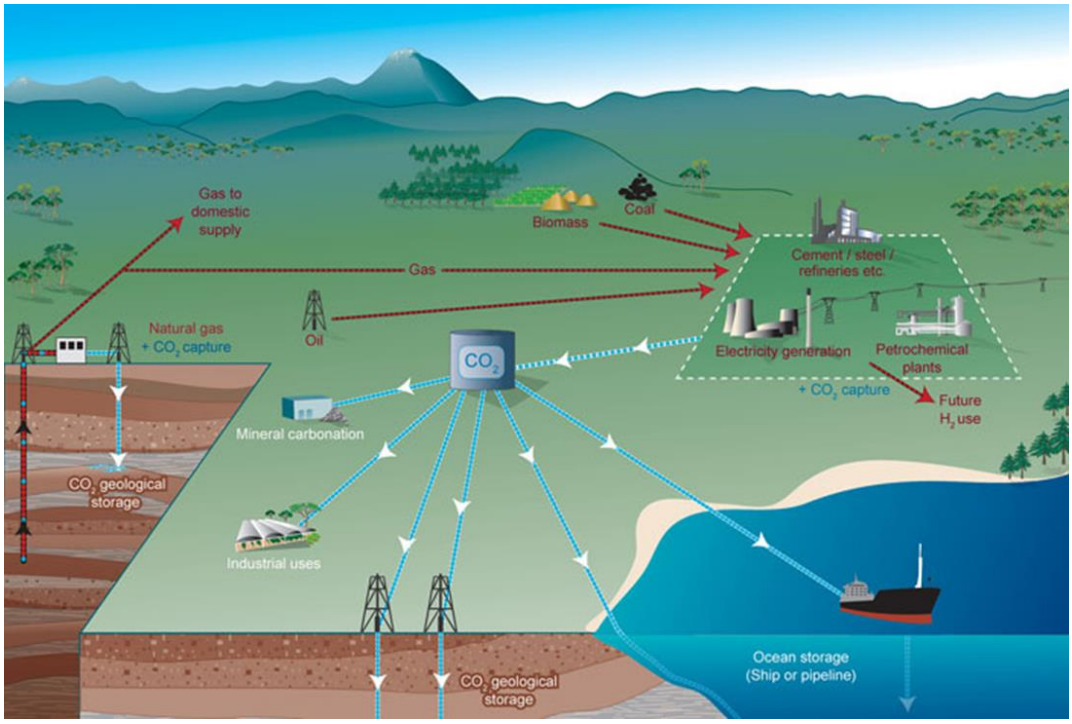

Figure 1.5. Schematic of possible CCS systems where CO_2 is captured and transported to a variety of storage sites [IPCC (2005) pp. 20].

1.6.1.2 Ocean Storage of CO_2

Several concepts have been presented for the ocean storage of CO_2. As CO_2 dissolves readily in water, one proposed method of storage is to pipe CO_2 to depths of 1000-3000 m forming an upward plume, the CO_2 subsequently dissolves in the seawater. By injecting the CO_2 at below depths of 3000 m the CO_2 liquefies, thus becoming denser than water and forms 'lake deposits' on the sea bed. The environmental impacts of such ocean storage methods are, however, poorly understood and much research and understanding will be required before such processes may be legally possible [IEA (2008) pp. 108].

1.6.1.3 Mineral Storage of CO_2

CO_2 can be exothermically reacted with metal oxides to form carbonates. Carbonates are stable and the process occurs naturally over many years. This process is responsible for much of the limestone found on the earth's surface. The stability of the carbonates means that the risk of release into the atmosphere is low and abundant minerals, such as olivine ($(MgFe)_2SiO_4$), make it an attractive option. Estimates expect the cost of a power plant to increase by 60 – 180 % with such a CCS system [IPCC (2005) pp. 330].

1.6.2 Transport of CO_2

Industrial pipelines are a well matured technology, routinely transporting oil, gas and water long distances through deserts, built up areas, the artic and under seas at depths of over 2000m. Enhanced oil recovery has also shown that CO_2 transport is possible on a large scale [Gale *et al.* (2003)]. To avoid corrosion, the CO_2 would be preferably dry and free of hydrogen sulphide.

1.6.3 Capture

1.6.3.1 Combustion Processes

The capture of CO_2 is expected to be from large point sources such as fossil fuel power plants, fuel processing plants and other industries such as those manufacturing steel, iron and cement. The capture of residential CO_2, that produced from transport or ambient CO_2, is costly and not under the potential regulatory scrutiny [Lackner (2003)], so will not be discussed here. For the capture of CO_2 from power plants three combustion processes have been proposed and most developed, they are: post-combustion capture, oxy-fuel capture and pre-combustion capture, each in its own state of maturity. In general, the technology for post-combustion currently exists, as too does pre-combustion capture, being widely applied in fertilizer manufacturing and hydrogen production.

Of key importance is that the different processes produce different flue gases, with temperature, gas mixtures, gas pressure and CO_2 partial pressures being variable. Oxy-fuel and pre-combustion capture have more complicated initial fuel conversion steps, but the higher CO_2 partial pressures make isolation of CO_2 easier.

1.6.3.1.1 Post Combustion Process

Post-combustion capture refers to the capture of CO_2 from a flue gas emitted when a fossil fuel or biomass is burnt in air. Combustion in air produces flue gas with a large quantity of nitrogen (70 %) and a variety of gases such as: CO_2, N_2 H_2O and O_2 along with air pollutants such as SO_x, NO_x and particulates [Rubin *et al.* (2005)]. Existing coal power plants use air for combustion, emitting a flue gas at ambient pressure containing around 15% CO_2 by volume, at a temperature expected to be between 50-120 °C for capture application [Arenillas *et al.* (2005)]. The CO_2 therefore needs to be selectively separated using a sorbent, membrane or cryogenic technique. The capture of CO_2 may be a problematic and energy intensive method but the combustion of fuels in air is such a widely used and economical approach for the extraction of energy from fuels that post-combustion capture is of high strategic importance.

1.6.3.1.2 Pre-Combustion Process

Pre-combustion capture involves the combustion of fuel in a stoichiometrically correct amount of oxygen (known as 'partial oxidation'), or steam/air (known as 'steam reforming') to produce H_2. In some cases the gas produced contains carbon monoxide and hydrogen and is known as a 'synthesis gas' (syngas) or 'fuel gas'.

$$C_xH_y + (x/2)O_2 \leftrightarrow xCO + (y/2)H_2 \quad \Delta H \text{ –ve} \quad \text{(partial oxidation)} \qquad \text{(Equation 1.1)}$$

$$C_xH_y + xH_2O \leftrightarrow xCO + (x + y/2)H_2 \quad \Delta H \text{ +ve} \quad \text{(steam reforming)} \qquad \text{(Equation 1.2)}$$

The carbon monoxide in the syngas is then reacted with steam in a catalytic reactor via a process called the water gas shift reaction to from carbon dioxide and more hydrogen.

$$CO + H_2O \leftrightarrow CO_2 + H_2 \quad \Delta H \text{ -41 kJ mol}^{-1} \quad \text{(water gas shift reaction)} \qquad \text{(Equation 1.3)}$$

The carbon dioxide is then removed leaving a hydrogen rich fuel that can be used in several applications. The flue gas is different dependant on fuel used (oil, coal, natural gas) and process conditions employed (gasification, integrated gasification combined cycle). Typically the gas entering the separation stage has a concentration of CO_2 of 15–60% on a dry basis, a pressure of 2–7 MPa, and is at ambient temperature [IPCC (2005) pp. 25, Martin *et al.* (2011a)]. Existing natural gas combined-cycle plants produce a flue gas containing around 3% CO_2 by volume [IPCC (2005) pp. 79].

1.6.3.1.3 Oxy-fuel Combustion Process

In oxy-fuel combustion, nitrogen is eliminated from the flue gas by burning a hydrocarbon or carbonaceous fuel in pure oxygen or a mixture of oxygen and a CO_2 rich recycled flue gas. Cryogenic air separation to obtain O_2 is required, making the process expensive (200 kWh/tCO_2) [IPCC (2005) pp. 118]. Combustion in pure oxygen environments occurs at temperatures of 3500 °C, too high for typical power plant materials, which would then have to be rebuilt if they are to operate with oxy-fuel combustion technology. The temperature of combustion must be controlled by the proportion of flue gas and gaseous or liquid water recycled. The flue gas consists mainly of carbon dioxide and water vapour with excess oxygen required to ensure complete combustion of the fuel. Cooling of the flue gas allows water to be removed via condensation and a flue gas containing 80–98% CO_2 is obtained [IPCC (2005) pp. 122], this flue gas mix makes the capture of CO_2 easier than for post-combustion.

Of these combustion processes, the large quantity of existing power plants that may be retrofitted with CCS technology and the scale of the challenge that represents, means that the development of materials for post-combustion capture is critical and will therefore be the focus of this thesis. The ramification of this is the CO_2 must be selectively captured from a mixed flue gas containing predominately CO_2, N_2 H_2O and O_2 along with air pollutants, at temperatures of 50-120 °C and at ambient pressures.

1.6.3.2 Capture and Separation Processes

As of May 2014, there were 60 large-scale integrated pilot plants [Global CCS Institute (2014)] adopting a variety of combustion processes, with no process as yet being a defined choice [Herzog *et al.* (2009)], giving subsequent reductions in costs the potential to be highly influential. One area where costs may be significantly reduced is in the capture process [Figueroa *et al.* (2008), Drage *et al.* (2012)]. Four different approaches to capture of CO_2 have been investigated with liquid amines being the current industry standard. It is likely that the flue gas will be dehydrated before CO_2 is isolated [Meadowcroft *et al.* (2009)], meaning separation of CO_2 from N_2 will be important.

1.6.3.2.1 Capture and Separation of CO_2 using Absorbent Materials

Absorption is a physical or chemical phenomenon whereby atoms, molecules or ions enter a bulk phase that may be solid, liquid or gas. The guest species are taken up in the volume of the absorbent material, differentiating it from adsorption where the adsorbate is taken up by the adsorbent surface. The process of CO_2 absorption by a liquid solvent or solid matrix is currently being tested and researched for scrubbing CO_2 from flue gas streams [IEA (2008) pp. 49].

Most existing industrial CO_2 capture systems are based on chemical absorption using a range of liquid aqueous amines such as monoethanolamine (MEA) in combination with heat induced CO_2 recovery [IEA (2008) pp. 49, Herzog *et al.* (2009)]. The flue gas is pumped through a column of solvent which selectively absorbs the CO_2. The CO_2 rich solution is then pumped to a tower and the solvent regenerated through thermodynamic manipulation (changes in temperature or pressure). High pressure and low temperature favour absorption, while low pressure and high temperature favour regeneration of the solvent. One main drawback is that during regeneration, the water content in the aqueous amines must also be heated, incurring a high energy penalty. The heating during regeneration amounts to 70-80 % of the operating costs when using liquid aqueous amines [Aaron *et al.* (2005)]. Problems are also caused by degradation of the solvent from fly ash and other flue gas particulates such as SO_x and NO_x. Oxygen content in the flue gas can corrode carbon steel facilities and cause excessive amine loss. The amines themselves are also corrosive and require specialised facilities. Furthermore high regeneration temperatures can also cause solvent loss and volatility. Various other forms of amines have been investigated such as sterically hindered amines that bind more CO_2 per molecule [Veawab *et al.* (1999)], MEA may also be blended with other amines to reduce corrosion and water content [Aroonwilas *et al.* (2004)].

Amines can interact with CO_2 via different mechanisms. Primary and secondary amines react directly with CO_2 to form carbamates through zwitterionic intermediates where the reaction is initiated by the lone-pair on the amine attacking CO_2. A free base deprotonates the zwitterion, H_2O can act as such a base meaning maximum efficiency for adsorption increases from 0.5 mol CO_2 per mol nitrogen in dry conditions to 1 mol CO_2 per mol nitrogen when wet [Choi *et al.* (2009), Caplow (1968), da Silva *et al.* (2004)]. Another mechanism, characteristic of tertiary amines yet also observed with primary and secondary amines, catalyses hydration of CO_2 to form a bicarbonate species.

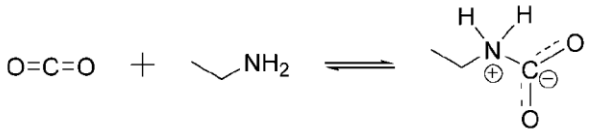

(Equation 1.4)

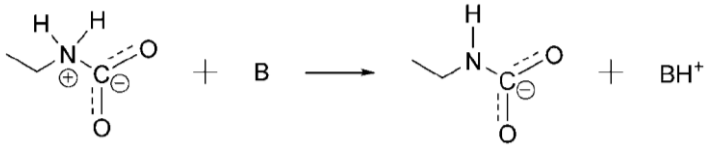

(Equation 1.5)

The replacement of liquid amines in CCS processes by an energy saving alternative is widely seen as a fundamental necessity for successful implementation of CCS systems [Figueroa *et al.* (2008)]. Solid absorbents, such as metal oxides could be utilised. Here metal oxides can react with CO_2 to produce a carbonate

$$M_xO + CO_2 \rightarrow M_xCO_3 \qquad \text{(Equation 1.6)}$$

The resulting carbonate can then be regenerated via calcination

$$M_xCO_3 \rightarrow M_xO + CO_2 \qquad \text{(Equation 1.7)}$$

As a natural mineral, limestone is cheap and widely available. It does not react with other species in the flue gas such as N_2 or O_2, therefore selectively removing CO_2. Calcination is carried out at high temperatures (900 – 1100 °C), but both calcination and carbonation steps require heating, so the overall energy penalty is not extreme [Florin *et al.* (2010)]. However, 'sintering' caused by heating dramatically decreases capture capacity over the first 20 cycles. After this there is a residual capacity that remains constant over many hundreds of cycles, this though is only around 7 % conversion by weight [Grasa *et al.* (2007)].

1.6.3.2.2 Capture and Separation of CO_2 using Membranes

Membranes are made from thin polymeric films and separate species based on their relative rates of permeation. Differences in permeation rates are generally due (with porous membranes) to the relative sizes of the permeating molecules or (for dense membranes) their solubilities and/or diffusion coefficients (i.e. mobilities) in the membrane material. Permeation rates change inversely with membrane thickness, therefore membranes are made as thin as possible. Membrane-based desalination of water and membrane-based gas separation are both mature technologies [Cabassud *et al.* (2003), Baker (2002)]. Membrane separation is pressure driven and requires high pressure of the feed gas or operation with vacuum conditions. The low

pressure of CO_2 in the flue gas make membranes unsuitable for post-combustion capture, they may though be suitable for pre-combustion capture [Pennline *et al.* (2008)]. Calculations looking at dependence of CO_2 capture costs on membrane permeability, selectivity and unit price, report that for membranes to compete with amine technology, CO_2/N_2 selectivity must be in the 200 range [Eric (2007), Zou *et al.* (2006), Powell *et al.* (2006)]. Typical selectivities are around 50-60 with rare exceptions [Powell *et al.* (2006)]. One such exception uses amine modified membranes reaching selectivity values of 170 [Huang *et al.* (2008)]. Cost of membranes is expected to be considerably less than the respective amine technology by around 65 %, membranes are heat sensitive and have low tolerance to temperatures over 100 °C [Davidson (2009)].

1.6.3.2.3 Capture and Separation of CO_2 using Cryogenic Distillation

Cryogenic distillation assumes that the flue gas is first purified to contain solely N_2 and CO_2. In a cryogenic chamber the temperature and pressure are then manipulated to cause the CO_2 to liquefy. The triple point of CO_2 is -56.6 °C and 7.4 atm [Aaron *et al.* (2005)] and at these conditions the condensation of CO_2 can be achieved, keeping N_2 as a gas. The CO_2 recovered from distillation can be highly pure (up to 99.95 % [Meratla (1997)]) and is in liquid form ready for transport via pipeline or tanker. However, the cryogenic process is very cost inefficient, requiring liquid nitrogen to keep the system cool. Furthermore, NO_x, SO_x, H_2O and O_2 all have to be removed before distillation can be carried out. Lab-scale trials of cryogenic distillation have predicted costs of \$32.7/t CO_2, the cost of absorption has been calculated as \$13.9/t CO_2 [Göttlicher *et al.* (1997)].

1.6.3.2.4 Capture and Separation of CO_2 via Adsorption on Solids

Adsorption is the process whereby an adsorbate, which could be atoms, ions, biomolecules or molecules of gas, liquids or dissolved solids, adhere to a surface. The adsorbate may form a film on the adsorbent surface and this film may consist of one or more layers of the adsorbate species. Adsorption processes can operate via weak physisorption processes or strong chemisorption interactions. Solid adsorbents are targeted for use in cyclic, mulimodule processes with adsorption and desorption being induced though temperature or pressure swing processes. A good adsorbent is characterised by: fast adsorption and desorption kinetics, large adsorption capacity, ease of regeneration, high stability and the ability to tune function to different operation conditions. In practice there is usually a trade-off between characteristics and

no ideal adsorbent is envisaged. Instead, strengths and weaknesses should be identified with regards to a practical and efficient CO_2 separation process.

The development of a solid adsorbent capture technology has been touted as one of the most promising alternatives to amine absorption for CCS [Figueroa *et al.* (2008)]. A key reason for this is studies suggesting an adsorbent system with a working capacity approaching or better than 3 mmol/g CO_2 could significantly reduce the energy requirement of post-combustion capture by 30-50% compared with amine solvent systems [Gray *et al.* (2008), Drage *et al.* (2012)].

The bulk of research into solid materials for the adsorptive capture of CO_2 from flue gases can be identified as being focused within four different classes of materials: zeolites, hydrotalcites, carbon based technologies and synthesised organic reticular frameworks.

1.6.3.2.4.1 Studies into the Adsorption of CO_2 on Zeolites

Zeolites are in a class of porous crystalline aluminosilicates built in periodic arrays of TO_4 tetrahedra (T = Si or Al). As a type of molecular sieve, they are heavily researched and the wide range of known topographies, synthetic and natural, is catalogued by the International Zeolite Association [www.iza-structure.org/databases]. The frameworks are organized through the negative charge introduced by aluminium atoms, balanced with cations (exchangeable, usually alkali) in the pore space. The variety of possible cations allows their structural characteristics to be tailored for specific applications, e.g. oil refinery, catalysis, water purification [Jansen *et al.* (1994)].

Adsorption of CO_2 onto zeolites occurs primarily via physisorption, with a small fraction (0.15 mmol g^{-1}) being chemisorbed in the form of a carbonate or carboxylate [Gallei *et al.* (1976), Ward *et al.* (1966)]. The physisorption properties can be affected by the electric field created by the charge balancing cations in the pores and by hydrogen bonding with surface silanol groups. With this in mind, zeolite composition may be altered to enhance CO_2 adsorption characteristics.

Porous characteristics of the zeolite's framework also affect the CO_2 adsorption properties. A range of zeolites (e.g. 4A, 5A, 13X, APG-II and WE-G 592) have been investigated for their adsorption capacities. It was found that 13X has the highest capacity, which may be due to it also having the largest pore volume. The contribution of individual zeolites structural characteristics can be seen in the wide range of CO_2 capacities: zeolite NaY (FAU) has been reported to reach 5 mmol g^{-1} at 273 K and 0.1 bar [Michelena *et al.* (1977)], HY-5 (1.2 mmol g^{-}

^{1}), 13X (4.5 mmol g^{-1}) [Harlick *et al.* (2004)] and ZAPS (2.6 mmol g^{-1}) [Hernández-Huesca *et al.* (1999)].

Zeolites show a rapid increase in CO_2 adsorption capacities with pressures increasing to 1 bar, from here capacity plateaus as pressure is increased up to 20 bar [Siriwardane *et al.* (2003)]. Measurements of 13X at three different temperatures (293, 308 and 323 K) show that CO_2 uptake decreases significantly with a small increase in temperature, meaning they may only operate in quite mild conditions.

Zeolites preferentially adsorb H_2O (potentially present in flue gas) over CO_2, an effect that may be favourable or detrimental. At low partial pressures of CO_2 pre-adsorbed H_2O can accelerate the adsorption of CO_2 for NaX zeolites [Bertsch *et al.* (1963)]. It is believed that the H_2O occupies high-energy sites within the zeolite decreasing the energy of activation for CO_2 diffusion. The H_2O may also be catalysing the formation of bicarbonate compounds on the adsorbent surface. Changes to the amount of H_2O present can cause substantial effects on the uptakes. The CO_2 uptake for a CaX zeolites measured at 0.06 bar CO_2 and 323 K decreased from 2.5 to 0.1 mmol g^{-1} as H_2O concentration increased from 0.8 to 16.1 wt% [Gallei *et al.* (1976)].

In conjunction with this water sensitive behaviour, zeolites are also hindered for practical application due to their low adsorbate-adsorbent binding enthalpies with CO_2, reducing capacity at elevated temperatures. In light of this various zeolites have been impregnated with basic amine functionality to enhance uptake capacity. MCM-41-PEI-50, a polyethylenimine impregnated mesoporous molecular sieve (MCM-41) achieved capacities of 4.8 mmol/g at 75 °C, 24 times higher than the original MCM-41 [Xu *et al.* 2002)]. Other modified zeolites include immobilized amine sorbent R-IAS which displayed a capacity of 4.1 mmol/g, an ethylendiamine-type modified mesoporous spherical particle sorbent EPA-modified-MSP with uptake of 3.5 mmol/g at capacity and tertiary amine DBU immobilised on PMMA beads which achieved uptake capacities of 3.0 and 2.3 mmol/g at 298 and 338 K respectively [Gray *et al.* (2005), Xu *et al.* (2003), Gray *et al.* (2008)]. However zeolites in general suffer from decreased capacity with regeneration [Gray *et al.* (2005), low stability and reduced textural properties with amine pore blocking [Drage *et al.* (2012), Yu *et al.* (2012)] .

The kinetic rates of adsorption for CO_2 on zeolites are good with 70 % of total capacity for natural zeolite ERI reached in the first 20 s at both 273 and 294 K, and full capacity reached after 100 s [Khodakov*et al.*(1995)]. Similar rates were recorded in other zeolites, such as zeolite NaA where saturation was achieved within 50 seconds, desorption took the same amount of time. Adsorption kinetics are not just dependent on the micropore structures but also the macro

and meso-porous character, a hierarchical structure favours fast adsorption kinetics [Zhou *et al.* (2007)].

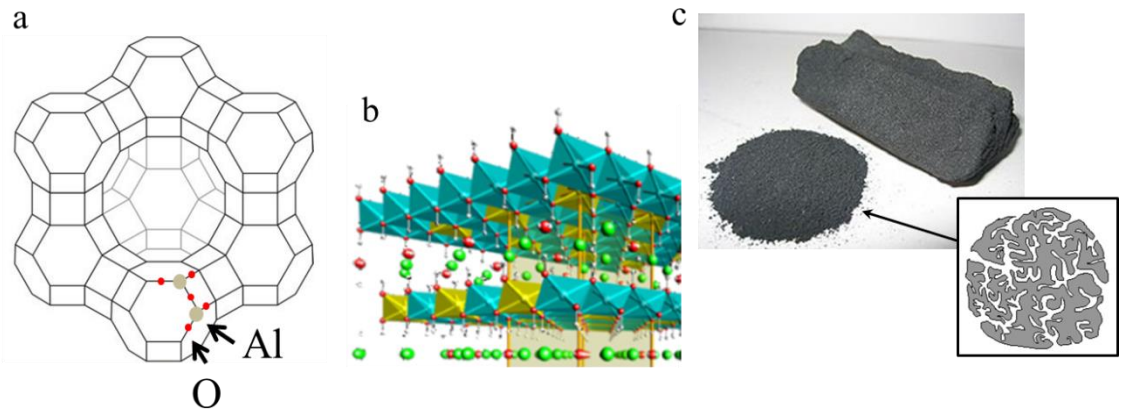

Figure 1.6. Schematic diagrams of (a) zeolites, showing positions of aluminium (Al) and oxygen (O) atoms, (b) hydrotalcite and (c) activated carbon with porous structure inset.

1.6.3.2.4.2 Studies into the Adsorption of CO_2 on Hydrotalcites

Hydrotalcites, also known as layered double hydroxides (LDHs), have the general formula $[(M^{2+}_{1-x}\ M^{3+}_{x}\ (OH_2)]^{x+}\ (A^{m-}_{x/m}.nH_2O)^{x-}$, where M^{2+} = Mg, Ni, Zn, Cu, or others, M^{3+} = Al, Fe, Cr, or others and A^{m-} = CO_3^{2-}, SO_4^{2-}, NO_3^-, Cl^-, OH^-, or others, with x typically in the range between 0.17 and 0.33 [Yong *et al.* (2002)]. They are composed of positively charged brucite-like $(MgOH)_2$ layers in which trivalent cations partially substitute for divalent cations located at the centre of octahedral sites in the hydroxide layer. Excess positive charge introduced by the cations is compensated for by species such as CO_3^{2-} anions and H_2O molecules in the interlayer region [Yong *et al.* (2002), Oliveira *et al.* (2008)]. They have modest sorption capacities, of up to and around 1 mmol g^{-1} [Oliveira *et al.* (2008)], but are of highlighted interest as their capacity for CO_2 increases in the presence of water, making them suitable for use with non-dehydrated flue gases. Capacity increases have been recorded from 2.74 wt% with a dry gas to 3.14 wt% with wet-gas conditions (equivalent to 0.62-0.71 mmol/g) [Ram Reddy *et al.* (2008)]. Hydrotalcites adsorb CO_2 via chemisorption onto adsorption sites, and do so optimally at around 573 K [Wang *et al.* (2007), Yong *et al.* (2000)]. At such elevated temperatures dehydration occurs and H_2O may maintain the hydroxyl content, a possible reason for the increase in capacity. Cyclic adsorbing and desorbing has been shown possible at 473 and 573 K respectively [Ram Reddy *et al.* (2008)], the formation of a unidentate form compared to a bidentate structure may hinder the ease of regenerability [León *et al.* (2010)]. Regeneration typically results in loss of capacity by around 10 % over the first ten cycles before stabilising [Ram Reddy *et al.* (2008)]. Generally, however, hydrotalcites offer a lower capacity then other

chemisorbents, though they may reach equilibrium capacity faster, taking tens of minutes. Modification by exchanging framework metal constituents or incorporating dopants has been attempted to increase performance; the optimal ratios of metals vary between species.

1.6.3.2.4.3 Studies into the Adsorption of CO_2 on Activated Carbon

Activated carbons are industrially common adsorbent materials and their potential for CO_2 capture is therefore not unexpected. They can be produced from coals, woods, biomass and industrial by-products such as petroleum, coke-pitch and scrap polymeric materials, and this wide availability makes their manufacture relatively low-cost. The preparation of activated carbon usually consists of two steps: carbonisation and activation. The carbonisation stage is a pyrolysis in an inert atmosphere, causing the material to release most of the non-carbon elements (oxygen, nitrogen, hydrogen) to give a carbonaceous material [Paolo (2002)]. Activation is either a physical or chemical treatment to produce suitable porosity, active sites and increase surface area. Physical activation can use steam, CO_2 or air in partial gasification at temperatures around 1100-1250 K. In chemical activation, chemicals such as potassium hydroxide (KOH), phosphoric acid (H_3PO_4) or zinc chloride ($ZnCl_2$) are used at lower temperatures to open up micropores [Ahmadpour *et al.* (1996) Maciá-Agulló *et al.* (2004)]. In conjunction with the activation process the initial starting material also has a large influence on the final properties. Commercial activated carbon has been reported to have highly varying CO_2 capacities due to their different pore characteristics. Temperature and pressure also have a large effect on the uptake capacity, and this again is influenced by the pore characteristics. Comparisons between commercial activated carbon and zeolites showed that the activated carbons have a lower capacity than zeolites at less than 1.7 bar for the materials tested [Siriwardane *et al.* (2001)], with uptakes greater for activated carbons at higher pressures. This has been attributed to activated carbons' usually larger surface area, pore size effects and zeolites' claimed higher surface affinity for CO_2. This stronger physical interaction between zeolites and CO_2 compared to activated carbon means the adsorbate-adsorbent binding enthalpies are higher for zeolites than activated carbons (36 and 30 kJ/mol^{-1} compared to 10.5−28.4 kJ/mol respectively [Chue *et al.* (1995), Guo *et al.* (2006)]). This binding enthalpy of adsorption between adsorbent and adsorbate (in this case CO_2) is calculated using the isosteric heat of adsorption method. This also means that desorption processes for activated carbons requires less energy than those for zeolites, it also may be the reason why activated carbons perform so well over multiple sorption/desorption cycles [Siriwardane *et al.* (2001)]. The kinetic rates of adsorption and desorption are much like zeolites, occurring over several minutes

[Wang *et al.* (2008)]. Similarly their uptakes are reduced due to the presence of water, which competitively adsorbs to the surface [Adams *et al.* (1988)].

Recent research activity in porous carbon solids tailored for CO_2 capture has resulted in exceptional capacities, especially at low pressures. Porous activated carbon monoliths (ACM) prepared from CO_2 activation of mesoporous polyacrylonitrile have exhibited uptakes of 5.1 mmol/g at 1 bar and 298 K. This porous carbon also achieved heats of adsorption as high as > 60 kJ/mol at zero CO_2 loadings [Nandi *et al.* (2012)], with the increase (from 10.5−28.4 kJ/mol [Guo *et al.* (2006)] ascribed to basic active sites created by nitrogen content doped into the carbon matrix. KOH activation of a variety of carbon precursors has also produced porous carbon solids with excellent uptake at ambient conditions. Various reports have achieved high uptake capacities using a meosoporous zeolite as hard-template, which can be etched using strong acid (HF) to yield porous carbon monoliths. Using mesoporous silica IBN-9 as template, polymerisation of nitrogen rich precursor p-diaminobenzene, etching and KOH activation, a nitrogen-doped porous carbon solid IBN9-NC1-A was obtained with uptake capacity of 4.5 mmol/g at 1 bar and 298 K [Zhao *et al.* (2012a)]. Similarly KNC-A-K and CHEM750 were synthesised using zeolites Silica SBA-15 and EMC-2 as templates and furfuryl alcohol and acetonitrile as carbon precursors respectively before template etching and KOH activation. CO_2 uptakes of the KNC-A-K and CHEM750 were 4.04 and 4.45 mmol/g respectively at 298 and 1 bar [Xia *et al.* (2011) and Zhao *et al.* (2012b). The use of pluronic F127 triblock copolymer as soft template with a phenolic-resin to produce porous carbon prior to activation yielded STC-R-500-A with an uptake capacity of 4.4 mmol/g [de Souza *et al.* (2013)]. Other nitrogen containing polymeric carbon precursors such as polypyrrole, polyacrylonitrile and polyaniline [Lee *et al.* (2013), Shen *et al.* (2011), Zhang *et al.* (2013)] have been synthesised and activated using KOH to obtained porous carbon solids with CO_2 capacities of 4.8, 4.4 and 4.5 mmol/g respectively. Biomass has also been used as a carbon precursor with KOH activation generating porosity: KOH activation of carbon obtained from lettuce leaves yielded porous carbon solids with uptake capacities of 4.3 mmol/g at 298 K and 1 bar [Wang *et al.* (2012a)], poplar anthers have also been carbonised and activated using KOH to achieve uptakes of 4.2 mmol/g [Song *et al.* (2014)]. A primary reason activated carbons achieve such good CO_2 uptakes at 1 bar (>4.0 mmol/g at 298 K) is their large micropore volumes. A study into KOH activated carbide-derived carbons (CDCs) shows the particular importance of pores 0.8 nm in diameter for CO_2 adsorption at 1 bar and 273 K (Figure 1.7) [Presser *et al.* (2011)].

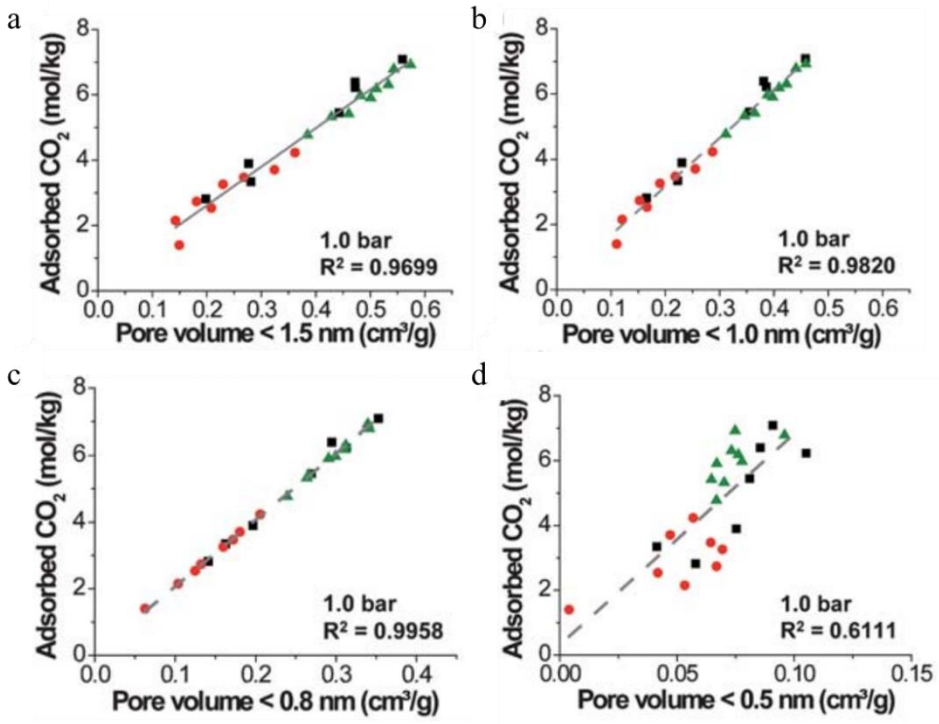

Figure 1.7. CO_2 uptake values at 273 K and 1 bar for the CDCs for pores smaller than (a) 1.5 nm, (b) 1.0 nm, (c) 0.8 nm and (d) 0.5 nm [Presser *et al.* (2011)].

1.6.3.2.4.4 Studies into the Adsorption of CO_2 on Synthesised Reticular Organic Frameworks

The term 'synthesised reticular organic frameworks' is used here to define a vast range of relatively novel materials that have received a large amount of recent research interest in gas storage application; such as metal organic frameworks and covalent organic frameworks. They are based on extended crystal structures of repeat units that utilize rigid bonding to create intrinsic porosity within the material.

Metal organic frameworks (MOFs) are crystalline solids consisting of three-dimensional organic-inorganic hybrid networks of metal centres bonded to multiple linking ligands. These networks have been formed from many different metal-ligand combinations (Figure 1.8) with the metals possessing multiple coordination sites and multidentate ligands bonding to more than one metal at a time.

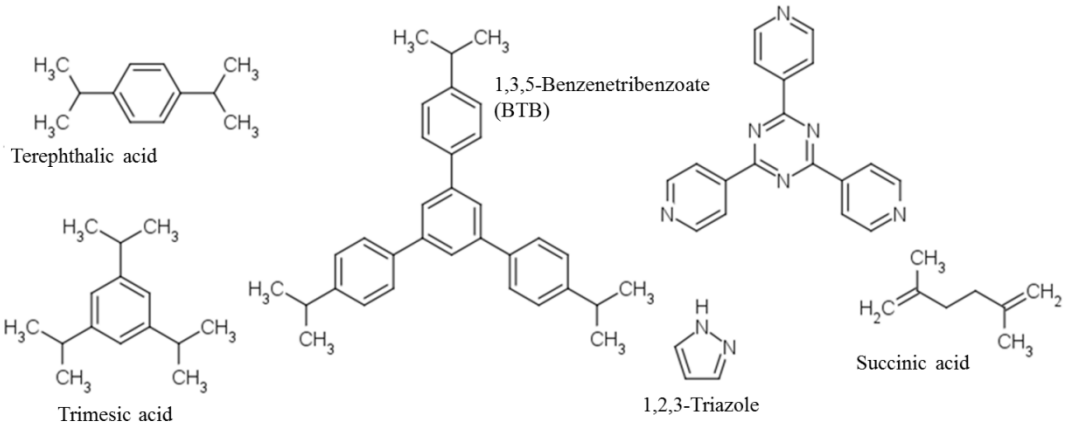

Figure 1.8. A range of bridging ligands that have been widely used in the generation of MOFs.

Many combinations of ligands and metal centres can be used to create MOFs, enabling control of pore sizes and surface areas [Eddaoudi *et al.* (2002)]. Although a wide range of MOFs can be produced, the methods of synthesis are usually similar, the metal precursors and appropriate ligands are mixed under hydrothermal or solvothermal conditions. The guest ions and solvents are then removed by applied vacuum or exchanges with volatile molecules to generate open coordination sites and therefore porosity. These open coordination sites, however, can be vulnerable to structural degradation by H_2O or other Lewis bases. H_2O is a common ligand for transition metals and thus open coordination sites in many MOFs show a strong affinity for it, with framework ligands being displaced generating defects in the crystal lattice.

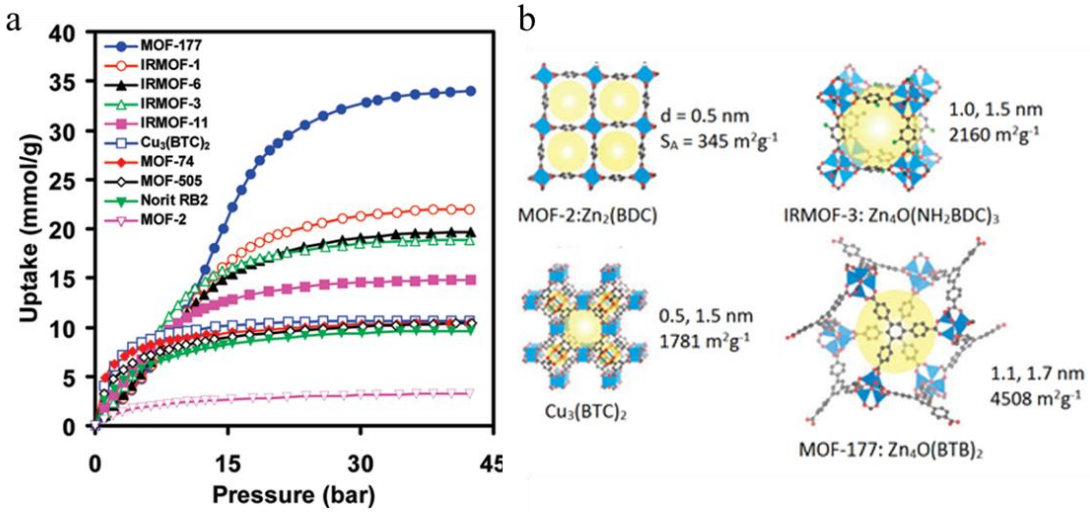

Figure 1.9. (a) Adsorption isotherms for several MOFs and commercial activated carbon Norit RB2, (b) Some MOF crystal structures giving values for pore diameter (d) and surface area (S_A) [Millward *et al* (2005)].

MOFs have exhibited exceptionally high BET surface areas of over 6000 m^2/g [Farha *et al.* (2010)], indicating potential for enormous CO_2 storage capacity. At high pressures, MOFs with

ultrahigh surface area are able to store up to nine times more CO_2 than an empty pressurized container [Llewellyn *et al.* (2008) Millward *et al.* (2005)]. Compared to zeolites and activated carbon sorbents MOFs typically exhibit greater surface areas, higher crystallinity with well-defined pore properties, and offer structural and chemical tunability through ligand and metal selection (Figure 1.9). MOFs however do not necessarily bind CO_2 selectively, also taking up large amounts of other small gases such as N_2, CH_4, CO and O_2. As a result the enhancement of CO_2 binding affinity in MOFs has seen extensive research using methods such as ligand functionalization, amine grafting and constriction of open metal sites, all increasing the MOFs affinity and selectivity for CO_2 [Panda *et al.* (2011), An *et al.* (2010)], Yazaydin *et al.* (2009a), Yazaydin *et al.* (2009b)]. Of note is zeolitic tetrazolate framework (ZTF-1), synthesised using a nitrogen rich tetrazolate ligand. It has a strongly Lewis basic character and is reported to adsorb 16.7 wt% CO_2 at 298 K and 1 bar (equivalent to 3.8 mmol/g) [Panda *et al.* (2011)]. Strongly basic sites have also been achieved grafting amine functionality onto crystalline MOFs. TEA@Bio-MOF-1 achieved an uptake of 4.2 mmol/g at 1 bar and 198 K after modifying bio-MOF-1 via a postsynthetic cation exchange with tetraethylammonium cations [An *et al.* (2010)]. The isosteric heats of adsorption at zero CO_2 loading were calculated as 25.4 and 35 kJ/mol for ZTF-1 and TEA@Bio-MOF-1 respectively. Another well documented route to enhance the affinity and selectivity of MOFs toward CO_2 is the generation of exposed metal cation sites on pore surfaces. Such open metal sites are typically obtained by incorporating solvent molecules (e.g. H_2O and DMF) as terminal ligands, which can be readily removed under vacuum or at elevated temperatures. Of these, notable are HKUST-1 with open Cu^{2+} sites and MOF-74 in which Co, Mg, Ni and Zn forms all exhibit high CO_2 affinities. The ultrahigh adsorption capacities at 1 bar and 298 K of 6.2 and 4.2 mmol/g for Mg-MOF-74 and HKUST-1 respectively coincide with high binding energies of 42 and 29 kJ/mol [Yazaydin *et al.* (2009a), Yazaydin *et al.* (2009b)]. At high pressure the large open pores in MOFs such as in MOF-77 and MOF-210 result in high total carbon dioxide storage capacities of 33.5 and 65.2 mmol/g [Furukawa *et al.* (2010), Millward *et al.* (2005)]. Such extraordinary capacity at high pressures coincides with s-shaped isotherms, where at low pressures small changes in relative pressure result in small changes in capacity [Bourrelly *et al.* (2005) Fletcher *et al.* (2001), Li *et al.* (2001)]. The reason for this has been mooted as a pressure driven change of crystal structure or attributed to electrostatic interactions between CO_2 molecules in the MOF pores. Materials that exhibit this adsorption step are unlikely candidates for post-combustion capture where CO_2 relative pressures are low.

Conversely, a range of entirely organic porous materials have been produced using a variety of tools to incorporate porosity into networks of monomeric building blocks consisting of light non-metallic elements (C, H, N, O and B). These materials include: covalent organic

frameworks (COFs), polymer of intrinsic microporosity (PIMs), porous aromatic frameworks (PAFs), conjugated microporous polymer (CMPs) and hyper-cross-linked polymers (HCPs) [Holst *et al.* (2010a)], and can be grouped in a class as microporous organic polymers (MOPs) when pore sizes are on average less than 2 nm [Jiang *et al.* (2010)].

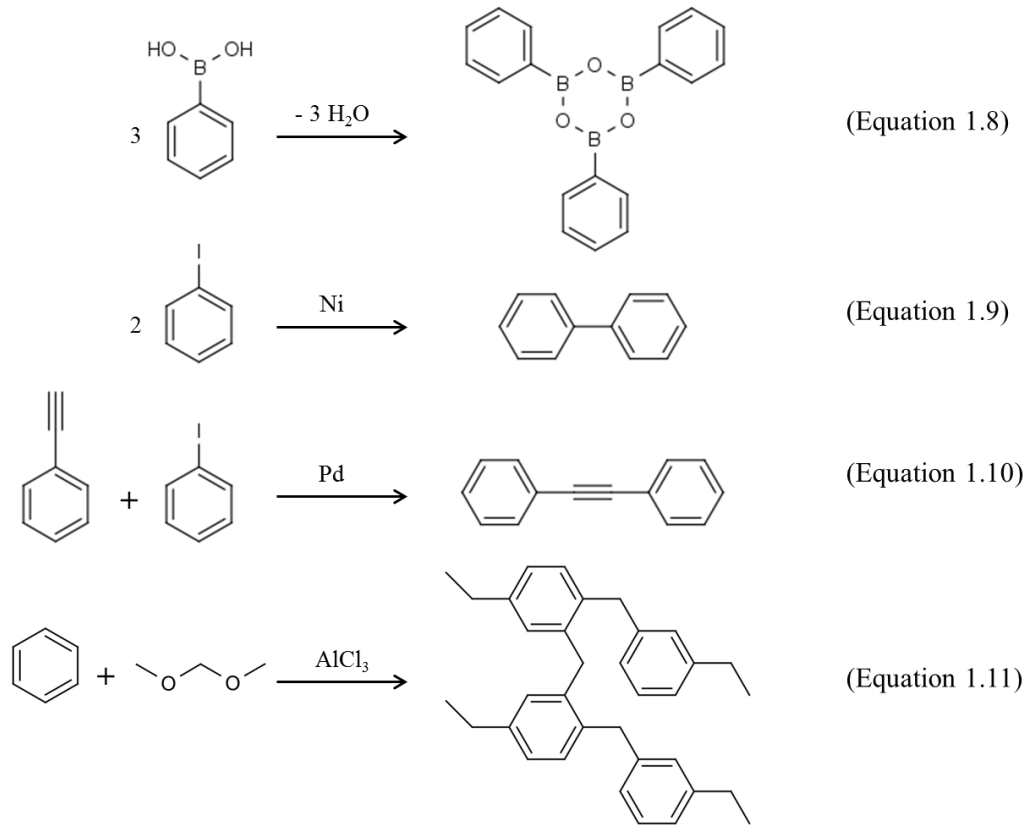

Figure 1.10. Reaction schemes commonly used for the synthesis of microporous organic polymers. Displaying the condensation of boronic acids, Yammamoto-type Ullmann coupling, Sonogashira coupling and Friedel-Crafts acylation, for equations 1.8, 1.9, 1.10 and 1.11 respectively [Jiang *et al.* (2010)].

The monomeric building blocks share similar traits: many are based around aryl groups and attempt to incorporate rigid bonds linking monomer subunits together to form rigid frameworks containing micropores and narrow mesopores (e.g. COF-10) [Côté *et al.* (2007)]. As polymers typically pack space to maximise attractive interactions between constituent groups, thus minimising the amount of void space, use of rigid monomeric units and linkages is vital for attainment of porosity in MOPs [Budd *et al.* (2005)]. Various chemical approaches have been explored (Figure 1.10), Yamamoto-type Ullmann (Equation 1.9) and Sonogashira coupling chemistry (Equation 1.10) have been used to produce 3-dimensional CMPs (Figure 1.11(a)) [Holst *et al.* (2010b)]. These networks exhibit BET surface areas over 3000 m^2 g^{-1}, micropore diameters centring around 1.4 nm and CO_2 adsorption capacities measured at 298 K and 1 bar of 1.7 mmol g^{-1}. PAF-1 was also produced using Yamamoto-type Ullmann coupling, the material has a recorded BET surface area of 5600 m^2 g^{-1} and a CO_2 adsorption capacity of 29.5 mmol g^1

at 40 bar and 298 K (Figure 1.11(b)) [Ben *et al.* (2009)]. COFs have primarily been produced via condensation reactions of boronic acids (Equation 1.8) to form boroxine anhydrides. Using a variety of different boronic acids 2- and 3-dimensional materials have been synthesised with pore diameters of up to 3.17 nm and BET surface areas up to 4210 m^2 g^{-1}. Their CO_2 uptakes at saturation reach around 27.3 mmol g^{-1}, comparable to high performing MOFs (22.1 mmol g^{-1} for MOF-5) and 9.5 and 7.9 mmol g^{-1} for activated charcoal Norit RB2 and zeolites respectively [Furukawa *et al.* (2009)]. Using reversible processes such as the boronic acid condensation reaction, COFs have been synthesised with exceptional crystallinity and long range order, less reversible reactions such as those used to produce CMPs result in a more amorphous structure.

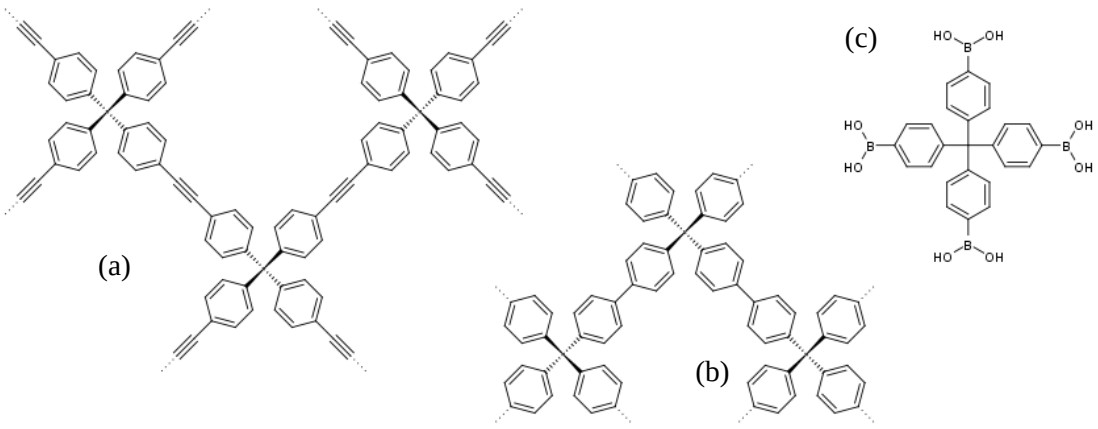

Figure 1.11. Several examples of porous organic molecules (a) CMP Network-4, (b) PAF-1, (c) 3-D COF monomeric unit, tetra(4-dihydroxyborylphenyl) methane (TBPM).

PIMs are continuous networks of interconnected intermolecular voids, which form as a direct consequence of the shape and rigidity of the component macromolecules. They combine rigidity with contorted molecular structures such as triptycene units to limit polymer components ability to rearrange, therefore maximising void space. BET surface areas in PIMs are typically <1000 m^2/g, however, they are solution-processable making them very attractive in membrane applications [McKeown *et al.* (2010)]. Structural characteristics such as surface area and CO_2 capacities for MOPs are attractive, however, the synthesis methods are frequently complicated, require expensive catalysts and reagents and are often hard to isolate. In response to this, HCPs have been produced using single step Friedel-Crafts coupling reactions that link rigid building blocks using the industrially available $FeCl_3$ catalyst (Equation 1.11). Using this approach and a 1,3,5-triphenylbenzene building block CO_2 uptakes of 3.6 mmol/g at 1 bar and 273 K, and a BET surface area of 1059 m^2/g have been achieved [Li *et al.* (2011a). In general MOPs are currently unsuitable for the large quantities of flue gas in post-combustion processes but with potential applications in catalysis, gas separation and storage, research is still on-going, with developments such as organic cages [Cooper (2011)].

This report has now outlined the need for high performance CO_2 capture materials and the environment in which they will need to operate. A variety of existing materials that may be suitable for this application have also been covered and the reasons why certain materials may be more applicable than others have been discussed, highlighting features that make a good sorbent such as: basicity [Nandi *et al.* (2012)], high surface area [Ben *et al.* (2009)] cyclability [Lu (2012)] and pore structure [Siriwardane *et al.* (2001)].

1.6.4 The Scope of this Work

So far this thesis has briefly outlined the fundamental characteristics of the principal solid adsorbent materials and the potential import of such materials for the capture of CO_2. However, it is clear that some are impractical and therefore hindered for industrial application. Hydrotalcites have only displayed moderate uptake capacities (<1 mmol/g at 1 bar and 298 K) and are deemed unlikely to achieve the target working capacity of 3 mmol/g [Drage *et al.* (2012)], their high operational temperatures also make them unsuitable for post-combustion applications. The COFs so far synthesised often use expensive catalysts in their synthesis regimes and would likely prove too expensive for large scale industrial applications, furthermore boronic anhydrides are sensitive to hydrolysis making them particularly unsuitable for post-combustion capture due to potential moisture in the flue gas. MOFs often require complex linker groups and in turn are sensitive to structural degradation by H_2O or other Lewis bases and unsuitable for similar reasons, and although the zeolitic imidazole framework (ZIF) class of MOFs are reported to have greatly improved hydrolytic stability [Park *et al.* (2006)], the linker molecules are frequently economically expensive and capacities moderate at ambient pressures. Water and other impurities in flue gases will bind to the open metal sites in MOFs, further diminishing their likelihood for real industrial applications, as the high CO_2 uptake performance is attributed to these sites. Zeolites have also exhibited large uptake capacities, and are in line with the working capacity of 3.0 mmol at >323 K for post-combustion capture applications, however the long term stability and reduced capacity over regeneration may hinder their use in an adsorption-desorption industrial cycle process.

Alternatively porous activated carbon solids present a highly attractive solution for the industrial capture of flue gasses. Their synthesis comes at a potentially low economic cost and they have shown excellent uptake capacities through use of various activation mechanisms, also they are highly stable and have exhibited no loss of capacity over many cycles [Li *et al.* (2013)]. For these reasons this thesis will focus on the development of porous solid carbon materials for CO_2 capture.

While porous solid carbon materials are attractive, the adsorption of CO_2 is achieved via weak physisorption and van der Waals interactions, as indicated by their relatively low heats of adsorption, <28 kJ/mol [Guo *et al.* (2006)]. This means that the adsorption capacities decline rapidly with increasing temperature and so may not achieve the required capacity at typical flue gas temperatures of over 323 K[Gray *et al.* (2008)]. It has been highlighted that to avoid energy-intensive CO_2 capture physisorptive processes should be used, i.e. where the enthalpy of adsorption is <40 kJ/mol, rather than chemisorptive processes where the enthalpy is >40 kJ/mol [Keskin *et al.* (2010)] and we can therefore use this as a guide to tune dopants in our carbon structures, aiming for enthalpies of adsorption around 40 kJ/mol. Furthermore the CO_2 selectivity over other gases present in the flue gas such as nitrogen is quite low for porous carbon solids, typically <10 when calculated using the IAST method [Zhang *et al.* (2013)]. For membrane separation processes to compete with the existing amine absorption technology selectivity values of 100-200 have been set as an essential prerequisite [Van der Sluijs *et al.* (1992)]. For adsorbent solid technology a prerequisiet has not been set, rather a trade-off between the materials capacity, lifetime, cost of regeneration and selectivity will determine competitivity relative to existing amine absorbents. Through the introduction of basic surface functionalities the working capacity at high temperatures and CO_2 selectivity may then be enhanced.

1.6.5 Mechanisms for the Enhancement of Porous Carbon Solids for the Industrial Capture of CO_2

The introduction of basic surface functionalities such as nitrogen groups into carbon materials to produce nitrogen-doped (N-doped) porous carbon is an area of significant interest, with various reports stating CO_2 capacities are higher in N-doped carbon when comparing with undoped materials of similar porous characteristics [Wu *et al.* (2012), Xia *et al.* (2011), Lv *et al.* (2012)]. For example, N-doped porous carbon has been produced using a silica-templated melamine-formaldehyde resin [Pevida *et al.* (2008b)]. Following polymerization the silica templates were removed (HF etching) and the resulting mesoporous melamine-formaldehyde resin was carbonized at temperatures between 400 and 700 °C. These products were analyzed showing a variety of nitrogen functional groups: triazine, pyrrole, pyridine and oxidized nitrogen, typical for most nitrogen-rich carbons. The samples were assessed for their CO_2 adsorption properties using a gravimetric process, performing tests at 298 and 348 K, the higher temperature giving a more realistic performance in real flue gas conditions. The best performing sample was carbonized at 600 °C and contained 24.4 mol% of nitrogen, it had a BET surface area of 490 m^2/g and capacity of 2.25 mmol/g at 298 K and 1 bar CO_2. Of the other samples synthesized,

several showed a notably higher surface area yet lower uptakes of CO_2 which was assigned to the role of the nitrogen dopants. Templated carbons (TCs) from zeolites (Y and EMC) were produced using either carbon based precursors such as furfuryl alcohol or the nitrogen containing precursor acetonitrile [Wang *et al.* (2012b)]. The resulting TCs shared similar textural properties but differed in that some were N-doped and others were undoped (Figure 1.12(a)). The relationship between the CO_2 adsorption capacities (298 K and 1 bar) and BET surface area of N-doped and undoped TCs clearly indicated N-doping enhances CO_2 uptake at these temperatures and pressures.

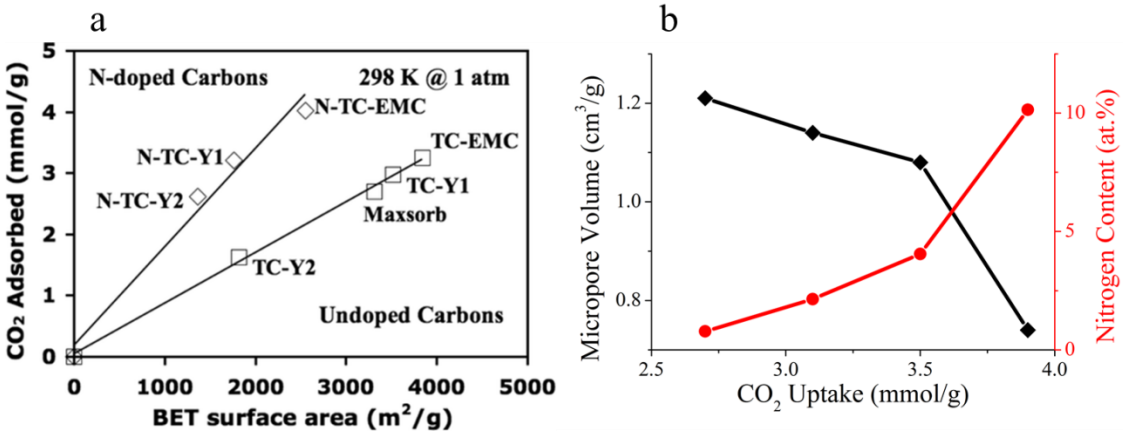

Figure 1.12. (a) Relationship between CO_2 uptake and BET surface area for N-doped and undoped template carbons [Wang *et al.* (2012b)] (b) Relationship between CO_2 uptakes, micropore volume and nitrogen content for a series of 4 N-doped carbons synthesised from polypyrrole (plotted from literature values) [Sevilla *et al.* (2011a)].

Further work highlighted the enhancement on CO_2 capacities from N-dopants with resorcinol-formaldehyde resins made using a lysine catalyst [Hao *et al.* (2010)]. The amino acid lysine enabled rapid gelation and afforded nitrogen functionality to the resulting carbons. Carbonisation at 500 °C yielded an N-doped porous carbon monolith with CO_2 uptake of 3.13 mmol/g at 298 K and 1 bar, as measured on a volumetric basis, the nitrogen content was reported as 1.92 at.% from XPS analysis. Again this sample exhibited a greater CO_2 capacity relative to undoped porous carbons despite the undoped carbons having greater surface areas. Polypyrrole polymers were activated using KOH to give N-doped porous carbons with nitrogen contents up to 10 at.% [Sevilla *et al.* (2011a)]. The best performing sample in the series achieved a CO_2 uptake of 3.9 mmol/g at 298 K and 1 bar CO_2, with a nitrogen content of 10.14 at.%. This material possessed the lowest BET surface area (1700 m^2/g) and micropore volume (0.88 cm^3/g) of the materials prepared, indeed a trend of increased CO_2 uptake is apparent as nitrogen content increases, despite a reduction in micropore volume (Figure 1.12(b)), giving further indication that N-doping within porous carbon solids enhances the CO_2 uptake capacities.

This increase of performance has been attributed to the electron rich nitrogen surface functional groups forming Lewis-base active sites that attract the Lewis-acidic CO_2 molecules. In these N-doped carbons the surface sites are typically aromatic groups of pyridinic, triazine, pyrrolic and pyridonic types which contain lone pair electrons capable of Lewis acid-base interactions [Vogiatzis *et al.* (2009)]. However, contrasting literature reports that CO_2 capture capacities of undoped and N-doped carbons are analogous to one another and nitrogen functionalities present in carbon materials do not influence CO_2 adsorption capacities [Sevilla *et al.* (2013)]. Instead the adsorption of CO_2 porous carbons is considered to be determined by the volume of the micropores with a size below 0.8 nm as indicated in Figure 1.7. To further investigate the role of N-dopants in porous carbon micropore volume and CO_2 capacities are plotted against nitrogen content for a variety of N-doped porous carbons found in literature (Figure 1.13(a), materials found in Table 1.1 and 1.2). It is important to note here that while CO_2 uptake is frequently correlated to a materials surface area, it is understood that CO_2 uptake is largely determined by micropore volume at ambient pressures [Zhang *et al.* (2013)], we therefore use micropore volume not surface area as a description of porous characteristics. The materials with greater nitrogen-doping are a darker blue colour with undoped carbon materials in grey. This highlights the fact that while the materials with highest nitrogen-doping are among those best performing, the appearance of undoped materials (grey) among these indicates nitrogen doping is not a prerequisite to achieving high uptakes.

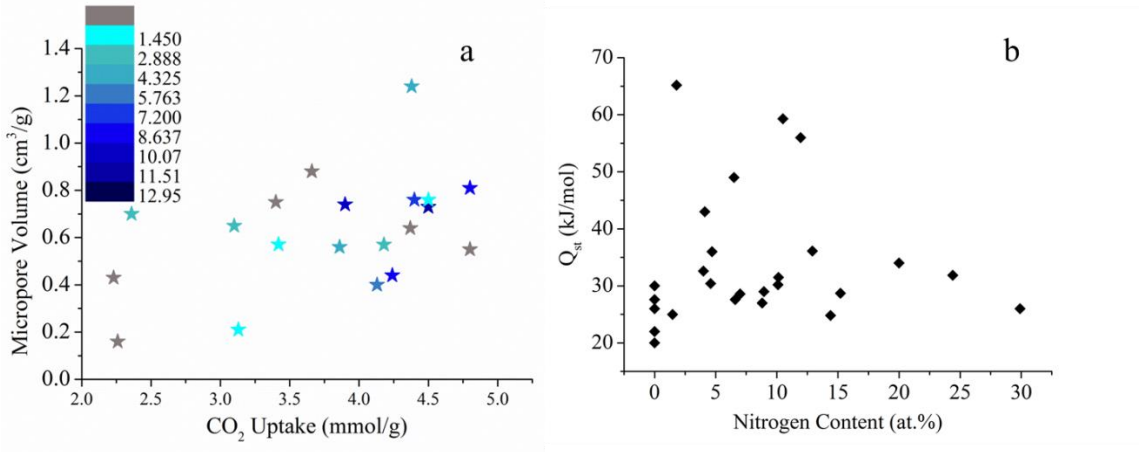

Figure 1.13. (a) Colour mapped scatter graph of micropore volume vs CO_2 uptake (298 K, 1 bar), highlighting the influence of nitrogen content (at.%) and (b) plot of isosteric heats of adsorption (Q_{st}) vs. nitrogen content for various porous carbon materials found in literature (materials listed in Table 1.1 and 1.2).

In undoped carbon sorbents the selectivity for CO_2/N_2 at 1 bar is reported as typically less than 10 [Sevilla *et al.* (2011a), Sevilla *et al.* (2012a), Hu *et al.* (2011a)]. However, this selectivity may be tuned through the introduction of dopants. For example, Polyacrylonitrile (PAN) containing a templating PBA block copolymer has been carbonised and activated using CO_2 to give copolymer-templated nitrogen-enriched carbons (CTNCs) [Zhong *et al.* (2012)]. The

resulting CTNCs showed a CO_2 capacity of up to 3.0 mmol/g at 298 K and 1 bar, with a BET surface area of 988 m^2/g and N/C ratio of 6.5 %. Interestingly the materials CO_2/N_2 selectivities increase remarkably with increasing nitrogen content. Using the ideal adsorption solution theory (IAST), a common method for evaluating the gas selectivity based on pure gas adsorption results, CO_2/N_2 selectivities of 33–42 were reported. Similar trends are shown by an IBN-9 silica templated N-doped carbon derived from the nitrogen-containing precursor, p-diaminobenzene (DAB) followed by KOH activation (IBN9-NC1) [Zhao *et al.* (2012a)]. The best performing sample showed CO_2 uptake of 4.5 mmol/g at 298 K and 1 bar with nitrogen content of 12.91 wt% and BET surface area of 1181 m^2/g. The CO_2/N_2 selectivities reached 42 with a strong trend indicating selectivity increased in line with nitrogen content.

For many N-doped carbon materials the CO_2 isosteric heat of adsorption (Q_{st}) has also been shown to increase with nitrogen content (Figure 1.13(b)). Highly porous N-doped activated carbon monoliths (AMCs) have been prepared from polyacrylonitrile precursors via a thermally induced phase separation (TIPS) technique followed by carbonisation using CO_2 activation [Nandi *et al.* (2012)]. The group reported high CO_2 uptakes of 5.14 mmol/g at 298 K and 1 bar, with a BET surface area of 2501 m^2/g and nitrogen content of 1.8 at.%. The Q_{st} was reported as 65.2 kJ/mol. The samples did not show correlation between nitrogen content increasing and Q_{st} increasing, indicating that pore characteristics, pore access and type of nitrogen site may also be important. Polyindole-derived microporous carbon materials (PIFs) have been synthesized via an oxidative template assembly route using cetyl trimethylammonium bromide (CTAB) before carbonisation and KOH activation [Saleh *et al*. (2013)]. At 298 K and 1 bar CO_2 this achieved an uptake of 3.2 mmol/g, CO_2/N_2 selectivities of 59 and heats of adsorption of 42.7 kJ/mol. These heats of adsorption are notably higher than undoped carbon-based materials (10.5−28.4 kJ/mol) [Guo *et al.* (2006)]. The Q_{st} values for these N-doped carbons is typically highest at zero loadings (CO_2), then decreases and then remains approximately constant with increasing CO_2 loading as the high energy N-sites get occupied and become saturated.

Lewis acid-base interactions have been widely cited as the foremost reason for the increased uptakes of N-doped materials with CO_2, however this may not be the full story. N-enriched activated carbons from bean dreg, a biomass waste, have been prepared using KOH chemical activation to enhance porosity [Xing *et al.* (2012)]. The best sample, with a BET surface area of 1060 m^2/g and 0.2 % nitrogen content, showed uptake of 4.24 mmol/g CO_2 at 25 °C and 1 bar. In conjunction with these results, computational work by the group suggests that hydrogen bonding interactions may also be important. Nitrogen atoms in the carbon lattice may alter the electronic structure of the graphitic layers and that of the graphene edge hydrogen atoms, which may in turn influence the interactions between the carbon surface and CO_2 molecules.

Table 1.1. Pore characteristics of high performing porous materials

Material	CO_2 uptake (1 bar)		SSA_{BET}	V_{micro}	Ref'
	273 K	298 K	(m^2/g)	(cm^3/g)	
TFM-1	1.73	-	738	0.139	Zhu *et al.* (2012)
CTNC-800	4.37	3.00	988	0.422*	Zhong *et al.* (2012)
CTF-0-400-20-5	4.22	-	2011	0.520	Katekomol *et al.* (2013)
BILP-3	5.11	3.30	1306	0.977*	Rabbani *et al.* (2012)
PIF7	-	3.42	1038	0.571	Saleh *et al.* (2013)
CMP-C	3.86	2.20	1237	0.487*	Dawson *et al.* (2011)
CP-2-600	6.20	3.90	1700	0.740	Sevilla *et al.* (2011a)
Amidoxime-PIM-1	2.74	1.65	531	0.204*	Patel *et al.* (2012)
IBN9-NC1-A	-	4.50	1181	0.730	Zhao *et al.* (2012a)
PPN-6-CH2DETA	-	4.30	555	0.192*	Lu *et al.* (2012)
PECONF-3	3.49	2.47	851	0.319*	Mohanty *et al.* (2011)
RFL-500	-	3.13	467	0.210	Hao *et al.* (2010)
MFB-600	-	2.25	490	0.116	Pevida *et al.* (2008)
KNC-A-K	-	4.04	614	0.260*	Zhao *et al.* (2012b)
SK-0.5-700	-	4.24	1060	0.440	Xing *et al.* (2012)
BILP-4	5.34	3.29	1135	0.530*	Rabbani *et al.* (2012)
ACM-5	11.51	5.14	2501	1.090*	nandi *et al.* (2012)
azo-COP-2	2.55	1.53	702	0.300*	Patel *et al.* (2013)
CS-6-CD-4	7.48	4.55	2284	0.990*	Wickramaratne *et al.* (2013)
YTC7	-	2.36	1685	0.70	Zhou *et al.* (2012)
CCI-30	5.57	5.14	831	0.367	Jin *et al.* (2013)
AC-2-635	-	3.86	1381	0.560	Fan *et al.* (2013)
ATS-4-700	5.40	3.40	1820	0.750	Sevilla *et al.* (2012a)
K4-700	-	3.45	1745	1.170*	Hu *et al.* (2011a)
AC-700-0.5	5.85	4.13	826	0.400	Zhang *et al.* (2013)
Micro-TiC-CDC (700 C)	7.09		1832	-	Presser *et al.* (2011)
STC-P-500-A	-	4.37	1743	0.640	do Souza *et al.* (2013)
PAN-PK	-	4.40	2231	0.760	Shen *et al.* (2011)
HPC-600-2	7.30	4.80	2003	0.810	Lee *et al.* (2013)
ZYC_1000	-		3010	1.220	Youn *et al.* (2011)
NPC-650	5.26	3.10	1561	0.650	Wang *et al.* (2013)
AG-2-700	7.40	4.50	1940	0.760	Sevilla *et al.* (2012b)
PA-400-KOH-2-600	-	4.18	1473	0.570	Song *et al.* (2014)
CEM750	6.92	4.38	3360	1.240	Xia *et al.* (2011)
AS-2-600	6.10	4.80	1260	0.550	Sevilla *et al.* (2011b)
K-PAF-1-600	-	3.66	2325	0.880	Li *et al.* (2013)
3C-60	-	2.26	758	0.160	Liu *et al.* (2011a)
AC Norit R1 Extra	-	2.23	1450	0.430	Himeno *et al.* (2005)

*When not directly reported, the uptake values have been taken from adsorption isotherms in the corresponding reference. CO_2 uptake at 298 K and 1 bar. SSA_{BET} = BET specific surface area, V_{micro} = micropore volume

In the carbons so far discussed the impact of the varying nitrogen species receives scant discussion [Arenillas *et al.* (2005)], with pyridinic, triazine, pyrrolic and pyridonic types all being typically present. A variety of porous polymers have been synthesised which may help

better understand the role of different nitrogen functionality in increasing the heats of adsorption and gas selectivity within CO_2 sorbents.

Table 1.2. Dopant characteristics, selectivity and Q_{st} of high performing porous materials

Material	Nitrogen content (at.%)	Nitrogen type	Selectivity CO_2/N_2 273 K (298 K)	Q_{st} (kJ/mol)	Ref"
TFM-1	9.0	Triazine	29	-	Zhu *et al.* (2012)
CTNC-800	6.5	N-doped carbon	7	49.0	Zhong *et al.* (2012)
CTF-0-400-20-5	20.0	Triazine	-	-	Katekomol *et al.* (2013)
BILP-3	7.0	Imidazole	59 (31)	28.6	Rabbani *et al.* (2012)
PIF7	2.6	N-doped carbon	-	-	Saleh *et al.* (2013)
CMP-C	20.0	Tetrazole	14.2	34.0	Dawson *et al.* (2011)
CP-2-600	10.1	N-doped carbon	5.3	31.5	Sevilla *et al.* (2011a)
Amidoxime-PIM-1	10.1	N-doped carbon	-	30.2	Patel *et al.* (2012)
IBN9-NC1-A	12.9	N-doped carbon	25-27 (15-3)	36.1	Zhao *et al.* (2012a)
PPN-6-CH2DETA	11.9	Diethylenetriamine	442	56.0	Lu *et al.* (2012)
PECONF-3	29.9	Secondary amine	77 (41)	26.0	Mohanty *et al.* (2011)
RFL-500	1.9	N-doped carbon	-	-	Hao *et al.* (2010)
MFB-600	24.4	N-doped carbon	-	31.9	Pevida *et al.* (2008)
KNC-A-K	10.5	N-doped carbon	48	59.3	Zhao *et al.* (2012b)
SK-0.5-700	8.8	N-doped carbon	-	27.0	Xing *et al.* (2012)
BILP-4	15.2	Imidazole	79 (32)	28.7	Rabbani *et al.* (2012)
ACM-5	1.8	N-doped carbon	-	65.2	nandi *et al.* (2012)
azo-COP-2	14.4	azo	110 (131)	24.8	Patel *et al.* (2013)
CS-6-CD-4	0.0	-	-	27.6	Wickramaratne *et al.* (2013)
YTC7	4.0	N-doped carbon	-	32.6	Zhou *et al.* (2012)
CCI-30	-	N-doped carbon	-	32.6	Jin *et al.* (2013)
AC-2-635	4.6	N-doped carbon	(21)	30.4	Fan *et al.* (2013)
ATS-4-700	0.0	-	(7)	26.0	Sevilla *et al.* (2012a)
K4-700	0.0	-	(8)	-	Hu *et al.* (2011a)
AC-700-0.5	6.6	N-doped carbon	(8)	27.6	Zhang *et al.* (2013)
Micro-TiC-CDC (700 C)	0.0	-	-	-	Presser *et al.* (2011)
STC-P-500-A	0.0	-	-	30.0	do Souza *et al.* (2013)
PAN-PK	8.1	N-doped carbon	-	-	Shen *et al.* (2011)
HPC-600-2	8.9	N-doped carbon	27	29.0	Lee *et al.* (2013)
ZYC_1000	0.0	-	-	-	Youn *et al.* (2011)
NPC-650	4.1	N-doped carbon	23 (12)	43.0	Wang *et al.* (2013)
AG-2-700	1.5	N-doped carbon	10	25.0	Sevilla *et al.* (2012b)
PA-400-KOH-2-600	3.8	N-doped carbon	-	-	Song *et al.* (2014)
CEM750	4.7	N-doped carbon	10	36.0	Xia *et al.* (2011)
AS-2-600	0.0	-	10	20.0	Sevilla *et al.* (2011b)
K-PAF-1-600	0.0	-	81	26.0	Li *et al.* (2013)
3C-60	0.0	-	-	-	Liu *et al.* (2011a)
AC Norit R1 Extra	0.0	-	-	22.0	Himeno *et al.* (2005)

Amines have been successfully grafted onto porous silicas [(Yang *et al.* (2013)] and organic polymers [Lu *et al.* (2012)]. Hyper-cross-linked networks have been produced using Friedel–

Crafts alkylation of benzene, and by the addition of aniline (amino benzene) copolymers containing amine functionality were afforded. This reduced uptake from 1.61 mmol/g to 0.35 mmol/g at 300 K and 1 bar for the 100% benzene polymer to the 100% aniline equivalent, ascribed to pore blocking effects. Incremental increase in amine quantity does though bring about incremental increase in CO_2/N_2 selectivity from 15.9 to 49.2 [Dawson *et al.* (2012a)]. Porous polymer network PPN-6 (also known as PAF-1 [Ben et al. (2009)]) has had various alkanoamines, such as mono, di- and tri-ethylenediamine (EDA, DETA and TETA) tethered inside the porous network [Lu *et al.* (2012)]. This resulted in improved uptakes at 1 bar CO_2 and 295 K from 1.3 mmol/g (PAF-1) to 4.3 mmol/g for the DETA (best performing) equivalent. It also showed exceptional CO_2/N_2 selectivity of 442 and isosteric heats of adsorption over 60 kJ/mol, calculated using dual-site Langmuir isotherm fitting. Polymers of intrinsic microporosity (PIM) contain nitrile (C≡N) groups, and PIM-1 has shown uptakes of 1.4 mmol/g at 298 K and 1 bar CO_2, with a Q_{st} of 28.4 mmol/g and a BET surface area of 889 m^2/g [Patel *et al.* (2012)]. The PIM-1 structure has been modified via conversion of nitrile groups into amidoximes. This decreases the BET surface area to 577 m^2/g but increases the uptake at 298 K and 1 bar CO_2 to 1.6 mmol/g and the heat of adsorption to 30.2 kJ/mol [Patel *et al.* (2012)]. The antioxime group may be enhancing the materials performance relative to the nitrile equivalent because it has a stronger interaction with the high quadruple moment of CO_2. Although carbon dioxide has no permanent dipole moment, there is a considerable charge separation in the C=O bonds. This results in a significant quadrupole moment. A molecule with a strong dipole moment, such as antioxime will then interact with the carbon of CO_2 through dipole-induced dipole and dipole-quadrupole interactions. It has been suggested, however, that the most important contribution comes from Lewis acid–Lewis base electrostatic interactions, due to the charge separation between the carbon and oxygen atoms of CO_2 [Vogiatzis et al. (2009)].

The triptycene units used in PIMs due their contorted structure can have amine functionality and have been used to produce benzimidazole-linked polymers (BILPs). BILP-3 shows a BET surface area of 1306 m^2/g, CO_2 uptake of 3.3 mmol/g, isosteric heats of adsorption of 28.6 kJ/mol, and CO_2/N_2 selectivity of 31 at 298 K and 1 bar. This BILP was constructed using rigid tetrahedral monomers as used in constructing PAF-1 and many COFs. Alternatively such BILPs synthesised to incorporate imidazole nitrogen functionality showed an uptake of 3.6 mmol/g at 1 bar CO_2 and 298 K, with a heat of adsorption of 28.7 kJ/mol. The BET surface area was 1135 m^2/g and CO_2/N_2 selectivity 32 [Rabbani (2012)]. PIMs have also been functionalised with tetrazole units, again replacing the nitrile groups. This has shown very good uptake of around 3 mmol/g at 0.03 bar CO_2 and good selectivities, for further details on this material I refer the reader to the graphs in the paper [Du *et al.* (2011)]. Various microporus organic polymers (MOPs) have been produced, many based on tetrahedral monomers [Dawson *et al.* (2011)]. Of

these MOPs, Network C containing tetrazoles units based on a structure from tetrahedral monomers showed an uptake of 2.2 mmol/g at 298 K and 1 bar, and a heat of adsorption of more than 33 kJ/mol at low coverage. An azo functionalised covalent organic polymer (azo-COP-1) has been synthesised, using a different synthetic procedure and tetrahedral monomers, this time achieving a BET surface area of 635 m^2/g and an uptake of 1.5 mmol/g at 1 bar CO_2 and 298 K [Patel *et al.* (2013)]. The authors reported an increasing CO_2/N_2 selectivity with increasing temperature, the opposite of the usual trend found in other porous solids. At 0 °C the CO_2/N_2 selectivity was 73.3 for azo-COP-3, and rose to 128.0 at 323 K This trend has been attributed to the azo functional group being N_2 "phobic" in character. The isosteric heat of adsorption for CO_2 was reported as 29.3 kJ/mol.

Yet another type of nitrogen containing functionality is the triazine ring, one commonly found in N-doped carbons. This has been incorporated into covalent triazine frameworks Prepared from 1,3,5-Tricyanobenzene with a molten $ZnCl_2$ catalyst [Katekomol *et al.* (2013)]. This achieved an CO_2 uptake of 4.22 mmol/g at 273 Kand 1 bar CO_2 with a BET surface area of 2011 m^2/g. Triazine functionality has also be included into a porous membrane using a superacid-catalyzed synthesis to produce triazine-framework-based porous membranes (TFMs) [Zhu *et al.* (1012)]. TFM-1 achieved a CO_2 uptake of 0.9 mmol/g at 298 K and 1 bar, with a BET surface area of 738 m^2/g/. The CO_2/N_2 selectivity was reported at 273 K to be 48.2 and the Q_{st} was 26.1-27.8 kJ/mol.

A variety of methods for the enhancement of porous solid carbon based materials for the post-combustion capture of CO_2 has now been highlighted and the impact of nitrogen dopants, activation techniques and carbon precursor are all pronounced on the obtained sorbent material. Specifically a successful design of a porous solid carbon for post-combustion CO_2 capture will likely include a highly microporous structure and contain nitrogen dopants, maximising CO_2 capacity at 1 bar and >323 K, and CO_2/N_2 selectivity. This thesis will therefore explore these themes for the development of novel solid porous carbon based sorbents and utilise various N-dopants: pyridine, triazine, quaternary and pyrrole to better understanding of the interaction between CO_2 and N-doped adsorbents.

To this end there are 6 chapters covering the results and discussion of the synthesised materials, with the first 5 outlining the synthesis and characterisation of the materials produced and the final chapter comparing their performance with one another and that of literature. From the first 5 experimental chapters, the first focuses on the potential use of the nitrogen-rich carbon nitride structure and the development of a microporous analogue. The second chapter is dedicated to further investigation of the role N-dopants play in the adsorption of CO_2 within porous carbon solids and this is achieved through carbonisation of various nitrogen-rich polymer carbon

precursors. The third outlines the synthesis of a porous N-doped graphene structure and will provide a good comparison to N-doped porous carbons which are typically highly defective. As the type of activated carbon synthesised from chemical activation using KOH is highly precursor dependent, the fourth chapter is therefore dedicated to an investigation of various carbon precursors, also enabling the effect of N-dopants to be more rigorously interpreted. A fifth chapter discusses the synthesis of a novel nitrogen-rich microporous organic polymer. Further motives for such investigations are presented at the start of each forthcoming chapter.

2. Experimental Details

2.1 Synthesis

2.1.1 Reagents and Materials

All glassware and ceramic boats were dried in an oven at 150 °C for 1 hour prior to use. Thermal treatments were carried out using either a Carbolite CWF 11/5 – chamber furnace or a Lenton LTF 12/50/300 horizontal wire-wound tube furnace fitted with a work tube of dimensions 38mm i/d x 46mm o/d x 900 mm long, with oxygen-free nitrogen (N4.8) used as protective gas. Chemicals were purchased from Sigma-Aldrich UK and used as received.

2.1.2 Carbon Nitride

2.1.2.1 Synthesis of Carbon Nitride

In air: melamine (10.001 g) was loaded in a ceramic boat and the boat covered with a lid. The boat was heated in a chamber furnace to 595 °C at 20 °C/min, with a dwell time of 1 hour. Yield = 4.388 g. The product was designated as g-C_3N_4.

2.1.2.2 Synthesis of Defective Carbon Nitride

Carbon nitrides with lattice structure defects were synthesized by mixing a carbon nitride precursor with a structure-defect directing agent.

2.1.2.2.1 Dicyandiamide and 3,5-Diaminobenzoic acid

Carbon nitride precursor dicyandiamide was mixed in weight ratios of 9:1, 7:3, 3:7 and 1:9 with structure-defect directing agent 3,5-diaminobenzoic acid and heated using the following procedure: dicyanamide and 3,5-diaminobenzoic acid were mixed together then added to a ceramic boat and covered with a lid. The boat was then loaded into a tube furnace and purged with N_2 for 30 minutes before heating at 3 °C/min to 595 °C, with a dwell time of 30 mins, under a steady N_2 flow. The products were designated as DCA:DBA X:Y, where X = weight ratio of DCA and Y = weight ratio of DBA used. See Table 2.1 for the yields obtained.

2.1.2.2.2 Dicyandiamide and Alkyamine

Carbon nitride precursor DCA was mixed with alkylamines butylamine (BA) and nonylamine (NA) in molar ratios of 2:1 and 5:1, using the following procedure: DCA and alkanoamine were added to water (4 ml) and stirred at 90 °C for 2 hours, the water was then removed in *vacuo* and the product dried in a vacuum oven at 150 °C overnight. The yellow solid was added to a ceramic boat and covered with a lid, then loaded into a chamber furnace and heated to 595 °C at

20 °C/min, with a dwell time of 2 hours. Hard brown macroporous cakes were obtained and designated as DCA:alkylamine X:Y, where X = weight ratio of DCA and Y = weight ratio of alkylamine used. See Table 2.2 for the yields obtained.

Table 2.1. Reagent quantities and yields for the DCA:DBA X:Y series

Sample Designated	Reagent quantities		Yield (g)
	DCA (g)	DBA (g)	
DCA:DBA 9:1	1.35	0.15	7
DCA:DBA 7:3	1.05	0.45	0.674
DCA:DBA 3:7	0.45	1.05	0.387
DCA:DBA 1:9	0.15	1.35	0.193
DBA 100 %	0	1	0.473

Table 2.2. Reagent quantities and yields for the melamine:alkylamine X:Y series

Material	Reagent quantities			Yield (g)
	Melamine	NA	BA	
Melamine:BA 2:1	1.00 g, 7.9 mmol	-	0.285 g, 3.9 mmol	0.230 g
Melamine:BA 5:1	1.00 g, 7.9 mmol	-	0.117 g, 1.6 mmol	0.312 g
Melamine:NA 2:1	1.00 g, 7.9 mmol	0.563 g, 3.9 mmol	-	0.283 g
Melamine:NA 5:1	1.00 g, 7.9 mmol	0.226 g, 1.6 mmol	-	0.275 g

2.1.2.3 Dissolving Carbon Nitride

Carbon nitride (synthesised as in air) (0.100 mg) was added to water (10 ml) and sonicated for 12 hours to form a milky solution with some precipitate. This was allowed to stand for 24 hours. The still milky liquid part was then isolated from the precipitate using a pipette and the water removed in a vacuum oven at 150 °C, yield = 0.007 g. The product was designated as g-C_3N_4 (aq).

The process was repeated and isolation of the milky solution attempted using centrifugation for 10 mins at 5000 rpm, leaving a clear colourless solution. This process was also carried out using N-butanol, gamma-butyrolactone and N, N-dimethylformamide.

2.1.2.4 KOH Activation of Carbon Nitride

Carbon nitride (synthesised as in air) (0.29 g) and KOH (0.58 g) were added to a mortar and well mixed using a pestle then added to a ceramic boat. This was loaded into a tube furnace and purged with N_2 for 30 minutes before heating at 5 °C/min, with a dwell time of 30 mins, under a steady N_2 flow. This was repeated at temperatures of: 700, 600, 450, 150 °C. Products were

added to water and stirred, isolating by Buchner filtration. This process was repeated until washes with a pH of 7 were achieved.

2.1.3 Carbonization of Nitrogen Precursors

2.1.3.1 Synthesis of a Melamine-formaldehyde Resin

Melamine (15.001 g) and formalin (7.142 g, 37 % formaldehyde) were added to distilled water (107.85 mL), sodium hydroxide (0.190 g) was then added and the mixture heated with stirring at 70 °C for 15 minutes. After this time, the mixture had formed a clear and colourless solution. The stirrer bar was removed and the solution allowed to cool. Hydrochloric acid (36 %) was added until a pH of 1.5-1.8 was achieved (final pH was 1.73). The resin was then cured at 50 °C for 2 days and at 95 °C for 5 days. The resin was placed in methanol for 2 days to extract water, changing the methanol 4 times a day. The resin was then transferred to tert-butanol for 1 day, changing the tert-butanol 4 times. The resin was isolated using Buchner filtration and freeze dried. A solid white polymer was obtained in yield of 16.910 g. The product was designated as MFR.

2.1.3.2 Carbonisation of Melamine-formaldehyde Resin

The melamine-formaldehyde resin was carbonised using the following procedure: MFR was added to a ceramic boat, loaded into the tube furnace and purged with N_2 for 30 minutes. The tube furnace was then heated to the desired temperature at a ramping rate of 3 °C/min, with a dwell time of 1 hour, under a steady N_2 flow. The heating temperatures used and yields for the derived carbons are given in Table 2.3.

2.1.3.3 Activation of Melamine-formaldehyde Resin

MFRDC 700 (0.303 g) was added to a ceramic boat, loaded into the tube furnace and purged with N_2 for 30 minutes. The tube furnace was then heated to 700 °C, ramping at 5 °C/min and with a dwell time of 15 minutes under a steady N_2 flow. Maintaining the temperature at 700 °C, the N_2 flow was switched to CO_2 flowing for 30 minutes at a flow rate of 3 L/min. The CO_2 flow was then switched back to N_2 and the furnace allowed to cool with a steady N_2 flow. A black powder was obtained in yield of 0.243 g. The product was designated as MFRDC 700 C30.

MFRDC 700 (0.302 g) was added to a ceramic boat, loaded into the tube furnace and purged with N_2 for 30 minutes. The tube furnace was then heated to 700 °C, ramping at 5 °C/min and dwelling for 15 minutes under a steady N_2 flow. Maintaining the temperature at 700 °C, the N_2 flow was switched to CO_2 and flowed for 60 minutes at a flow rate of 3 L/min. The CO_2 flow

was then switched back to N_2 and the furnace allowed to cool with a steady N_2 flow. A black powder was obtained in yield of 0.114 g. The product was designated as MFRDC 700 C60.

Melamine resin and KOH (1:2) were added to a mortar and well mixed using a pestle. This was added to a tube furnace and heated to 700 °C, ramping at 3 °C/min and dwelling for 1 hour under nitrogen. Yield = 0 %.

Table 2.3. Reagent quantities, temperature and yields for the carbonisation of MFR

Material	Temperature (°C)	Quantity of MFR (g)	Yield (g)
MFRDC 600	600	1.002	0.185
MFRDC 700	700	0.998	0.174
MFRDC 900	900	1.001	0.079

2.1.3.4 Carbonisation of Polyacrylonitrile and Polyvinylpyrrolidone

The carbonisation of polyacrylonitrile and polyvinylpyrrolidone was carried out using polyacrylonitrile of Mw 150,000 and polyvinylpyrrolidone of Mw 10,000, with the following procedure: the polymer was added to a ceramic boat, loaded into the tube furnace and purged with N_2 for 30 minutes. The furnace was then heated to the desired temperature at a ramping of 3 °C/min, with a dwell time of 1 hour, under a steady N_2 flow. Products were obtained as black powders, the heating temperatures used and yields are given in Table 2.4.

Table 2.4. Reagent quantities, heating temperature and yields for the carbonisation of polyacrylonitrile and polyvinylpyrrolidone

Material	Temperature (°C)	Polymer used	Quantity (g)	Yield (g)
PAN 700	700	Polyacrylonitrile	5.232	2.528
PAN 900	900	Polyacrylonitrile	8.278	3.602
PVP 700	700	Polyvinylpyrrolidone	14.300	1.029
PVP 900	900	Polyvinylpyrrolidone	15.574	1.043

2.1.3.5 KOH Activation of Polyacrylonitrile and Polyvinylpyrrolidone Derived Carbons

The polyacrylonitrile and polyvinylpyrrolidone derived carbons were activated with KOH using the following procedure: the derived carbon and KOH were added to a mortar and well mixed into a grey powder using a pestle. The mixture was then added to a ceramic boat, loaded into a tube furnace and purged with N_2 for 30 minutes. The furnace was then heated to 700 °C, ramping at 3 °C/min, with a dwell time of 1 hour under a steady N_2 flow. After cooling, the samples were washed by stirring with distilled water until a pH of 7 was achieved, isolating the

product using Buchner filtration. The black powders obtained were vacuum oven dried at 150 °C, the yields are given in Table 2.5.

Table 2.5. Reagent quantities, heating temperature and yields for the activation of polyacrylonitrile and polyvinylpyrrolidone derived carbons

Material	KOH (g)	Derived carbon	Quantity (g)	Amount transferred from mortar (g)	Yield (g)
PAN 700 KOH	3.079	PAN 700	1.531	4.396	0.666
PAN 900 KOH	3.035	PAN 900	1.420	4.050	0.855
PVP 700 KOH	2.824	PVP 700	1.420	4.028	0.803
PVP 900 KOH	1.573	PVP 900	0.784	2.111	0.406

2.1.4 N-Doped Porous Graphene

2.1.4.1 Synthesis of Graphene Oxide

Graphene oxide was prepared using a modified Hummer's method [Pei *et al*. (2012)]. Graphite powder (10 g, <20 μm) and sulfuric acid (230 mL) were added to a beaker (5 L) and cooled to 0 °C using an ice bath. To this was added potassium permanganate (30 g) slowly, avoiding rapid temperature rise (less than 20 °C). The reaction mixture was then cooled to 2 °C. The ice-bath was removed and the mixture stirred at room temperature for 30 min. Over this time, distilled water (230 mL) was slowly added to the reaction to keep the temperature under 98 °C. The diluted suspension was stirred for an additional 30 minutes and further diluted with distilled water (1.4 L), before adding hydrogen peroxide (100 mL). The mixture was left overnight. The graphene oxide was separated by centrifugation followed by decantation. In repeated washes using centrifugation followed by decantation, the graphene oxide was washed and neutralised to a pH >6.5 by excess water (approx. 15 L). The final product was obtained by freeze-drying to remove water in yield of 9.8 g. The product was designated as GO.

2.1.4.2 Thermal Reduction of Graphene Oxide

GO (1.002 g) was added to a ceramic boat, loaded into a tube furnace and purged with N_2 for 30 minutes. The furnace was heated to 500 °C, at a ramping rate of 20 °C/min, with a dwell time of 10 minutes, under a steady N_2 flow. After cooling, a jet black fluffy product was obtained in yield of 0.412. The product was designated as thermally reduced GO.

2.1.4.3 Ammonia Treatment of Graphene Oxide

GO (2.0 g) was added to a ceramic boat and loaded into a quartz tube and the tube vacuum purged with nitrogen. From being under vacuum the quartz tube was then filled with ammonia (100 %) up to a pressure of 1 bar. An outlet valve was then opened to allow ammonia to flow

through tube during heating. The quartz tube was heated to 500 °C at a ramping rate of 20 °C/min, with a dwell time of 10 mins. The ammonia flow was then switched for nitrogen flow and the tube allowed to cool. A fluffy black powder was obtained in yield of 0.82 g. The product was designated as NH_3-GO.

2.1.4.4 Dicyandiamide Treatment of Graphene Oxide

The treatment of graphene oxide with dicyandiamide was carried out using the following procedure: GO and dicyandiamide were mixed together using a pestle and mortar until a fine grey powder was obtained. The fine grey powder was then added to a ceramic boat, loaded into a quartz tube and the quartz tube vacuum flushed with N_2. With a steady N_2 flow the quartz tube was then lowered into the centre of a pre-heated furnace at a range of temperatures (250, 300, 350 and 400 °C) and heated for 10 minutes, with the expulsion of white fumes. After 10 minutes the tube was removed and allowed to cool under a steady flow of N_2. Black solids were obtained and designated as DCA-GO X, where X is the heating temperature used. See Table 2.6 for the yields obtained.

Table 2.6. Reagent quantities and yields for the DCA-GO X series

Material	Reagent quantities		Amount transferred from mortar (g)	Yield (g)
	GO (g)	DCA (g)		
DCA-GO 250	0.100	0.202	0.269	0.142
DCA-GO 300	0.102	0.201	0.272	0.157
DCA-GO 350	0.100	0.203	0.283	0.179
DCA-GO 400	0.101	0.202	0.293	0.180

2.1.4.5 Synthesis of a Monolayer-patched Nitrogen-doped Graphene

Following a literature procedure [Li *et al.* (2012a)], dicyandiamide (4.000 g, vacuum oven dried (120 °C)) and glucose (0.100 g) (weight ratio of 40:1) were mixed, added to a ceramic boat and loaded into the tube furnace purging with N_2 for 30 minutes. Under a steady N_2 flow the furnace was heated at 2 °C/min, to 600 °C with a dwell time of 1 hour, then to 800 °C, at 1.6 °C/min, with a dwell time of 1 hour. After cooling a black fluffy solid was obtained. The procedure was carried out 4 times achieving yields of 0.032, 0.029, 0.028 and 0.028 g. The samples were mixed and designated as MPNG.

2.1.5 Synthesis of Activated Carbon from Various Carbon Precursors

Activated carbon was synthesised using KOH as activating agent and 4 different precursors: D-glucose monohydrate, cellulose, used coffee grounds and a soft template polymer. The D-glucose monohydrate was uses as purchased from Sigma-Aldrich. For cellulose, cosmetic cotton

wool balls (100 % pure cotton) were purchased from Boots UK Limited. Wet fresh grounds of Starbucks Dark Roast coffee were removed from a DeLonghi ECAM 23.450.S machine, these were dried in a vacuum oven for 24 hours at 120 °C, obtaining dry grounds (CG). Details of the synthesis of the soft template polymer are given in 2.1.5.3.

2.1.5.1 Carbonisation of Carbon Precursors

Prior to activation, all of the carbon precursors were carbonised using the following procedure: the carbon precursor was added to a ceramic boat and loaded into a tube furnace and purged with N_2 for 30 minutes. The furnace was then heated to the desired temperature, ramping at 3 °C/min, with a dwell time of 1 hour under a steady N_2 flow. The yields are given in Table 2.7.

2.1.5.2 KOH Activation of the Derived Carbons from Various Carbon Precursors

The carbon derived from the carbon precursors given in Table 2.7 were activated with KOH using the following procedure: the derived carbon and KOH were added to a mortar and well mixed into a grey powder using a pestle. The mixture was then added to a ceramic boat, loaded into a tube furnace and purged with N_2 for 30 minutes. The furnace was then heated to 700 °C, ramping at 3 °C/min, with a dwell time of 1 hour, under a steady N_2 flow. After cooling, the samples were washed by stirring with distilled water until a wash with a pH of 7 was achieved, isolating the product using Buchner filtration. The black powders obtained were vacuum oven dried at 150 °C. See Table 2.8 for the obtained yields.

Table 2.7. Reagent quantities, heating temperature and yields for the carbonisation of a range of carbon precursors

Material	Temperature (°C)	Precursor	Quantity (g)	Yield (g)
Glucose 700	700	Glucose	14.419	3.057
Glucose 900	900	Glucose	17.474	3.372
CB 700	700	Cotton wool balls	4.767	0.682
CB 900	900	Cotton wool balls	3.117	0.420
CG 400	400	Coffee grounds	15.644	4.740
CG 700	700	Coffee grounds	5.003	1.303
CG 900	900	Coffee grounds	4.987	1.277
STP 700	700	Soft template polymer	11.283	3.376
STP 900	900	Soft template polymer	8.075	2.425

2.1.5.3 Synthesis of a Soft Template Polymer

A soft template polymer (STP) was synthesised using a preparation from literature [Liang *et al.* (2006)] via the following procedure: phloroglucinol (12.5 g) and pluronic F127 (12.5 g) were dissolved into 10:9 weight ratio mixture of ethanol (47.36 g) and water (42.63 g). After the

solids were dissolved under magnetic stirring at room temperature, HCl (1.0 g, 37%) was added to the solution as a catalyst. The solution was stirred at room temperature for an additional 30 mins. Subsequently, formalin (13.0 g, 37% formaldehyde) was added to the above solution. The solution turned cloudy after 30 minutes and separated into two layers after ~1 hour. The upper layer mainly consisted of the mixture of water and ethanol, while the lower layer was a colourless polymer-rich solution. The liquid layer was removed and the highly viscous portion left overnight. The resulting gelatinous resin was dried in an oven at 100 °C for 24 hours, obtaining a hard dark blue solid in yield of 24.4 g. The product was designated as STP.

Table 2.8. Reagent quantities and yields for the activation of carbons derived from a range of carbon precursors

Material	KOH (g)	Derived carbon	Quantity (g)	Amount transferred from mortar (g)	Yield (g)
Glucose 700 KOH	3.000	Glucose 700	1.523	4.262	2.971
Glucose 900 KOH	3.020	Glucose 900	1.503	4.323	1.060
CB 700 KOH	1.916	CB 700	0.915	2.590	0.492
CB 900 KOH	1.476	CB 900	0.780	2.043	0.458
CG 400 KOH	3.112	CG 400	1.546	4.445	0.780
CG 700 KOH	2.003	CG 700	1.021	2.860	0.506
CG 900 KOH	2.034	CG 900	1.013	2.641	0.676
CG 400 4-1	8.346	CG 400	2.104	10.257	0.740
CG 700 4-1	8.098	CG 700	2.028	9.775	0.949
STP 700 KOH	3.930	STP 700	2.047	5.687	1.380
STP 900 KOH	2.984	STP 900	1.426	4.012	0.950

2.1.6 Synthesis of the Phenolic Triazine Framework

2.1.6.1 Synthesis of 2,4,6-Tris(2,4,6-trihydroxyphenyl)-1,3,5-trizaine

The synthesis of 2,4,6-tris(2,4,6-trihydroxyphenyl)-1,3,5-trizaine was taken from literature [Conn *et al*. (2011)] and carried out using the following process: an oven-dried Schlenk flask was charged with a stirrer bar, cyanuric chloride (0.100 g, 0.542 mmol), phloroglucinol (0.206 g, 1.63 mmol) and vacuum flushed with nitrogen. To this was injected a 1:4 solution of 1,2-dichloroethane and diethyl ether (5.0 mL). The solution was cooled over ice and anhydrous aluminium chloride (0.216 g, 1.62 mmol) was added portionwise over 5 minutes. Upon completion of this addition the Schlenk flask was fitted with a condenser and the reaction transferred to an oil bath at 60 °C. The condenser was connected to a caustic soda bubbler. After 16 hours the solvent of the reaction was removed in *vacuo* and the solid resuspended in 10 % HCl (10 mL). The resulting colloidal solution was then spun in a centrifuge at 3500 rpm for 5 mins and the supernatant removed. The isolated solids were resuspended several times in further

HCl, then 3 times in distilled water (10 mL), isolating each time using centrifugation. The solids were finally resuspended in diethyl ether (10 mL), isolating again through centrifugation, before dissolving in ethanol and concentrating in *vacuo*; ^{1}H NMR (600 MHz, d_6-DMSO) δ 12.25 (br s, 6H), δ 10.15 (br s, 3H) and δ 5.89 (s, 6H); ^{13}C NMR (100 MHz, d_6-DMSO) δ 166.32, δ 163.31, δ 162.73, δ 98.53 and δ 95.19

2.1.6.2 Synthesis of Phenolic Triazine Framework using 1,2-Dichloroethane as Solvent

The phenolic triazine framework polymer was synthesised with 1,2-dichloroethane as solvent using the following procedure: an oven-dried Schlenk flask was charged with a stirrer bar, cyanuric chloride (3 mmol, 0.552 g) and either phloroglucinol (3 mmol, 0.378 g) or resorcinol (3 mmol, 0.330 g), and vacuum flushed with nitrogen. To this 1,2-dichloroethane (5 mL) was injected. The solution was cooled over ice and anhydrous aluminium chloride (9 mmol, 1.197 g) was added portionwise over 5 minutes. Upon completion the Schlenk flask was fitted with a condenser and the reaction transferred to an oil bath at 85 °C. The condenser was connected to a caustic soda bubbler. After 16 hours the reaction was allowed to cool. The obtained solids were cleaned by washing well with distilled water, then HCl (10 %) and further water until the pH of the wash reached 6-7. Soxhlet extraction was carried out for 2-3 days using methanol. The products were vacuum oven dried at 80 °C and designated as PTF P DCE (phloroglucinol equivalent) and PTF R DCE (resorcinol equivalent).

2.1.6.3 Synthesis of Phenolic Triazine Framework using 1,4-Dioxane as Solvent

The phenolic triazine framework polymer was synthesised with 1,4-dioxane as solvent using a range of scales, temperatures and concentrations using the following procedure: an oven-dried Schlenk flask was charged with a stirrer bar, cyanuric chloride (1 eq), either phloroglucinol or resorcinol (1 eq) and vacuum flushed with nitrogen. To this the solvent was injected. The solution was cooled over ice and anhydrous aluminium chloride (3 eq) was added portionwise over 5-10 minutes. Upon completion of this addition the Schlenk flask was fitted with a condenser and the reaction transferred to an oil bath at the desired temperature. The condenser was connected to a caustic soda bubbler. After 16 hours the reaction was allowed to cool. Typically, hard resinous solids were obtained and cleaned by washing well with distilled water, then HCl (10 %) and further water until the wash reached a pH of 6-7. Soxhlet extraction was carried out for 2-3 days using methanol. The synthesis was carried out using phloroglucinol with a range of temperatures and concentrations as outlined in Table 2.9.

Table 2.9. Reagent quantities and conditions for the synthesis of phenolic triazine framework

Material	Temperature (°C)	Dioxane (mL)	P	CC	$AlCl_3$
PTF 70 20	70 °C	20			
PTF 70 10	70 °C	10			
PTF 70 5	70 °C	5			
PTF 90 20	90 °C	20	0.378 g	0.552 g	1.197 g
PTF 90 10	90 °C	10	3 mmol	3 mmol	9 mmol
PTF 90 5	90 °C	5	Mr = 126	Mr = 154	Mr = 133
PTF 105 20	105 °C	20			
PTF 105 10	105 °C	10			
PTF 105 5	105 °C	5			

P = phloroglucinol, CC = cyanuric chloride and $AlCl_3$ = aluminium chloride

2.1.6.4 Carbonisation of Phenolic Triazine Frameworks

Phenolic triazine frameworks were synthesised on a larger scale using the procedure in 2.1.6.3 with cyanuric chloride (15 mmol, 2.76 g) and either phloroglucinol (15 mmol, 1.89 g) or resorcinol (15 mmol, 1.65 g), 1,4-dioxane (30 mL) and anhydrous aluminium chloride (45 mmol, 6.00 g). The reaction was carried out at 75 °C. The products were vacuum oven dried at 80 °C and designated as PTF P (phloroglucinol equivalent) and PTF R (resorcinol equivalent).

For carbonisation, the following procedure was used: the dried polymer was added to a ceramic boat, loaded into a tube furnace and purged with N_2 for 30 minutes. The furnace was then heated to the desired temperature, ramping at 3 °C/min, with a dwell time of 4 hours, under a steady N_2 flow. Temperatures used, products and their yields are given in Table 2.10.

Table 2.10. Reagent quantities, yields and conditions for the carbonisation of phenolic triazine frameworks

Material	Temperature (°C)	Precursor	Quantity (g)	Yield (g)
PTF P 300	300	PTF P	0.202	0.172
PTF P 500	500	PTF P	0.214	0.161
PTF P 700	700	PTF P	0.201	0.123
PTF P 800	800	PTF P	0.214	0.118
PTF R 300	300	PTF R	0.208	0.185
PTF R 500	500	PTF R	0.198	0.160
PTF R 700	700	PTF R	0.212	0.131
PTF P 800	800	PTF P	0.214	0.118
PTF R 800	800	PTF R	0.222	0.129

2.1.6.5 An Alternative Work-up for the Synthesis of the Phenolic Triazine Framework

The phenolic triazine framework was synthesised following the procedure in 2.1.5.3. Prior to Soxhlet extraction the solids were well broken up using a pestle and mortar, isolating using centrifugation at 4000 rpm for 10 mins and the supernatant poured off. Ammonium hydroxide solution (50 mL, 28 % NH_3 in H_2O) was added, stirring for 10 mins. The solids were isolated using centrifugation and further ammonium hydroxide solution (50 mL, 28 % NH_3 in H_2O) added, stirring for 10 mins and isolating again using centrifugation. The solids were washed twice with distilled water (50 mL), then HCl (50 mL, 37 %) twice, distilled water until pH 7 was achieved, then diethyl ether (50 mL) twice and finally ethanol (50 mL) twice, isolating the solids each time using centrifugation at 4000 rpm for 10 mins.

2.2 Characterisation

2.2.1 XRD

X-ray diffraction (XRD) was performed using a Bruker axs, D4 endeavor with Cu-K-alpha radiation. The Cu ion beam source has a wavelength of 1.5406 Å. Such X-ray sources work under vacuum, where a filament (often tungsten) is heated by a current causing it to liberate electrons, these liberated electrons are accelerated to a Cu target where Cu X-rays are generated.

Röntgenstrahl-interferenzen, commonly termed X-ray diffraction, is the diffraction of X-rays by crystals and first discovered by German physicist Max von Laue. X-ray Diffraction was initially largely developed through work done by Sir William Henry Bragg and his son William Lawrence Bragg. The Bragg's law states that

$$n\lambda = 2d.\sin\theta \qquad \text{Equation 2.1}$$

and explains why the cleavage faces of crystals appear to reflect X-ray beams at certain angles of incidence (theta, θ). In Braggs law n is an integer and equal to 1, d is the distance between atomic layers in a crystal and λ is the wavelength of the incident x-ray beam.

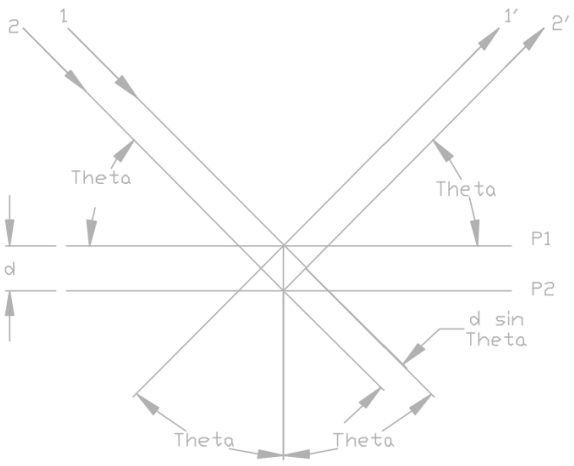

Figure 2.1. Diagram of incident X-rays being diffracted by the layers of atoms in a crystalline material.

Consider a pair of parallel planes, a distance of d apart. If we have parallel x-ray beams, 1 and 2, making an angle theta with these planes, a reflected beam of maximum intensity results if the refracted waves, 1' and 2', are in phase (Figure 2.1). The intensities of the reflection are determined by the distribution of electrons in the unit cell. Planes going through areas with high electron density will reflect strongly, planes with low electron density will give weak intensities.

2.2.2 Fourier Transform Infrared Spectroscopy (FTIR)

FTIR spectroscopy was recorded in transmission mode using a Thermo Scientific Nicolet iS10.

Infrared spectroscopy is the study of rotational, vibrational and rotation-vibration energy changes in the ground state of molecules. Infrared spectroscopy deals with the interaction between a molecule and radiation from the IR region (IR region = 4000 - 400 cm^{-1}) of the electromagnetic spectrum. Appearance of a vibrational transition in the infrared region depends on an overall change of the electric dipole moment during the vibration and the intensity of the bands are dependent on the magnitude of the dipole moment change. It is worth noting that many of the materials presented in this thesis are black carbons and absorb intensely in the IR region, meaning FTIR analysis is used wherever appropriate.

2.2.3 X-ray Photoemission Spectroscopy (XPS)

XPS analysis was carried out using a Thermo Scientific Al-K-alpha surface analysis instrument.

XPS spectra are obtained by irradiating sample surfaces with an x-ray beam, measuring the energy and electrons that are emitted from the top 1-10 nm of the material being analysed. The spectra represent a record of the ejected electrons over a range of kinetic energies, with elements and bonding environments emitting electrons of characteristic energy. Such analysis therefore is

representative of a materials surface rather than the bulk. Elemental analysis was carried using CASA XPS software giving the elements in atomic % (at.%).

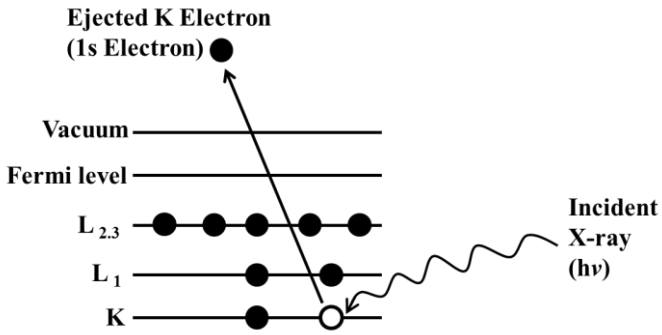

Figure 2.2. The photoemission process involved for XPS surface analysis.

2.2.4 Thermogravimetric Analysis (TGA)

TGA was carried out using a Setaram Setsys 16/18 machine with vertical overhead hanging balance. Heating was carried out under argon gas at 2 °C/min. Background runs were performed with an empty crucible and subtracted manually using appropriate software.

2.2.5 Nuclear Magnetic Resonance Spectroscopy (NMR)

Liquid NMR were carried out using a Bruker Avance 600 NMR spectrometer at 600 MHz using 600 MHz for ^{1}H NMR and 100 MHz for ^{13}C NMR. Solid-state NMR were recorded using a Varian VNMRS 400 at 400 MHz for ^{1}H NMR and 100 MHz for ^{13}C NMR. Spectra were referenced to neat tetramethylsilane.

2.2.6 BET Surface Area

Specific surface areas were calculated using the Brunauer-Emmett-Teller method (SSA_{BET}) and measured by nitrogen (N_2) adsorption at 77 K on a quantachrome IQ2 sorption analyser. All SSA_{BET} values reported are multi-point values from a minimum of 3 points in the appropriate relative pressure (P/P_0) range. Samples were degassed at a minimum temperature of 150 °C for 12 hours under vacuum (x 10^{-5} bar) before analysis. The BET specific surface areas were all calculated over a relative pressure range of 0.01 to 0.3 bar. Pore size distributions were calculated using both DFT and BJH methods. For pores of width <50 nm a QSDFT equilibrium model for slit and cylindrical pores was used, unless otherwise stated. Pore volumes in pores of width >50 nm were derived using the BJH model from the desorption curve, ignoring pressure below P/P_0 = 0.35. Total pore volumes (V_{tot}) were calculated from isotherms at maximum P/P_0 in the adsorption curve, where P/P_0 = 0.99 bar. Pore widths were calculated using the same

QSDFT method as outlined above, giving a modal value. Micropore volumes (V_M) were taken from the QSDFT analysis as the cumulative volume at pore width of 2.0 nm.

The Brunauer-Emmett-Teller (BET) method allows the determination of the surface area of solid materials using the BET theory [Brunauer *et al.* (1938)]. It extends the Langmuir theory which considers monolayer molecular adsorption, developing it to take multilayer adsorption into consideration. In the BET theory, the following assumptions are made (a) gas molecules are physically adsorbed on a solid in infinite layers, (b) there is no interaction between each adsorption layer and (c) the Langmuir theory can be applied to each layer.

The BET equation can be expressed by

$$\frac{1}{W\left(\left(\frac{P_0}{P}\right)-1\right)} = \frac{1}{W_m C} + \frac{C-1}{W_m C}\left(\frac{P}{P_0}\right) \qquad \text{Equation 2.2}$$

where:

W = weight of gas adsorbed at relative pressure P/P_0

W_m = weight of adsorbate constituting a monolayer of surface coverage

C = BET constant, related to the energy of adsorption in the first adsorbed layer and consequently its value is an indication of the magnitude of the adsorbent/adsorbate interactions. This BET constant can be expressed as

$$C = \exp\left(\frac{E_1 - E_L}{RT}\right) \qquad \text{Equation 2.3}$$

where:

E_1 = heat of adsorption for the first layer of adsorbate

E_L = the heat of adsorption for all following layers

The BET equation is an adsorption isotherm and can be plotted with $1/[W(P_0/P)-1]$ vs. P/P_0. The linear relationship can only be maintained in the P/P_0 range of 0.05 to 0.35.
Using a multi-point procedure the weight of a monolayer of adsorbate W_m can then be obtained from the slope s and intercept i of the BET plot (Figure 2.3)

$$s = \frac{C-1}{W_m C} \qquad \text{Equation 2.4}$$

and

$$i = \frac{1}{W_m C} \qquad \text{Equation 2.5}$$

giving

$$W_m = \frac{1}{s+i}$$ Equation 2.6

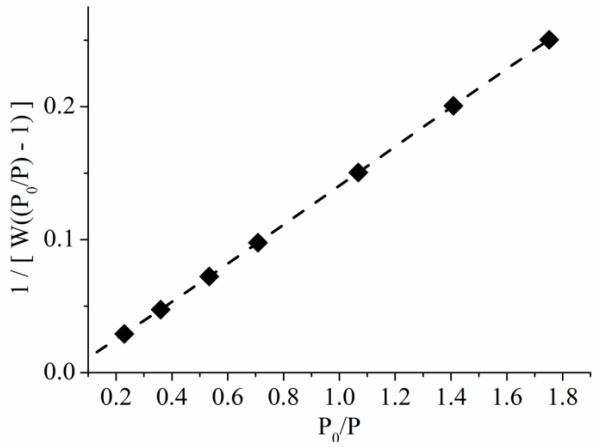

Figure 2.3. A typical multi-point BET plot.

The surface area can then be calculated with the molecular cross-sectional area (A_{CS}) of the adsorbate molecule. The total surface area S_t of the sample can be expressed as

$$S_t = \frac{W_m N A_{CS}}{M}$$ Equation 2.7

where:

N = Avagadro's number (6.0221415 x 10^{23} molecules/mol)

M = molar mass (molecular weight) of adsorbate

Assuming a hexagonal close-packed nitrogen monolayer at 77 K we use the cross-sectional area A_{CS} of 16.2 A^2.

The specific surface area can then be calculated from the total surface area S_t and the sample weight w

$$S_{BET} = {S_t}/{w}$$ Equation 2.8

It is worth noting that the BET equation is applicable to nonporous solids and materials consisting of pores of wide pore diameter. However, in a strict sense, it is not applicable to microporous adsorbents. Notwithstanding the problems arising from the chemical and geometrical heterogeneity of the surface, the type of porosity (i.e. macro-, meso-, or micropores) also plays an important role in the applicability of the BET equation. The problem is that it is difficult to separate the processes of mono-multilayer adsorption from micropore filling, usually completed at relative pressures (P/P_0) below 0.1. Another problem is associated with the size and shape of the adsorptive molecule, i.e. the effective yardstick used to assess the surface area. In case of very narrow cylindrical micropores (ultra-micropores <0.7nm), the area calculated by the BET analysis from the area covered by the adsorptive is significantly smaller than the total geometric area, so the BET analysis underestimates the true surface area. Conversely, in broader

super-micropores (>0.7 nm), a number of molecules, those filling in the centre of the pores, do not touch the surface, and this leads to an overestimation of the surface area. Therefore, the surface area obtained by applying the BET method on adsorption isotherms from microporous solids does not reflect the true internal surface area, but should be considered as a kind of characteristic or equivalent BET area.

2.2.7 CO_2 Uptake Analysis

2.2.7.1 Volumetric Analysis

CO_2 isotherms up to 1 bar were measured at 273, 298 and 323 K using the Quantachrome IQ2, taking non-ideality factors of: 9.08 $x10^{-6}$, 6.84 $x10^{-6}$ and 5.66$x10^{-6}$ respectively. Where units of cc/g at STP are used, STP (Standard Temperature and Pressure) is defined as air at 0 °C (273.15 K) and 1 bar. Under these conditions the molar volume is the volume occupied by one mole of ideal gas = 22.4 L/mol (22400 cc/g).

Carbon dioxide isotherms up to 10 bar were measured using a High Energy PCT Pro 2000. Samples were outgassed at 150 °C for 12 hrs prior to measurement. Between measurements, re-activation was carried out at 180 °C for 30 mins under vacuum (x 10^{-3} bar).

2.2.7.2 Gravimetric Analysis

Gravimetric CO_2 uptake analysis was carried out using the Setaram Setsys 16/18 machine with between 10-20 mg of sample. Samples were loaded into the TGA and outgassed at 150 °C, under argon flow, for 1 hour. The sample was cooled under argon flow to the desired temperature. The gas flow was then switched from argon to carbon dioxide (99.99 %) at 1 bar. Background runs were all performed with an empty crucible and subtracted manually using appropriate software.

Temperature programed desorption (TPD) profiles were carried out at a ramping rate of 2 °C/min, from 25 °C to 170 °C under a steady CO_2 flow.

Due to the easy availability of the Setaram Setsys 16/18 machine, samples were typically screened for CO_2 uptake using gravimetric analysis prior to volumetric analysis.

2.2.8 Isosteric Heats of Adsorption

The isosteric heats of adsorption (Q_{st}) were calculated from isotherms at temperatures of 0, 25 and 75 °C. The isotherms were fitted using the Hall-Langmuir isotherm model, with Origin 8.6. From these isotherms the pressure was recorded for various molar volume gas uptakes (see Table 2.11 for a given example).

The Clausius-Clapeyron equation concerns the characterisation of a discontinuous phase transition between two phases of mater of a single constituent. On a pressure-temperature diagram, the line separating two phases can be described by the Clausius-Clapeyron relationship where the slope and tangent are given. The Clausius-Clapeyron equation is:

$$\frac{dP}{dT} = \frac{L}{T\Delta_v} \qquad \text{Equation 2.9}$$

Where:

L = specific latent heat

Δ_v = specific volume change of the phase transition

For our adsorption purposes this equation can be rewritten as:

$$\ln(P_i) = -\Delta H_{ads} \times \frac{1}{R \times T_i} + constant \qquad \text{Equation 2.10}$$

Where:

ln(P*i*) = log of pressure *i* (bar)

$-\Delta H_{ads}$ = heat of adsorption (kJ/mol)

R = gas constant (8.315 J/K mol)

T*i* = temperature for isotherm i (k)

As this fits the form of y = mx + c, for any gas uptake we can take a plot of lnP vs. 1/T. A linear slope of this, accounting for the gas constant, gives us Q_{st} at this uptake.

2.2.9 Ideal Adsorbed Solution Theory (IAST)

In order to determine the ability of materials for separation of CO_2/N_2 the IAST method [Myers and Prausnitz (1965)] has been used. In the case of an ideal solution the partial pressure of an adsorbed component is given by the product of its mole fraction in the adsorbed phase and the pressure it would exert as a pure adsorbed component at the same temperature and spreading pressure as those of the mixture.

We can state that the selectivity of preferential adsorption of component 1 over component 2 in a mixture containing 1 and 2 can be formally defined as

$$S_{ads} = \frac{q_1/q_2}{p_1/p_2} \qquad \text{Equation 2.11}$$

where q1 and q2 are the absolute component loadings of the adsorbed phase in the mixture, and p1 and p2 are gas components CO_2 and N_2 at partial pressures of 0.15 and 0.85 bar respectively, the pressures of a post-combustion flue gas system.

Table 2.11. Relative pressure and gas uptake values taken from isotherms at 273, 298 and 348 K for a melamine-resin derived carbon material. Such data can be used in the determination of the Clausius-Clapeyron equation

Gas uptake	Pressure (bar)		
(mmol/g)	273 K	298 K	348 K
0.5037	0.00362	0.02215	0.40608
0.5111	0.00413	0.02399	0.41586
0.5818	0.00608	0.03555	0.51041
0.6134	0.00864	0.03889	0.55322
0.7088	0.01440	0.05840	0.79077
0.8818	0.02748	0.12573	1.06891
0.9958	0.05060	0.18540	1.36854
1.1029	0.07088	0.26259	1.73628
1.2177	0.10775	0.37133	2.22843
1.2663	0.12894	0.42848	2.47736
1.3123	0.14461	0.49207	2.74454
1.3605	0.17040	0.56580	3.057898
1.4630	0.23987	0.74230	3.91940
1.5096	0.26933	0.82684	4.27320

3. Carbon Nitride: Synthesis of a Microporous Analogue

The presence of nitrogen dopants (N-dopants) within porous carbon CO_2 sorbents has been correlated with increased relative uptake capacities, binding enthalpies and CO_2/N_2 selectivity relative to undoped counterparts. With this in mind, carbon nitride, a nitrogen-rich polymer with the empirical formula C_3N_4, appears to be an attractive material for novel sorbent synthesis. Specifically, interest in carbon nitride for carbon dioxide capture stems from the type of aromatic nitrogen atoms present in tri-s-triazine structural units and how this form of nitrogen may interact with gaseous CO_2. Carbon nitride (CN) also has a high thermal stability, being stable up to 600 °C [Thomas *et al.* (2008)], giving it an inorganic/organic character and indicating it may have a long lifetime in cyclic temperature swing industrial processes. The synthesis of CN, its characterisation, graphitic nature and use for potential applications in energy conversion and storage, and environmental applications including direct methanol fuel cells, and catalysis have all made it an area of recent research interest [Zheng *et al.* (2012)]. However, the synthesis of a microporous CN still remains challenging to materials science.

Microporous and mesoporous carbon nitride structures have been synthesised using nanocasting techniques with zeolite templates [Liu *et al*. (2008)]. However, to remove the template it must be etched using a strong acid (HF), making the process unappealing and an alternative method for creating porosity attractive. In search of such a method, this chapter focuses on the utilisation of methods common to the synthesis of porous carbon solids, applying them to carbon nitride.

3.1 Synthesis of Carbon Nitride

The history of carbon nitride (CN) is an interesting chapter in polymer history, and its characterisation has only been achieved recently alongside developments in NMR and XPS technology [Thomas *et al.* (2008)]. Berzelius first synthesised CN by treating potassium or sodium thiocyanate with chlorine, giving the product the name melon as described by Liebig [Liebig (1834)]. Melon was characterised as having the empirical formula $H_3C_6N_9$ and structural models based on tri-s-triazine (heptazine) core units were proposed [Redemann *et al.* (1940)] (Figure 3.1(a) and (b)). However, variations in the hydrogen content were common and this was rationalised by assuming that a mixture of several compact condensation products had resulted with the conjecture that “it is probably incorrect to assign any one structure to melon, for it is

more than likely a mixture of molecules of different sizes and shapes. This gives rise to its amorphous character" [Pauling *et al.* (1937)].

An alternative 3-dimensional form of carbon nitride (β-C_3N_4) has also been proposed, with a predicted hardness similar to that of diamond [Cohen (1985)]. This has been an active area of research with applications in the field of low-compressibility materials and recently synthesised using complex mechanochemical techniques [Niu *et al.* (2003)].

At ambient conditions however, the thermodynamically favoured allotrope is in fact a layered form that has become known as graphitic carbon nitride (g-C_3N_4) [Teter *et al.* (1996)]. Two structures were proposed for g-C_3N_4, one based on triazine core units and the other on heptazine units (Figure 3.1(c) and (d)). However, the heptazine form has been found to be energetically more favourable relative to triazine at ambient pressures and the hepatzine form is therefore likely to dominate [Thomas *et al.* (2008)].

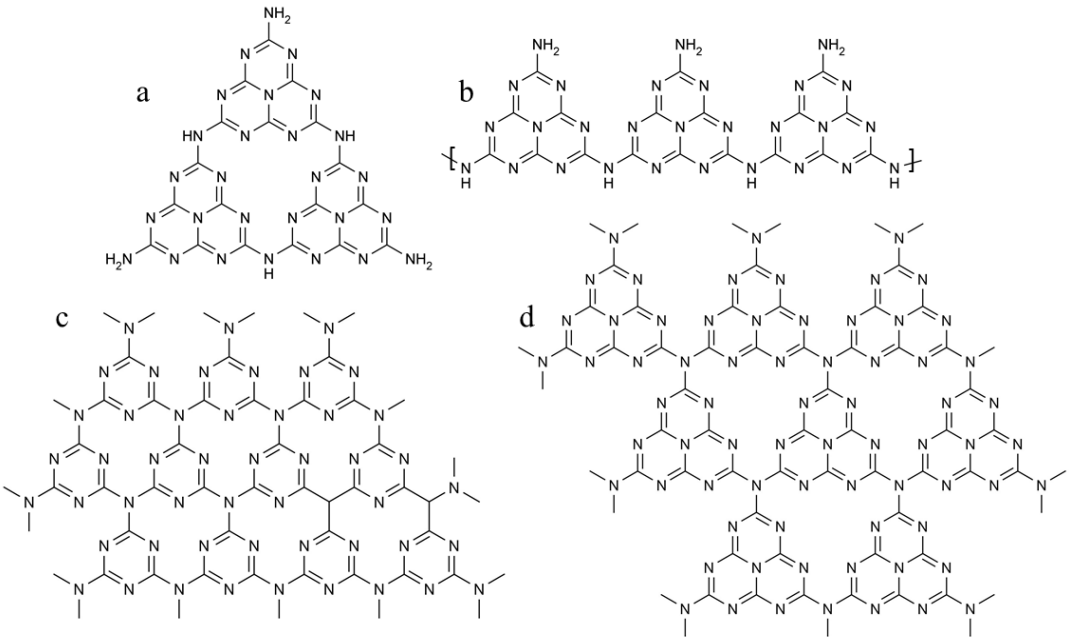

Figure 3.1. Forms of carbon nitride: (a) and (b) are proposed structures for melon, (c) and (d) portray the hypothetical structural models for g-C_3N_4 based on the triazine and tri-s-triazine (heptazine) forms respectively.

For the synthesis of g-C_3N_4 various precursors such as melamine, urea and dicyandiamide have been typically used [Zheng *et al.* (2012)]. The reaction is a combination of polyadditions and polycondensations where precursors such as cyanamide and dicyandiamide condense to form triazine ring structures like melamine. These then undergo condensation processes where ammonia is eliminated. The reaction process has been well documented [Thomas *et al.* (2008)] and it is understood that the melamine groups are stable up to 350 °C and form heptazine units

via rearrangement at 390 °C, condensing into non-linear polymeric units at temperatures up to 520 °C (Figure 3.2).

This chapter focuses on the development of a porous carbon nitride analogue and testing its affinity for the sorption of CO_2. To do this g-C_3N_4 was first synthesised and then several novel procedures were attempted in order to synthesise a porous form. A suitable synthesis for g-C_3N_4 was taken from literature [Yan *et al.* (2009)] where melamine was heated at 595 °C, using a dwell time of 1 hour and achieving a 43 % yield, the product was designated as g-C_3N_4.

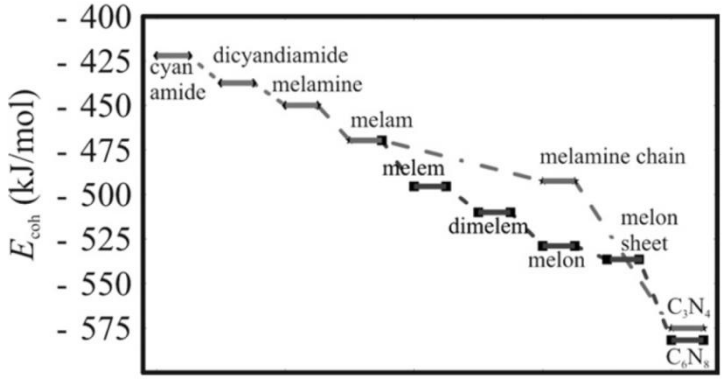

Figure 3.2. Calculated energy diagram for the synthesis of carbon nitride. The starting precursor cyanamide is condensing into melamine. Further condensation can then proceed via the triazine route (dash-dot line) to C_3N_4, or melamine can form melem and then follow the tri-*s*-triazine route (dashed line) to form C_6N_8 (energies presented per atom) [Thomas *et al.* (2008)].

The chemical structure of the as synthesised g-C_3N_4 was analysed using FTIR and XPS analysis. In the FTIR spectrum (Figure 3.3(a)) the peaks at 1200-1650 cm^{-1} are typical of the stretching modes of C-N bonds in CN heterocycles. Singles C-N bonds are found at 1200-1500 cm^{-1} and a doublet can be seen at 1414 and 1458 cm^{-1}, attributed to C-N stretching modes of the fused triazine rings in heptazine [Ferrari *et al.* (2003)]. C=N double bonds are typically found at 1500-1650 cm^{-1} [Thomas *et al.* (2008)], with non-fused triazine groups showing strong C-N stretching modes bands at 1580-1520 cm^{-1} [Socrates (1980) p.95]. A sharp peak is observed at 1577 cm^{-1} corresponding to such triazine C=N stretching modes. A peak at 1636 cm^{-1} is also present and this can be attributed to C=N stretching modes of fused triazine rings within heptazine units [Ferrari *et al.* (2003)]. NH_2 deformation modes are also expected in this region and are found in the melamine starting material, the presence of such peaks though is not thought to be due to unreacted starting material, thanks to analysis using deuterated samples that indicate this is not the case [Ferrari *et al.* (2003)]. The breathing mode of the heptazine unit (out of plane ring bending) is seen at 807 cm^{-1} [Li *et al.* (2009b)]. The broad band at 3100-3500 cm^{-1} can be attributed to adsorbed water, but may also be primary and secondary N-H stretching and deformation modes, indicating that the product is not fully condensed but amorphous [Yan *et al.* (2009), Bojdys *et al.* (2008)]. This incomplete condensation is typical of graphitic carbon nitrides synthesised at ambient pressure and is accepted as being a predominately kinetic

problem, with the reaction not proceeding significantly past the polymeric melon form [Bojdys *et al.* (2008)].

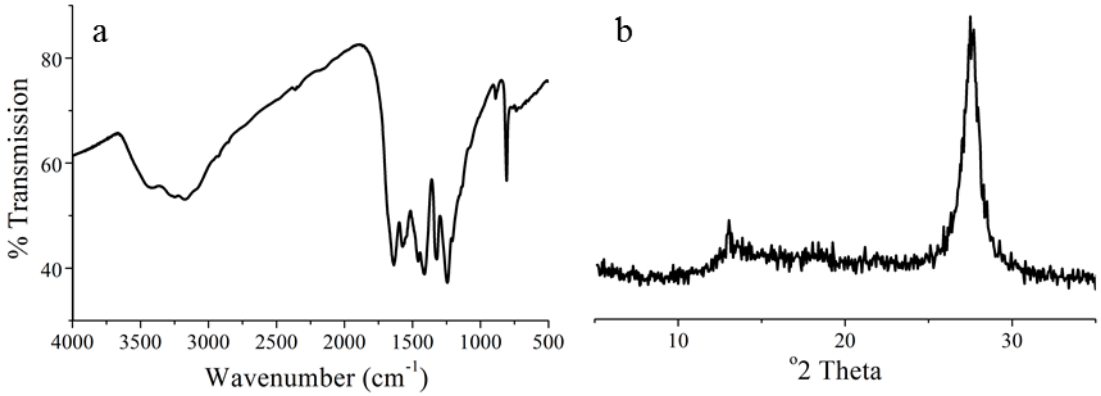

Figure 3.3. (a) FTIR spectroscopy and (b) XRD pattern of the as synthesised g-C_3N_4.

Structural analysis was carried out using XRD (Figure 3.3(b)), where a peak centred at 27.5° 2θ corresponds to the characteristic interlayer stacking of aromatic systems, indexed as (0 0 2), giving an interlayer distance of 0.324 nm. The small angle peak at 13.05°, corresponding to a distance of 0.679 nm, is indexed as (1 0 0). This is related to an in-plane structural packing motif of the lattice planes perpendicular to the *c*-axis [Thomas *et al.* (2008)]. This peak will be stronger when the distance between polymeric melon units has a narrow distribution range, giving rise to high long range order. The polycondensation of the carbon nitride precursor at elevated temperatures will result in loss of nitrogen, meaning the distances between strands will have a wider distribution range, and a reduced long range order [Niu *et al.* (2012)].

From XPS analysis the elemental atomic concentrations are calculated to be N: 57.1, C: 42.1 and O: 0.8, with no other elements present (Figure 3.4(a)). This results in an empirical formula of $C_3N_{3.9}$, equating well to the g-C_3N_4 formula. The presence of oxygen is not unexpected and relatively low at <1 at.% [Lotsch *et al.* (2007)]. The symmetrical peak at a binding energy of 288.2 eV in the core level C 1s spectrum (Figure 3.4(b)) corresponds to nitrogen bound carbon in an sp^2-bonded array, C=N-C [Thomas *et al.* (2008)].

The core level N 1s spectrum (Figure 3.4(c)) is dominated by a peak at 398.5 eV, that corresponds to sp^2 hybridized aromatic nitrogen bonded to carbon atoms (C-N=C) [Hu *et al.* (2011b)]. The small peak at 404.4 eV can be attributed to NO_2-terminal groups and charging effects. The broad shoulder between 400-402 eV indicates several other nitrogen environments. Tertiary amine groups would be found within this region and it may be reasonably argued that the g-C_3N_4 has formed with triazine units rather than heptazine. This is supported through deconvolution of the peak, to imply a ratio of aromatic nitrogen atoms to amine groups close to the 3:1 ratio we would expect (in fact 3.65). However, current literature [Liu *et al.* (2011b), Hu *et al.* (2011b), Lee *et al.* (2010)] suggest that a peak at 399.7 eV represents tertiary nitrogen

atoms at the heart of the heptazine unit, therefore bonded to three carbon atoms. From the peak:peak ratio analysis between the aromatics at 398.5 eV and tertiary nitrogen atoms at 399.7 eV, a value of 6:1 supports the heptazine core unit form. The peak at 400.9 eV is assigned to terminating amine groups and its dominance is assigned to enhanced surface density resulting from the surface specific nature of XPS analysis [Thomas *et al.* (2008), Lee *et al*. (2010)].

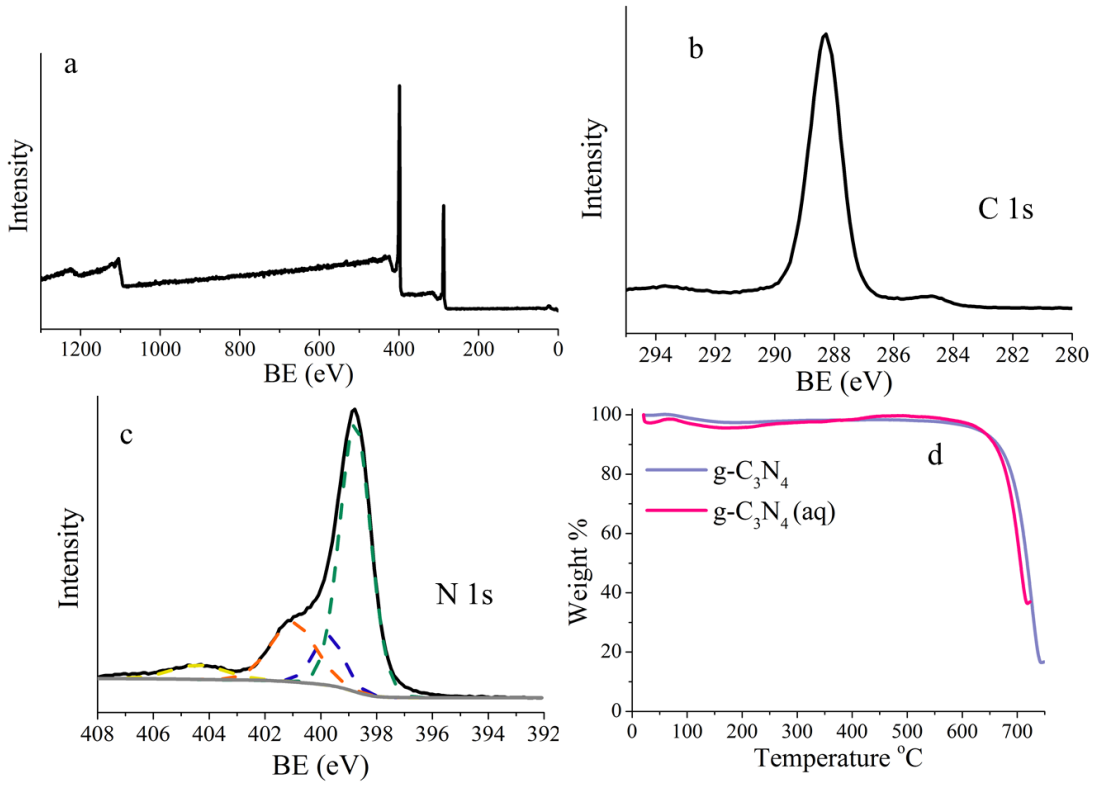

Figure 3.4. (a) XPS survey analysis for the as synthesised g-C_3N. Core level C 1s (b) and N 1s (c) XPS spectra for g-C_3N. (d) TGA for g-C_3N_4 and g-C_3N_4 (aq) under an N_2 atmosphere heating at 2 °C/min.

3.2 Exfoliation of Carbon Nitride

One way a porous derivative of carbon nitride may be achieved is through exfoliation of the graphene-type layers. This exfoliation would involve peeling apart the layers and suspending them in a suitable solution. Once in solution a porous structure may be synthesised chemically by pillaring the layers creating a porous network, or through the formation of aerogels. Similar work has been carried out with graphite based layered structures where sonication was used to separate the graphene layers [Burress *et al.* (2010), Li *et al.* (2012b)]. Initial tests as to the solubility of carbon nitride were therefore carried out, guided by the Hildebrand and Hansen solubility parameters, choosing γ-butyrolactone (GBL) and n-butanol, due to their high polar bonding and hydrogen bonding parameters respectively. Water and dimethylformamide (DMF)

were also used, based on their strong polarity and success in work with graphene, another layered aromatic structure [Park (2009)]. Mixtures of 1 wt% were made up and sonicated for 12 hours. For the n-butanol, DMF and GBL there was no indication that dissolution of the g-C_3N_4 had occurred, based on the colour and transparency of solvent and amount of g-C_3N_4 solids. In the water equivalent a cloudy milky white solution had been achieved, suggesting some dissolution. This was left to stand for 24 hours, after which time the solution became markedly thinner with precipitation evident at the bottom of the test tube. This solution was isolated and dried in a vacuum oven at 150 °C to obtain a pale yellow solid, designated as g-C_3N_4 (aq). Using TGA in a nitrogen environment up to 700 °C at a ramping rate of 2 °C/min the decomposition properties of g-C_3N_4 (aq) were tested (Figure 3.4(d)). The decomposition profile of the g-C_3N_4 (aq) can be seen to be analogous with the g-C_3N_4. However, decomposition of the g-C_3N_4 (aq) begins at a slightly lower temperature than for the g-C_3N_4, such that a mass loss of 20 % had occurred at a temperature of 679.8 °C for g-C_3N_4 (aq), while a mass loss of 20 % for g-C_3N_4 required a temperature of 689.5 °C. This may be attributed to the dissolving portion consisting of shorter and more thermally labile carbon nitride/melon units. Nonetheless, this does indicate some g-C_3N_4 had become dissolved. Centrifugation of the dissolved g-C_3N_4 milky solution at 5000 rpm for 10 minutes resulted in a clear colourless solution and full precipitation of the g-C_3N_4. While it seemed apparent some success was achievable, the quantity of dissolved g-C_3N_4 was very limiting for the first step in a synthetic process. After this work was carried out the dissolution of g-CN_4 in water was published, and in similarly low yields as achieved here [Zhang *et al*. (2012)].

3.3 Installing Porosity in Carbon Nitride Using Structure-defect Directing Groups

As discussed in the introduction, activated carbons have a highly microporous structure, with BET surface areas up to 3000 m^2/g [Siriwardane *et al.* (2001)]. The structure of activated carbon is not composed of well crystalline graphite, but disorderly micrographite crystallites. It is the small crystallite thickness and short range ordering between crystallites that enable activated carbons to exhibit their high surface areas [Kaneko *et al*. (1992)]. Conversely, the structure of carbon nitride exhibits long-range order. In order to enhance the surface area of carbon nitride, a similar defective structure of carbon nitride is envisaged. The potential for the addition of defective constituents into the carbon nitride structure was therefore investigated. To do this organic structure-defect directing groups were selected that may partake in the condensation reactions leading to carbon nitride formation, isolating microcrystallite carbon nitride regions,

but burn-off at the elevated final synthesis temperature to leave disordered carbon nitride crystallites with short range order.

As the amine condensation step is known to be crucial in the mechanistic process of carbon nitride formation, additives containing amine groups capable of partaking in these condensation steps were chosen. The process of burn-off may differ depending on the type of structure-defect directing agent and it is well known that chemical structure controls the degree of graphitisation of organic materials [Lewis (1982)], thus dictating the manner of burn-off. The initial thermal reaction in the carbonisation of hydrocarbons is complex, but the first step is expected to involve the formation of free radical intermediates [Lewis (1982)]. Radical stability is dependent on chemical structure and following their formation aromatic groups may undergo thermal rearrangement and alkyl groups may aromatize, while both may decompose into smaller gaseous molecules. Amine structure-defect directing agents based on the aromatic unit, 3,5-diaminobenzoic acid (DBA) and the alkane chains butylamine and nonylamine were therefore selected.

Dicyandiamide (DCA) was used as the carbon nitride precursor, due to the increased quantity of condensation steps required in its transformation into g-C_3N_4 [Thomas *et al*. (2008)]. A series of structure-defect directed carbon nitrides were synthesised using varying ratios of DCA:DBA, whereby the DCA and DBA were ground together in ratios of: 1:9, 3:7, 7:3 and 9:1 DCA:DBA and heated following the literature process used above, to 595 °C with a dwell time of 1 hour. The materials were then designated as DCA:DBA X, where X = the ratio of DCA:DBA. As the amount of DBA was increased the product took on a darker colour, until with DBA 100 %, the product was a silver glassy carbon.

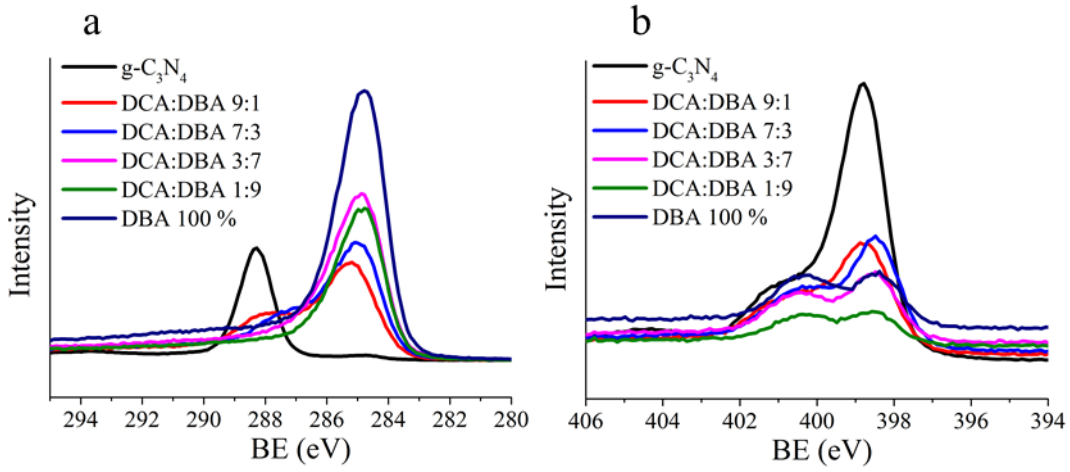

Figure 3.5. (a) C 1s and (b) N 1s core level XPS spectra for DCA:DBA X:Y series.

From the core level XPS C 1s spectra of the DCA:DBA series (Figure 3.5(a)), the typical peak for the g-C_3N_4 at 288.2 eV is shifted to 284.5 eV. This shift is indicative of an overhaul of the

chemical composition, with peaks at 284.5 eV being assigned to sp^2 hybridised carbon, typical of graphitic-type carbons [Sheng *et al*. (2011)]. Therefore disordered g-C_3N_4 microcrystallites were not obtained, rather the g-C_3N_4 synthesis has been retarded and a graphitic-type carbon material was obtained. From the N 1s spectra a defined alteration can also be observed (Figure 3.5(b)), whereby the heptazine N 1s peak at 398.5 eV is largely reduced to form twin peaks centred at 400.5 and 398.5 eV. These are typical of N-doped carbon environments such as quaternary and pyrrole (399-401 eV), and pyridine (398.5 eV) groups [Wu *et al*. (2012)].

The samples were analysed using gravimetric CO_2 uptake analysis 298 K and 1 bar (Figure 3.6). Figure 3.6(a) shows that the samples with a greater portion of DBA are capable CO_2 sorbents, achieving capacities of 1.99, 2.11 and 2.09 mmol/g for DCA:DBA 3:7, DCA:DBA 1:9 and DBA 100 % respectively. The other samples indicated no affinity for CO_2 sorption. Temperature programmed desorption (TPD) analysis was carried out for the samples with an affinity for CO_2 sorption (Figure 3.6(b)). It can be seen that for DCA:DBA 3:7 and DCA:DBA 1:9 the CO_2 is removed as temperature increases, such that at 170 °C the samples retained only 0.12 and 0.24 mmol/g of the CO_2 adsorbed. For the DBA 100 % equivalent less of the samples capacity is being regenerated under these conditions, such that at 170 °C the DBA 100 % retains 0.55 mmol/g of the CO_2 adsorbed, equivalent to 30 % of capacity. This reduction in the regenerated capacity indicates that some of the CO_2 may be chemisorbed onto the sorbent. This chemisorption is also indicated by the wider knee and more gradual uptake found in the adsorption curve. Using N_2 isotherms at 77 K the BET specific surface area of the DCA:DBA 3:7, DCA:DBA 1:9 and DBA 100 % were <1.0, 10.3 and 4.9 m^2/g respectively. This very low apparent surface area, yet significant CO_2 physisorption, is indicative of an ultramicroporous (pores of width <0.7 nm) material.

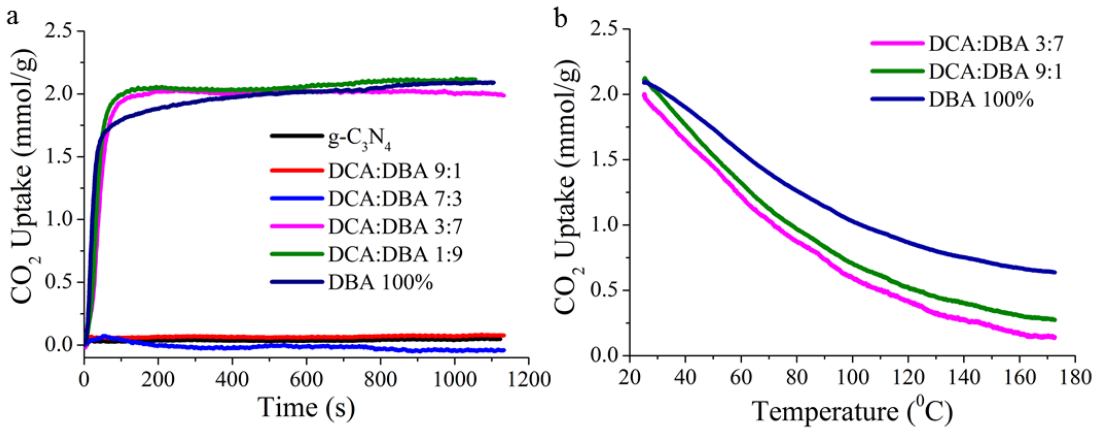

Figure 3.6. (a) CO_2 uptake capacities at 298 K and 1 bar, measured on a gravimetric basis (b) temperature programmed desorption (TPD) from 25-170 °C, under a dynamic CO_2 flow, for DBA:DCA series.

To further investigate the adsorbent-adsorbate interaction volumetric CO_2 uptake analysis was carried out for both the DBA 100 % and DCA:DBA 9:1. Figure 3.7 shows the CO_2 uptake

capacities at 273, 298 and 323 K and 1 bar. Of note is that the capacity for the DBA 100 % is lower when calculated using volumetric analysis relative to gravimetric analysis, 1.64 compared to 2.09 mmol/g respectively. The isosteric heats of adsorption (Q_{st}) (Figure 3.7(d)), a measure of the adsorbate-adsorbent interaction energy, are 33.37 and 34.70 kJ/mol at near zero loadings for the DBA 100 % and DCA:DBA 9:1 respectively. This opposes the indications from the TPD that there is a greater chemical interaction between the DBA 100 % and CO_2 relative to the DCA:DBA 9:1. Alternatively, it may be that a lack of mesopores in this ultramicroporous material results in a low mass transfer diffusion rate, this will cause hindered regeneration and reduced capacity in measurements made using volumetric analysis where the equilibrium times are set for carbon materials with hierarchical porosity [de Souza *et al*. (2013)]. The gradual increase in the gravimetric analysis (Figure 3.6(a)) for the DBA 100 % also supports this.

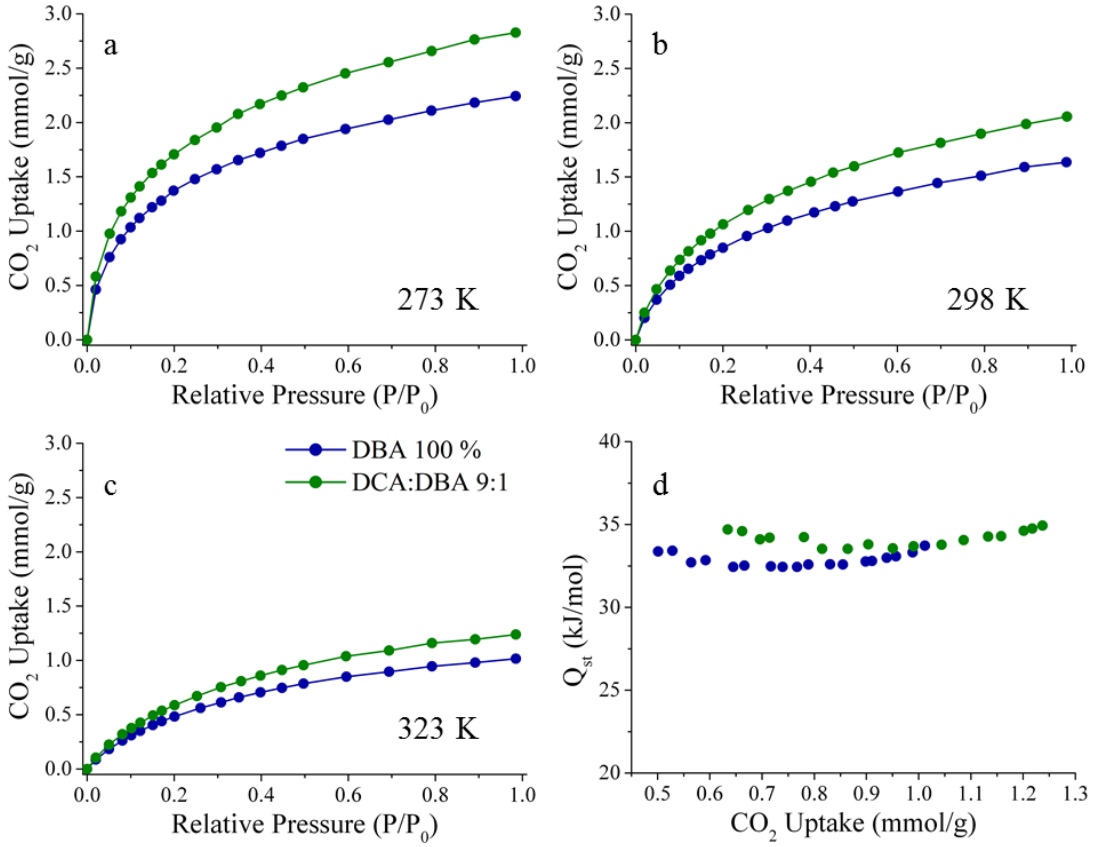

Figure 3.7. CO_2 adsorption isotherms (0-1 bar) for the DBA 100 % and DCA:DBA 9:1 carbons at (a) 273 K, (b) 298 K and (c) 323 K. (d) Isosteric heats of adsorption (Q_{st}) calculated from CO_2 adsorption isotherms.

In addition, a series of structure-defect directed carbon nitrides were synthesised using varying ratios of DCA to amine functionalised alkyl chains. For this alkyl chains of 9 and 4 carbon atoms long were chosen, nonylamine (NA) and butylamine (BA) respectively (Figure 3.8). The reagents were mixed with 2:1 and 5:1 ratios of DCA to alkylamine, heating in the procedure taken from literature for g-C_3N_4 synthesis as above; to 595 °C with a dwell time of 1 hour. The resulting materials were designated as DCA:X Y, where X = the alkane used and Y is the ratio

of DCA:alkane. Structural and chemical analysis was carried out using XRD and XPS techniques. In the core level C 1s XPS analysis (Figure 3.8(a)) the characteristic g-C_3N_4 C-N-C coordination peak is observed at 288.2 eV for all samples in the series. The smaller peak at 284.5 eV is typical of some graphitic-type adventitious surface carbon [Niu *et al.* (2012)]. This increase in surface adventitious carbon has likely arisen from the carbonisation of the alkylamine additive. The core level N 1s spectra (Figure 3.8(b)) for the series all exhibit the main C-N-C group peak at 398.8 eV and identical profiles to the g-C_3N_4. Altogether this indicates that the g-C_3N_4 chemical structure is still present. From the XRD pattern (Figure 3.8(c)) all the materials in the series exhibit a peak at 27.6° 2θ. As this is assigned to reflection from the (0 0 2) plane, it indicates the g-C_3N_4 structure is also still present. Gravimetric CO_2 uptake analysis at 298 K and 1 bar showed the samples had no affinity for CO_2 and BET specific surface areas calculated from N_2 adsorption at 77K was very low, <25 m^2/g for all samples, indicative of normal carbon nitride. This suggests that the alkylamines are not effective as porosity inducing structure-defect directing agents when used in this process. This may be because the alkanoamines are boiling-off before amine condensation reactions can take place.

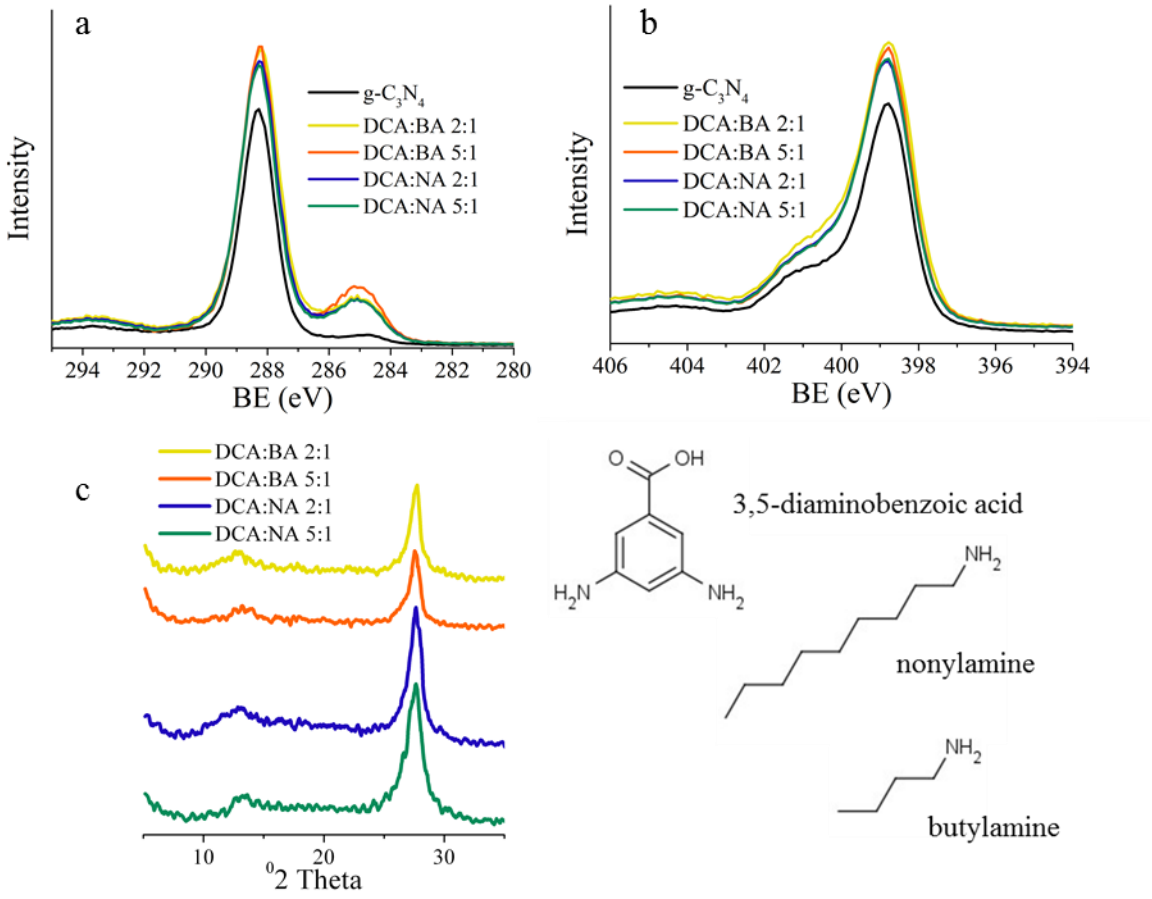

Figure 3.8. Core level C 1s (a) and N 1s (b) XPS spectra and (c) XRD patterns for the DCA:alkylamine series.

3.4 Chemical Activation of Carbon Nitride

The process of chemical activation in porous carbon is now well understood [Wang *et al.* (2012a)]. In particular, the use of KOH as activation agent has yielded activated carbon with excellent gas sorption properties [Souza *et al.* (2013)]. For the synthesis of activated carbon, carbon based materials with high aromatic content, such as lignocellulosic materials [Kalderis *et al*. (2006)] and coke pitch [Lu *et al*. (2005)] are carbonised to graphitic-type carbons, which are then activated using KOH and thermal treatment. These graphitic-type carbons consist of layered graphitic crystallites with some long range order; a similar lamella-type structure to g-C_3N_4. The KOH activation of g-C_3N_4 was therefore attempted to create a porous g-C_3N_4 analogue. For KOH activation the KOH and carbon precursor are ground together and heated, during which time the KOH melts permeating the precursor. The KOH then reacts with the carbon structures to release hydrogen gas and metal potassium complexes which act to separate the lamellae [Lillo-Rodenas (2004)].

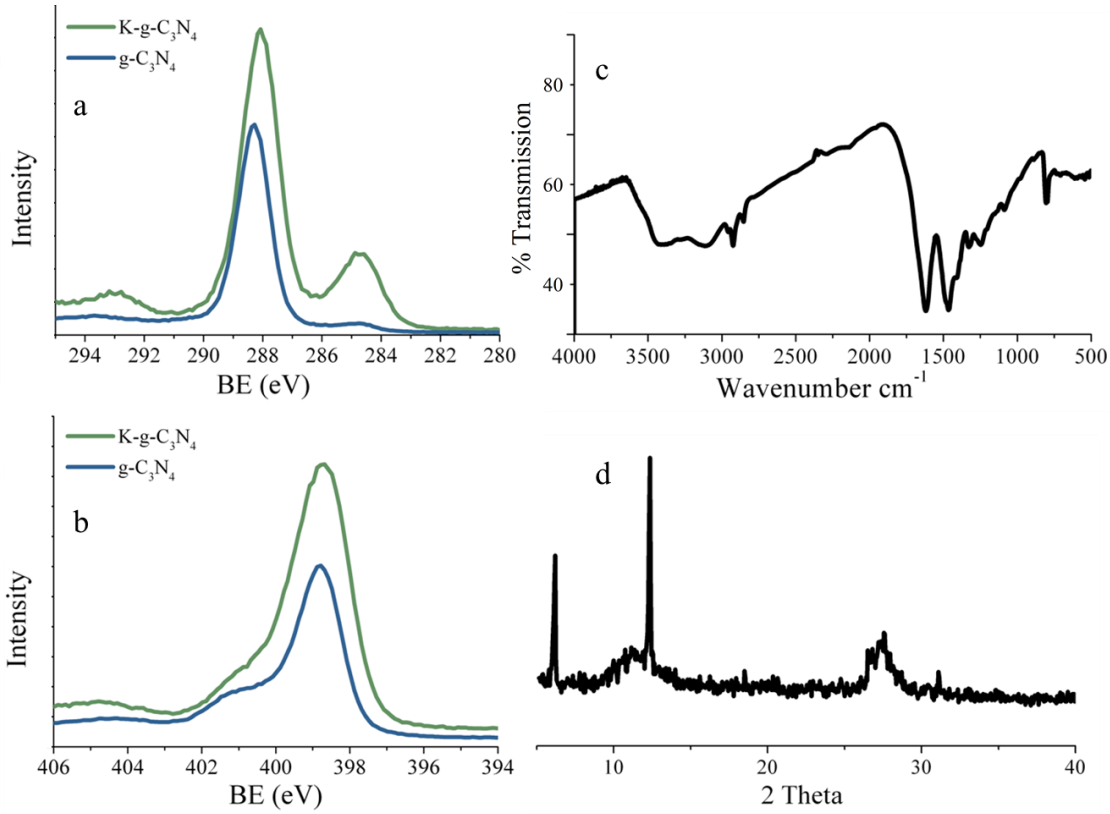

Figure 3.9. Analysis of the K-g-C_3N_4, with (a) C 1s and (b) N 1s core level XPS spectra. FTIR spectroscopy (c) and XRD pattern (d).

KOH was mixed and ground with g-C_3N_4 in a 2:1 ratio. This mixture was heated under a nitrogen atmosphere at 5 °C/min, to 700 °C, with a dwell time of 30 mins, resulting in a zero yield. The process was repeated at 600, 555 and 450 °C, also resulting in zero product yields. Heating to 150 °C a white monolith was obtained which was washed thoroughly with water

until neutrality, designating the product as K-g-C_3N_4. From the FTIR and XPS chemical analysis the carbon nitride structure can be seen to be still largely present. This is indicated in the XPS analysis where the core level C 1 s spectrum (Figure 3.9(a)) is dominated by an sp^2-bonded carbon C=N-C peak at 288.5 eV and in the N 1s spectrum (Figure 3.9(b)) which is dominated by a peak at 398.5 eV, typical of nitrogen in an sp^2 hybridized aromatic environment bonded to carbon atoms (C-N–C). From FTIR spectroscopy (Figure 3.9(c)) the peak at 1623 cm^{-1} is assigned to C=N stretching modes of fused triazine rings in heptazine groups, peaks at 1466 and 1327 cm^{-1} arise from the in-plane stretching of triazine and at 804 cm^{-1} the triazine out of plane ring deformation further supports that the carbon nitride structure is still present. Some decomposition of the carbon nitride structure is though apparent. This is indicated by the C-H stretching peaks at 2900 cm^{-1} and the C 1s XPS spectra displaying graphitic type C=C bonding at 284.5 eV. Gravimetric CO_2 uptake analysis of the materials showed it to have no affinity for CO_2 and the BET specific surface area calculated from N_2 adsorption at 77 K was 19 m^2/g, typical of g-C_3N_4.

Interestingly the XRD analysis (Figure 3.9(d)) showed a loss of the carbon nitride long range order, with the sharp (0 0 2) peak at 27.5° 2θ becoming a broad hump. Instead sharp peaks at 6.2 and 12.4° 2θ can be noticed. In addition to this, despite thorough washing after activation, XPS elemental analysis showed potassium species present (10 at.%). These new XRD peaks may correspond to K ions becoming intercalated between the g-C_3N_4 layers, being (0 0 1) and (0 0 2) for 6.2 and 12.4° 2θ respectively. Such intercalation is common in graphitic materials [Guo *et al*. (2012), Doll *et al*. (1989)] and has since been published in carbon nitride systems [(Gao *at el*. (2013), Bojdys *et al*. (2013)]. While this result was considered interesting it was deemed too far a departure from the goal of this thesis for further exploration. It was concluded that chemical activation with KOH was not suitable for g-C_3N_4.

In this chapter carbon nitride has been investigated, focusing on the ‘graphitic’ structural form, its synthesis and characterisation. The synthesis of a microporous allotrope has been attempted by: sonication in various solvents to dissolve the carbon nitride, inducing defects within and activating the g-C_3N_4; methods that have all been utilized with graphitic carbon structures. A microporous allotrope of graphitic carbon nitride has not been obtained using these approaches, and a carbon nitride capable of CO_2 sorption has therefore not been achieved.

4. Carbonisation of Nitrogen Containing Precursors

In response to the demands for greater CO_2/N_2 selectivity and increased uptake capacity at elevated temperatures (≥50 °C) within porous carbons, N-doping has been utilized exhibiting a positive impact [Zhong *et al.* (2012)]. This positive effect has been rationalized through the Lewis acidity of CO_2, enabling it to accept an electron pair and therefore react with a Lewis base to form a Lewis adduct [Vogiatzis *et al.* (2009)]. The influence of nitrogen doped groups is therefore believed to be due to their action as Lewis basic sites and the form of nitrogen present will impact upon the strength of interaction with the CO_2 Lewis acid [Pevida *et al*. (2008b)]. The common forms of nitrogen in N-doped carbon have been identified as pyridinic, pyrrolic and quaternary (Figure 4.1) [Pevida *et al*. (2008a)]. Of these each has differing basicity due to the nature of their bonding within the carbon matrix.

Pyridine and pyrrole groups both have electron lone pairs on the nitrogen atom. They are aromatic and have filled stabilised bonding orbitals. They differ in that the pyridine has a lone pair that is not part of the aromatic π system, while the pyrrole lone pair is part of the π system [Solomon (1980) pp. 458]. In contrast, the quaternary form of nitrogen is bonded to three carbon atoms in the plane of the carbon matrix, meaning there is no extra electron pair. The result of this is that pyridine is the most basic of these weak bases, with a pK_b of 8.8 compared to 13.6 for pyrrole. It is due to the greater basicity of pyridine that it is predicted responsible for Lewis acid-base interactions with the Lewis acidic CO_2 and the resultant increase in Q_{st} [Vogiatzis *et al.* (2009)]. However, this mechanism has been questioned, with many N-doped carbons being synthesised but not exhibiting increased selectivities and Q_{st} values [Sevilla *et al*. (2013), Xing *et al.* (2012)]. To therefore increase understanding into the role played by N-dopants this chapter focusses on the synthesis of N-doped carbons via the carbonisation of 3 different nitrogen-rich polymers: melamine-formaldehyde resin, polyvinylpyrrolidone and polyacrylonitrile. The obtained materials which have varied chemical and porous characteristics were tested as to their CO_2 capacities, which can be rationalised through porosity and N-dopant effects. The materials can then be compared with others synthesised in this work and literature to help answer mechanistic questions and tune CO_2/N_2 selectivity and Q_{st} based on N-dopants effects, with a Q_{st} of around 40 kJ/mol preferential for a post-combustion capture system.

4.1 Carbonisation of Polyvinylpyrrolidone and Polyacrylonitrile

Carbonisation via heating is a complex process in which many reactions take place concurrently such as condensation, dehydration and isomerization. The resultant carbonaceous product then consists of carbon in a largely sp^2 hybridised form. Notably, this chapter focusses on polymeric

precursors as they are typically less thermally labile than simple molecules, so favour greater yields producing a carbon more readily [Marsh (2006) pp. 454-458].

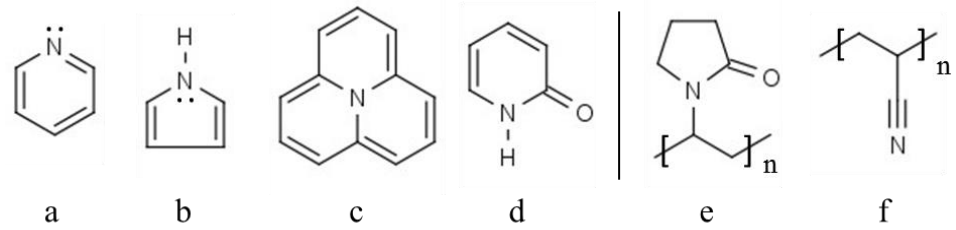

Figure 4.1. Schematic showing pyridine (a), pyrrole (b), quaternary (c) and pyridonic (d) nitrogen forms. Also shown are the polymeric units for polyvinylpyrrolidone (e) and polyacrylonitrile (f).

Various nitrogen containing polymers are readily available and mass produced. Two which have high nitrogen content and are suitable for carbonisation are polyvinylpyrrolidone (PVP) and polyacrylonitrile (PAN) (Figure 4.1(e) and (f) respectively). PVP is known to be thermally labile, subliming readily with the decomposition of intra and intermolecular bonds occurring above 275 °C, to leave only a little carbonised product (Figure 4.2). PAN on the other hand is commonly used as a precursor to synthesise carbon nanofibers, it is less thermally labile and the thermal chemistry is well understood [Pels *et al*. (1995), McGann *et al*. (2012)]. During carbonisation of PAN the cyano groups undergo cyclisation by polymerisation at 200-300 °C to form conjugated imines. With further heat treatment, up to 700-800 °C, hydrogen is released and a series of aromatic pyridine rings formed [Pels *et al*. (1995)]. Further heat treatment (>900 °C) introduces small components of nitrogen into the basal plane of the nanographenes in a quaternary state [McGann *et al*. (2012)]. As a result carbonisation at 700 °C is suitable to deliver a pyridine rich N-doped carbon. Furthermore to control the ratio of pyridine/quaternary nitrogen in the carbon matrix and elucidate the role of the different groups, carbonisation at 900 °C was also selected. The polymers were carbonised separately in a tube furnace under a steady flow of nitrogen. The furnace was heated at a ramping rate of 3 °C/min to the desired temperature, with a dwell time of 1 hour. The four N-doped carbons obtained were: PVP X and PAN X, where X is the temperature of carbonisation, either 700 or 900 °C. The yields of PAN and PVP at 700 and 900 °C are shown in Table 4.1.

The products of carbonisation were tested using TGA analysis for their CO_2 uptake capacity at 298 K and 1 bar, revealing that none excepting PVP 900 (with a capacity of 0.36 mmol/g) had any affinity for CO_2 (Figure 4.3(a)). Indeed using BET specific surface area analysis these carbonised materials can be seen to be non-porous, again excepting the PVP 900, which displayed a small BET specific surface area of 55.5 m^2/g (Figure 4.3(b) and Table 4.1). From XPS analysis (Table 4.1) these PVP and PAN derived carbons can be seen to possess considerable nitrogen contents, up to 12.3 at.%.

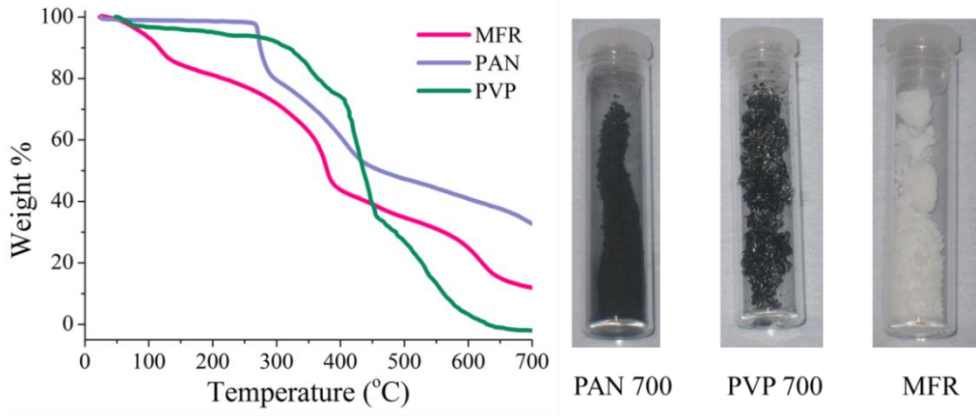

Figure 4.2. TGA plots for PAN, PVP and the melamine-formaldehyde resin (MFR), heating to 700 °C at 2 °C/min under argon. Photos of samples PAN 700, PVP 700 and MFR.

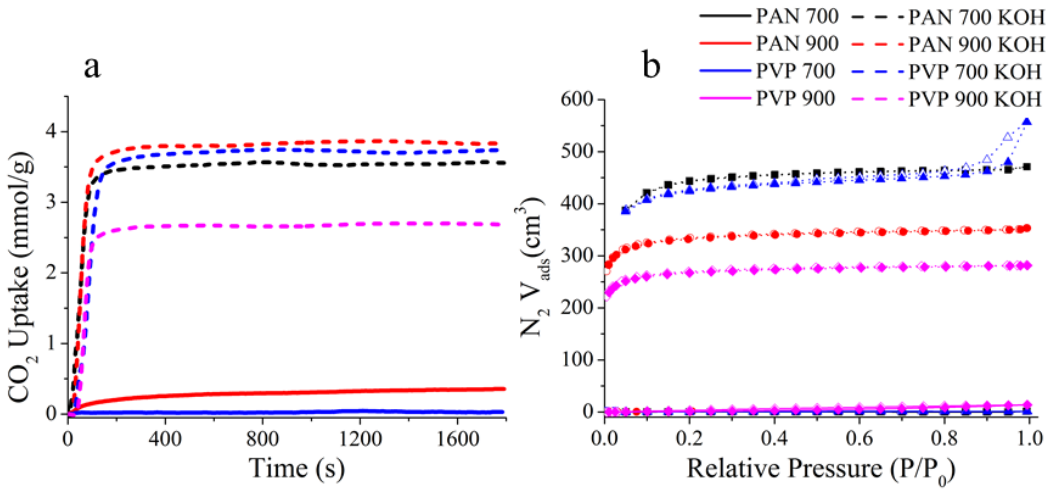

Figure 4.3. (a) CO_2 uptake analysis at 1 bar CO_2 and 298 K, on a gravimetric basis for PAN and PVP derived and activated carbons. (b) N_2 isotherms at 77 K showing adsorption (filled symbols) and desorption (open symbols) between 0-1 bar for the PAN and PVP series.

4.2 Carbonisation of Polyvinylpyrrolidone and Polyacrylonitrile

Due to the low apparent porosity obtained following carbonisation, the carbonised products were then activated using chemical activation with KOH, a common chemical activant that has been shown to produce porous materials dominated by microporosity in good yield [Lee *et al*. (2013), Shen *et al*. (2011), Zhang *et al*. (2013), Xing *et al*. (2012), Sevilla *et al*. (2011a)]. For the activation process a ratio of 2:1 KOH:carbon were ground into a fine grey powder using a pestle and mortar then heated at 3 °C/min to 700 °C, with a dwell time of 1 hour. The remaining chemical activation agents were then removed by washing with distilled water and the obtained products were designated as PVP X KOH and PAN X KOH, where X is the temperature of initial carbonisation, either 700 or 900 °C. From XPS analysis (Figure 4.4(a)) the chemical activation agent is successfully removed as indicated by absence of potassium ions (K 2p species are usually found at a binding energy of 294-296 eV).

Table 4.1. Collated data for the PAN and PVP series including: porous characteristics, CO_2 performance, sample yields and elemental analysis

Material	SSA_{BET} (m^2/g)	V_{tot} (cm^3/g)	V_M (cm^3/g)	CO_2 uptake (mmol/g)	Yield (%)	Elemental analysis (at.%)		
						C	O	N
PAN 700	1.0	-	-	-	48.3	82.6	4.9	12.3
PAN 900	19.6	-	-	-	43.5	88.5	4.0	7.4
PVP 700	2.3	-	-	-	7.2	90.5	3.9	5.5
PVP 900	55.5	-	-	0.36	5.8	93.0	3.8	3.2
PAN 700 KOH	1691.0	0.729	0.541	3.64	26.5	87.8	9.5	2.7
PAN 900 KOH	1311.2	0.548	0.465	3.59	67.9	85.1	13.2	1.6
PVP 700 KOH	1599.6	0.861	0.563	3.43	48.9	84.5	14.7	0.8
PVP 900 KOH	1052.4	0.437	0.377	3.22	57.8	82.5	15.2	1.8

CO_2 uptake was measured at 298 K and 1 bar CO_2 on a volumetric basis, expect for PAN 900 and PVP 900 which is taken from gravimetric tests. Yields are based the amount of direct precursor used, e.g. amount of PAN 700 KOH is based on amount of PAN 700 starting material. Elemental analysis is taken from XPS surface analysis.

XPS analysis was used for further chemical and elemental analysis of the PAN and PVP derived and activated carbons. Table 4.1 shows the PAN derived materials achieve greater nitrogen dopant levels than their PVP equivalents. It also shows that the activation with KOH significantly reduces the nitrogen content, with the activated nitrogen doped porous materials derived from PAN and PVP containing nitrogen in 0.8-2.7 at.%. From the core level C 1s spectra (Figure 4.4(b)) the majority of the carbon atoms in the PAN and PVP derived carbons are in sp^2-hybridised graphitic type forms, with binding energies centred at 284.6 eV. The shoulder peak at 286.3 eV for the activated carbons can be ascribed to carbon in various oxygen bound environments [Yang *et al*. (2009), Sheng *et al*. (2011)]. As expected from the low content from elemental analysis, the N 1s spectra is weak for the activated materials. The non-activated carbons show peaks at 398.4 and 400.8 eV, typical for pyridine and pyrrolic/quaternary nitrgoen respectively [Wu *et al*. (2012), Sheng *et al*. (2011)]. It is also evident that at 900 °C the pyridinic form is reduced in prevalence and the quaternary form is favoured. The N 1s peaks of the activated carbon materials are centred around 400.2 eV, indicative of pyrrolic, quaternary and pyridonic forms [Pevida *et al*. (2008a)]. However, pyridonic nitrogen forms are known to decomposes at 500 °C, and pyrrolic groups convert to pyridinic nitrogen forms at 600 °C [(Pels *et al*. (1995)], so it can be assumed this is mostly quaternary nitrogen. From the symmetrical O 1s spectra at 532.8 eV for the activated carbon the oxygen is typically in single bonded environments to carbon atoms within aromatic rings, such as phenolic and esters groups

[Larciprete *et al*. (2011)]. Chemical analysis using FTIR reveals little chemical information due to the high absorbance of the materials and is not included.

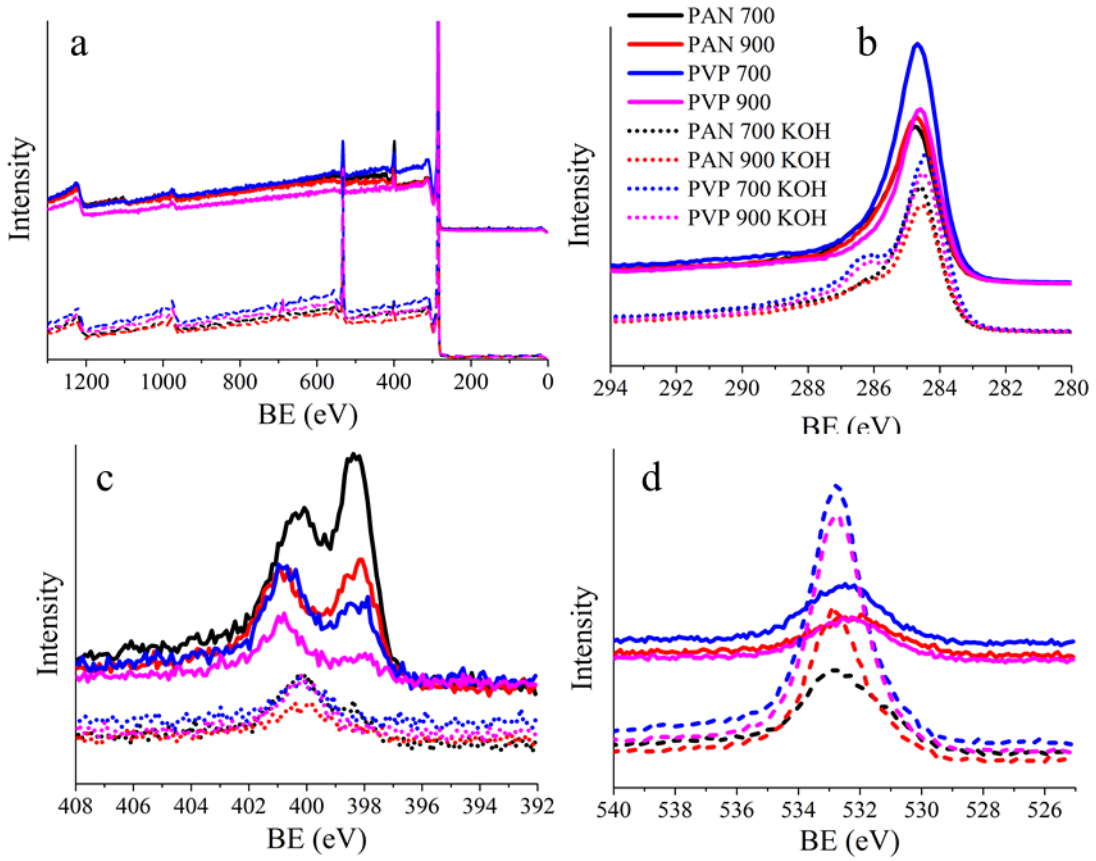

Figure 4.4. The XPS survey spectra (a) and core level C 1s (b), N 1s (c) and O 1s (d) for the PAN and PVP derived and activated carbons.

The pore and structural characteristics of the materials were anlaysed using nitrogen iostherms at 77 K (Figure 4.3(b)). While the non-activated carbons have very little apparent porosity, the activation process develops significant porosity with BET specific surface areas of up to 1691.0 m^2/g for PAN 700 KOH the most porous and 1052.4 m^2/g for PVP 900 KOH the least porous. Both the samples carbonised at 700 °C gave higher surface areas after activation than those carbonised at 900 °C. From the type-I nature of the N_2 isotherm and the narrow knee in the adsorption curve at low relative pressure, the activated samples can be seen to have structures dominated by micro and narrow mesoporosity. This is further supported by the QSDFT pore size distribution plots (Figure 4.5(a)) that show all sample porosity lies in pores ≤3 nm in diameter, excluding the PVP 700 KOH which has some larger mesopore volume. Indeed, the majority of all activated samples total pore volume is microporous: 74, 85, 65 and 86 % for PAN 700 KOH, PAN 900 KOH, PVP 700 KOH and PVP 900 KOH respectively (Table 4.1). The activation mechanism of pore opening carried out by KOH is discussed in chapter 6, where a more in depth analysis of the process is undertaken. Therefore through this controlled activation technique moderately N-doped highly porous carbon based materials have been

synthesised, dominated by pores in the micropore region and thus they could be favourable for the adsorption of CO_2 at atmospheric pressures.

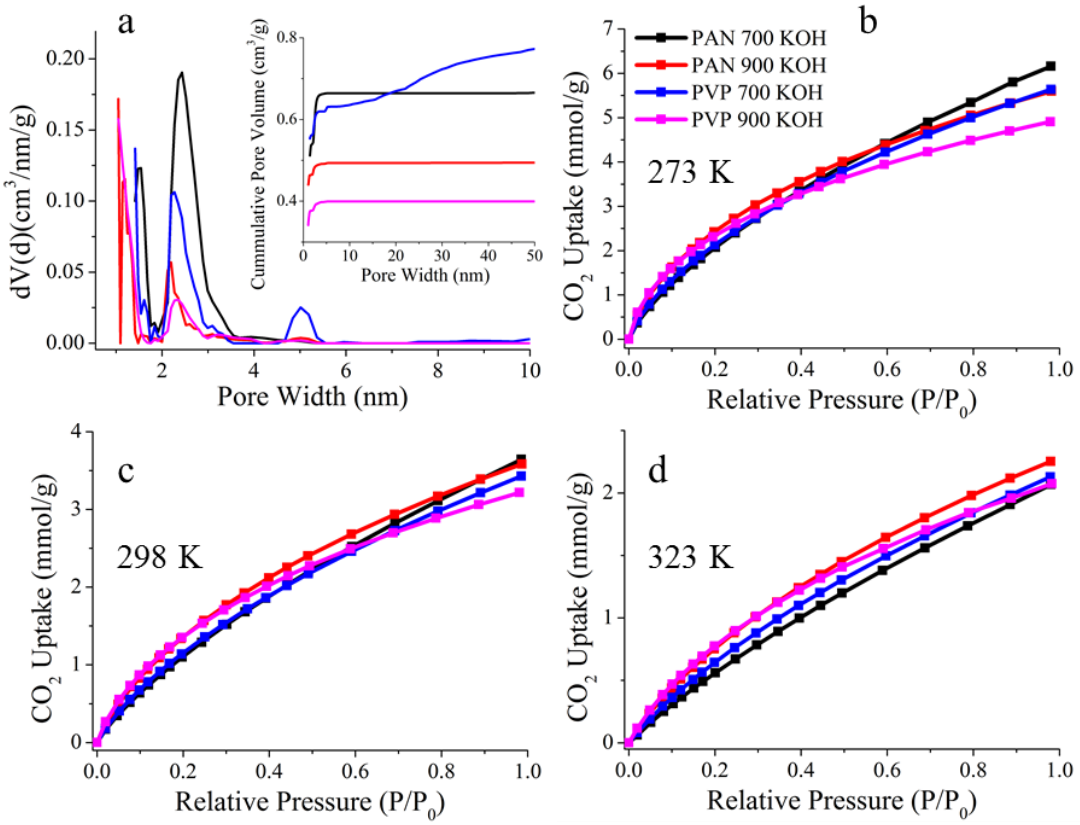

Figure 4.5. (a) QSDFT pore size distribution plot for the PAN and PVP series, showing cumulative pore volumes in pores of up to 50 nm (inset) for the PVP and PAN activated carbons and CO_2 adsorption isotherms (0-1 bar) at (b) 273 K, (c) 298 K and (d) 323 K.

The resulting CO_2 uptake performance of these highly microporous N-doped carbons can be seen in Figure 4.5, where tests have been carried out at 273, 298 and 323 K, up to 1 bar CO_2. It can be noted that the PAN 700 KOH, the sample with the highest nitrogen content, has the greatest CO_2 capacity at 273 and 298 K, despite not having the greatest surface area or micropore volume; a potential indication that nitrogen content may be linked to an increase in uptake capacity. When compared to other activated carbon materials these capacities are good and typical of other KOH activated porous carbon materials that use the same ratio of KOH to carbon precursor. Such activated carbons normally achieve CO_2 capacities of 2-4.5 mmol/g at 298 K and 1 bar, with the variation in capacity the result of different precursors used and activation method (see Table 1.1). While many of the materials with particularly high capacities (>4.0 mmol/g) contain N-dopants, not all do.

The role of the nitrogen content in the activated PVP and PAN carbons can be further understood by calculating the enthalpy of adsorption (Q_{st}) (Figure 4.6(a)). From this the PAN and PVP carbons exhibit enthalpies of adsorption typical for undoped carbon materials (10.5-28.4 kJ/mol [Guo et al. (2006)]), suggesting the N-dopants do not play an active part in CO_2

uptake, instead it is a totally micropore dependant process. Such low Q_{st} values in spite of the N-doping can be attributed to the absence of the Lewis basic pyridine functionality.

The CO_2/N_2 selectivity was calculated for the PAN and PVP activated carbons, a characteristic of a material that may be enhanced through N-doping [Zhao *et al*. (2012a)]. The CO_2/N_2 selectivities were calculated using the ideal adsorbed solution theory (IAST) method that predicts mixture adsorption equilibriums using single-component adsorption isotherms. The CO_2 and N_2 adsorption curves at 273 and 298 K are shown in Figure 4.6(b) giving selectivities of 14-17 at 273 K and 14-17 at 298 K. These values are typical for undoped activated carbons in which CO_2/N_2 selectivities typically fall as temperature increases [Zhang *et al*. (2013)], so it is notable that the selectivities remain similar at 273 and 298 K for the PVP and PAN activated carbons.

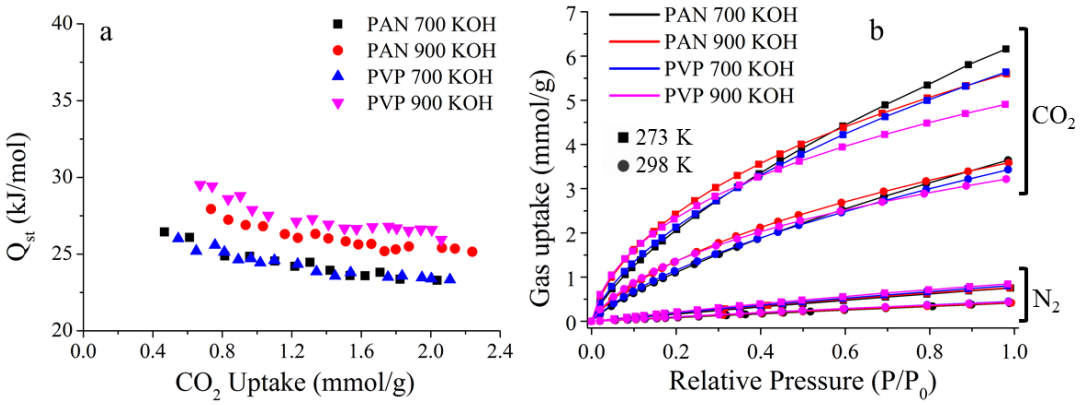

Figure 4.6. (a) (Q_{st}) calculated from CO_2 adsorption isotherms up to 1 bar at 273, 298 and 323 K (b) CO_2 and N_2 adsorption isotherms up to 1 bar at 273 and 298 K for the PAN and PVP series.

4.3 Synthesis of a Melamine-formaldehyde Resin

Alternatively, a melamine-formaldehyde resin (MFR) polymer as carbon precursor is also of interest. MFRs are attractive as they are well understood, industrially available, nitrogen rich and largely aromatic. MFRs have been the subject of research for several years, and their synthesis is well understood [Leidl *et al*. (2005), Pevida *et al*. (2008b), Wilson *et al*. (2000), Bauer *et al*. (1980), Ruben *et al*. (1995), Pekala *et al*. (1992)].

The polymerisation (resin curing) of melamine and formaldehyde (Figure 4.7) proceeds via two stages. The first step, called methylolation, is the addition reaction of formaldehyde to melamine and is carried out in an aqueous phase under typically basic conditions. The second stage of curing mainly consists of two types of condensation reactions leading to the formation of methylene and methylene ether bridges (Figure 4.7) and this is carried out via heating under

acid/basic conditions. During the curing chain extension and crosslinking takes place to form a hard insoluble 3-dimensional network.

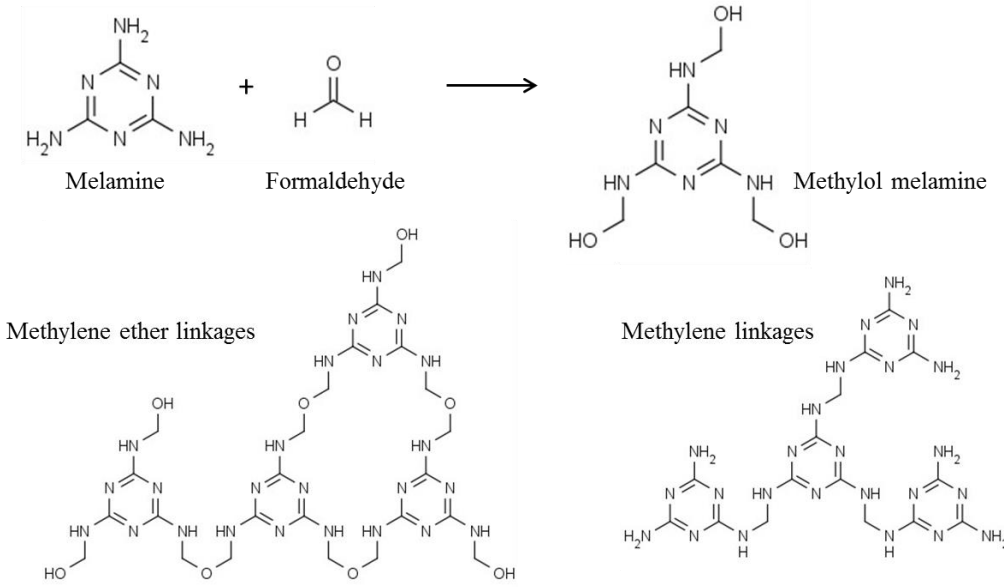

Figure 4.7. Schematic showing melamine, formaldehyde and structural forms that occur during the curing process.

On addition of melamine to formalin nine distinct methylolmelamines are formed in a complex series of competitive and consecutive equilibria [Tomita (1977)].

A monomethylolated amino group may form:

$$-NH_2 + HOCH_2OH \leftrightarrow -NHCH_2OH + H_2O \qquad \text{(Equation 4.1)}$$

Subsequent reaction gives a disubstituted group:

$$-NHCH_2OH + HOCH_2OH \leftrightarrow -N(CH_2OH)_2 + H_2O \qquad \text{(Equation 4.2)}$$

Two types of condensation reactions are then possible:

Reaction of a methylol group with an amino group to form a methylene linkage:

$$-NH_2 + -NHCH_2OH \leftrightarrow -NH-CH_2-NH- + H_2O \qquad \text{(Equation 4.3)}$$

Reaction of two pairs of methylol groups in mutual condensation to give a methylene ether linkage:

$$2\ -NHCH_2OH \leftrightarrow -NH-CH_2OCH_2-NH- + H_2O \qquad \text{(Equation 4.4)}$$

The various possible reactions lead to formations of oligomeric melamine structures by random combination of possible forms of methylolmelamines connected via either methylene ether or methylene bridges (Figure 4.7). Reaction conditions play a complicated role influencing the exact make-up of the final polymer with formation of a methylene linkage favoured by low pH,

low formaldehyde to melamine ratios and by relatively high temperatures during curing. In turn the formation of methylene ether linkages is believed to be favoured by high pH and by high F/M rations. Of these two linkages (methylene and methylene ether) the oxygen present in the ether form can be considered detrimental to the formation of N-doped carbon due to the generation of oxygen dopants. As a consequence the methylene form is considered preferential. Indeed, the MFR was synthesised using a low melamine-formaldehyde ratio of 1:2 with a sodium hydroxide catalysed first step. Following formation of the methylolmelamine, observable by the insoluble melamine fully dissolving in aqueous solvent, the pH was adjusted to 1.5-1.8, a suitably low value and curing was carried out at 95 °C [Merline *et al*. (2013)].

As discussed in the introduction the use of rigid bonds, such as aryl-aryl and alkynes, that forbid bond rotation in polymeric structures has been utilised in MOPs to delivery porosity intrinsic to the structure. Conversely, the MFR contains structural units such as the methylene bonds, around which rotation is possible, enabling the polymer to adopt the most energetically favourable structural conformation, typically one with a low pore volume. While MFR does not contain rigid bonding, porosity can still be obtained through transformation of the wet resin to an aerogel; a porous material obtained by replacing the liquid component with a gas.

As the MFR is cured in an aqueous environment the polymer is swollen, containing H_2O molecules that permeate the structure. Upon traditional drying a liquid-vapour meniscus is formed due to the surface tension of the liquid, which recedes during the emptying of the pores in the wet resin. As the meniscus recedes a capillary pressure gradient builds in the pore walls and collapses most of the pore volume. To avoid this, the liquid surface tension must be removed and this is possible by freeze drying, whereby the wet resin is first frozen and dried by sublimation. Furthermore, for successful freeze-drying the water can be replaced with tert-butanol using solvent-exchange, a solvent with a low expansion coefficient and a high pressure of sublimation [Pierre *et al*. (2002)].

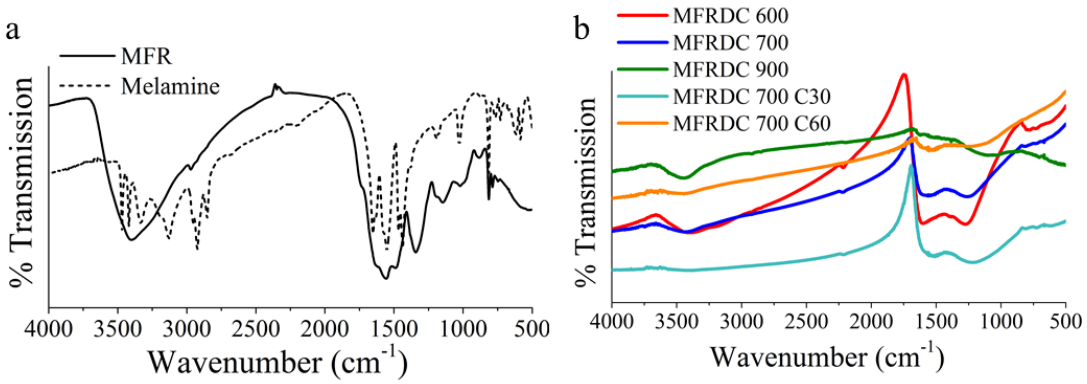

Figure 4.8. FTIR analysis of (a) MFR and melamine starting material (b) MFR derived carbon.

The thus obtained MRF was then analysed chemically using XPS and FTIR spectroscopy. From the FTIR analysis (Figure 4.8(a)) primary amine stretching and bending modes (3469, 3419 cm^{-1} and 3331, 3130 cm^{-1} respectively) in melamine are lost and replaced by a broad secondary amine stretching at 3401 cm^{-1} in the MFR [Scheepers *et al*. (1993)]. The MFR polymer methylene linkages can be identified by their aliphatic C-N vibration modes at 1151 cm^{-1} and their aliphatic C-H stretching peaks at 2974 cm^{-1}, though this is largely obscured by the broad amine stretching peak [Merline (2013)]. The triazine IR modes for the MFR can be observed at 1563 and 1343 cm^{-1} due to in-plane stretching vibrations and 811 cm^{-1} as a result of out-of-plane ring deformation [Pevida *et al*. (2008b)].

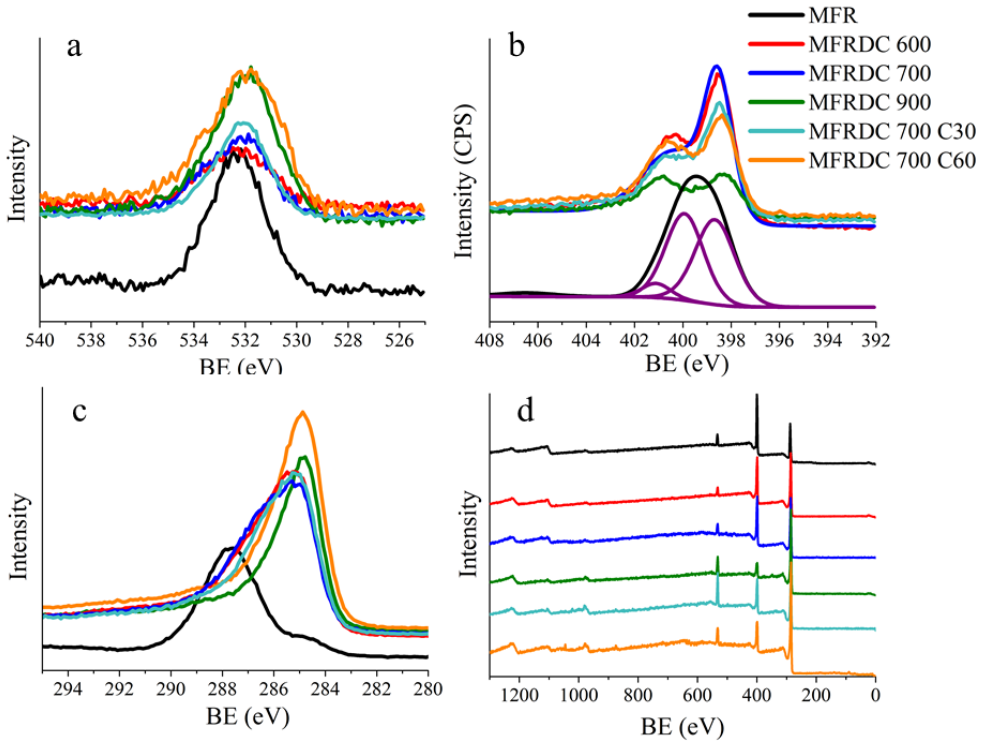

Figure 4.9. Core level O 1S (a), N 1s (b) and C 1s (c) XPS spectra for MFR and its derived carbons, MFR N 1s peak includes deconvolution fitting with three peaks at 398.7 and 399.9 and 401.1 eV (purple). The survey spectra are also shown (d).

Using XPS elemental analysis (Table 4.2 and Figure 4.9) the atomic ratio of C:N is 1:1.08 which deviates from the theoretical ratio of 1:1 (see the polymers in Figure 4.7, both those with methylene ether and methyene linkages). However, this deviation from 1:1 can be accounted for by the presence of polymer end groups [Merline *et al*. (2013)]. There is also 5.6 at.% oxygen present which from the core level O 1s analysis peak at a binding energy of 532.2 eV (Figure 4.9(a)) indicates that some of the polymer linkages may be methylene ether (C-O-C). Indeed, deconvolution of the N 1s spectra (Figure 4.9(b)) shows 5 % of the nitrogen is bonding in the methylene ether linkage form (401.1 eV), the two equivalent peaks at binding energies of 399.9 and 398.7 eV can be ascribed to methylene linkages and triazine forms [Coullerez *et al*. (2000)],

showing the methylene linkage dominates as proposed. In the C 1s spectrum (Figure 4.9(c)) the peak at a binding energy of 287-288 eV is attributed to carbon in a triazine ring environment and in methylene/methylene ether form, the smaller peak at 285.0 eV as attributed to adventitious hydrocarbon contamination, which is not unexpected upon curing [Coullerez *et al*. (2000)].

The porous characteristics of the MFR are given in Table 4.2. The MFR has a BET specific surface area of 327.1 m^2/g and total pore volume of 1.78 cm^3/g. Micropores only contribute 0.015 cm^3/g of this total pore volume indicating a largely meso-macroporous structure. From the N_2 isotherm at 77 K (Figure 4.10) the MFR can be seen to have a type-II isotherm indicating a hierarchical pore structure with meso, macro and microporosity. The presence of wide mesopores is evident due to the increase in the N_2 adsorption as relative pressure increases, where many layers of adsorbate are forming. This is further supported by the QSDFT pore size distribution plot (Figure 4.11) which shows dominant mesoporosity, with some micropores of 1-1.5 nm in width. The volumetric analysis (Figure 4.12) shows the MFR has a CO_2 uptake capacity of 0.99 mmol/g at 1 bar and 298 K. Hence this represents the synthesis of an as made porous melamine-formaldehyde resin with reasonable CO_2 uptake performance, interestingly the polymer obtained is not synthesised using rigid building blocks. Instead, through aerogel formation it retains open micropore volume making it capable of CO_2 sorption. While relatively moderate the CO_2 uptake capacity of the MFR aerogel makes it competitive with a range of other porous polymer materials synthesised from more complex approaches such as Yamamoto coupling and Sonogashira cross-coupling [Holst *et al*. (2010)], Friedel-Crafts chemistry [Dawson *et al*. (2012b) and silica templated melamine-formaldehyde polymers [Wilke *et al*. (2011)], all of which show capacities of ~1.0 mmol/g.

Table 4.2. Collated data for MFR and its derived N-doped carbons including: porous characteristics, CO_2 performance, yields and elemental composition

Material	SSA_{BET} (m^2/g)	V_{tot} (cm^3/g)	V_M (cm^3/g)	CO_2 uptake (mmol/g)	Yield (%)	Elemental analysis (at.%)		
						C	N	O
MFR	327.1	1.778	0.015	0.99	92.2	49.3	44.9	5.6
MFRDC 600	142.8	0.310	0.026	1.35	18.5	68.2	28.9	2.9
MFRDC 700	48.2	0.085	0.012	1.58	17.4	66.2	30.1	3.6
MFRDC 900	20.1	0.031	0.003	0.39	7.9	82.2	10.5	7.2
MFRDC 700 C30	177.7	0.145	0.072	1.76	80.2	65.2	23.1	11.5
MFRDC 700 C60	388.4	0.349	0.117	1.79	37.7	79.8	15.1	5.0

Uptake was measured at 298 K up to 1 bar CO_2 on a volumetric basis, expect for MFRDC 900 which is taken from gravimetric tests. MFR yield is based on 100 % methylene linkages. The MFRDC yields are relative to amount of MFR used and the yield of MFRDC 700 Cs are relative to amount of MFRDC 700.

4.4 Carbonisation of the Melamine-formaldehyde Resin

To greater enhance the MFR material as a CO_2 sorbent the polymer was carbonised. Carbonisation of the MFR enables the N-dopant chemistry to be tuned, converting the triazine rings into other forms, such a pyridine groups. The porous structure will also be altered. It has been documented that the triazine ring, of which the MFR mainly consists, will decompose around 600-700 °C [Pevida *et al*. (2009)]. Using TGA analysis of the decomposition under an inert atmosphere (Figure 4.2) three main regions of mass loss can be identified: up to 150 °C mass loss due to adsorbed water occurs, at 280-400 °C the mass loss can be ascribed to methylene linkage decomposition and the mass loss at over 600 °C occurs due to the decomposition of the triazine rings. While the triazine ring is not stable over 700 °C, pyridinic and quaternary forms of nitrogen have been reported as stable up to 1000 °C [Peks (1995)]. Carbonisation of the MFR was therefore carried out at 600 and 700 °C, the temperatures before and after decomposition of the triazine structure, in order to obtain nitrogen doped carbon containing contrasting nitrogen forms. Furthermore carbonisation was also carried out at 900 °C to further document the effect of contrasting nitrogen forms on CO_2 sorption and for ease of comparison with the PAN and PVP carbons. Using the same procedure as for the PVP and PAN carbons the MFR was carbonised in a tube furnace under a steady flow of nitrogen. The furnace was heated at a ramping rate of 3 °C/min to the desired temperature, with a dwell time of 1 hour. The melamine-formaldehyde resin derived carbons (MFRDC) obtained were labelled as MFRDC X, where X is the temperature of carbonisation: 600, 700 or 900 °C.

The chemistry of the MFRDCs was analysed using FTIR and XPS. From the XPS elemental analysis (Table 4.2) there is little difference in the MFRDC 600 and MFRDC 700, with both displaying high quantities of N-dopants at around 30 at.%. The MFRDC 900 displays considerable nitrogen loss having only 10 at.%. The nitrogen forms can be analysed using XPS (Figure 4.9(b)) where the core level N 1s spectra for MFRDC 600 and 700 are dominated by pyridinic nitrogen, evident at a binding energy of 398.5 eV. A smaller peak is present at a binding energy of 400.6 eV, this can be assigned to contributions from pyrrolic, pyridonic [Pels *et al*. (1995)] and quaternary nitrogen groups [Lv (2012)] with the different types hard to deconvolute. Of note is that in the MFRDC 700 N 1s spectrum a reduction of the peak at 400.6 eV is evident, this can be ascribed to loss of pyridonic nitrogen which decomposes at 500 °C, and pyrrolic groups which convert to pyridinic nitrogen at 600 °C [Pels *et al*. (1995)]. For the MFRDC 900 the two peaks (398.4 and 400.8 eV) are more equivalent in size, attributed to conversion of pyridinic (398.4 eV) into quaternary nitrogen (400.8 eV) at elevated temperatures. The core level C 1s spectra for the derived carbons (Figure 4.9(c)) all show a peaks at binding

energies of 284.8-285.1 eV, which are assigned to sp^2 hybridised carbon in aromatic graphite-type domains. In the MFRDC 600 and 700, the asymmetric nature of the peak centred at 285.1 eV, broadened to give a shoulder peak at higher binding energies, is attributed to carbon bound to heteroatoms, in this case nitrogen groups. The C 1s spectrum of the MFRDC 900 is centred at 284.7 eV, shifted slightly from the 700 and 600 equivalents in agreement with a greater degree of graphitisation, the peak is also less asymmetric due to fewer N-dopants.

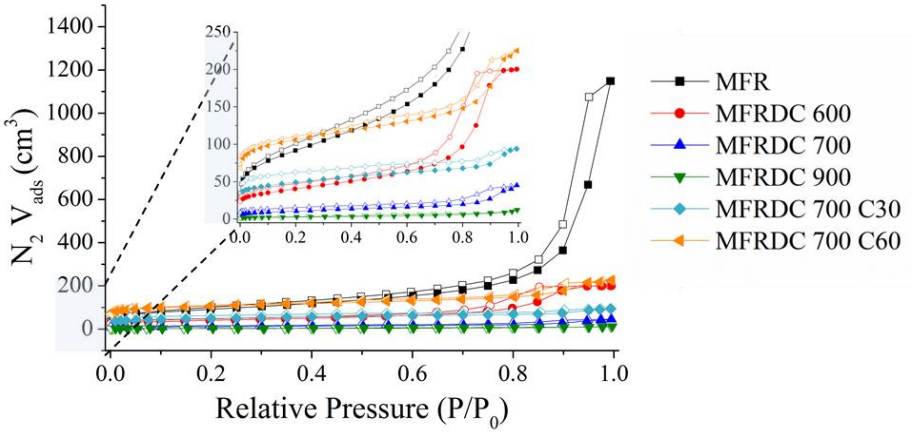

Figure 4.10. N_2 isotherm at 77 K showing adsorption (filled symbols) and desorption (open symbols) between 0-1 bar for MFR and its derived carbons.

FTIR analysis of the MFRDCs (Figure 4.8(b)) shows peaks at 1550-1600 cm^{-1} that are from aromatic ring C=C stretching vibrations and at 1250-1280 cm^{-1} from C-N stretching vibrations. The broad peaks at 3400 cm^{-1} can be assigned to N-H symmetric stretching vibrations, O-H group stretching or the O-H stretching from interacting water. In the MFRDC 600 a peak at 808 cm^{-1} can be assigned to the out-of plane deformation modes of triazine rings that are still present. The absence of this peak in the MFRDC 700 and MFRDC 900 indicates the triazine rings decompose after carbonising at and above 700 °C.

Structural analysis carried out using nitrogen isotherms at 77 K, shows all the MFRDCs exhibit a type-I N_2 isotherm (Figure 4.10) consistent with a microporous structure, indicating that under carbonisation the mesoporous structure of the melamine-formaldehyde resin shrinks to form microporous domains. This shrinking is further evidenced from the incremental decrease of surface area, total and micropore volume as carbonisation temperature increases. Volumetric CO_2 sorption analysis was carried out on the MFRDCs, with isotherms at 1 bar and 273, 298 and 323 K shown in Figure 4.12 and uptake capacities at 1 bar and 298 K given in Table 4.2. Of the derived carbons the best performing was the MFRDC 700 with a capacity at 298 K and 1 bar of 1.58 mmol/g, notably better than the MFR (0.99 mmol/g).

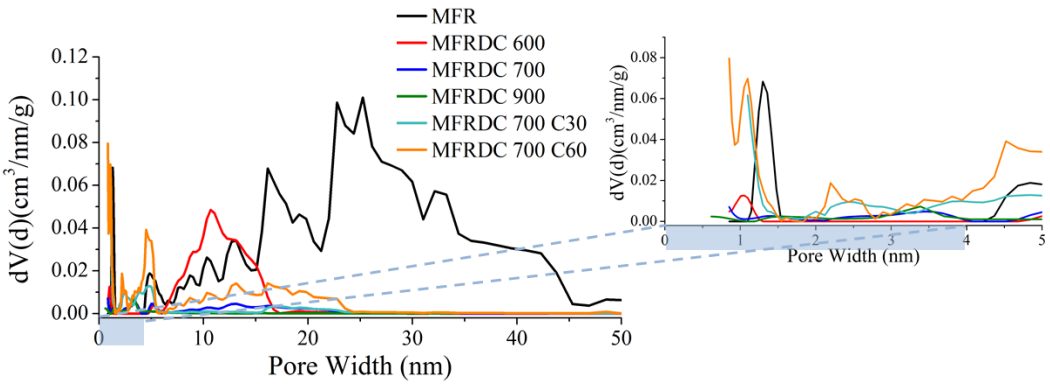

Figure 4.11. QSDFT pore size distribution plot for MFR and its derived carbons, showing distributions in pores of up to 50 nm, with 0-5 nm inset.

4.5 Activation of the Melamine-formaldehyde Resin

To further enhance the micropore volume of the MFRDCs, activation was carried out. KOH activation was attempted from the MFR, achieving a zero yield. Alternatively, publications have achieved excellent uptake capacities using CO_2 activation, in particular porous N-doped activated carbon monoliths [Nandi (2012)], so a CO_2 activation regime was undertaken. For this CO_2 activation, the MFRDC 700 was selected, due to it exhibiting the highest CO_2 capacity. CO_2 activation was carried out for 30 and 60 minutes giving MFRDC 700 C30 and C60 in yields of 80.2 and 37.7 % respectively, relative to the MFRDC 700 starting material (Table 4.2). Due to the dark absorptive nature of the materials the FTIR gives little evidence as to the chemical composition (Figure 4.8(b)). The XPS elemental analysis on the other hand shows that the N-dopants are volatile under the activation regime, with N-dopant concentration decreasing with an increase in residence time (23.1 to 15.1 at.% from C30 to C60, Table 4.2). Correlated to this is an increase in oxygen concentration initially, 11.5 at.% for MFRDC 700 C30 compared with 3.6 at.% in the MFRDC 700, this then falls with activation time to 5.0 at.% for the MFRDC 700 C60. From the core level N 1s spectra (Figure 4.9(b)) of C30 and C60 the ratio of pyridinc:quaternary/pyrrolic nitrogen decreases with activation time, indicating the decomposition of pyridinic groups, while the quaternary form is more stable. The oxidation of pyridinic groups to pyridonic forms can be ruled out due to their instability at such elevated temperatures [Pels *et al*. (1995)].

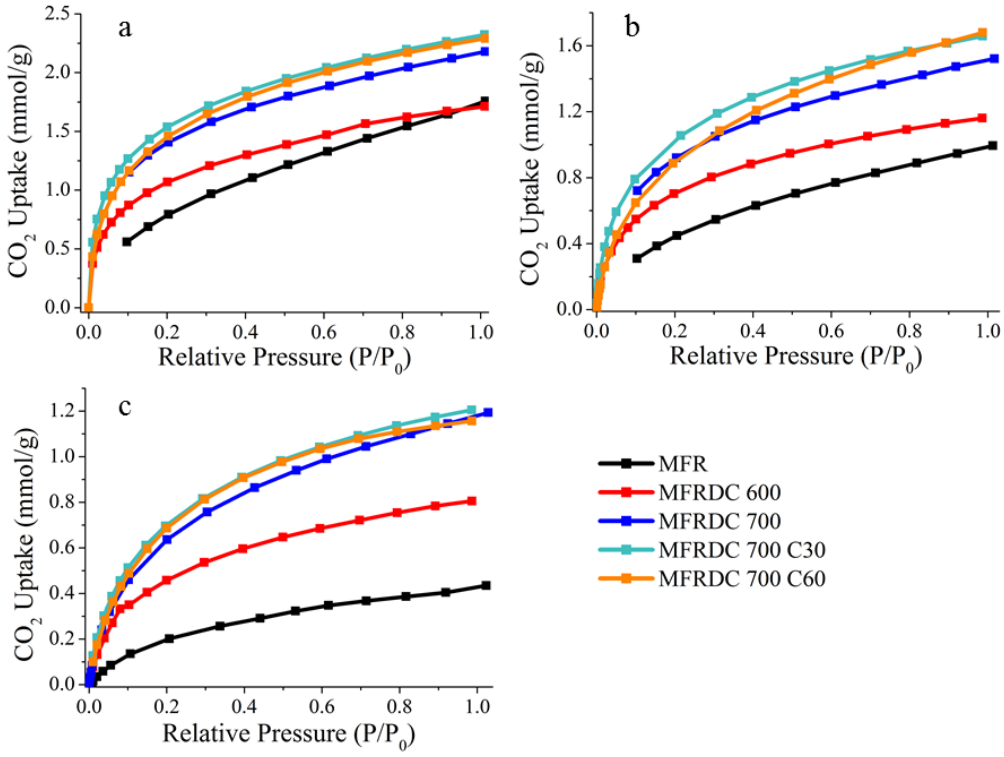

Figure 4.12. CO_2 adsorption isotherms (0-1 bar) for MFR its derived and activated carbons at (a) 273, (b) 298 and (c) 323 K.

From the type-I N_2 isotherms at 77 K (Figure 4.10) the BET specific surface area increases with activation residence time to 177.7 and 388.4 m^2/g for C30 and C60 relative to 48.2 m^2/g for MFRDC 700 (Table 4.2). The total and micropore volume also increases with residence time. The total pore volume is 0.145 and 0.349 cm^3/g for C30 and C60 relative to 0.085 cm^3/g for MFRDC 700, and micropore volume is 0.072 and 0.117 cm^3/g for C30 and C60 relative to 0.012 cm^3/g for MFRDC 700. The effect of activation is also apparent from the pore size distribution curves which also reveal a development of microporosity (Figure 4.11). Corresponding to this developed microporosity accordingly enhanced CO_2 capacities are 1.76 and 1.79 mmol/g for C30 and C60 respectively at 298 K and 1 bar. This CO_2 capacity increase from activation, relative to the MFRDC 700 (1.58 mmol/g), can be attributed to the activation regime opening micropore volume. Previous melamine-formaldehyde derived carbons have achieved CO_2 uptakes of 2.25 mmol/g at 1 bar and 298 K [Pevida et al. (2008b)], however, for these materials a hard-template was used that required a harsh HF etching process to remove. Interestingly the increase in micropore volume from C30 to C60 does not correlate to a significant increase in CO_2 uptake, this may be ascribed to either effects of the greater nitrogen concentrations in the less porous materials, or to the ultramicropores (<0.7 nm in diameter) that are not observed using N_2 adsorption at 77 K due to kinetic effects [Garrido *et al*. (1987)].

The effect of N-dopants can be further understood by measuring the isosteric heats of adsorption (Q_{st}) (Figure 4.13(a)), calculated from the isotherms at 273, 298 and 323 K (Figure 4.12).

Interestingly, all of MFRDC N-doped porous carbons exhibit elevated Q_{st} values relative to those of undoped porous carbons (10.5-28.4 kJ/mol [Guo et al. (2006)]), with values all around 50 kJ/mol at near zero CO_2 loadings, among the very highest reported for porous carbon materials [Nandi *et al*. (2012), *et al*. Zhong (2012), Zhao *et al*. (2012b)]. Also of note is that the MFR, with triazine nitrogen functionality, has a markedly lower enthalpy of adsorption, 28.5 kJ/mol. This indicates that through a controlled carbonisation process not only has the uptake capacity for CO_2 increased but also the binding energy through conversion of the triazine functionality into the nitrogen groups discussed. It also indicates that when regarding the functionality of nitrogen most beneficial for enhancing binding energy, and thus uptake at elevated temperatures (323 K, as required in post-combustion systems), the use of nitrogen in forms found in doped carbon such as quaternary, pyrrolic and pyridinic may be more suitable than nitrogen in triazine form.

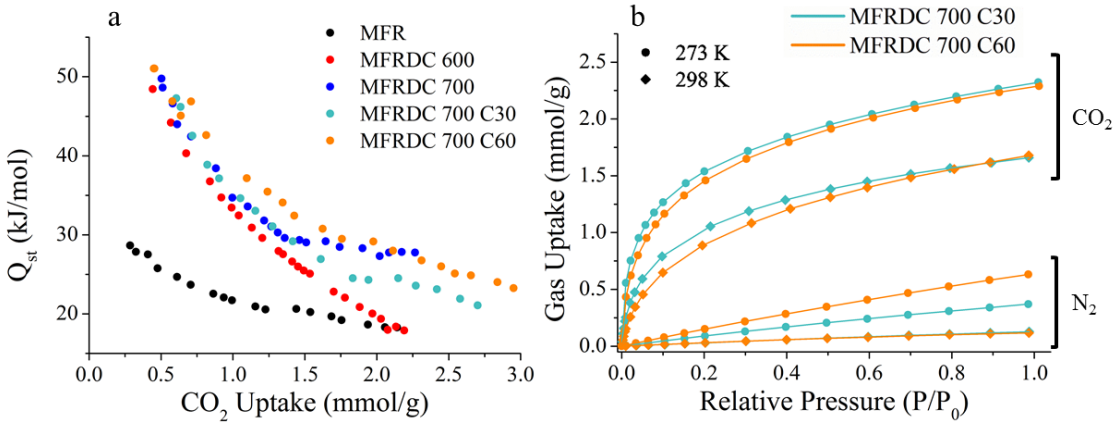

Figure 4.13. (a) Isosteric heats of adsorption (Q_{st}) calculated from CO_2 adsorption isotherms up to 1 bar at 273, 298 and 323 K (b) CO_2 and N_2 adsorption isotherms up to 1 bar at 273 and 298 K.

As the N-doping in the MFRDCs appears to influence the materials interaction with CO_2, the CO_2/N_2 selectivity was calculated for MFRDC 700 C30 and C60 using the IAST method from the CO_2 and N_2 adsorption curves at 273 and 298 K (Figure 4.13(b)). At 273 K the CO_2/N_2 selectivities are 14.5 and 23.0 for C30 and C60 respectively, while at 298 K they are 47.4 and 43.2 for C30 and C60 respectively. These are higher than found in undoped porous carbon materials (Table 1.1) and notably increase with temperatures which is the reverse of that typically found in other porous polymers reported which exhibit significant loss in CO_2/N_2 selectivity on going from 273 to 298 K [Rabbani *et al*. (2012), Dawson *et al*. (2012a)]. Indeed, this increase observed for CO_2N_2 selectivity with temperature has been ascribed to an N_2-phobic character of N-doped materials, ascribed to entropic factors [Patel *et al*. (2013)]. Similar high CO_2/N_2 selectivities (>40) when calculated using the same IAST method have been reported in a range of N-doped porous carbon materials, typically citing the high selectivity as a result of the high nitrogen content in the materials [Zhao et al. (2012a), Lee (2013)]. However, pore size has also been cited as an important factor on the CO_2/N_2 selectivity with small micropores

favouring high selectivity [Dawson *et al*. (2012b)], likely due to the smaller kinetic diameter of CO_2 (0.330 nm) than N_2 (0.364 nm) [D'Alessandro *et al*. (2009)]. While pore size effects cannot be excluded, the lower CO_2/N_2 selectivity and Q_{st} values found in the nitrogen-poor PVP and PAN activated carbons compared to the nitrogen-rich MFRDCs can be ascribed to the influence of N-dopants.

5. N-doping in a Porous Graphene

The temperature of flue gas in post-combustion systems is expected to be between 40-60 °C [Gray *et al*. (2008)]. For solid adsorbents to be competitive with existing liquid amine-based wet scrubbing capture systems, an uptake capacity of ≥3 mmol/g CO_2 at 1 bar is necessary at these temperatures [Dawson *et al*. (2012a), Gray *et al*. (2008)]. High isosteric heats of adsorption have been found in N-doped porous amorphous carbon solids and ascribed to the nitrogen functionality [Nandi *et al*. (2012)]. This increased heat of adsorption has been shown to increase capacity at the elevated temperatures found in post-combustion systems [Sevilla *et al*. (2011a)]. In this chapter synthetic routes towards the synthesis of a porous N-doped graphene material and its potential as a CO_2 capture material are explored. The contrasting carbon matrix of graphene and amorphous carbon solids will also make for an interesting comparison.

Graphene-based materials are of great current scientific interest [Geim (2009)] and their use here is particularly interesting for several reasons: graphene has been shown to possess a very high theoretical specific surface area of 2630 m^2/g [Zhu *et al*. (2010)], making it very attractive as a porous material. Also, the high adsorption heats (ΔH) produced by N-doped functionality can generate over-heating during CO_2 capture, this unavoidably leads to partial degradation of the sorbent, reduced working capacity, poor cycle stability and even safety problems [Yang *et al*. (2013)]. A graphene based material may overcome this due to its high thermal-conductivity, allowing rapid thermal transfer [Zhu *et al*. (2010)]. Furthermore, the incorporation of amine-type nitrogen functionality in porous solids frequently leads to loss of surface area and accessible pores [Lu *et al*. (2012)], graphene-type materials can contain N-doping in various forms such as: pyridine, pyrrole and quaternary, this will incorporate desired nitrogen functionality without such losses [Dawson *et al*. (2012a), Du *et al*. (2009)].

Graphene is a 2-dimensional sheet-like material comprising of sp^2 hybridized carbon atoms ordered in a honeycomb array. Graphene sheets stack together in an ABA pattern through van der Waals interactions to form the non-porous graphite (Figure 5.1(a)). The XRD pattern of graphite powder shows a sharp narrow peak at 26.5° 2θ, representing the (0 0 2) reflection of graphite and corresponding to an interlayer distance between sheets of 0.335 nm. For graphite to be converted into a high-surface area graphene-based material the layers therefore need to be exfoliated. This work then encompasses two main objectives: the exfoliation of graphite and the doping of nitrogen atoms into the honeycomb lattice.

The interest of graphene as a key next generation material for nanoelectronic devices has led to a vast interest in its synthesis [Novoselov *et al*. (2005), Park *et al*. (2009)], with chemical

vapour deposition [Zhou *et al*. (2013)] and expitatal growth [Berger *et al*. (2004)] producing large-domain single crystalline graphene with few defects. These methods are, however, impractical for large scale applications. Instead physical and chemical exfoliation of bulk graphite is more cost-effective and can be combined with the desired chemical functionalisation [Boukhvalov *et al*. (2008)]. Exfoliation can be carried out from starting materials such as graphite oxide, pristine graphite and graphite intercalation compounds (GICs). From pristine graphite, exfoliation can be achieved using sonication with non-ionic surfactants, however, yields are usually quite low [Guardia *et al*. (2011)]. The intercalation of alkali metal atoms or acid molecules in between graphitic layers in GICs increases the inter-layer distance and weakens the van der Waals interactions, facilitating exfoliation [Park *et al*. (2009)]. Alternatively, graphite can be oxidised to form graphene oxide, whereby oxygen functional groups are chemically introduced, increasing the distances between layers. Due to the hydrophilic nature of the oxygen functional groups, the graphene layers can then be dispersed in a wide range of solvents [Stankovich et al. (2007)]. Thermal exfoliation of graphene oxide can also be carried out. Rapid heating to temperatures >200 °C results in the decomposition of the oxygen functional groups at a rate that surpasses the diffusion rate of the evolved gases, creating a pressure that overcomes the van der Waals interaction between graphene layers [McAllister et al. (2007)].

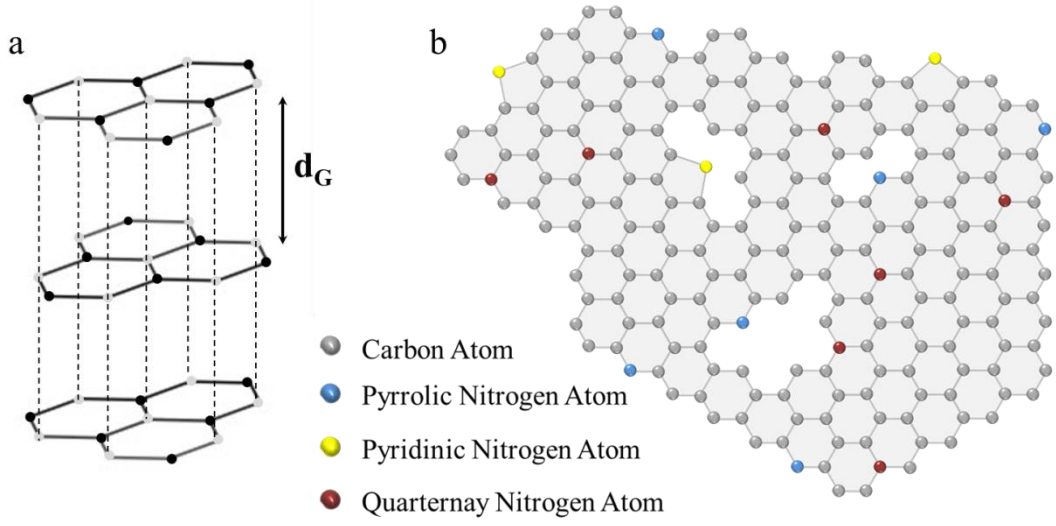

Figure 5.1. (a) Schematic displaying graphite and the ABA stacking arrangement (b) structure of N-doped defective graphene.

The loss of oxygen functionality during the thermal reduction of graphene oxide has been highlighted as a facile route to chemical functionalisation at the reactive sites created [Li *et al*. (2009a)]. The high yield and more realistic scalability of the synthesis also make this an attractive route for the synthesis of N-doped graphene.

Graphene oxide sheets are known to range in size from several hundred nanometres to 1 or 2 μm, they contain vacancy defects, epoxides, hydroxyls, phenols, carbonyl, lactone and quinone functionality resulting in disrupted conjugation [Gao *et al*. (2009)]. It has been shown that such carbonyl, carboxylic, lactone and quinone groups can react with nitrogen containing molecules to form N-doped graphene under thermal treatment [Li *et al*. (2009a)]. The types of N-dopants included in graphene are known to include quaternary, pyridinic and pyrrolic forms (Figure 5.1(b)) [Lv *et al*. (2012)].

5.1 Synthesis of Graphene Oxide

Graphene oxide (GO) was therefore synthesised using what has become known as the modified Hummers method (Pei *et al*. (2012)], where graphite powder is treated with sulfuric acid and potassium permanganate. The potassium permanganate reacts with concentrated sulfuric acid producing manganese (VII) oxide (Mn_2O_7), a very reactive oxidiser. Hydrogen peroxide is added at the end reducing the residual permanganate and manganese dioxide to colourless soluble manganese sulphate [Hummers *et al*. (1958)].

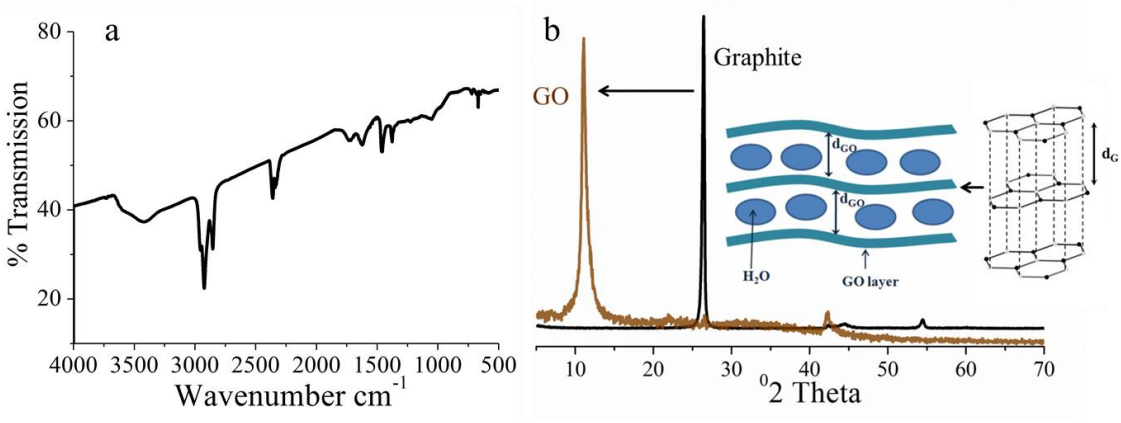

Figure 5.2. (a) FTIR analysis for GO (b) XRD pattern for GO and graphite, with schematic showing structural transformation from graphite to GO with intercalated H_2O.

GO is a tan brown colour and can be well characterised using XRD, FTIR and XPS analysis. From FTIR analysis [Gao *et al*. (2009), Socrates (1980) pp. 44-51], of the as synthesised GO (Figure 5.2(a)) peaks for asymmetric bending modes in carbonyls (C=O) are found for ketones at 1732 cm^{-1} and carboxyls at 1623 cm^{-1}. The peak at 1460 cm^{-1} is assigned to contributions from in-plane stretching modes of C=C and C-O groups. Epoxide asymmetric C-H stretching is present at 1377 cm^{-1}. Asymmetric and symmetric C-H bond stretches can be seen at 2800-3000 cm^{-1}. Hydroxyls stretching vibrations due to adsorbed water and surface acid and alcohol -OH groups lie at 3000-3600 cm^{-1}. XRD analysis allows us to interpret the interlayer spacing for graphitic materials. As already discussed the most stable and common form of graphite is the

ABA stacking array with an interlayer spacing (d) of 0.335 nm, this (0 0 2) facet can be seen in XRD patterns at 26.5° 2θ; a sharp peak indicative of a highly crystalline material with long range order (Figure 5.2(b)). Conversely, graphene oxide layers are known to have intrinsic nanocurvature distortions [Fujimoto (2003)] (Figure 5.2(b, inset)) with edge and basal plane oxygen functional groups and intercalation of H_2O molecules, resulting in $d_{GO} >> d_G$. d_{GO} can vary (0.5-0.9 nm) depending the amount of intercalated water [Burress *et al*. (2010)], the XRD pattern (Figure 5.2(b)) for the as synthesised GO shows the (0 0 2) peak at 11.1° 2θ, corresponding to an interlayer spacing of 0.8 nm.

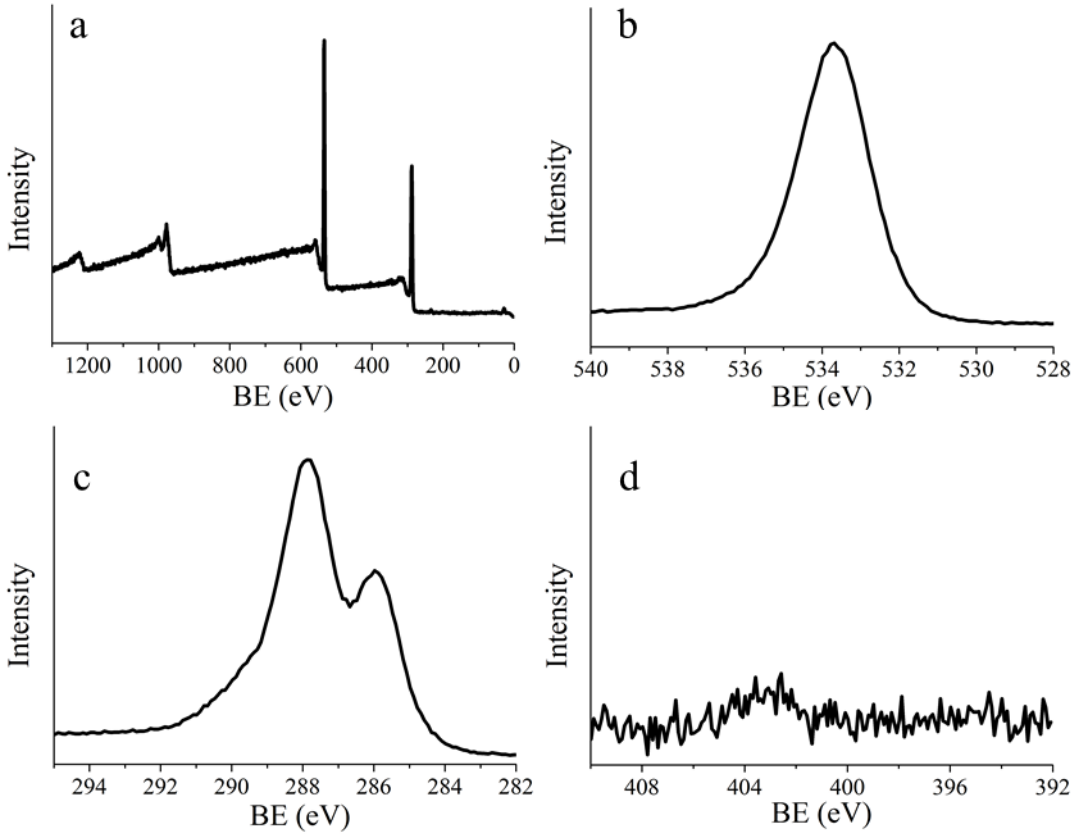

Figure 5.3. XPS analysis for GO showing (a) the survey spectrum and core level XPS analysis showing (b) C 1s, (c) N 1s and (d) O 1s peaks.

Elemental XPS analysis for the GO shows that carbon and oxygen are present in atomic ratios of 65:35, C:O (Figure 5.3(a)), with no other elements present. Analysis of the carbon environments from core level C 1s XPS analysis (Figure 5.3(b)) shows 2 main peaks. A graphite-like sp^2 hybridised carbon peak is present, assigned at a binding energy of 284.5-285 eV. The larger peak at 286-290 eV corresponds to large amounts of sp^2 and sp^3 hybridised carbon atoms bonded to heteroatoms, in this case oxygen bonded environments. Of the oxygen bonding environments chemical shifts at 286-287 eV correspond to C-OH, 287-289 eV to C=O, and 289-291 eV to O=C-OH [Yang *et al*. (2009), Sheng *et al*. (2011)]. The O 1s spectrum (Figure 5.3(c)) gives us further information of the type of oxygen functionality present with

C=O and O=C-OH at 531-533 eV, C-OH at 533-534 eV, C-O-C at 532-534 eV and H_2O at >534.5 eV [Larciprete *et al*. (2011), Lin *et al*. (2012), Yang *et al*. (2009)]. The N 1s spectrum (Figure 5.3(d)) shows that nitrogen is not present.

5.2 Ammonia Mediated Reduction of Graphene Oxide

Various literature reports have highlighted that the thermal reduction of GO in the presence of nitrogen-rich precursors, such as: melamine [Sheng *et al*. (2011)], urea [Lin *et al*. (2012), Sun *et al*. (2012)] and ammonia [Li *et al*. (2009a)], can yield N-doped graphene materials. Of these, the thermal reduction of GO in the presence of ammonia was initially tried, as it had been shown to lead to the highest specific surface areas and good nitrogen content (600 m^2/g and 5 at.% nitrogen) [Geng *et al*. (2011)]. Following the literature preps [Li *et al*. (2009a), Geng *et al*. (2011)] the GO was treated with ammonia gas at 500 °C for 10 minutes, resulting in a fluffy black product. A fast heating rate (20 °C/min) was used as this was reported to enable rapid thermal exfoliation of the GO, maximising surface area [Yang *et al*. (2009)]. The reduction temperature of 500 °C resulted in the highest surface area and nitrogen content as reported in the literature.

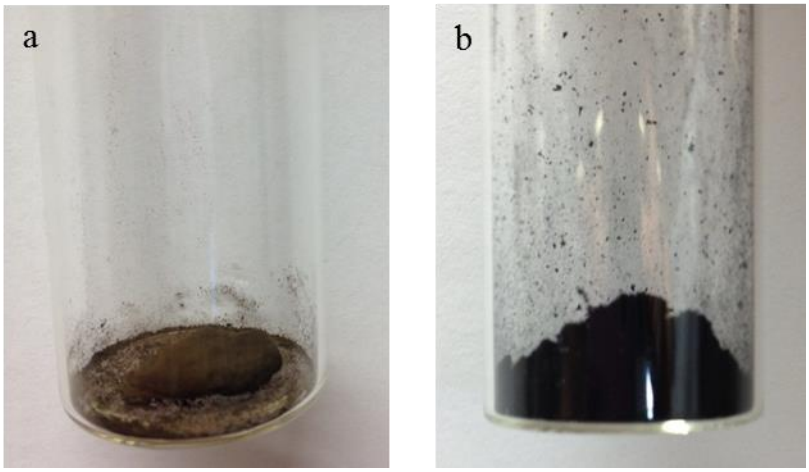

Figure 5.4. Photographs of (a) GO and (b) the same piece of GO after thermal reduction at 500 °C. The increase in volume from exfoliation is evident.

Mechanistic studies show the thermal reduction of GO begins to occur at around 200 °C, with the release of H_2O, CO and CO_2 in the gas phase [Larciprete *et al*. (2011)]. This instigates vacancies in the graphene basal plane and consumes the edge defects. This thermal reduction results in a rapid conversion of the brown GO powder into a jet black flocculent solid of low density (Figure 5.4). Alternatively it is understood that if thermal reduction is carried out in the presence of ammonia an amidated graphene will form [Mou *et al*. (2011)], i.e. where ammonia

is connected to the oxygen containing functional groups in the graphene sheets and this forms at temperatures below 300 °C. The amine in the amidated graphene is then transformed to pyrrolic, pyridinic and quaternary nitrogen at the graphene edges and defective sites above 300 °C.

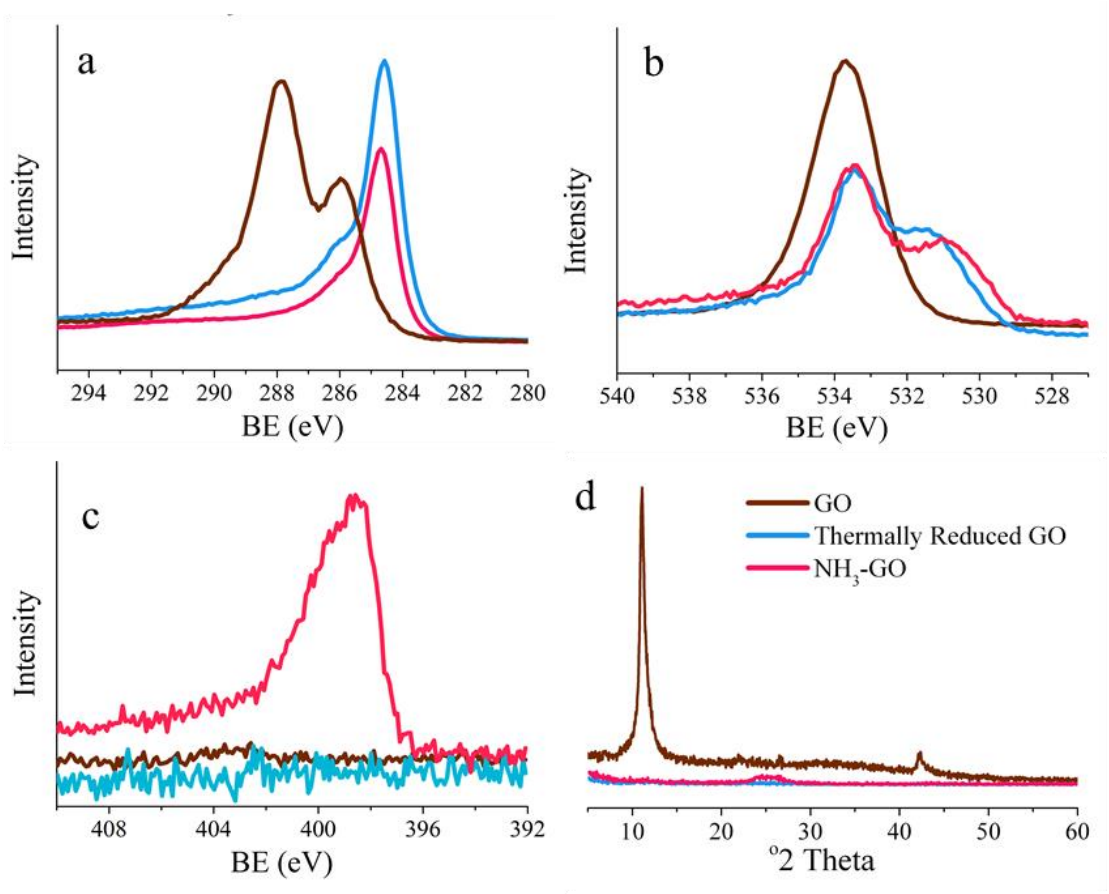

Figure 5.5. Characterisation of the NH_3-GO, showing core level XPS C 1s (a), O 1s (b) and N 1s (c) analysis for NH_3-GO, GO and thermally reduced GO. (d) XRD patterns for the GO, thermally reduced GO and NH_3-GO.

The N-doped graphene product from the thermal treatment of GO in an ammonia environment was designated as NH_3-GO. It was analysed and compared to the GO starting material and a thermally reduced GO exfoliated under an argon atmosphere, using the same temperature profile as for NH_3-GO. The XPS elemental analysis of the NH_3-GO detected 5 at.% nitrogen was present; 8 at.% oxygen functionality also remained (Table 5.1). The core level C 1s XPS spectra (Figure 5.5(a)) of the NH_3-GO and thermally reduced GO both show defined peaks at 284.5 eV corresponding to carbon atoms in an sp^2 hybridised environment, indicating reduction to the graphitic honeycomb chemical structure. However, rather than a single symmetrical peak with a constant width, as found in graphite, the C 1s peaks of the thermally reduced GO and NH_3-GO are asymmetric, broadened toward the high binding energy side. This broadening is indicative of heteroatom functional groups (N and/or O) being present. For the NH_3-GO formation of doped nitrogen atoms, accounting for sp^2-C (pyridine, quaternary) and sp^3-C

(amine) systems would be indicated by new peaks at 285.8-288.5 eV [Lin *et al*. (2012)]. However, these are concealed by the oxygen bound carbon systems and are hard to interpret. The core level O 1s spectra of the the thermally treated graphenes (Figure 5.5(b)) show peak formation at 530-532 eV, indicative of developed C=O and O=C-OH oxygen environments [Larciprete *et al*. (2011), Lin *et al*. (2012), Yang *et al*. (2009)]. The type of nitrogen functionality in the NH_3-GO can be analysed from the core level N 1s spectrum (Figure 5.5(c)), which shows a broad and asymmetric peak at 398-402 eV; nitrogen can be seen to be absent in GO and thermally reduced GO. At binding energies of 398-402 eV: pyridinic (398.1-398.6 eV), pyrrolic (399.5-400.2 eV), amine (400.3-401.3) and quaternary (400.8-401.6 eV) forms may all be present [Wu *et al*. (2012), Sheng *et al*. (2011) Lin *et al*. (2012) and Sun *et al*. (2012)]. The asymmetric nature of the peak towards lower binding energies indicates that pyridinic forms are most common.

From the XRD analysis (Figure 5.5(d)), the (0 0 2) lattice plane observable in GO at 11.1° 2θ is not present following thermal treatment to form NH_3-GO and thermally reduced GO. That strong peaks cannot be identified in the XRD pattern, suggests the graphene sheets have been well separated and no 3-dimensional long range order is present. The BET specific surface area for the NH_3-GO calculated from N_2 adsorption at 77K is 128 m^2/g. Qualitative analysis of the curve (Figure 5.6(a)) shows an s-shaped or type-II isotherm representing hierarchical pores with dominant mesoporosity. A porous N-doped graphene based material, with 5 at.% nitrogen content predominately in pyridinic form and a BET specific surface area of 128 m^2/g was therefore synthesised. Using gravimetric CO_2 uptake analysis the NH_3-GO and thermally reduced GO were tested for their abilities as sorbents. Both showed no affinity for the uptake of CO_2, one likely reason for this is that while both materials are porous they do not possess porosity in the micropore region (Figure 5.6(a)).

5.3 Dicyandiamide Mediated Reduction of Graphene Oxide

Qualitative analysis of the N_2 isotherms at 77 K for the N-doped graphene materials from literature, using various nitrogen-rich precursors: melamine [Sheng *et al*. (2011)], urea [Lin *et al*. (2012), Sun *et al*. (2012)] and ammonia [Li *et al*. (2009a)], indicates that precursor has a distinct effect on porosity. For a microporous material, the N_2 isotherms at 77 K show greater uptake at low relative pressures and such behaviour is more evident in the melamine and urea literature equivalents, when compared to the ammonia equivalents. An approach using melamine as a nitrogen precursor was identified [Sheng (2011)], with the added feature that a greater amount of N-dopants may also be introduced. In this process the melamine is known to

decompose into ammonia gases at temperatures above 600 °C [Thomas *et al*. (2008)], and it is these gases that are known to be the active species in the nitrogen doping mechanism [Mou *et al*. (2011)]. The thermal annealing temperature used in this process was therefore 700 °C. However, at 700 °C the surface area of the material is limited due to graphitisation taking place as more elevated temperatures are reached. Alternatively, it is known that dicyandiamide (DCA) decomposition into ammonia species begins at around 250 °C [Zhang *et al*. (1997)]. It was therefore envisaged that through the use of DCA in place of melamine as an N-rich precursor, the synthesis of a microporous N-doped graphene material may be achieved.

Table 5.1. XPS elemental analysis and BET surface area analysis for GO, N-doped graphene and thermally reduced GO materials

Sample	Elemental Analysis (at.%, XPS)			SSA_{BET}
	C	N	O	(m^2/g)
GO	66.0	0	34.0	-
Thermally Reduced GO	86.8	0	13.2	94.3
DCA-GO 250	48.5	45.2	6.3	15.3
DCA-GO 300	49.0	43.9	7.1	6.0
DCA-GO 350	47.9	45.8	6.3	9.3
DCA-GO 400	44.0	50.4	5.6	12.7
NH_3-GO	87.2	5.0	7.8	128.4
MPNG	73.0	24.7	2.3	505.1

To then synthesise N-doped exfoliated graphene from DCA and GO, the DCA and GO were well mixed together in a pestle and mortar in ratio of 2:1. The mixture was then placed in a pre-heated furnace at four different annealing temperatures: 250, 300, 350 and 400 °C, for ten minutes, under an inert nitrogen atmosphere. The black powders obtained were designated as DCA-GO X, where X = the thermal treatment temperature. The nitrogen atomic percentages achieved for each different temperature DCA-GO 250 to DCA-GO 400 as calculated from XPS elemental analysis can be seen in Table 5.1. DCA-GO 250, 300 and 350 can be considered to give similar results and nitrogen content of around 45 at.%, significantly higher than the NH_3-GO. DCA-GO 400 has higher nitrogen content (50 at.%) at the expense of carbon content. All the samples in the DCA:GO series retained oxygen functionality of 6-7 at.%.

From the core level C 1s XPS spectra of the DCA:GO series (Figure 5.6(b)) a high proportion of carbon atoms appear to remain in sp^3 environments bound to heteroatoms as found in GO (287-289 eV), contrasting to the carbon atoms predominately found in sp^2 hybridised graphene-like systems (284.5 eV) in the thermally reduced GO. However, this peak at 287-289 eV cannot

be the result of carbon bound in sp^3 hybridised environments to oxygen heteroatoms as the DCA:GOs only contain 6-7 at.% oxygen (Table 5.1). Amine functionalities can therefore be expected to be prevalent as carbon bound to nitrogen heteroatoms in sp^2 environments, such as pyridine, pyrrole and quaternary groups are found at 285.8-288 eV [Lin *et al*. (2012)]. By looking at the core level N 1s spectra (Figure 5.6(c)) an asymmetric peak centred at 398.5 eV can be seen, indicative of pyridine type nitrogen.

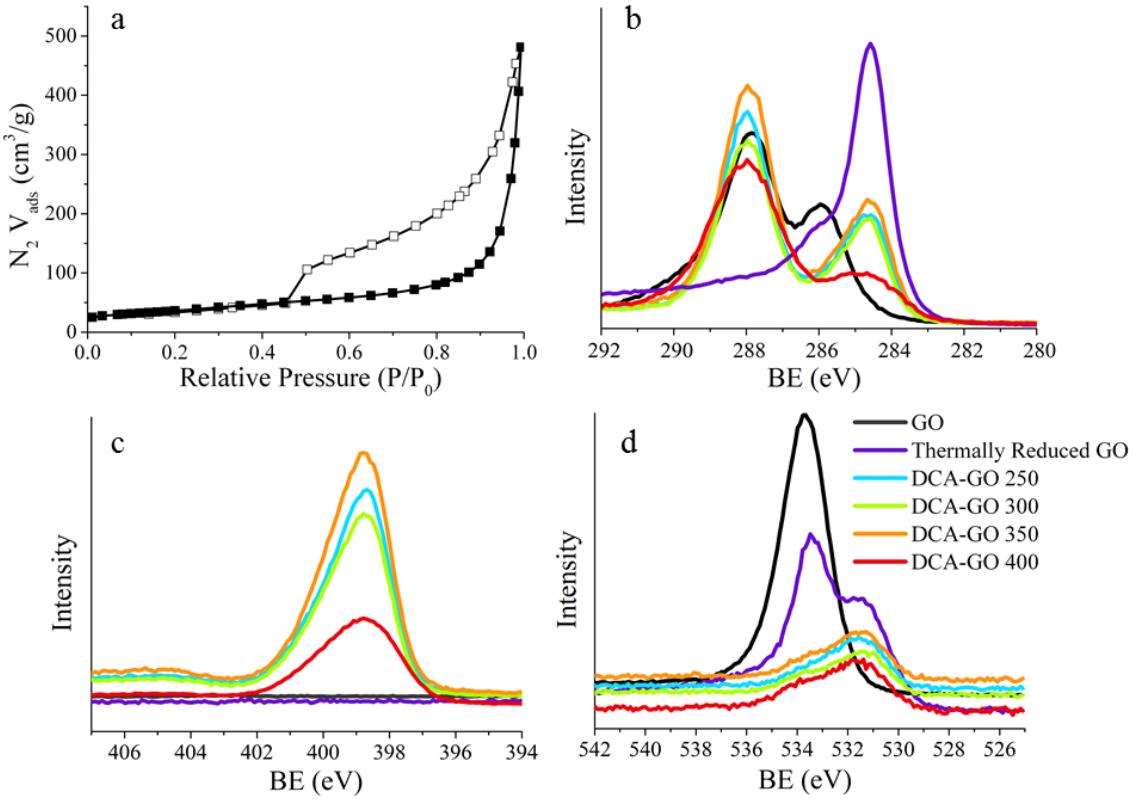

Figure 5.6. (a) N_2 isotherm at 77 K showing adsorption (filled symbols) and desorption (open symbols) between 0-1 bar for the NH_3-GO. Core level XPS C 1s (b), N 1s (c) and O 1s (d) spectra for the DCA-GO series, GO and thermally reduced GO.

The tail towards higher binding energies shows that some pyrrolic, amine and quaternary nitrogen forms may also be present. However, amine groups are typically expected at 400.3-401.3 eV [Wu *et al*. (2012), Sheng *et al*. (2011)], so the prevalence of amines as expected based on the C 1s analysis interpretation is not observed.

Alternatively, it is known that DCA can decompose to form triazine containing compounds like melamine and heptazine at elevated temperatures [Thomas *et al*. (2008)]. The C 1s spectra of such triazine and heptazine structures show peaks at 288.0-288.5 eV, and this fits in with the C 1s spectra of the DCA:GO. It is therefore likely that the DCA is converting into triazine and heptazine structures. This is further supported by the N 1s spectra, as triazine and heptazine structures can be seen in the region of 398-399 eV [Hu *et al.* (2011b)].

Further chemical analysis can be carried out using FTIR spectroscopy (Figure 5.7(a)). The peaks for carbonyl and carboxyl groups found in GO at 1730 and 1625 cm^{-1} respectively, are lost during the reduction and nitrogen doping process. The peaks at 2800-3000 cm^{-1}, corresponding to asymmetric and symmetric stretching of edge and defect C-H groups in GO are not present for the DCA-GOs and reduced GO. These C-H bonds are lost as the carbon atoms are returning to a graphite-type sp^2 hybridised, conjugated honeycomb lattice, as indicated by the C 1s peaks at 289.5 eV. The DCA-GO FTIR spectra all show distinct peaks at around 1605 cm^1 and 1470-1420 cm^1 which are typical of aromatic nitrogen ring C=C and C=N stretching vibrations as would be expected from pyridines and triazines [Socrates (1980) pp. 95]. Ring stretching vibrations from poly-nitrogen containing ring structures such as quinazoline and triazine groups can be ascribed to the peak at 1320 cm^{-1}. The sharp peak at 808 cm^{-1} is characteristic of out of plane ring deformation in triazines or C-H deformation vibrations in substituted pyridine and pyrrole groups [Socrates (1980) pp. 93].

As the triazine and heptazine units observed from the decomposition of the DCA are typical of carbon nitride structures, it is possible a separate carbon nitride phase was synthesised. To understand if the DCA is indeed reacting with the GO during annealing or forming separate phases, XRD analysis was carried out (Figure 5.7(b)). XRD patterns of the DCA-GO 250, 300 and 350 all show a broad peak at 26.5° 2θ, indicative of graphite (0 0 2) interlayer spacings. A separate carbon nitride phase would be seen by a peak at 27.5° 2θ, the absence of this indicates that the triazine and heptazine units are likely incorporated within the graphene structure. Highly N-doped (45 %) amorphous graphene products, with a predominately triazine and pyridine-type nitrogen functionality were therefore synthesised.

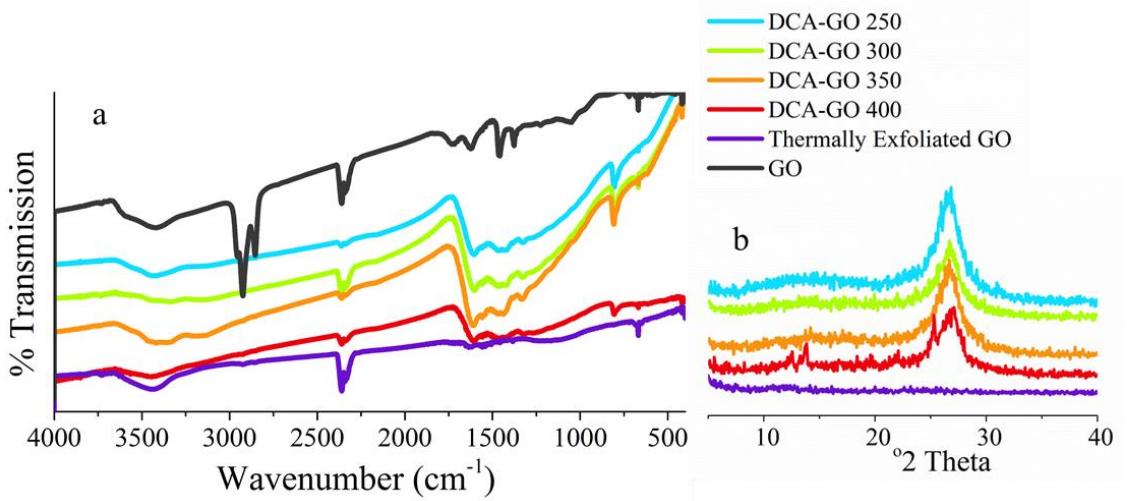

Figure 5.7. (a) FTIR spectra and (b) XRD patterns for the DCA-GO series, compared with GO and thermally reduced GO.

BET specific surface area analysis using N_2 isotherms at 77 K shows all DCA-GO samples to have very little accessible surface areas, ranging 6-15.3 m^2/g (Table 5.1). Using gravimetric CO_2

uptake analysis these materials also did not show affinity for CO_2 sorption, this can be attributed to the lack of porosity. It also shows that nitrogen content of the types so far produced: triazine, pyridine, pyrrole and quaternary are not capable of chemically binding CO_2.

5.4 Synthesis of a Monolayer Patched N-doped Graphene

While this work was being carried out a report of a novel route to a porous N-doped graphene material, with high nitrogen content was published [Li *et al*. (2012a)]. The reported synthesis utilises glucose as a graphene precursor in a process whereby DCA acts as in-situ template for graphene formation and nitrogen dopant. The literature synthesis reported a nitrogen content of up to 26 at.% and a BET specific surface area up to 975 m^2/g. The synthesis was achieved by mixing DCA and glucose with a ratio of 2.5-40:1, and heating to 600 °C, whereby formation of a graphitic carbon nitride (g-C_3N_4) is achieved which acts as template to graphene sheet synthesis. The article purports that glucose between the graphitic carbon nitride layers is templated into forming graphene sheets, and via a second heating step to 800 °C, decomposition of the carbon nitride template leads to patchworks of graphene sheets. Furthermore, upon decomposition of the g-C_3N_4 template, nitrogen atoms become incorporated into the graphene matrix, resulting in high N-dopant levels. The results showed that the higher the DCA:Glucose ratio, the higher the surface area and nitrogen dopant atomic % achieved.

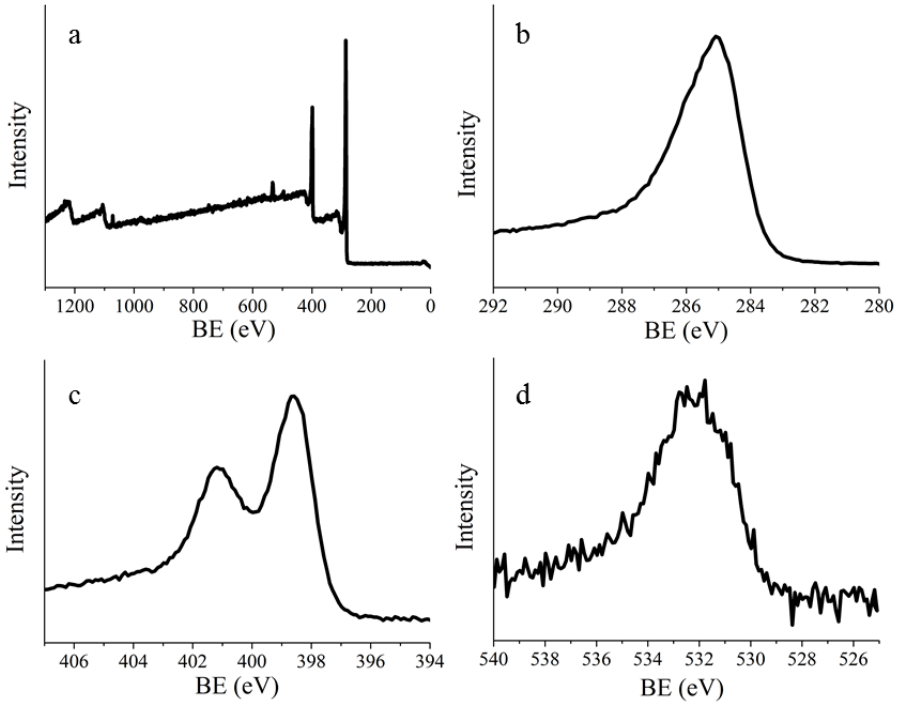

Figure 5.8. XPS analysis of the MPNG, showing (a) survey spectrum and core level spectra for (b) C 1s, (c) N 1s and (d) O 1s.

Therefore, following the literature script, DCA (vacuum oven dried at 120 °C) and glucose were mixed in a ratio of 40:1. This was then heated under a protective nitrogen flow to 600 °C at 2 °C/min, with a dwell time of 1 hour. A second heating stage at 1.6 °C/min to 800 °C was then carried out with a dwell time of 1 hour, allowing to cool naturally. A jet black flocculent solid was obtained, with very low apparent density. This process was carried out 4 times to achieve a suitable quantity for full characterisation. The literature reported the product as a 'monolayer patched graphene', this precedence is followed here using monolayer-patched N-doped graphene (MPNG).

Elemental analysis from XPS shows the MPNG to have atomic ratios of: 73% C, 25% N and 2% O (Figure 5.8(a)). From the C 1s spectrum (Figure 5.8(b)) the peak centred at 285.1 eV can be seen to be asymmetric, indicating it to be multi-component. This peak is dominated by a peak at 284.8-285.0 eV corresponding to carbon in a graphite-like sp^2 hybridised environment. Also included in the broad peak may be sp^2 C=N bonded structures at 285-286.5 eV [Lv *et al.* (2012)] and oxygen bound carbon species at 286-288 eV (C-OH, and C=O) [Yang *et al*. (2009), Sheng *et al*. (2011)]. From the N 1s spectra (Figure 5.8(c)) the peak at 398.6 eV can be assigned to pyridinic forms of nitrogen, while that at 401.0 eV can be assigned to quaternary nitrogen [Lv *et al*. (2012)]. Lower quantities of pyrrolic (399.5-400.2 eV) and amine (400.3-401.3 eV) forms may also be present [Wu *et al*. (2012), Sheng *et al*. (2011), Lin *et al.* (2012) and Sun *et al.* (2012)].

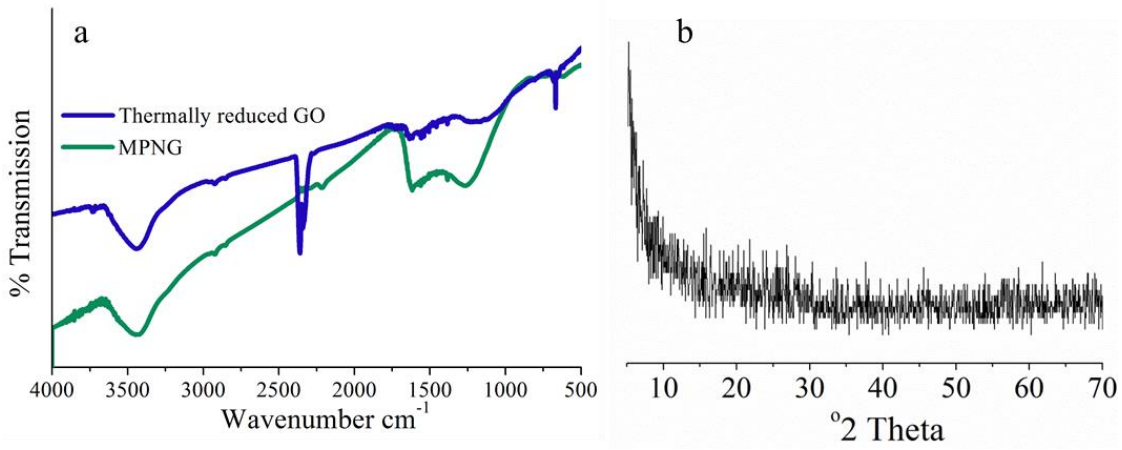

Figure 5.9. (a) FTIR and (b) XRD analysis for the MPNG.

Like the thermally reduced GO the MPNG is a jet black solid that due to high adsorption results in poor quality FTIR analysis. Use of % transmission and % reflectance FTIR modes were experimented with. Nevertheless, FTIR analysis for MPNG is given (Figure 5.9(a)). The peak at 3400 cm^{-1} is attributed to adsorbed H_2O or covalently bound O-H stretching, at 1620 cm^{-1} the peak can be assigned to aromatic N-containing ring stretching vibrations or graphitic domain skeletal vibrations [Xu *et al*. 2008)] and the peak at 1270 cm^{-1} may be interpreted as either C-O

stretching modes [Kumar *et al*. (2012)] or pyridinic ring bending [Socrates (1980) pp. 93]. Absence of clear C=N stretching vibrations at 1520-1450 cm^{-1}, which are expected for pyridine type forms means that this FTIR analysis technique is likely flawed.

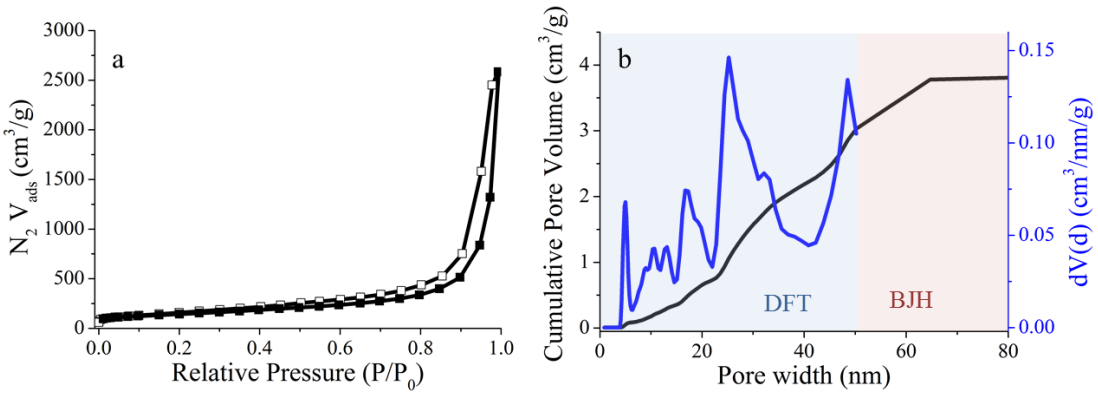

Figure 5.10. (a) N_2 isotherm at 77 K showing adsorption (filled symbols) and desorption (open symbols) between 0-1 bar for MPNG. (b) QSDFT pore size distribution plot and cumulative pore volume plot calculated using the DFT and BJH method obtained from the N_2 isotherm for the MPNG.

Structural analysis was carried out using XRD (Figure 5.9(b)) the featureless pattern indicates that the MPNG material has no 3-dimensional long range order, in particular no (0 0 2) peak is observed indicating that graphene type forms and not graphitic types have been produced. This is further supported by TEM images (Figure 5.11) where the materials can be seen to have a homogeneous, sheet-like structure, containing both crumpled and folded domain areas, these folded areas can be seen in the highlighted region (Figure 5.11(b)), very typical of graphene sheets and observed in the report followed [Li *et al*. (2012a)].

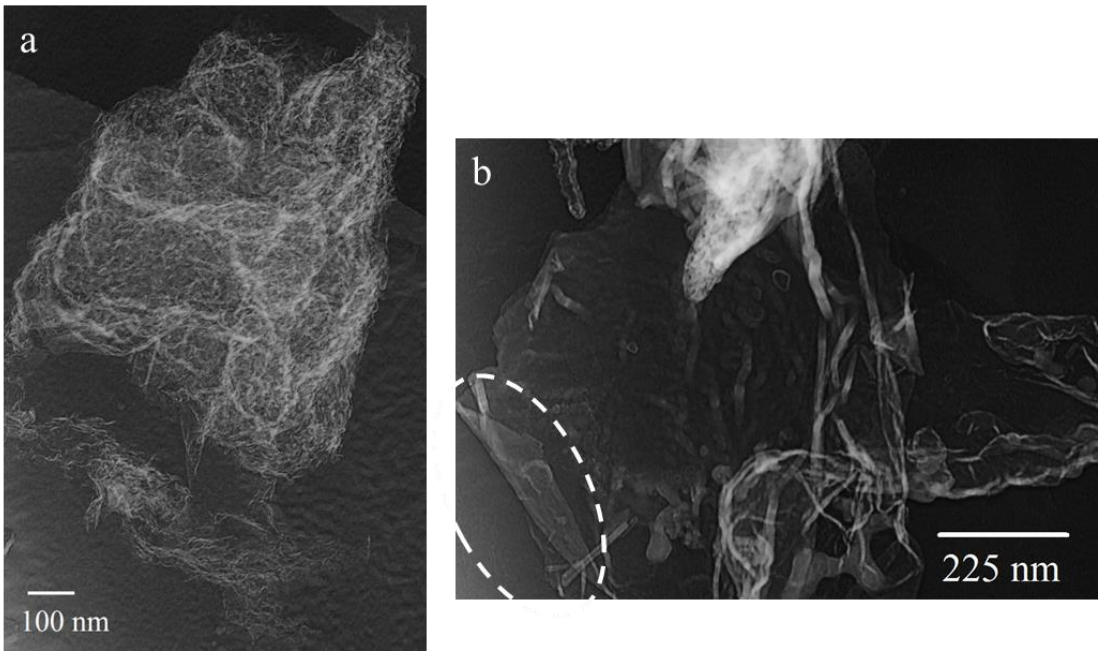

Figure 5.11. TEM images of the MPNG, highlighting a folded sheet domain.

Pore structural analysis was carried out using N_2 isotherms at 0-1 bar and 77 K (Figure 5.10(a)). From the adsorption-desorption curve a type-II isotherm can be identified, representing hierarchical pores within the mesopore range. The BET specific surface area was calculated as 505.1 m^2/g and the total pore volume = 4.007 cm^3/g. The mesoporous nature is further evidenced from the QSDFT pore width of 25.2 nm and the sample also shows some microporous character with a micropore volume = 8.0 x 10^{-3} cm^3/g. Such pore characteristics are in line with those reported by the literature followed. With a micropore volume as low as 8 x 10^{-3} cm^3/g, CO_2 uptake capacity at 1 bar can be expected to be low due to the vital role micropores play in physisorption up to 1 bar [Garrido *et al*. (1987)].

The CO_2 adsorption characteristics were then analysed using volumetric measurements up to 5 bar at 273, 298 and 348 K (Figure 5.12(a)) and the uptake capacities at 5 and 1 bar shown in Table 5.2. From these volumetric measurements the MPNG achieves an uptake capacity of 1.21 mmol/g at 1 bar and 25 °C. At 1 bar CO_2 adsorption has been shown to be an ultramicropore dominated process [Zhang *et al*. (2013), Hu *et al*. (2011a), Presser *et al*. (2011)]. As pressure increases, the isotherms show continued uptake, up to 5 bar, which is attributed to filling within narrow mesopores [Gadipelli *et al*. (2014)]. By calculating the isosteric heat of adsorption (Q_{st}) from the isotherms at 273, 298 and 348 K using the Clausius-Clapeyron equation (Figure 5.12(b)), the effect of the nitrogen functionality can be further assessed. The Q_{st} value reflects the strength of adsorbate-adsorbent interaction between CO_2 and carbon adsorbents and would be elevated by favourably interacting functional groups. The MPNG shows a Q_{st} of 23.5-17 kJ/mol at near zero loading, typical for a physisorption process as found for normal carbon sorbents [Zhang *et al*. (2013), Hu *et al*. (2011a), Presser *et al*. (2011)] and does not indicate that the nitrogen functionality is increasing the adsorbate-adsorbent interaction. It can be observed that the value of Q_{st} falls with gas uptake (Figure 5.12(b)), whereby at low loadings the Q_{st} is higher (23.5 kJ/mol), then significantly drops and becomes nearly constant at 17 kJ/mol. Such higher Q_{st} values at low gas loadings are believed to be the result of the strong interaction between CO_2 and small micropores [Zhang *et al*. (2013)], although the effect of active site on functional nitrogen groups present cannot be ruled-out and more will be discussed in the later chapters. Therefore CO_2 adsorption here is determined by the pores arising from the folding and corrugation of the graphene structures.

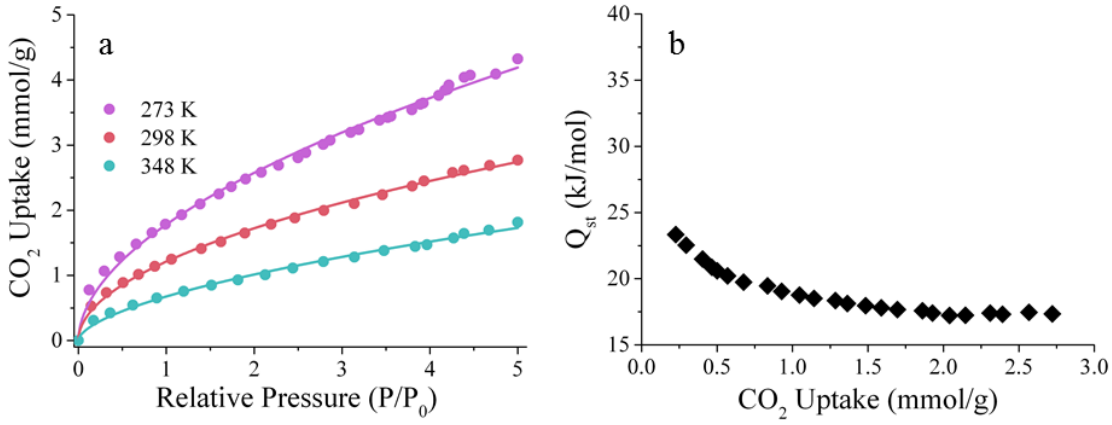

Figure 5.12. (a) Volumetric CO_2 uptake analysis (0-5 bar) at 273, 298 and 348 K. (b) Isosteric heats of adsorption (Q_{st}) calculated from CO_2 adsorption isotherms up to 5 bar at 3 temperatures 273, 298 and 348 K.

A highly N-doped porous graphene solid material, containing pyridinic, quaternary and likely pyrrolic forms of nitrogen was synthesised. The pore architecture was characterised and it contains a hierarchical pore structure with narrow micropores, meso and macropores. Analysis of the capacity for CO_2 uptake shows the MPNG has a positive affinity for CO_2 at low and elevated pressures. The impact of the nitrogen functionality on the enthalpy of adsorption was also characterised and indicates that the present nitrogen functionality do not have a strong impact on adsorption at elevated temperatures, rather the narrow micropores within the structure appear principally responsible for the CO_2 uptake.

Table 5.2. Volumetric CO_2 uptake capacity of the MPNG at relative pressures of 1 and 5 bar

Temperature (K)	Relative Pressure	
	(1 bar)	(5 bar)
273	1.78	4.19
298	1.21	2.74
348	0.68	1.73

6. Carbon Precursors to Porous Carbon Materials

The use of chemical activation with KOH has led to a series of publications yielding highly microporous solid activated carbon materials (Table 6.1). Of pertinent interest is that the carbon precursor used has varied markedly and has a profound impact on the resulting activated carbon. Furthermore, as a good part of this thesis focusses on the use of nitrogen dopants within porous carbons to enhance their performance as CO_2 capture materials, synthesis of undoped carbon sorbents will provide a suitable comparison. In this chapter the synthesis of activated carbon from 4 different carbon precursors: cellulose, glucose, spent coffee grounds and a soft-template polymer is discussed and their suitability as post-combustion CO_2 capture materials analysed.

Table 6.1. CO_2 uptake capacities for leading porous solid sorbents derived from KOH activation

Material	CO_2 Uptake* (mmol/g)	Precursor & Methodology	Reference
TiC-CDC	4.1	Synthesised from Titanium carbide powder	[Presser *et al*. (2011)]
IBN9-NC1-A	4.5	Hard-template approach using a sacrificial zeolite template	[Zhao *et al*. (2012a)]
KNC-A-K	4.0		[Zhao *et al*. (2012b)]
ATS-4-700	3.4		[Sevilla *et al*. (2012a)]
K-PAF-1-750	4.2	Polymer synthesised for carbon precursor	[Li *et al*. (2013)]
AC-750-0.5	4.3		[Zhang *et al*. (2013)]
STC-R-500-A	4.4		[de Souza *et al*. (2013)]
PAN-PK	4.4		[Shen *et al*. (2011)]
600-2	4.8		[Lee *et al*. (2013)]
NPC-650	3.1		[Wang *et al*. (2013)]
AG-2-700	4.5	Naturally existing biomass and waste materials	[Sevilla *et al*. (2012b)]
AS-2-600	4.8		[Sevilla *et al*. (2011b)]
a-CL	4.3		[Wang *et al*. (2012)]
PA-400-KOH-2-600	4.2		[Song *et al*. (2012)]
AC-2-635	3.8		[Fan *et al*. (2013)]

*When not directly reported, the uptake values have been taken from adsorption isotherms in the corresponding reference. CO_2 uptake at 298 K and 1 bar.

Table 6.1 displays the CO_2 uptake performance for a variety of leading activated carbons that have been synthesised from the KOH activation of a range of carbonaceous precursors. Precursors that have seen most focus in literature are typically: polymers, mesoporous carbons achieved through synthesis and carbonisation of polymers using hard-templates, and biomass. Of these precursors, the hard-template processes utilise zeolites as hard templates which must be removed using harsh HF acid washes, making them unattractive for investigation here. In turn some polymer syntheses can be complex, such as that for K-PAF-1-750 where PAF-1 is synthesised from Yamamoto-type Ullmann cross-coupling chemistry. Alternatively, this

chapter focuses on the use of biomass materials and uncomplicated polymeric structures due to their greater prospects economically, with use in industrial applications stringently limited by cost. In conjunction to this the performance of materials in Table 6.1 is not evidently improved through use of precursors of greater complexity.

In this chapter 4 different carbon precursors are investigated: cellulose (a natural and abundant polymer), glucose (an abundant chemical utilised for graphitic synthesis [Li *et al*. (2012a)], used coffee grounds (an abundant lignocellulosic biomass) and a soft-templated phenolic resin polymer. All of which contain carbon, oxygen and hydrogen and no other elements, they are highly abundant and readily available, or can be achieved through a facile scalable process.

6.1 Synthesis of a Soft-templated Polymer

For the synthesis of the soft-templated phenolic resin polymer a literature preparation was followed using a commercially available triblock copolymer (pluronic F127, $EO_{106}PO_{70}EO_{106}$) as a structure directing agent and a polymer of phloroglucinol and formaldehyde as an inexpensive carbon precursor [Liang *et al*. (2006)]. The self-assembly of block copolymers such as pluronic F127 facilitates structure direction without use of hard silica templates, and the associated harsh conditions of their removal. The comparatively facile removal (achieved through carbonisation) of such block copolymers for the generation of porous carbon structures denotes the term "soft-template".

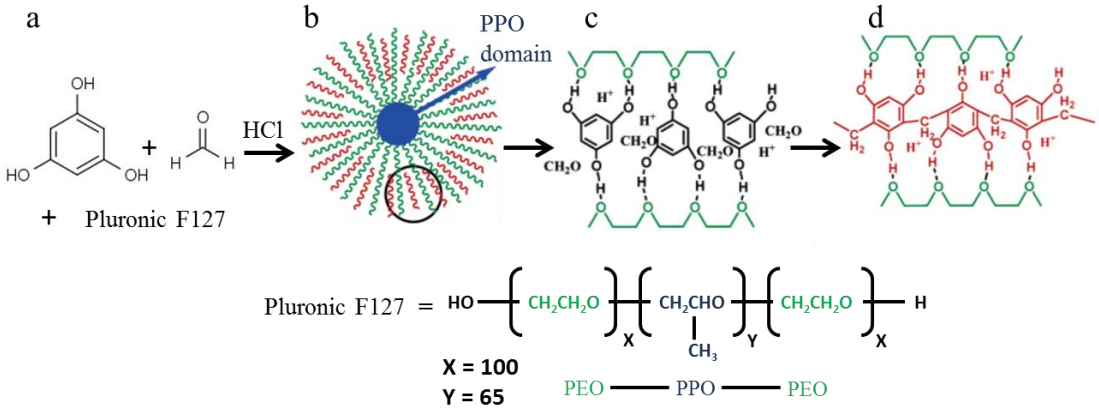

Figure 6.1. Schematic modified from literature displaying the process of structure-directed polymerisation of phloroglucinol and formaldehyde [Liang *et al*. (2006)]. (a) Phloroglucinol, formaldehyde and pluroinic F127 (shown in detail with the PEO-PPO-PEO structure). (b) Spherical hydrogen bonded array (c) hydrogen bonding reinforced PEO aggregations. (d) Localized polymerization in the PEO domain

The block copolymer pluronic F127 is amphiphilic and contains polyethylene oxide (PEO) and polypropylene oxide (PPO) regions. The hydrophilic PEO region interacts with the hydrophilic

phloroglucinol via hydrogen bonding enabling self-assembly, while the hydrophobic PPO chains form an isolated domain in the centre (Figure 6.1(b)). Polymerisation of the phloroglucinol and formaldehyde occurs via a hydroxymethylation reaction whereby a hydroxymethyl group from the formaldehyde is introduced into the aromatic nucleus at positions adjacent to the phenolic groups through electrophilic aromatic substitution (Figure 6.1(c) and (d)) [Mitsunaga *et al*. (2000)]. The polymerisation was acid catalysed and carried out at room temperature. Following polymerisation the polymer was cured at 100 °C for 24 hours. The resulting polymer resin is designated as STP (soft-templated polymer). To remove the triblock copolymer the STP is carbonised which converts the phenolic polymer portion into carbon and removes the triblock copolymer structural directing agent to yield a porous carbon. This carbonisation process is discussed later.

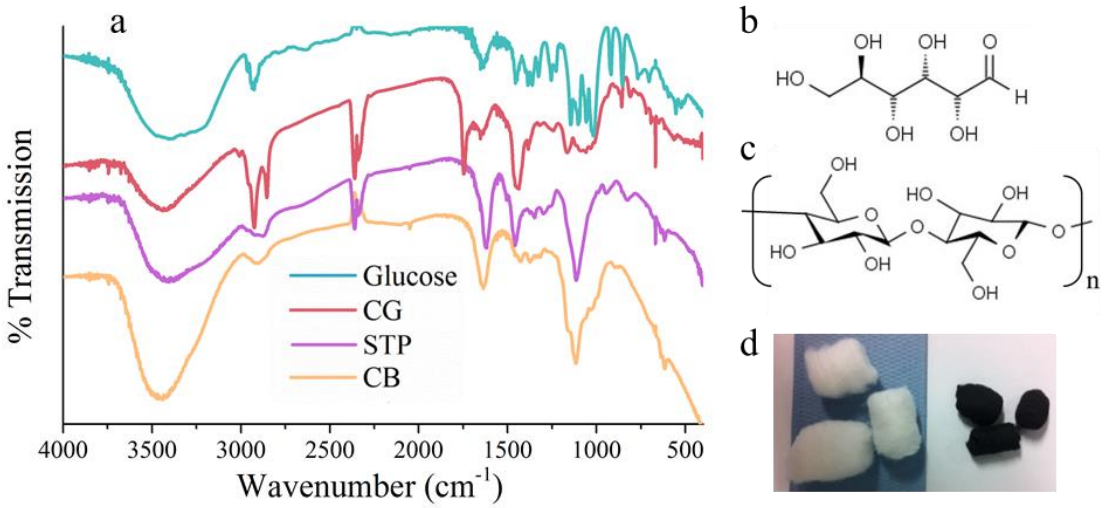

Figure 6.2. (a) FTIR spectra for the carbon precursor starting materials. Chemical structure of D-glucose (b) and cellulose (c). (d) Photo of cotton balls before and after carbonisation.

6.2 Carbonisation of Carbon Precursors

For the other carbon precursors investigated: used coffee grounds were removed from the office coffee machine (a DeLonghi ECAM 23.450.S) and vacuum oven dried at 120 °C to obtained dry coffee grounds (CG), glucose was used as purchased and cellulose was obtained in the form of cotton wool balls (CB) from a high-street pharmacist. Chemical analysis of the starting materials was carried out using FTIR spectroscopy (Figure 6.2(a)). Briefly, the chemical structure of the glucose (Figure 6.2(b)) is evident from the –OH vibrational stretching at 3000-3700 cm^{-1}, -CH vibrations at 2051 cm^{-1}, -C=O stretching at 1653 cm^{-1}, a combination band of O-CH and C-OH deformation at 1324-1455 cm^{-1}, in plane –CH and –OH deformation from 1255-1011 cm^{-1} and C-O and C-C stretching at 1191-995 cm^{-1} [Ibrahim *et al*. (2006)]. The FTIR

spectrum of the CG reveals a complex lignocellulosic structure with various types of C-H stretching at 2930 and 2850 cm^{-1}, C=O stretching at 1740 cm^{-1}, C=C stretching from aliphatic and aromatic groups centred at 1650 cm^{-1}, scissoring alkanes at 1444 cm^{-1}, and C-O and C-C stretching at 1000-1200 cm^{-1}. For the as synthesised STP the FTIR spectrum is dominated by -OH stretching vibrations at 3700-3000 cm^{-1} and C=C aromatic stretching at 1630 cm^{-1} from the phenolic resin, while scissoring alkanes are observed at 1457 cm^{-1} from the pluronic F127. Symmetrical stretching of aromatic esters (the phenolic resin) and C-O-C asymmetric stretches of saturated aliphatic esters are observed in the peak centred at 1107 cm^{-1}. The cellulosic nature of the cotton wool balls (Figure 6.2(c)) can be seen in the hydrogen bonded -OH stretching at 3700-3000 cm^{-1}, -OH bending of adsorbed water at 1636 cm^{-1}, -CH stretching at 2920 cm^{-1}, HC-H and OC-H in-plane vibrations at 1430 cm^{-1}, -CH deformation vibrations at 1375 cm^{-1}, and antisymmetrical C-O-C oxygen and C-O stretching vibration modes at 1120 cm^{-1} [Oh *et al.* (2005)].

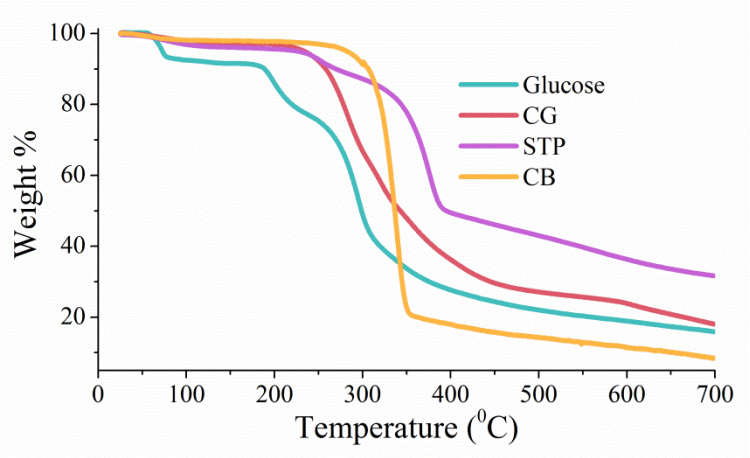

Figure 6.3. TGA analysis of the 4 carbon precursors, heating under argon to 700 °C at 2 °C/min.

In correlation with the other materials synthesised in this thesis the carbon precursors were carbonised at 700 and 900 °C. Carbonisation was carried out using a tube furnace under a steady flow of nitrogen. The furnace was heated at a ramping rate of 3 °C/min to the desired temperature, with a dwell time of 1 hour. The resulting chars are designated as X Y, where X is the precursor used and Y is the temperature of carbonisation, e.g. Glucose 900. The yields obtained are given in Table 6.2.

Using TGA analysis up to 700 °C the carbonisation process of the materials can be understood (Figure 6.3). Taking the precursors in turn, the carbonisation of glucose begins with melting at 180 °C and this terminates at 240 °C. During this stage the glucose polymerises with the formation of oligo and polysaccharides resulting in the loss of water and corresponding mass. Above 240 °C these saccharides decompose giving rise to char formation [Őrsi (1973)]. The carbonisation of glucose and the resulting polymerisations and decomposition are dependent on heating rate and it has been shown that using rates of ≥2 °C/min are suitable to obtain

reasonable yields [Őrsi (1973)]. For the CGs weight loss at 200-400 °C can be ascribed to degradation of the lignocellulosic materials into heavier hydrocarbons (tars) and gaseous products such as of H_2O, CO, CO_2, CH_4 and aldehydes [Hu *et al*. (2001). Distillation of the heavier hydrocarbons then occurs up to 500 °C, with the consolidation of the char occurring at 600-700 °C [Plaza *et al*. (2012)]. The STP can be considered first a phenolic resin with weight loss at 175 to 335 °C understood to be water released from breakdown of the –OH groups, with some loss due to short side chains not fully incorporated into the cross-linked resin. Above 340 °C the thermal breakdown of the polymer via methylene bridge decomposition and resulting char formations can be observed [Gallet *et al*. (2002)]. Yields for phenolic-formaldehyde resins are expected between 45-60 % [Tennison (1998)], yields here of ~30 % (Table 6.2) are indicative of the loss of the pluronic F127 template, which can be expected to degrade at upwards of 150 °C. For cellulose (CB) an initial period of inactivity can be explained by the high activation energy required to convert cellulose from an "inactive" to an "active" form. The cellulose degradation can then be considered to occur directly via char formation with the corresponding release of volatiles [Bradbury *et al*. (1979)]. Following carbonisation the cellulose cotton wool balls retain their shape, shrinking slightly (Figure 6.2(d)).

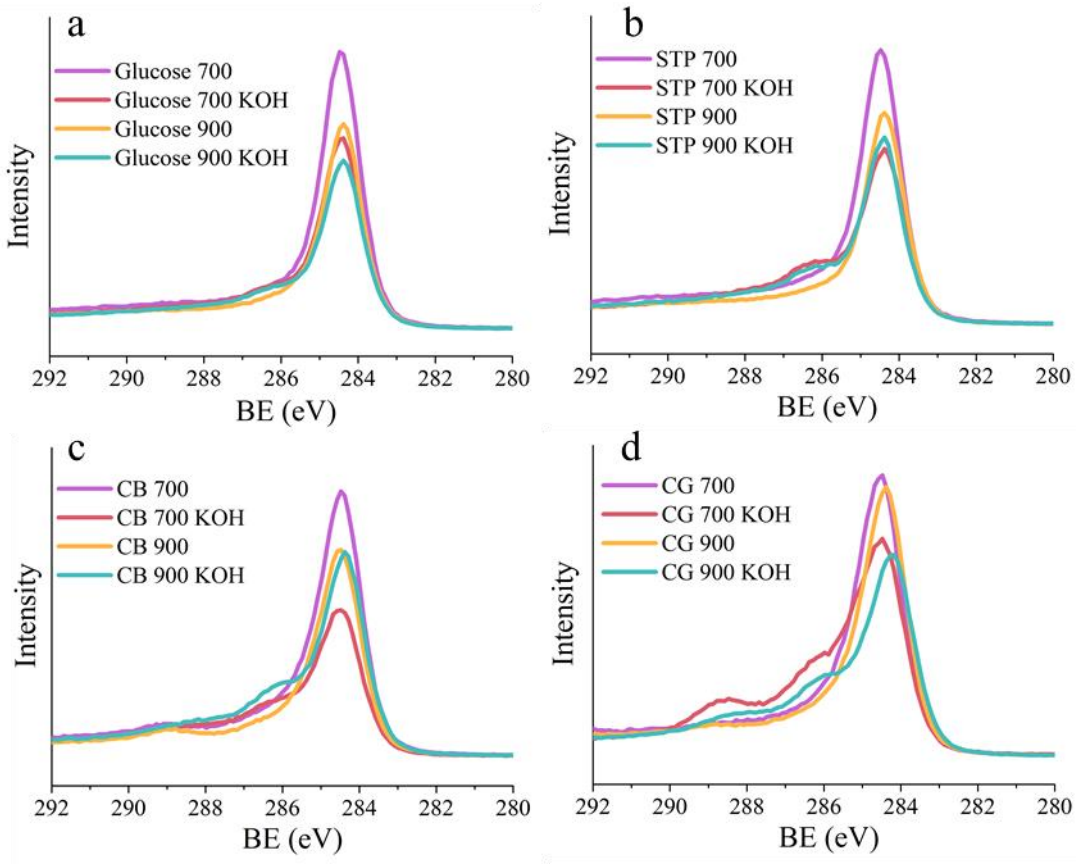

Figure 6.4. Core level C 1s XPS spectra for (a) glucose (b) STP (c) CB and (d) CG derived carbons.

6.3 Chemical Activation of the Carbon Materials

Following carbonisation the chars were activated using a KOH:char ratio of 2:1. The KOH and char were ground together in a pestle and mortar until a fine grey powder obtained, this was then heated at 700 °C for 1 hour, using a heating rate of 3 °C/min under a protective nitrogen atmosphere. Washing with distilled water successfully removed all the potassium ions, leaving activated carbon consisting of carbon, oxygen and hydrogen only (elemental composition from XPS elemental analysis is given in Table 6.2). The activated carbons are designated as X Y Z, where X is the type of char precursor, Y the temperature of carbonisation and Z indicates the char has been activated using KOH, e.g. Glucose 700 KOH. Due to the dark nature of the black chars and activated carbons, FTIR analysis yielded no chemical information.

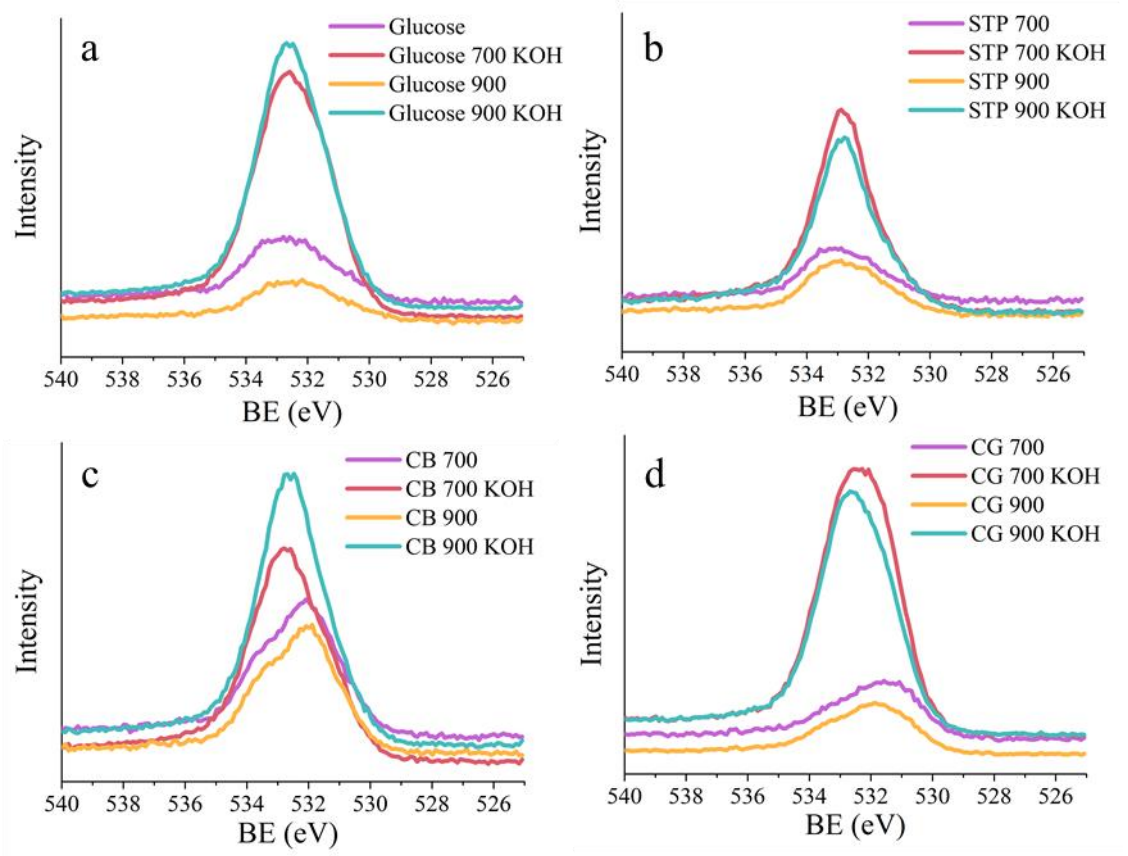

Figure 6.5. Core level O 1s XPS spectra for (a) glucose (b) STP (c) CB and (d) CG derived carbons.

XPS analysis was therefore used to interrogate the chemical properties of the carbons. C 1s analysis of the derived carbons (Figure 6.4) shows that the carbons all have a largely sp^2 hybridised graphitic-type chemical composition, as indicated by the dominant peaks at a binding energy ~284.4 eV [Lv *et al.* (2012)]. The KOH activated samples show shoulder peaks at 286-290 eV indicative of carbon in an oxygen bound environment with groups such as C-OH at 286-287 eV, C=O at 287-289 eV, and O=C-OH at 289-291 eV [Yang *et al.* (2009), Sheng *et al.* (2011)]. The form of these oxygen groups can be further understood using core level O 1s

analysis (Figure 6.5), where C=O and O=C-OH groups are observed at 531-533 eV, C-OH at 533-534 eV and C-O-C at 532-534 eV [Larciprete *et al*. (2011), Lin *et al*. (2012), Yang *et al*. (2009)]. It can be noted that the prior to activation both the glucose and STP derived chars show peaks centred at 533 eV, while for CB and CG derived chars the peaks are centred at 532 eV. This indicates that the CB and CG derived chars are domintaed by C=O and O-C=O and in glucose and STP derived chars C-OH and C-O-C may be more prevalent. Following activation the spectra are dominated by broad peaks centered at 533-332 eV.

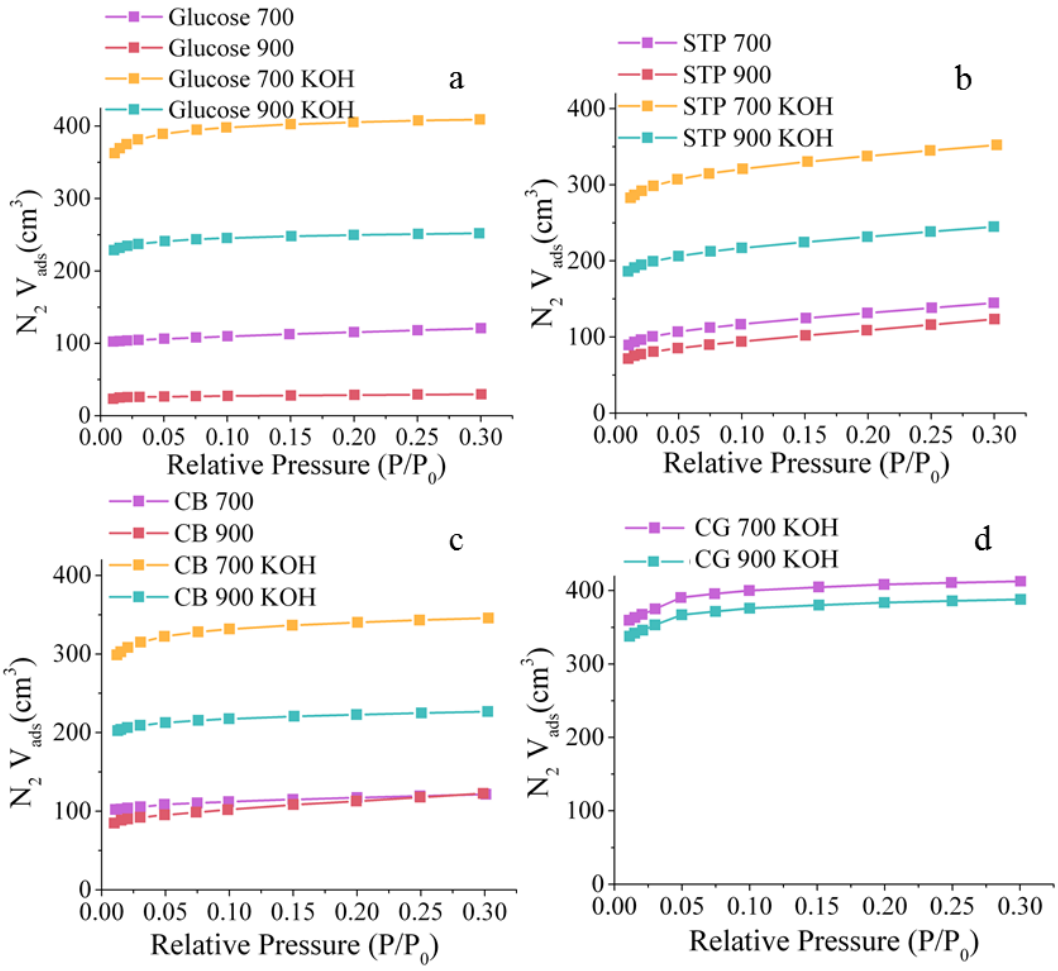

Figure 6.6. N_2 adsorption curves at 77 K up to a relative pressure of 0.3 bar for (a) glucose, (b) STP, (c) CB and (d) CG derived chars and activated carbons.

Using N_2 adsorption at 77 K the influence of activation on the pore structure of the carbon solids can be observed (Figure 6.6). Here, the nitrogen adsorption analysis goes up to a relative pressure of only 0.3 bar, enabling us to most efficiently characterise the materials' BET specific surface area and estimate micropore volume (using a QSDFT model assuming slit and cylindrical pores) (Table 6.2). While efficient, the limited nature of these measurements means that total pore volumes were not ascertained. From Figure 6.6 the curves can be seen to generally plateaux by a relative pressure of 0.3 bar, indicating saturation has occurred and validating the choice of BET analysis method. This substantial uptake at low relative pressures

and rapid saturation is a characteristic of highly microporous materials. However, for the STP derived carbons gas uptake is still occurring at 0.3 bar indicating mesoporosity is also present. This also shows the influence precursor has on the porous characteristics of activated carbons. With this activation regime the microporous character of the micro-mesoporous STP chars was greatly enhanced, from 0.131 to 0.439 cm^3/g and 0.098 to 0.287 cm^3/g for STP 700 KOH and STP 900 KOH respectively, while retaining the same mesoporous profile. Of these activated carbons the Glucose 700 KOH with a BET specific surface area of 1643.5 m^2/g is the most porous. The CG chars CG 700 and 900 were not porous, yet the derived activated carbons are also noteworthy with BET specific surface areas of 1624.7 and 1526.6 m^2/g. Therefore indicating that KOH activation does not require porous chars to yield highly porous materials. Activation can be seen to increase the surface area in each case with chars carbonised at 700 °C typically yielding activated carbons of higher porosity, relative to those carbonised at 900 °C.

Table 6.2. Collated data for the carbon based derived carbons including: porous characteristics, CO_2 uptake performance, yields and elemental composition

Material	SSA_{BET}	V_M	CO_2 uptake	Selectivity	Yield	Elemental analysis (at.%)	
	(m^2/g)	(cm^3/g)	(mmol/g)	CO_2/N_2	(g)	C	O
CB 700	450.8	0.161	2.19	26.2	14.3	89.4	9.3
CB 700 KOH	892.0	0.494	3.78	15.3	58.8	81.7	18.3
CB 900	403.2	0.124	2.31	17.6	13.5	88.5	10.3
CB 900 KOH	892.1	0.320	3.57	16.2	67.4	82.8	17.2
Glucose 700	443.5	0.157	1.99	23.9	21.2	95.2	4.8
Glucose 700 KOH	1643.5	0.601	4.37	15.3	69.7	80.6	19.4
Glucose 900	114.1	0.039	2.27	21.9	19.3	96.2	3.9
Glucose 900 KOH	1011.2	0.365	3.74	16.5	70.5	82.7	17.3
STP	-	-	-	-	-	70.6	28.6
STP 700	468.9	0.131	1.50	18.7	29.9	96.1	3.9
STP 700 KOH	1289.7	0.439	3.75	19.9	70.9	85.8	13.1
STP 900	385.7	0.098	1.53	9.7	30.0	80.9	17.5
STP 900 KOH	864.4	0.287	2.30	16.3	73.2	85.1	12.3
CG 700	-	-	-	-	26.0	89.9	7.1
CG 700 KOH	1624.7	0.585	4.66	13.6	55.0	78.2	20.8
CG 900	-	-	-	-	25.6	94.2	5.8
CG 900 KOH	1526.6	0.55	4.49	16.0	59.0	83.1	16.9

V_M was calculated using a QSDFT model from the adsorption curve up to a relative pressure of 0.35 bar, assuming slit and cylindrical pores. CO_2 uptake was measured at 298 K and 1 bar. Yield of activated carbons is relative to the char used. Elemental analysis was taken from XPS.

The enhancement of surface area and porosity by the chemical activation can be understood through looking at the mechanism of the KOH activating agent. As an etching agent the KOH

reacts with the char to release hydrogen gas and potassium complexes [Lillo-Rodenas *et al*. (2004)].

$$6KOH + 2C \leftrightarrow 2K + 3H_2 + 2K_2CO_3 \qquad \text{(Equation 6.1)}$$

The potassium metal ions (or carbon bound adducts thereof) may be incorporated within the carbon matrix and lead to a separation of the lamellae or destruction of carbon structures [Diaz-Teran *et al*. (2003)]. The K-complexes incorporated within the carbon structures are eliminated by washing after cooling, but the structure cannot relax to the original form revealing permanent porosities. Additionally, at elevated temperatures K_2CO_3 generated in Equation 6.1 may go on to react further with the char to give K metallic species and CO/CO_2 [Ehrburger *et al*. (1986)].

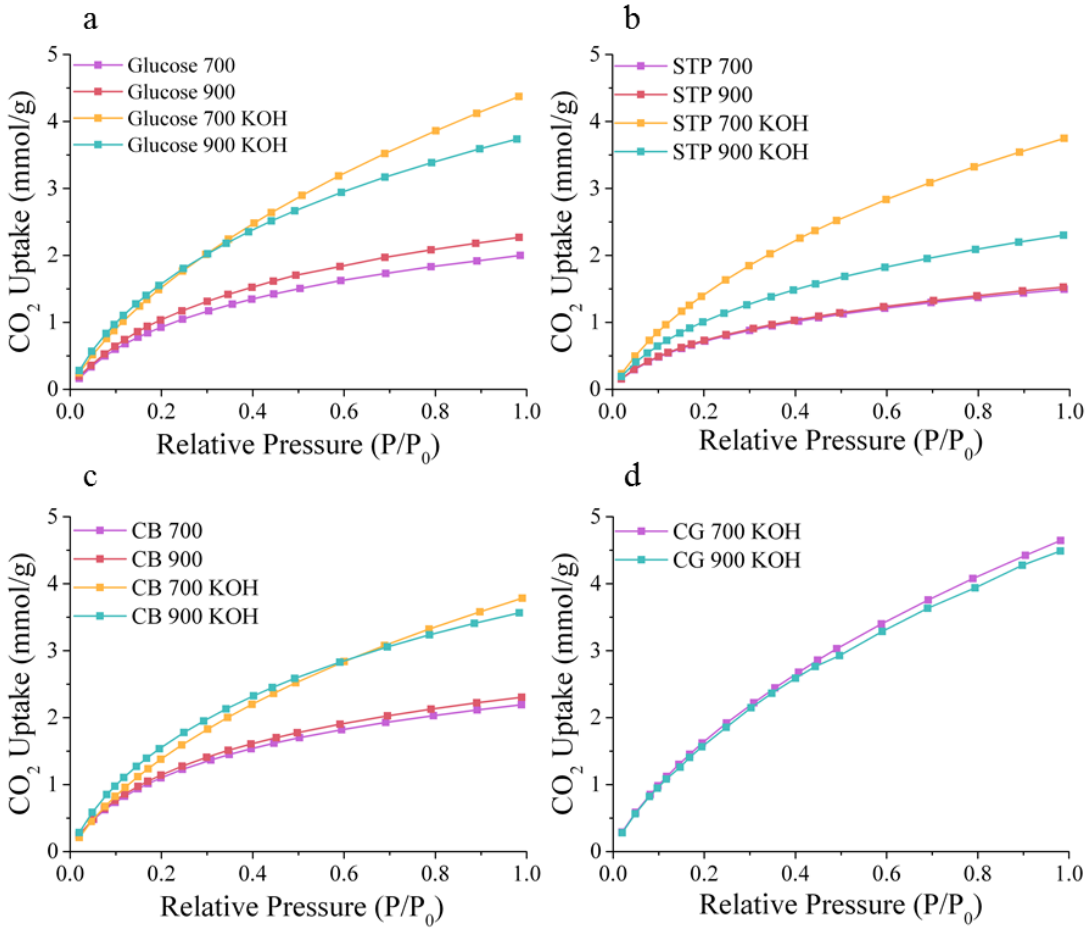

Figure 6.7. CO_2 adsorption isotherms from 0-1 bar for the porous carbon based materials at 298 K for (a) glucose (b) STP, (c) CB and (d) CG derived carbons.

The CO_2 uptake performance of the materials was tested at 298 K using isotherms from 0-1 bar (Figure 6.7) with uptake capacities reported at 1.0 bar (Table 6.2). In line with the increased surface area following activation, the activated samples also exhibit greater CO_2 uptake in all cases. Of particular note is that the CG 700 KOH, CG 900 KOH and glucose 700 KOH all

achieve uptakes of >4 mmol/g at 298 K and 1 bar, comparable with the leading solid sorbents to date (Table 6.1).

To characterise the materials CO_2/N_2 selectivity, N_2 isotherms were run from 0-1 bar N_2, and 298 K (Figure 6.8). The resulting selectivities are presented in Table 6.2 and typical of porous carbons when calculated using the IAST method, of note is CB 700 with the highest selectivity of 26.2.

6.4 Adsorbents from Spent Coffee Grounds

Due to the high CO_2 uptakes, availability and abundance of the CG activated carbons, further experimentation was carried out to further develop sorbents from coffee grounds. Coffee grounds have been investigated as a precursor to porous carbon previously, however, the resulting sorbents do not achieve CO_2 uptake capacities comparable with those in this work (ca. 3 mmol/g at 298 K and 1 bar), likely due to differences in activation method (they did not use grinding, rather heating KOH for impregnating) [Plaza *et al*. (2012), González *et al*. (2013)].

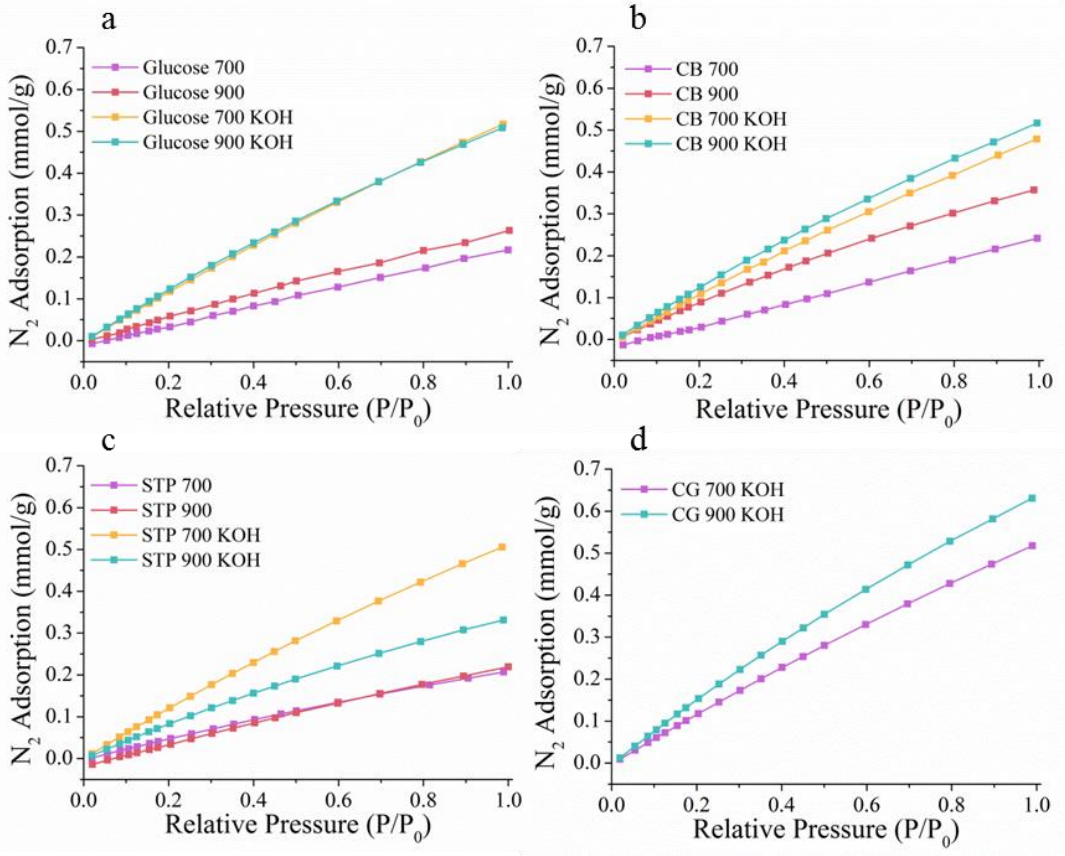

Figure 6.8. N_2 adsorption isotherms for the porous carbon based materials at 298 K for (a) glucose (b) CB (c) STP and (d) CG derived carbons.

From TGA analysis of the CG carbonisation degradation of the lignocellulosic materials can be seen to occur at 200-400 °C, yielding a tar based char which then consolidates at 600-700 °C (Figure 6.3). It is therefore of interest to utilise the char before consolidation as a precursor to activated carbon. Furthermore, as KOH concentration also influences the resultant carbon porous structure [Sevilla *et al*. (2011b)] a ratio of 4:1 KOH:char was used in conjunction with the 2:1 ratio. The same activation program was used, heating the KOH/char mixture to 700 °C at 3 °C/min under a protective nitrogen atmosphere, with a dwell time of 1 hour and then washing with distilled water when cool to remove the remaining potassium ions. The CG derived activated carbons obtained were therefore named CG 400 2-1 and CG 400 4-1 for activation of the CG 400 char with a ratio of 2:1 and 4:1 KOH:char respectively, and CG 700 2-1 and CG 700 4-1 for activation of the CG 700 char with a ratio of 2:1 and 4:1 KOH:char respectively. These were achieved in yields of 12-16 % relative to the amount of initial CGs used (Table 6.3), therefore fitting in with commercial activated carbons [Wu *et al*. (2012)]. With increased KOH activant concentration the yields are reduced, this can be ascribed to increased reactions of KOH and K_2CO_3 with carbon structures to produce gaseous products (CO, CO_2, H_2).

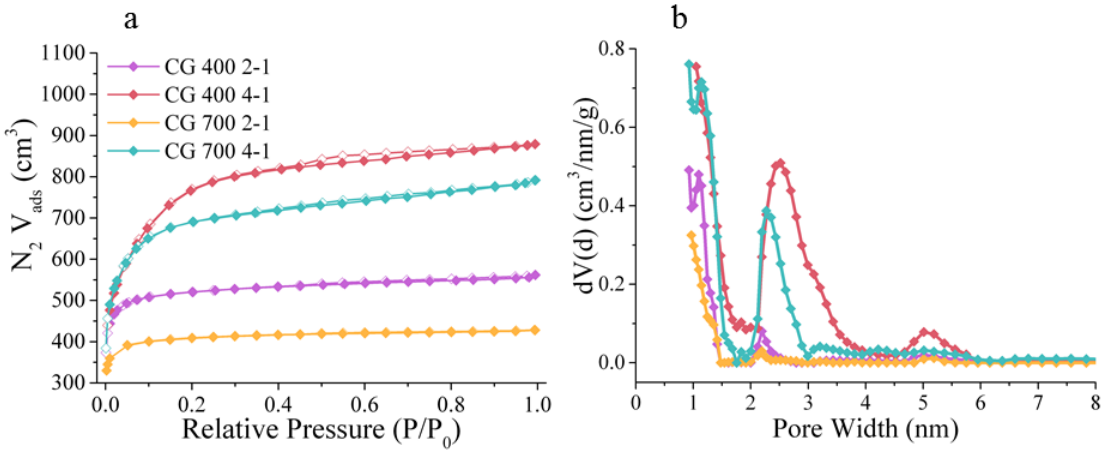

Figure 6.9. (a) N_2 isotherms at 77 K showing adsorption (filled symbols) and desorption (open symbols) between 0-1 bar and (b) QSDFT pore size distribution plot for the CG derived activated carbons.

The pore structural characteristics of the CG activated carbons were analysed using a full N_2 isotherm at 77 K (Figure 6.9(a)), with the calculated BET specific surface areas and pore volumes reported in Table 6.3. The isotherms are all type-I and indicative of highly microporous materials, yet the 4:1 activated samples exhibit a greater extent of mesoporosity as indicated by the wider knee in the adsorption curve at relative pressures of between 0.1-0.3 bar. It is evident that the use of a greater KOH concentration leads to increased surface area, 2875.5 and 2650.9 m^2/g for CG 400 4-1 and CG 700 4-1 compared to 2073.2 and 1624.7 m^2/g for CG 400 2-1 and CG 700 2-1, this trend is also found in the total pore volume. However, the micropore volume does not necessarily increase with KOH concentration. The pore size

distribution plot (Figure 6.9(b)) shows the activated carbons synthesised using the concentration ratio 2:1 are greatly dominated by micropores, with no pore architecture above 2.5 nm in diameter. For those activated with a concentration ratio of 4:1 pore opening in narrow mesopores of 2-4 nm in width is observed.

Table 6.3. Physical properties and CO_2 capacities for KOH activated CG-derived carbon

Material	SSA_{BET} (m^2/g)	V_{tot} (cm^3/g)	V_M (cm^3/g)	Yield* (g)	CO_2 at 1 bar (mmol/g) 273 K	298 K	323 K	CO_2 at 10 bar (mmol/g) 273 K	298 K
CG 400 2-1	2073.2	0.869	0.731	16.3	7.17	4.21	2.47	16.44	12.74
CG 400 4-1	2785.5	1.360	0.716	11.8	5.09	2.81	1.52	23.27	16.05
CG 700 2-1	1624.7	0.662	0.589	14.4	7.55	4.42	2.86	13.34	11.59
CG 700 4-1	2620.9	1.225	0.793	12.6	6.89	4.00	2.38	23.26	16.81

*Yield of the activated carbon is relative to amount of dry CGs initially used.

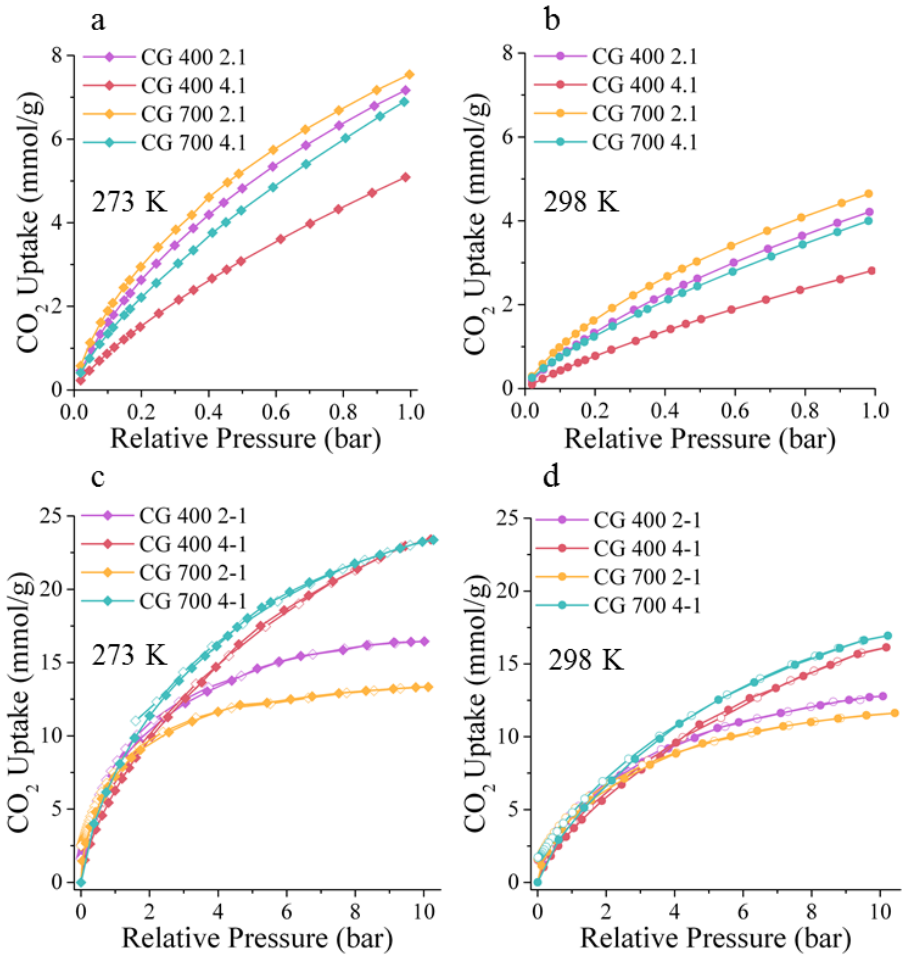

Figure 6.10. Volumetric CO_2 uptake analysis for the CG derived activated carbons. CO_2 adsorption isotherms at 0-1 bar and 273 K (a) and 298 K (b). CO_2 adsorption and desorption isotherms showing adsorption (filled symbols) and desorption (open symbols) at 0-10 bar and 273 K (c) and 298 K (d).

Analysis of the CG derived activated carbons for CO_2 sorption at various temperature and pressures (0-1 and 0-10 bar) can be seen in Figure 6.10 with uptakes capacities reported in Table 6.3. At low pressure (0-1 bar) (Figure 6.10(a) and (b)) the carbons activated with a concentration of 2:1 achieve higher uptakes than those activated with KOH concentration of 4:1. It is noteworthy that this uptake does not increase directly with micropore volume, despite micropores being reported as principally responsible for CO_2 uptake at such low pressures [Presser *et al*. (2011)]. This discrepancy can be ascribed to kinetic effects in the pore analysis using nitrogen at 77 K, where nitrogen molecules access to ultramicropores (<0.7 nm) is hindered and results in the true micropore volume being underestimated [Garrido *et al*. (1987)]. Indeed it has been reported that CO_2 uptake at 1.0 bar occurs in pores ≤0.8 nm in diameter [Presser (2011)]. The activated carbons synthesised using ratios of 4:1 show lower uptake capacities at pressures up to 1 bar than the 2:1 counterparts. This indicates that the 4:1 activated carbons have a lower ultramicropore volume and this is likely due to the greater pore opening associated with increased KOH concentration, where ultramicropores are widened into wide micropores and narrow mesopores. At the higher pressure (10 bar) (Figure 6.10(c) and (d)) the activated carbons synthesised with a concentration of 4:1 achieve greater CO_2 uptakes relative to the 2:1 counterparts due to the increased presence of mesopores which dominate adsorption at such pressures. This demonstrates that controlled increase in KOH concentrations leads to greater pore opening, and sorbent porosity can be tuned for optimised performance in low and high pressure applications.

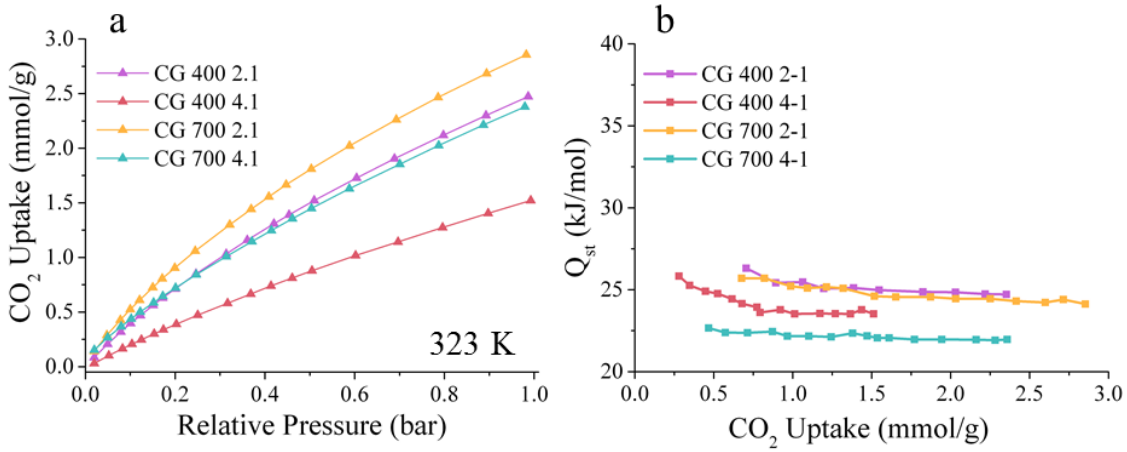

Figure 6.11. (a) CO_2 adsorption isotherms at 0-1 bar and 323 K, and (b) isosteric heats of adsorption (Q_{st}) calculated from CO_2 adsorption isotherms up to 1 bar at 273, 298 and 323 K for the CG derived activated carbons.

With post-combustion capture applications in mind, studies indicate an adsorbent system with a working capacity of approaching or better that 3 mmol/g could significantly reduce the energy requirement of post-combustion capture by 30-50 %, relative to amine solvent systems [Drage *et al*. (2012)]. It is therefore of note that CG 700 2-1 achieves a CO_2 working capacity of 2.86 mmol/g in a 0-1 bar pressure swing at 50 °C, the temperature and pressures of post-combustion

flue gas, and with a CO_2/N_2 selectivity of 13.6 (Table 6.2). Importantly there is no hysteresis in the desorption curves (Figure 6.10(c) and (d)), indicating sorption is fully reversible. The Q_{st} values for the CG derived carbons have been calculated from isotherms at 273, 298 and 323 K (Figure 6.11(b)) and are typical of undoped porous carbon sorbents [Guo *et al*. (2006)] lying between 23 and 26 kJ/mol at near zero loadings.

7. Microporous Organic Polymers: Phenolic Triazine Frameworks

It is understood that microporosity and nitrogen content are important for the selective capture of CO_2 at ambient pressures by a solid physisorbent. The synthesis of a nitrogen-rich polymer with intrinsic microporosity is therefore of great interest. However, such syntheses, as frequently found in many covalent organic frameworks (COFs), microporous organic polymers (MOPs) or polymers of intrinsic microporosity (PIMs), often use expensive reagents, catalytic systems and reaction processes; furthermore the garnered products can be highly air and water sensitive. In contrast a subclass of MOPs known as hyper-cross-linked polymers (HCPs) have often achieved reasonable porosity and CO_2 uptake capacities without the use of expensive reagents and syntheses procedures [Li *et al*. (2011a and b), Wood *et al*. (2007), Mart *et al*. (2011), Germain *et al*. (2009)]. These HCPs have utilised facile Friedel-Crafts chemistry with simple reagents, often derivatives of benzene. This chapter focuses on the synthesis of a novel nitrogen-rich microporous polymer, utilising Friedel-Crafts chemistry. To achieve this aim inspiration was taken from recently published work on the Friedel-Crafts aryl-aryl coupling of the nitrogen-rich cyanuric chloride with the familiar phloroglucinol (Figure 7.1(a)) [Conn *et al*. (2011)]. The aryl-aryl bond formation achieved in this reaction is of import due to the bond rigidity which can be expected to yield intrinsic porosity, and notably different from the sp^3 linkages encountered in most HCPs [Li *et al*. (2011a and b), Wood *et al*. (2007), Mart *et al*. (2011) Germain *et al*. (2009)]. The synthesis therefore of a nitrogen-rich microporous polymeric framework from this reaction was therefore investigated.

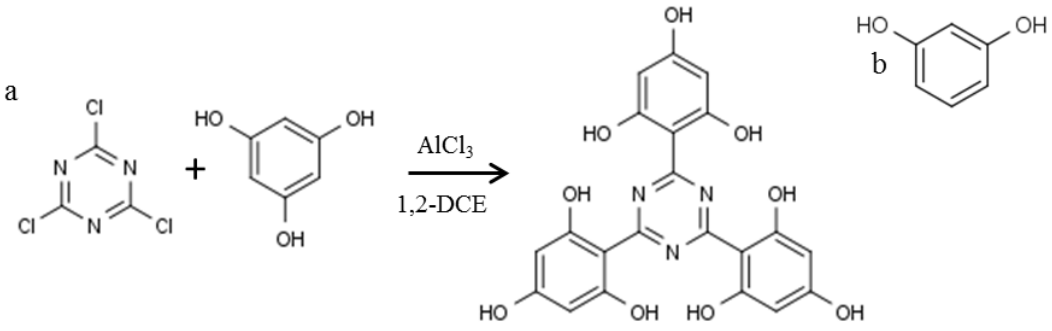

Figure 7.1. (a) Friedel-Crafts reaction of cyanuric chloride with phloroglucinol to give 2,4,6-tris(2,4,6-trihydroxyphenyl)-1,3,5-trizaine with an aluminium chloride catalyst [Conn *et al.* (2011)]. (b) Resorcinol molecular structure.

7.1 Synthesis of 2,4,6-tris(2,4,6-trihydroxyphenyl)-1,3,5-triazine

Firstly the 2,4,6-tris(2,4,6-trihydroxyphenyl)-1,3,5-triazine (Figure 7.1(a)) was synthesised following the literature procedure at 60 °C using a ratio of 1:3 cyanuric chloride:phloroglucinol

in 1,2-dichloroethane (DCE), and obtained in a yield of 87%. The reaction proceeds via an electrophilic aromatic substitution reaction with the mechanism displayed in Figure 7.2. Analysis using ^{1}H and ^{13}C NMR shows that the desired product was obtained, with peak position and integration corresponding with those reported in the literature (Figure 7.3) [Conn *et al.* (2011)].

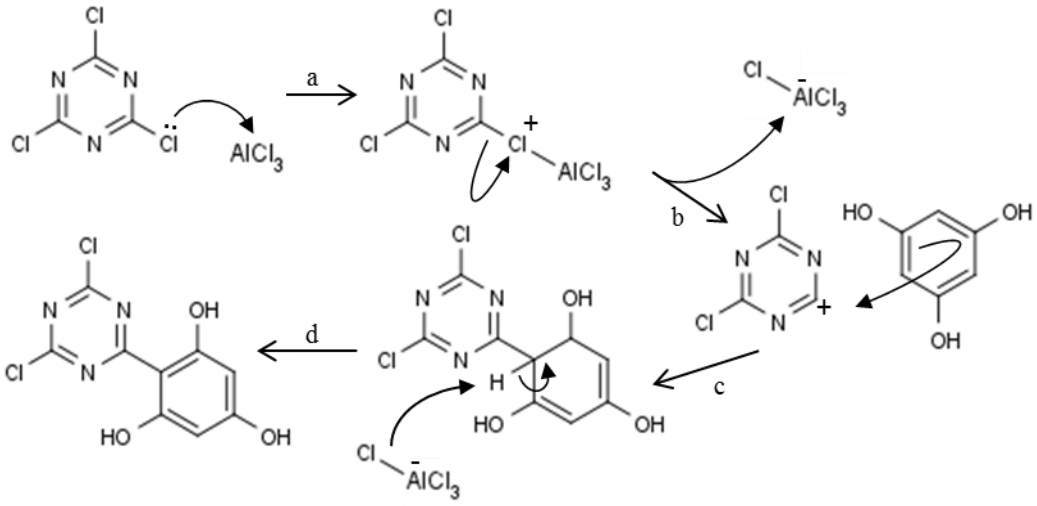

Figure 7.2. Plausible reaction mechanism for the electrophilic aromatic substitution reaction between phloroglucinol and cyanuric chloride, whereby (a) the cyanuric chloride complexes with the Lewis acidic aluminium chloride (b) abstraction of the chlorine by aluminium chloride to leave an electrophilic acylium ion (c) nucleophilic attack of the electrophilic acylium ion by the p orbital electrons of the aromatic phloroglucinol (d) phloroglucinol undergoes proton loss to regain aromaticity and generate HCl. [Smith *et al.* (2007)].

The assignation of the ^{1}H peaks is facile due to their contrasting environments and them matching the literature (Figure 7.3), however the ^{13}C environments need greater attention. The carbon environments a, c & e are easily separated from those of b and d due their proximity with electron withdrawing groups, yet within these two groups the environments are not instantly determined. The literature does not give a detailed analysis of the ^{13}C NMR peak positions and further NMR analysis was therefore carried out using heteronuclear single quantum coherence (HSQC), distortionless enhancement by polarization transfer (DEPT) and heteronuclear multiple-bond correlation (HMBD) which enables a better understanding of these characterisations and peak positions (Figure 7.4). Firstly the ^{13}C peaks at 98.53 and 95.19 ppm can be differentiated and assigned to carbon environments b and d respectively. The protonated aryl carbon, environment d in Figure 7.3, can be identified through HSQC (Figure 7.4(a)), a method which detects correlations between nuclei of two different types separated by one bond; in this case the two different nuclei are the ^{1}H and ^{13}C nuclei. The proton at 5.89 ppm (proton b in Figure 7.3) is coupled directly to the carbon at 95.2 ppm, indicating that this is the protonated aryl carbon (carbon d in Figure 7.3). This is further supported using DEPT ^{13}C NMR (Figure 7.4(b)) analysis in which quaternary carbons are always suppressed, the peak at 98.53 ppm is

suppressed while that at 95.2 ppm is not, indicating it is non-quaternary and therefore the protonated aryl carbon (carbon d in Figure 7.3). Conversely the peak at 98.53 ppm is quaternary so likely carbon b in Figure 7.3. While HSQC experiments detect correlation between atoms separated by one bond, HMBC detects heteronuclear correlations over longer ranges of about 2-4 bonds, and this provides further evidence. In the HMBC spectra (Figure 7.4(c)) the carbon environments d and b are both coupled to the proton peak at 5.89 ppm. Differentiation can be made as the peak between bonded pairs ^{13}C 95.2 ppm and ^{1}H 5.89 ppm is symmetric indicating they are directly bonded, alternatively that between ^{13}C 98.5 ppm and ^{1}H 5.89 ppm is a single spot so indirectly linked and therefore environment b corresponds to the peak at 98.5 ppm [Mirau (2005) pp. 89-91]. Conversely environments a, c and e are less easily differentiated.

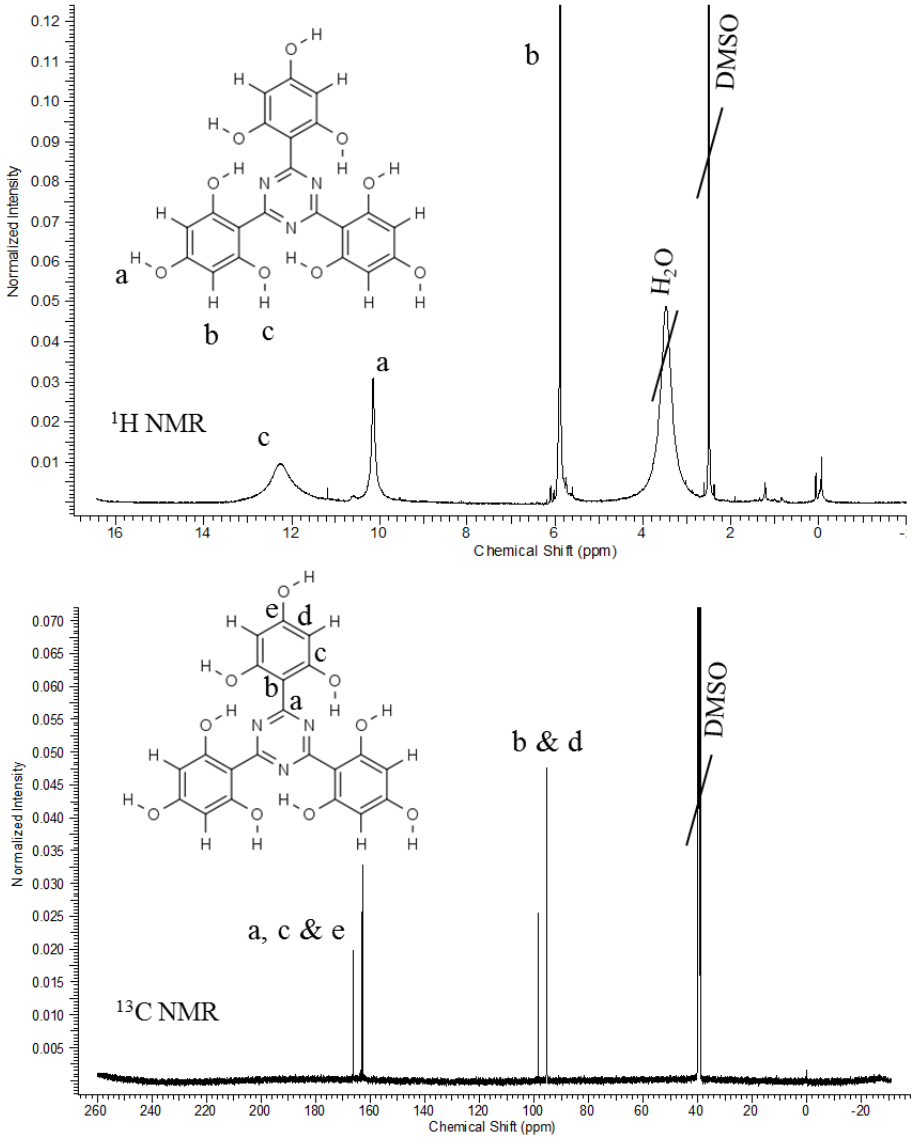

Figure 7.3. ^{1}H NMR and ^{13}C NMR for the synthesised tris(2,4,6-trihydroxyphenyl)-1,3,5-trizaine, highlighting atom environments responsible for peak positions, and corresponding with those reported in literature. Peak positions are δ 12.25, 10.15 and 5.89 ppm for ^{1}H NMR and δ 166.32, 163.31, 162.73, 98.53 and 95.19 ppm ^{13}C NMR.

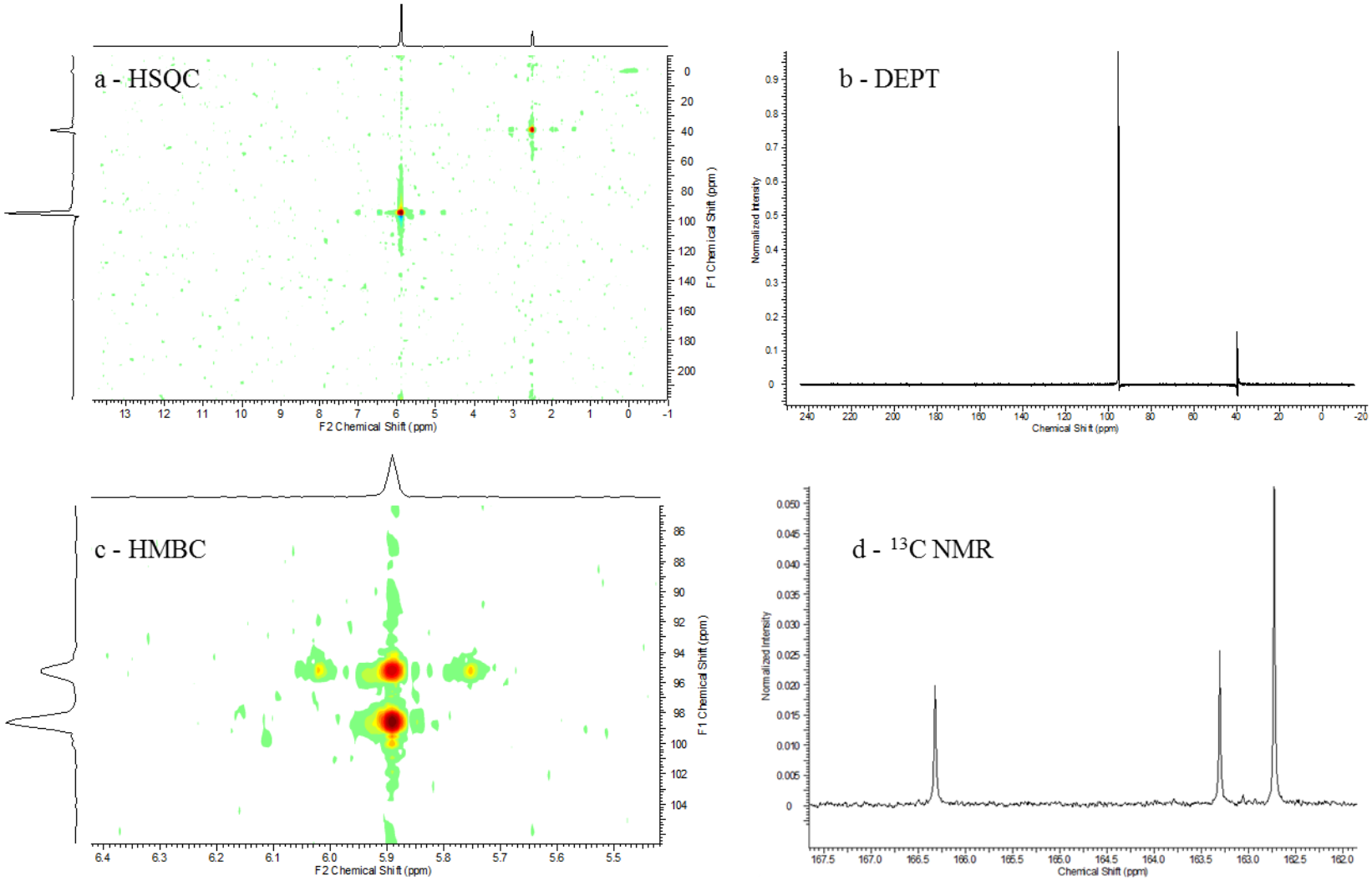

Figure 7.4. Various types of NMR analysis for Tris(2,4,6-trihydroxyphenyl)-1,3,5-trizaine. (a) Heteronuclear single quantum cohenrence (HSQC) spectra with ^{1}H NMR chemical shift (ppm) as x-axis and ^{13}C NMR chemical shift (ppm) as y-axis, (b) distortionless enhancement by polarization transfer (DEPT) ^{13}C NMR (c) heteronuclear multiple-bond correlation (HMBC) spectra with ^{1}H NMR chemical shift (ppm) as x-axis and ^{13}C NMR chemical shift (ppm) as y-axis (d) expanded ^{13}C NMR at 167-162 ppm.

7.2 Synthesis of a Phenolic Triazine Framework Using 1,2-dichloroethane

For the synthesis of a polymeric structure, the reaction was carried out using 1:1 molar equivalents of the cyanuric chloride and phloroglucinol starting materials (Figure 7.5(a)). Initially the reaction was carried out at 60 °C, but after several days reaction a solid had not been achieved. The solvent used, DCE, has a boiling point of 84 °C, and as a result the reaction was then carried out at 85 °C, a temperature typical of HCPs [Wood *et al.* (2007)], affording a hard black/red resinous solid after 16 hours. To gain a greater insight into these polymers a resorcinol linker was used (Figure 7.1(b)), as a replacement for the phloroglucinol, a black/red resinous solid was also obtained after 16 hours. The solids were then washed well in distilled water before Soxhlet extraction in methanol and vacuum oven drying at 80 °C.

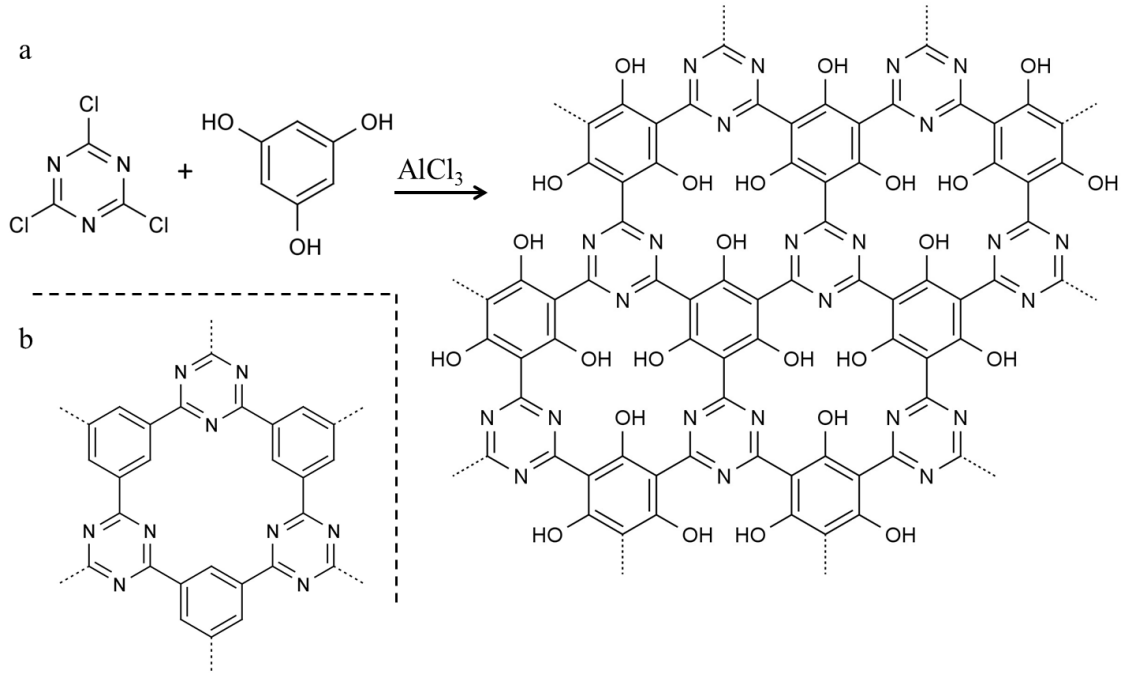

Figure 7.5. (a) Synthesis of a phenolic triazine polymer. (b) Structure of covalent triazine framework CTF-0.

The theoretical polymer structure is very similar to that of covalent triazine framework CTF-0 [Katekomol *et al.* (2013)] (Figure 7.5(b)), a material synthesised using a $ZnCl_2$ catalyst at 400 °C from a cyanobenzene that is not widely available. This is in contrast with the relatively low temperature and available starting materials used in synthesis of the phenolic triazine polymer here. Aside from the conditions for the synthesis, the phenolic groups (-OH) represent the only theoretical chemical difference. Due to this similarity this novel structure is called a phenolic triazine framework (PTF). The chemical structure of the PTFs from phloroglucinol and resorcinol using DCE as solvent at 85 °C are designated as PTF P DCE and PTF R DCE

respectively. Using FTIR analysis the phenol and triazine forms can be observed in both PTF P DCE and PTF R DCE (Figure 7.6(a)): O-H stretching vibrations from the phenol and adsorbed water show broad peaks at 3000-3700 cm^{-1}, C=C phenolic aromatic ring stretching is at 1615 cm^{-1}, C=N triazine ring in-plane stretches are at 1558 cm^{-1} and 1361 cm^{-1} (1363 cm^{-1} for PTF R DCE), O-H out-of-plane deformations are observed at 1200-1000 cm^{-1} and out-of-plane C=N ring deformation are at 830 cm^{-1}, weaker for PTF R DCE.

The resorcinol linker has 2 -OH groups on the aromatic ring, leaving 4 protonated ring carbon atoms capable of nucleophilic attack on the electrophilic acylium ion (Figure 7.2(c)). In the FTIR for PTF R DCE aromatic ring C-H stretching is seen at 2965 and 2926 cm^{-1}, indicating the resorcinol is not binding to 4 triazine groups. In the FTIR for PTF P DCE a shoulder indicative of C-H stretching is also present, at 2967 and 2930 cm^{-1}, though week this may indicate that not all of the phloroglucinol is linked with 3 triazine groups as the theoretical structure predicts (Figure 7.5(a)).

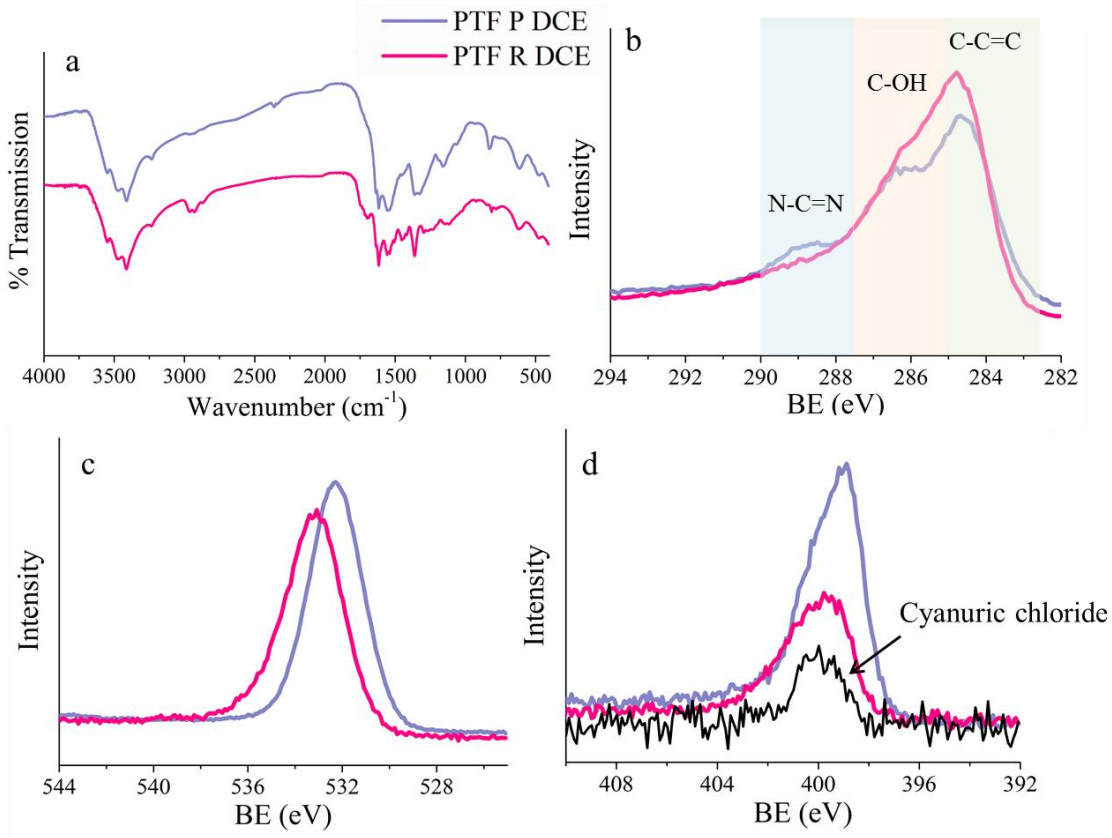

Figure 7.6. (a) FTIR spectra and core level C 1s (b), O 1s (c) and N 1s (d) XPS analysis for the PTF P DCE and PTF R DCE.

From core level XPS C 1s spectra of the PTF P DCE and PTF R DCE both polymers show the 3 different carbon environments expected: sp^2 aromatic tertiary carbon (C-C=C) at 284.6 eV, aromatic -OH functionalised phenolic carbon at 285-287 eV and the triazine (N-C=N) carbon environment at 288-290 eV. The O 1s spectra, centred at 532.3 and 533.1 eV for the PTF P

DCE and PTF R DCE respectively are typical for phenolic -OH groups, shifted for the different polymers due to the differing ring environments. The N 1s spectra of the PTF P DCE shows an asymmetric peak, centred at 398.9 eV, typical of nitrogen in the 2,4,6-Triphenyl-1,3,5-Triazine form of the predicted structure [Gammon *et al.* (2003)]. The asymmetry of the peak is caused by a shoulder at 399.5-401.5 eV, which may be ascribed to presence of nitrogen in chlorinated triazine as found in cyanuric chloride (Figure 7.6(d)). For the PTF R DCE the N 1s peak at 399.5-401.5 eV, appears indicative that some nitrogen is in the chlorinated triazine form, a result of unreacted material or starting material trapped within the network.

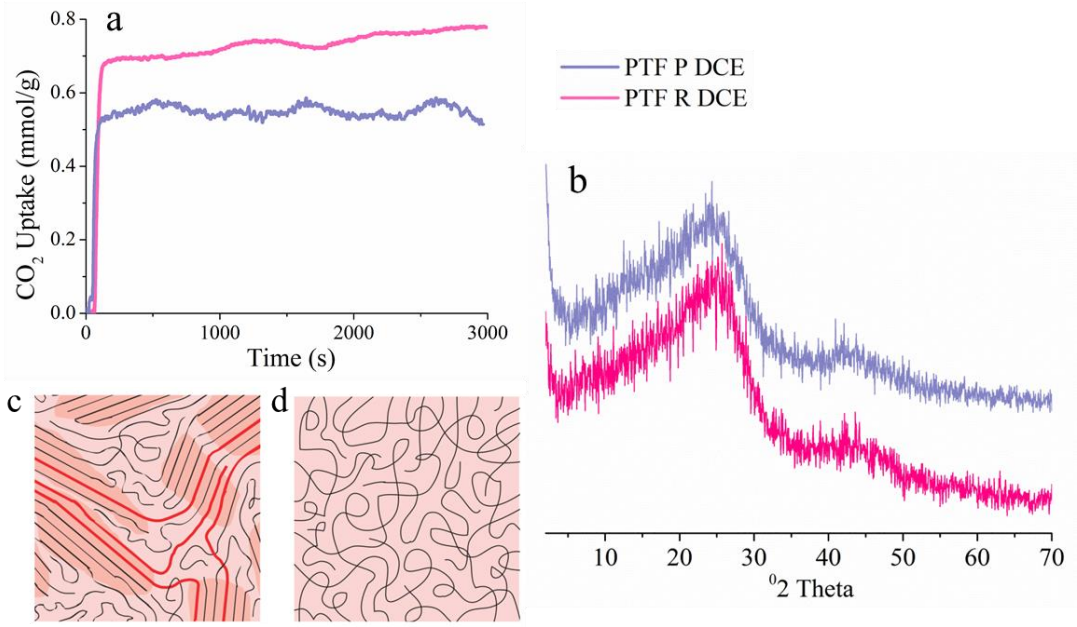

Figure 7.7. (a) Gravimetric CO_2 uptake analysis at 298 K and 1 bar and (b) XRD pattern for the PTF P DCE and PTF R DCE. (c) Schematic of the microstructure of a semicrystalline polymer and (d) a completely amorphous polymer [Noriega *et al*. (2013)].

Gravimetric analysis of the PTFs CO_2 uptake capacities (Figure 7.7(a)) indicate the frameworks are capable of CO_2 sorption, however, the uptake is low; PTF P DCE the better performing material shows an uptake of 0.65 mmol/g. The rapid kinetics of sorption are indicative of a physisorption process. XRD patterns of the frameworks (Figure 7.7(b)) show broad peaks centred at 24-26 and 44° 2θ. These broad peaks indicate the material is semi-crystalline, a state common in polymers where some semi-ordered and amorphous 'spaghetti-like' regions coexist (Figure 7.7(c) and (d)). Long polymer chains will connect adjacent 'crystallites', and these crystallites may be semi-ordered regions comprising of large domains with 3-dimensional (3D) long range periodicity or smaller domains with short-range ordering of a few molecular units [Noriega *et al*. (2013)]. The XRD pattern is also analogous with the broad peaks corresponding to the (0 0 2) and (1 0 1) planes of graphite in amorphous carbon [Xu *et al.* (2010)]. It is worth noting that the CTF-0 is claimed to consist of layered 2-dimensional (2D) sheets, and these PTFs may be exhibiting a similar structure. Furthermore the initial paper from which influence

was taken from for the reaction [Conn *et al*. (2011)], discusses how the phenolic -OH groups form conjugated hydrogen-bonded networks with the triazine ring nitrogen, increasing planarity and also system conjugation, this would therefore favour formation of a 2D sheet-like polymer. Assuming that the peak at 24-26° 2θ corresponds to an inter-planer reflection, the d spacing would be between 0.34-0.37 nm. The increase in the d spacing relative to other planar materials like graphite (0.335 nm), carbon nitride (0.324 nm) and CTF-0 (0.33 nm) can be ascribed to the presence of phenolic groups, that may lie slightly out of plane.

7.3 Synthesis of a Phenolic Triazine Framework Using 1,4-dioxane

The presence of cyanuric chloride nitrogen in the N 1s core level XPS spectra (Figure 7.6(d)) and C-H bond stretching in FTIR (Figure 7.6(a)) indicate unreacted chlorinated triazine groups and unreacted aromatic positions respectively. The solvent so far used, DCE has a boiling point of 84 °C, alternatively 1,4-Dioxane is a polar basic solvent suitable for Friedel-Crafts reactions with a higher boiling point of 101 °C (Figure 7.8(b)). At such elevated temperatures the effects of hydrogen-bonding between the phenolic -OH and triazine nitrogen groups are reduced, allowing investigation of such an effect on structure. Therefore to further explore the structural character and to promote a more complete reaction for the PTF systems the reaction was tried using 1,4-Dioxane as solvent.

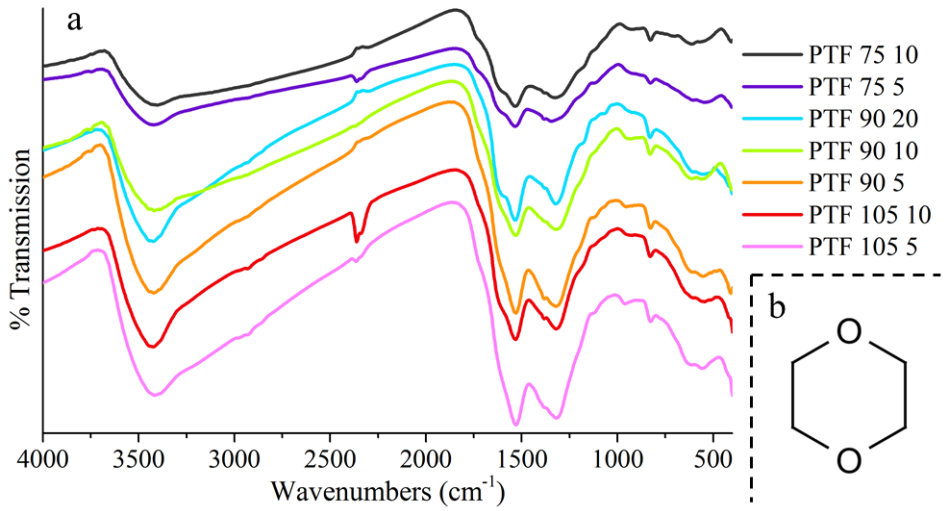

Figure 7.8. (a) FTIR spectra of PTFs synthesised using 1,4-dioxane under various conditions, (b) 1,4-dioxane molecular structure.

The reaction was carried using the phloroglucinol linker with 3 mmol of both cyanuric chloride and the phloroglucinol, with variations in temperature and concentrations: reactions at 75, 90 and 105 °C, using 20, 10 and 5 mL of 1,4-dioxane. The solids were then washed well in distilled

water before Soxhlet extraction in methanol and vacuum oven drying at 80 °C, giving PTF Y X, where Y = temperature and X = the amount of 1,4-dioxane used. After several days reaction for PTF 75 20, the formed solid dissolved in methanol during work up. All the others formed a hard insoluble resin after 16 hours, with PTF 105 5 being hard and brittle and PTF 75 10 much softer and more gelatinous. FTIR analysis of the chemical structure shows the phenol and triazine forms presents in all the frameworks (Figure 7.8(a)), with little change observable for the differing conditions. O-H stretching vibrations from the phenol and adsorbed water show broad peaks centred at 3400-3450 cm^{-1}, a shoulder at 1620-1615 cm^{-1} represents C=C phenolic aromatic ring stretching, C=N triazine ring in-plane stretches are at 1530-1535 cm^{-1} and 1320 cm^{-1}, and out-of-plane C=N ring deformation are at 830 cm^{-1}, the O-H out-of-plane deformations are observed at 1200-1000 cm^{-1}. All frameworks show some aromatic ring C-H stretching shoulder peaks at 2850-3000 cm^{-1}. The chemical structure was analysed using XPS (Figure 7.9) and elemental analysis from XPS given in Table 7.1 and shows that some of the aluminium catalyst is still present.

As XPS surveys the surface (top 1-10 nm) of a material a depth probe analysis was used, with an etch time of 15s from a 3000 eV ion gun, to better understand the bulk structure. Table 7.1 gives the elemental composition for the PTF materials synthesised using 1,4-dioxane at the surface and after the 15 s etch. The Aluminium content is higher within the bulk of the material relative to the surface and some chlorine is present, which may be from unreacted $AlCl_3$ or cyanuric chloride starting material. It is worth noting that the quantity of chlorine is much lower than that of the aluminium, indicating the aluminium is not all present in $AlCl_3$ form. From the core level C 1s analysis (Figure 7.9(a)) all samples show the 3 different carbon environments in the polymer product: sp^2 aromatic tertiary carbon (C-C=C) at 284.6 eV, aromatic -OH functionalised phenolic carbon at 285-287 eV and the triazine (N-C=N) carbon environment at 288-290 eV. Of note is that after etching (Figure 7.9(b)) the prominence of the phenolic carbon peak at 285-287 eV is reduced. From the core level N 1s XPS analysis (Figure 7.9(c)) all the samples show the same broad peaks at 398-402 eV, suggestive of chlorinated triazine as found in cyanuric chloride. However, the lack of chlorine found from elemental analysis (Table 7.1) shows this is not the case and that partially or unreacted cyanuric chloride is not that prevalent. The peaks become asymmetric after etching, leaning to lower binding energies (Figure 7.9(d)). The O 1s spectra (Figure 7.9(e) and (f)) are centred at 532.3 eV, typical for phenolic -OH groups, notable is that after etching despite the reduction in atomic ratio (Table 7.1) the chemistry of the groups does not change. This -OH group prevalence at the surface of materials may be ascribed to polymer terminating groups or within a 2D structure, they are covering atoms of the deeper-lying layers.

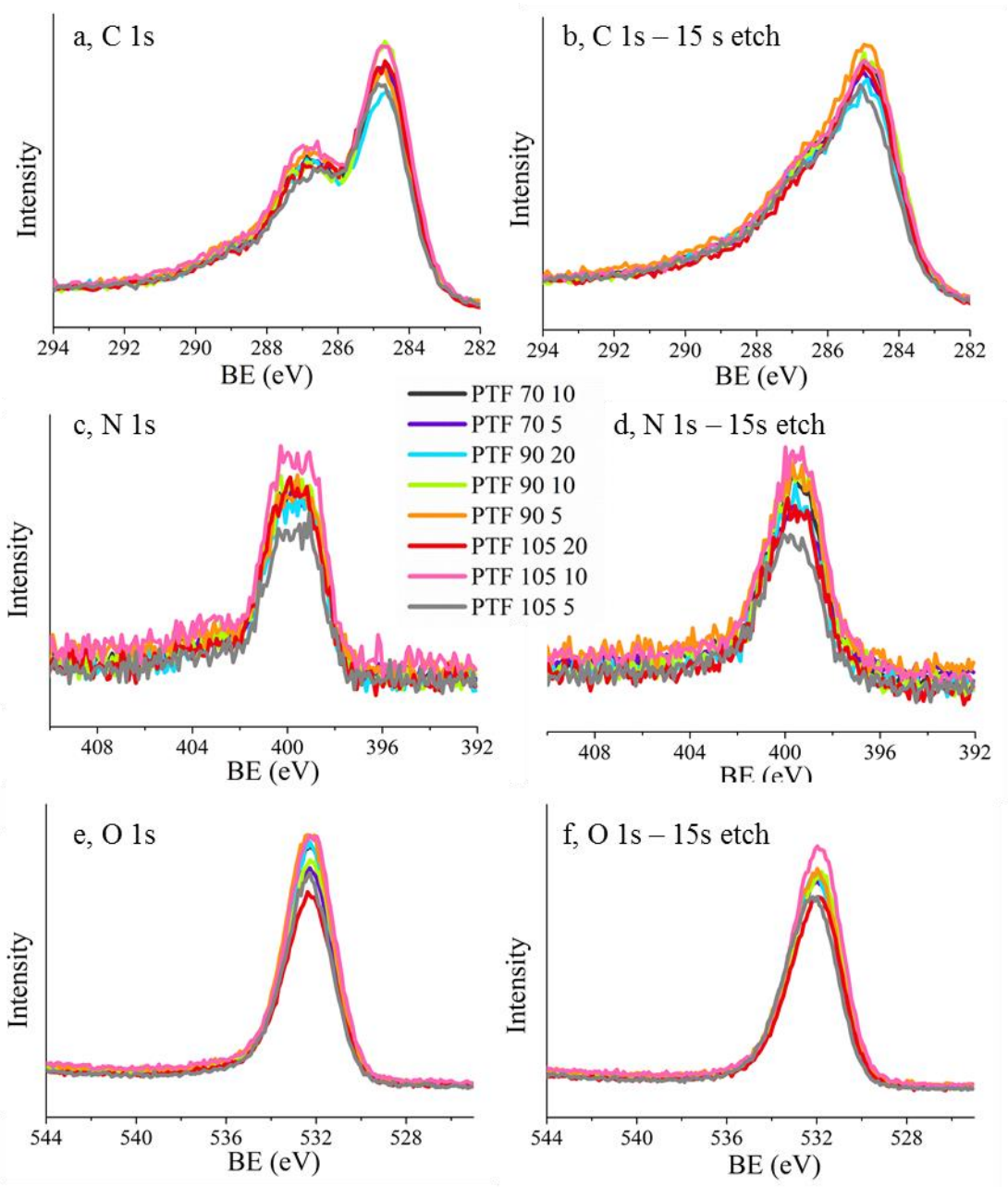

Figure 7.9. Core level XPS analysis for the PTF samples synthesised using 1,4-dioxane showing the (a) C 1s, (c) N 1s and (e) O 1s spectra on the surface and (b) C 1s, (d) N 1s and (f) O 1s after a 15s depth probe etch.

XRD patterns of the PTFs synthesised using 1,4-dioxane all show broad peaks centred at 24-26 and 44° 2θ (Figure 7.10(a)). These broad peaks indicate all the materials are semi-crystalline, without long range order. A trend giving indication of specific conditions favouring extended 2D sheet formation is not observable. Of note is that PTF 90 10 and PTF 105 10 both exhibit broad peaks at 6-8° 2θ. Being a low angle reflection this corresponds to a larger spacing, of 14.7-11.0 nm. This may be ascribed to intercalated solvent, though it is significantly larger than that experienced for water or methanol intercalated in GO (0.5-0.9 nm) [Barroso-Bujans *et al.* (2010)] so perhaps unlikely. The CTF-0, also exhibits a second peak at a lower angle (14° 2θ),

ascribed to reflections from the (1 0 0) plane. However, this is much too large to be from (1 0 0) plane reflections. Alternatively, it may be from crystalline phase formation by coordination with remaining Al species, as were visible in the CTF materials from remaining Zn catalyst [Katekamol *et al*. (2013)].

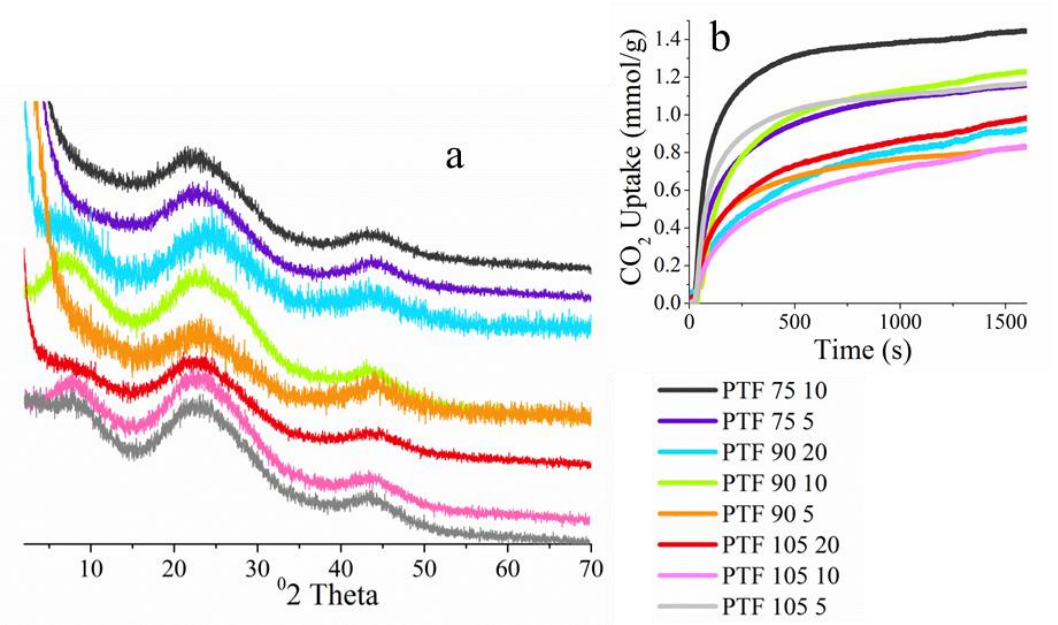

Figure 7.10. (a) XRD pattern and (b) gravimetric CO_2 uptake analysis at 298 K and 1 bar, for the PTFs synthesised using 1,4-dioxane from a range of temperatures and concentrations.

Table 7.1. Sample characteristics for PTF-dioxane series, giving XPS elemental analysis and CO_2 uptake capacities from gravimetric analysis

Material	Etch time (S)	XPS Analysis (at.%) Al	Cl	C	N	O	CO_2 Uptake 298 K, 1 bar (mmol/g)
PTF 75 10	0	1.7	0	64.1	11.9	22.2	1.45
	15	2.9	0	72.5	11.4	13.2	
PTF 75 5	0	2.3	0	66.6	7.7	23.3	1.16
	15	3.2	0.4	66.3	7.2	22.6	
PTF 90 20	0	1.8	1	64.4	10.7	22.1	0.94
	15	2.7	1.3	70.3	10.5	14.7	
PTF 90 10	0	1.4	0.4	65.4	9.1	23.5	1.23
	15	3.9	0	69.2	10.3	15.6	
PTF 90 5	0	2.2	0	63.1	10.7	23.9	0.84
	15	4.2	0	69.8	12.6	12.6	
PTF 105 20	0	6.1	0	64.0	8.4	21.5	0.99
	15	6.9	1.3	68.6	7.8	16.4	
PTF 105 10	0	2.2	0	62.8	9.2	25.7	0.84
	15	4.1	0.7	73.3	9.1	12.8	
PTF 105 5	0	3.2	1.2	63.6	8.3	23.7	1.17
	15	4.5	1.3	73.6	7.6	13.0	

The materials were tested using gravimetric analysis as to their affinity for CO_2 sorption (Figure 7.10(b)), with PTF 75 10 exhibiting the greatest uptake at 298 K and 1 bar CO_2 of 1.45 mmol/g (Table 7.1). BET surface area analysis was carried out for several of the PTF polymers, but none showed any apparent surface area. That the materials show no adsorption of N_2 at 77 K, yet sorption of CO_2 at 298 K, indicates that the PTFs so far synthesised are porous only in the ultramicropore region (<0.7 nm). These PTF polymers can be compared with the HCPs that use a similar Friedel-Crafts reaction. These HCPs achieve a similar CO_2 capacity to the PTF, achieve typically 1.5-1.7 mmol/g CO_2 at 298 K and 1 bar [Li *et al*. (2011a), Li *et al*. 2011b), Martín *et al*. (2011b)], with the PTF polymer achieving 1.5 mmol/g. Interestingly, the HCPs all have much higher apparent surface areas, typically 1000-1700 m^2/g, than the ultramicroporous PTFs which displays no apparent surface area when analysed using N_2 adsorption.

7.4 Carbonisation of the Phenolic Triazine Framework

From the ultramicroporous and nitrogen-rich nature of the PTFs it was envisaged that carbonisation would lead to an N-doped microporous derived carbon of interest for CO_2 capture. For the PTF starting material a synthesis analogous to that for PTF 75 10 was chosen, as this showed the greatest CO_2 uptake observed among the different conditions of synthesis using 1,4-dioxane. A resorcinol equivalent was also synthesised using the same conditions. Carbonisation was carried out using a tube furnace under a steady flow of nitrogen. The furnace was heated at a ramping rate of 3 °C/min to the desired temperature, with a dwell time of 4 hours. Temperatures of 300, 500, 700 and 800 °C were used, obtaining PTF P X and PTF R X for the phloroglucinol and resorcinol equivalents respectively, where X = temperature of carbonisation.

The chemical change from carbonisation over the range of temperatures used was monitored using FTIR and XPS analysis. The core level C 1s spectra for both the phloroglucinol and resorcinol derived PTFs (Figure 7.11(a) and (d)) shows the same profile after carbonisation at 300 °C as for the PTF polymer with: aromatic tertiary carbon (C-C=C) at 284.6 eV, aromatic -OH functionalised phenolic carbon at 285-287 eV and the triazine (N-C=N) carbon environment at 289 eV. An indication carbonisation at 300 °C does not alter the chemistry of the structure. At 500 °C a reduction in the peaks are evident at higher binding energies, corresponding to loss of -OH groups at 285-287 eV and maybe the triazine (N-C=N) carbon environment at 289 eV. At 700 and 800 °C decomposition of these structures can be further observed, with the peak at 284.6 eV indicative of a graphitization process occurring and a largely sp^2 hybridised C-C=C environment the result. The asymmetry of the C 1s peaks at 700 and 800 °C towards higher binding energies indicates that heteroatom doping is present. From the O 1s spectra the phenolic

groups at 532-533 eV are shifting to lower binding energies as temperature of carbonisation increase for both the phloroglucinol and resorcinol equivalents (Figure 7.11(b) and (e)), this may be due to conversion to C=O and O=C-OH [Larciprete *et al*. (2011), Yang *et al*. (2009)]. From the N 1s spectra the triazine nitrogen groups observed at a binding energy of 389 eV can be seen to decompose above 500 °C to form pyridinic (398.1-398.6 eV) and quaternary (400.8-401.6 eV) forms [Wu *et al*. (2012), Sheng *et al*. (2011].

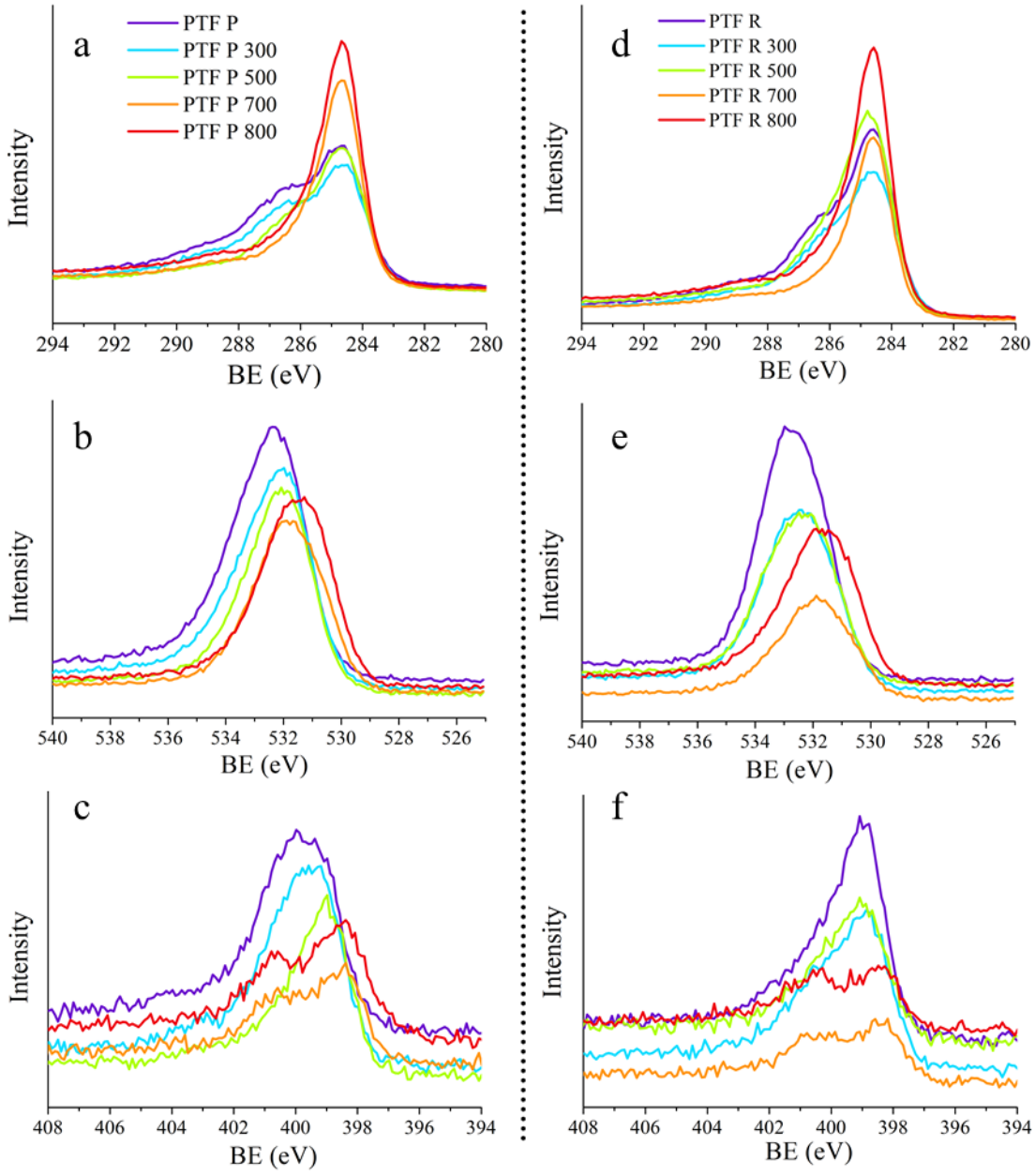

Figure 7.11. Core level C 1s (a), O 1s (b) and N 1s (c) XPS spectra for the carbonised phloroglucinol derived PTF. Core level C 1s (d), O 1s (e) and N 1s (f) XPS spectra for the carbonised resorcinol derived PTF.

FTIR analysis of the phloroglucinol derived PTF and its derived carbons is shown in Figure 7.12(a), for the polymer the C=N triazine ring in-plane stretches are at 1535 cm^{-1} and a shoulder

at 1630 cm^{-1} is from C=C phenolic aromatic ring stretching. A broad peak at 1319 cm^{-1} is also from C=N triazine ring in-plane stretches and the shoulder at 1175 cm^{-1} is from O-H out-of-plane deformations. Out-of-plane C=N triazine ring deformations are at 825 cm^{-1}. Following carbonisation the C=C aromatic ring stretching becomes more dominant, converting to a strong doublet at 1619 and 1637 cm^{-1}. The C=N triazine ring in-plane stretches at 1535 cm^{-1} remain up to 500 °C, decomposing by 700 °C, coinciding with the same observations made from XPS analysis. While the broad peak at 1319 cm^{-1} also from C=N triazine ring in-plane stretches is lost above 500 °C, small peaks at 1384 and 1326 cm^{-1} can be assigned to pyridinic and quaternary nitrogen.

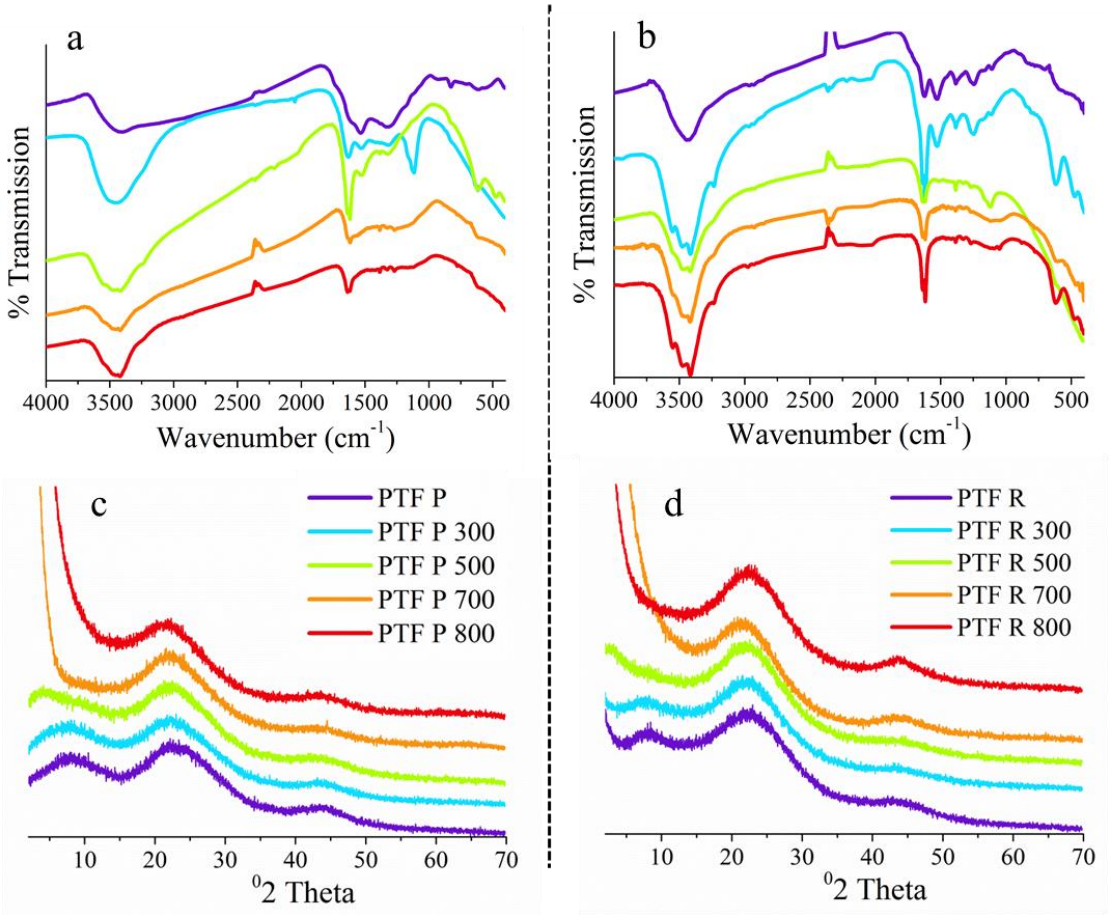

Figure 7.12. (a) FTIR spectroscopy and (b) XRD pattern for the phloroglucinol derived PTF and products of carbonisation. (c) FTIR spectroscopy and (d) XRD pattern for the resorcinol derived PTF and products of carbonisation.

The FTIR for the resorcinol derived PTF (Figure 7.12(b)) shows C=C phenolic aromatic ring stretching at 1628 cm^{-1} and C=N triazine ring in-plane stretches at 1529 and 1385 cm^{-1}. The O-H out-of-plane deformations can be seen at 1245 cm^{-1} and out-of-plane C=N triazine ring deformation at 840 cm^{-1}. Following carbonisation the aromatic ring stretching peak increases in intensity and becomes a defined doublet at 1619 and 1639 cm^{-1}, indicative of a graphitisation process. The C=N triazine ring in-plane stretches at 1529 cm^{-1} are present in the PTF R 300, but

reduced at higher carbonisation temperatures, indicating decomposition of the triazine structures. The peak at 1245 cm^{-1} due to O-H out-of-plane deformations is also lost at temperatures over 500 °C, supporting the XPS data that suggests -OH groups are converting into carbonyl and acid groups.

Table 7.2. Sample characterisation for the carbonisation of resorcinol and phloroglucinol derived PTFs

Material	SSA_{BET} (m^2/g)	V_{tot} (cm^3/g)	V_M (cm^3/g)	CO_2 uptake (mmol/g)	Q_{st} (kJ/mol)	Selectivity CO_2/N_2	Elemental Analysis (at.%)			
							C	N	O	Al
PTF P	-		-	-	-	-	65.1	8.1	21.3	5.5
PTF R	-	-	-	-	-	-	69.0	7.5	19.5	2.0
PTF P 300	18.6	0.016	-	-	-	-	63.2	8.3	22.7	5.8
PTF R 300	15.0	0.026	-	-	-	-	70.0	7.2	19.3	3.5
PTF P 500	-	-	-	-	-	-	65.4	7.0	21.4	6.1
PTF R 500	21.8	0.031	-	-	-	-	74.0	5.5	16.5	4.0
PTF P 700	321.5	0.193	0.154	2.14	30.15	18.91	67.7	5.2	18.9	8.1
PTF R 700	68.6	0.045	0.039	2.14	32.67	23.20	77.6	4.4	13.5	4.0
PTF P 800	158.2	0.116	0.083	2.13	31.04	23.74	67.1	5.4	17.7	9.8
PTF R 800	26.4	0.028	0.014	2.28	28.91	21.68	76.5	3.8	14.0	5.7

V_M was calculated using a QSDFT model from the adsorption and desorption curves up to a relative pressure of 0.35 bar, assuming slit pores. CO_2 uptake was measured using volumetric analysis at 298 K and 1 bar. Elemental analysis is taken from XPS.

Structural analysis from XRD (Figure 7.12(c) and (d)) for the carbonised PTFs shows the broad peaks at 23 and 44° 2θ, understood to be from the (0 0 2) and (1 0 0) diffractions of layered, graphitic-type structures [Wang *et al.* (2013)]. Of interest is that while the XPS and FTIR analysis both indicate that the structure is undergoing graphitisation, the peak corresponding to (0 0 2) diffractions does not shift to a more graphite-like position (26.5°). The broad peak at 8° 2θ can be seen to shift to 4° 2θ at 500 °C and at 700 and 800 °C the peak is replaced by low-angle scatter. This suggests that these broad low angle peaks are due to scatter resulting from open void and pore space, the increase in low-angle scatter can then be attributed to an increase in the density of pores [(Zhu *et al*. (2011)]. Carbon materials with ordered meoporosity, such as zeolite templated carbon [Sevilla *et al*. (2012a)] and azo-COPs [Patel *et al*. (2013)] show defined low-angle peaks; that low-angle scatter is seen here rather than defined low-angle peaks is an indication of an amorphous porous morphology.

The structure of the PTF derived carbons was further investigated using N_2 isotherms at 77 K. The derived carbons obtained at 300 and 500 °C show very little accessible porosity, with type-

III isotherms (Figure 7.13(a)), and BET specific surface areas of at most 21.8 m^2/g (PTF R 500, Table 7.2). Both PTF P and PTF R gave no indication of accessible porosity, with isotherms unsuitable for BET multi-point surface area analysis, analogous to that for PTF P 500. For the derived carbons obtained at 700 and 800 °C the type-I isotherms are indicative of micropore dominated materials (Figure 7.13(b)). This opening of micropores at 700 °C is further highlighted by the pore size distribution analysis (Figure 7.13(c)), where the vast majority of the porosity exists in pores of diameter <1.0 nm, some mesoporosity is also present (see inset) with pores 2-4 nm in width. From the XRD patterns the PTF layered structure can be seen to remain following carbonisation. Despite this accessible porosity opens-up after heating to 700 °C. Taken in conjunction with the XPS and FTIR analysis it can be observed that while the aromatic layered structures remain and consolidate over carbonisation, it is the decomposition of the triazine ring and the resulting defects produced that are likely responsible for the microporous structure.

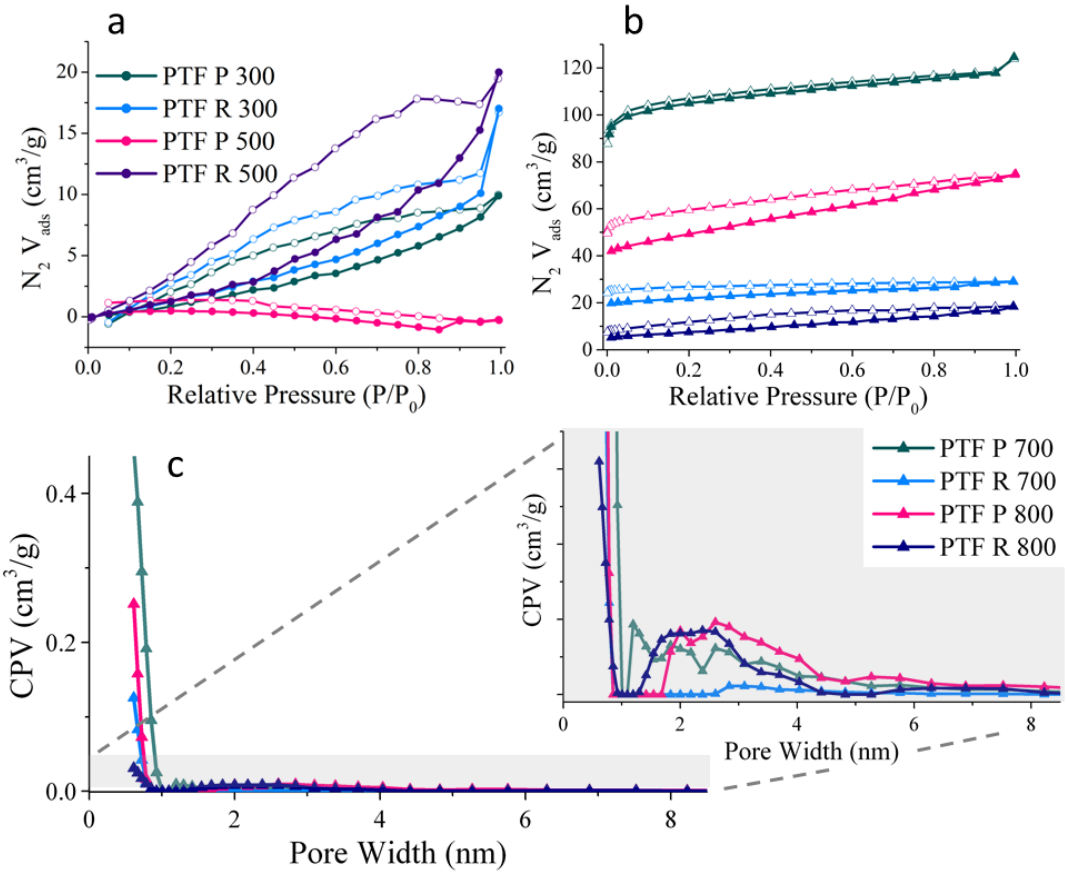

Figure 7.13. Structural characterisation from N_2 isotherms between 0-1 bar at 77 K for the PTF derived carbons showing adsorption (filled symbols) and desorption (open symbols). (a) Isotherms for derived carbons obtained at 300 and 500 °C. (b) Isotherms for derived carbons obtained at 700 and 800 °C, with pore size distribution analysis (c) derived from QSDFT using a slit pore equilibrium model (CPV is cumulative pore volume).

Due to the apparent microporosity of the PTF derived carbons obtained at 700 and 800 °C, volumetric gas sorption analysis was carried out to determine their CO_2 uptake capacities

(Figure 7.14). In spite of the apparent differences in apparent surface areas, the CO_2 capacities are quite similar at 1 bar for the 4 PTF derived carbons, all lying between 2.13 and 2.28 mmol/g at 298 K and 1 bar, with PTF P 800 exhibiting the greatest uptake (Table 7.2). Analysis of the isosteric heats of adsorption (Q_{st}) calculated from CO_2 adsorption isotherms up to 1 bar at 273, 298 and 323 K, showed that the enthalpy of adsorption at near zero loading reached up to 32.67 kJ/mol (for PTF R 700), indicative of an enhanced physisorption process, likely due to the presence of the pyridinic N-dopants. CO_2/N_2 selectivities were also calculated at 298 K, being between 19 and 22 (Table 7.2).

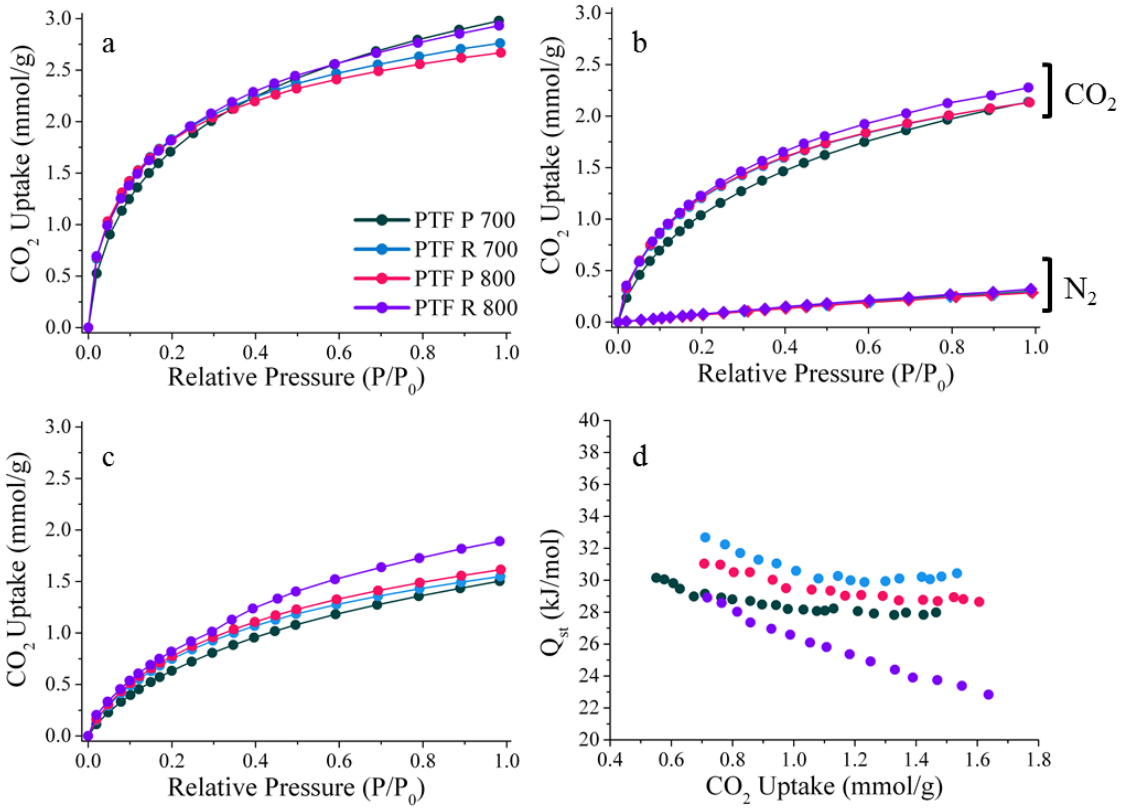

Figure 7.14. Gas sorption analysis for PTF derived carbons, (a) CO_2 isotherms up to 1 bar at 273 K, (b) CO_2 and N_2 isotherms up to 1 bar at 298 K, (c) CO_2 isotherms up to 1 bar at 323 K and (d) (Q_{st}) calculated from CO_2 adsorption isotherms up to 1 bar at 273, 298 and 323 K.

7.5 Removal of the Aluminium from the Phenolic Triazine Framework

The PTF derived carbons are N-doped strictly microporous carbon material, and therefore of considerable interest for CO_2 capture. However, XPS analysis indicates aluminium species still remain within the structure from the catalyst used during synthesis, and these may be reducing accessible porosity. To remove these aluminium species a different work-up was developed. From the XPS analysis of the PTF polymers the prevalence of aluminium species is far greater than that of chlorine species, indicating that the aluminium does not persist in the $AlCl_3$ form.

Alternatively, it may be in the highly stable aluminium hydroxide form or be ligating with the PTF structure, as the -OH and C-N=C groups are common features of hard ligands that would favour ligation to the hard aluminium metal centre. To ensure that the aluminium species be dissolved it was envisaged that ammonium hydroxide NH_4OH could be used to convert any ligated aluminium to $Al(OH_3)$, which can then be readily dissolved in subsequent strong acid (HCl) washes, before neutralising and Soxhlet extraction. Another batch of the phloroglucinol and resorcinol derived PTFs was therefore synthesised, using 1,4-dioxane as solvent and temperatures of 75 and 105 °C. The obtained products are designated as PTF P X b2 and PTF R X b2 for the phloroglucinol and resorcinol equivalents respectively where X = the synthesis temperature and b2 stands for 'batch 2'.

The resulting products were analysed using depth probe XPS elemental analysis with an etch time of 15 s, enabling the existence of aluminium on the surface or bulk of the materials to be determined (Table 7.3). For the PTF R 70 b2, the aluminium was still present on the surface of the material and within the bulk structure. However, for the other samples the aluminium was successfully removed, from both the surface and the bulk of the material.

Table 7.3. Elemental analysis of the PTF b2 materials

Material	XPS Analysis (at.%)										CHN Analysis (wt.%)		
	0s Etch					15s Etch							
	C	N	O	Al	C/N	C	N	O	Al	C/N	C	N	C/N
PTF P 70 b2	65.3	11.9	22.8	0.0	5.5	68.9	13.5	17.6	0.0	5.1	46.7	13.7	3.4
PTF R 70 b2	67.5	11.2	20.2	1.6	6.0	71.5	10.4	16.5	1.6	6.8	52.3	12.8	4.1
PTF P 105 b2	67.6	10.9	21.5	0.0	6.2	71.5	11.7	16.5	0.0	6.1	47.4	13.4	3.6
PTF R 105 b2	73.5	9.0	17.4	0.0	8.1	79.1	8.6	12.7	0.0	9.2	56.3	10.5	5.4

C/N is the ratio of carbon to nitrogen

From the XPS elemental analysis it can be observed that the ratio of C:O:N, which should be 3:1:1 if the proposed structure is achieved, are not ideal. CHN elemental analysis for the 4 samples was therefore carried out, to better ascertain the C/N ratio (Table 7.3). From the CHN analysis for the phloroglucinol derived b2 PTFs the C/N ratio is 3.4 and 3.6 for reactions carried out at 70 and 105 °C respectively. This is indicative of the reaction product being in-line with the proposed structure, but indicative that the reaction is not quite reaching completion; it should be noted though that solvent trapped within inaccessible pore voids might be the cause of this discrepancy [Patel *et al*. (2013)]. For the resorcinol derived PTFs the C/N ratio is much higher, indicating that the resorcinol structure may vary from the hexagonal proposed structure (Figure 7.5(a)), as described for CTF-0. The difference in structure resulting from the different phenol starting materials is attributable to the 2 resorcinol -OH groups relative to the

phloroglucinol's 3. This leaves 4 non-substituted positions on the resorcinol ring that may be susceptible to electrophilic attack, with the -OH groups being ortho-para directing [Solomon (1980) pp. 480)]. In turn, it is understood that an aryl substituent will act as an activating group for further ring substitution and that such aryl groups are also ortho-para directing [Solomon (1980) pp. 518)]. As the -OH groups on the resorcinol are in the 1,3-positions, substitution at the 2, 4 and 6-positions is favoured, being ortho/ortho, ortho/para and ortho/para to the -OH groups respectively (Figure 7.15(a)) [Conn *et al*. (2011)]. The result of this is that substitution at the 5-position is expected to be least favoured and likely hindered due to steric factors following aryl addition at the 4 and 6-positions. The resulting possible polymer structure may therefore be the hexagonal type structure described in CTF-0 or a more branched polymer structure (Figure 7.15(b)). However, for the branched and hexagonal structures a C/N ratio of 3 would still be expected. The high C/N ratios may therefore be from trapped solvent and monomers or due to a large number of resorcinol terminating groups.

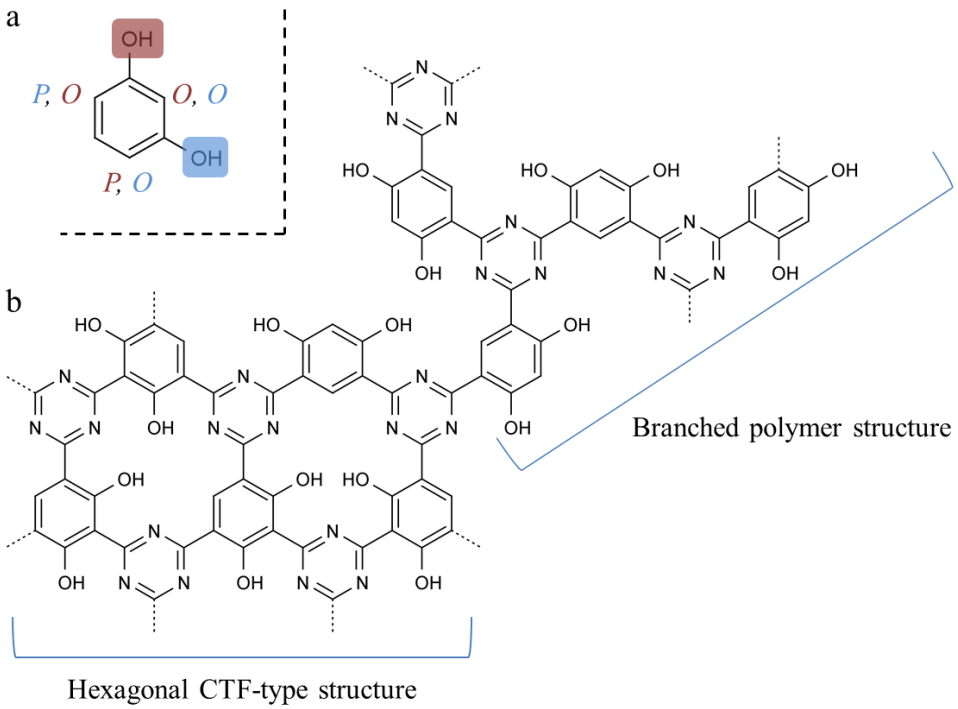

Figure 7.15. (a) Resorcinol showing the ortho- and para- positions. (b) Pictorial representation displaying the hexagonal CTF-type and branched polymer structures.

The chemistry of the PTF P and R b2 materials was further analysed using core level XPS on the PTFs surface and bulk through depth probe analysis after a 15 s etch (Figure 7.16). From the surface C 1s analysis (Figure 7.16(a)), for the PTF P and R b2 samples, the sp^2 aromatic tertiary carbon (C-C=C) at 284.8 eV and the aromatic -OH functionalised phenolic carbon at 286-288 eV are well visible, while the peaks corresponding to triazine (N-C=N) carbon environments at 288-290 eV are more discrete. After the 15s etch the -OH peaks weaken in intensity and

broaden. Of interest is that for the resorcinol derived PTFs the -OH groups are present at a lower binding energy, likely due to the fewer -OH groups and a reduced cumulative effect on the aromatic ring. In the core level N 1s spectra the nitrogen peaks at 398-401 eV fit with a 2,4,6-triphenyl-1,3,5-triazine structure and in the core level O 1s spectra the peaks at 531-534 eV fit with phenolic -OH; the peaks are shifted as a result of the different phenol monomer used. Of note is the large breadth of these O 1s and N 1s peaks, indicating that several different bonding environments may be occurring, possibly due to terminating groups or strain within the structure.

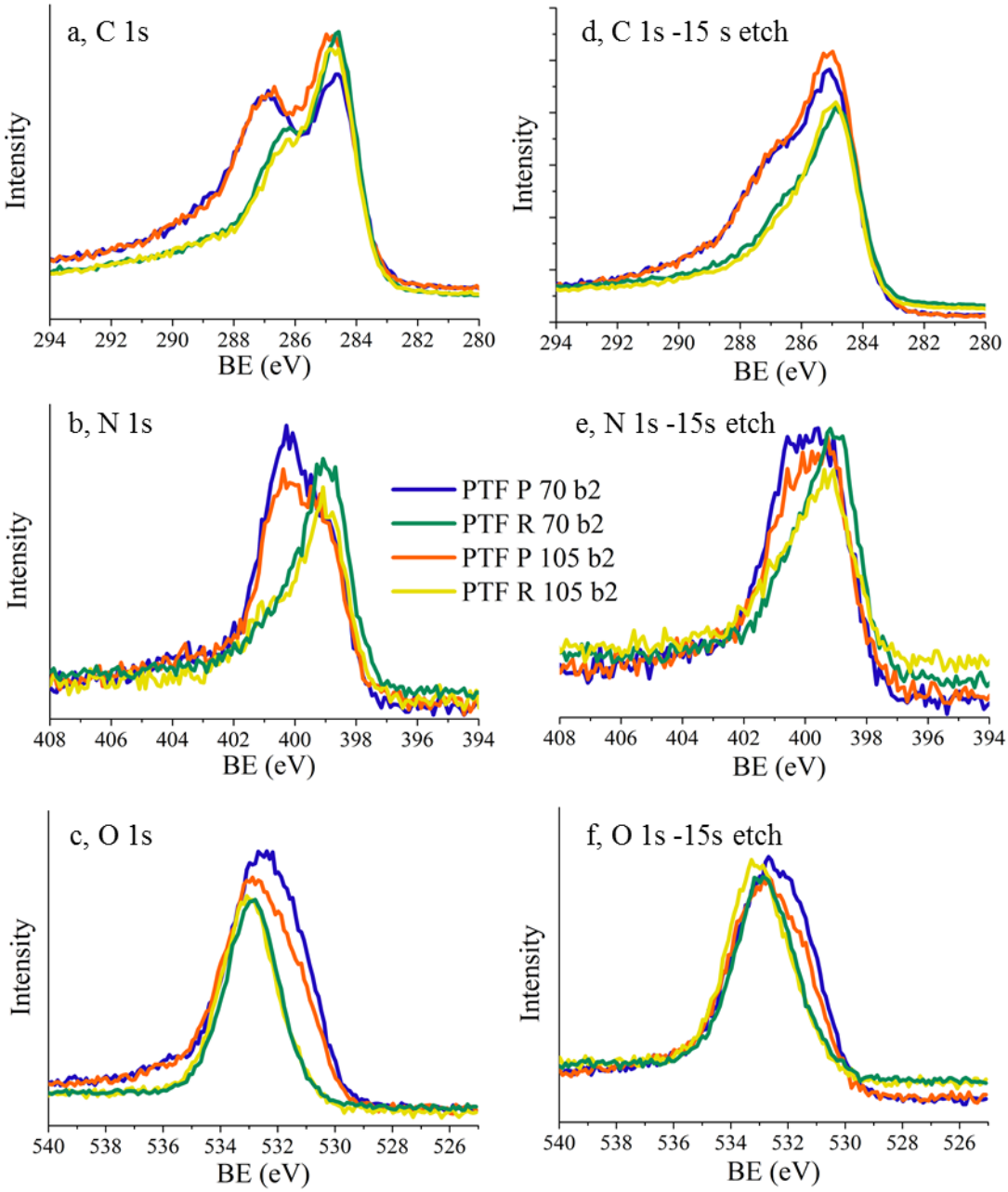

Figure 7.16. Core level XPS analysis for the PTF b2 samples showing the (a) C 1s, (b) N 1s and (c) O 1s spectra on the surface and (d) C 1s, (e) N 1s and (f) O 1s after a 15s depth probe etch.

The XRD analysis of the b2 PTFs also indicates a different structure for the materials derived from resorcinol and phloroglucinol. From Figure 7.17(a) the PTF P b2 samples show a broad peak centred at 26° 2θ with a shoulder centred at 21.5° 2θ and a smaller peak at 44° 2θ understood to be from the (0 0 2) and (1 0 0) diffractions of layered graphitic-type materials respectively. Low angle peaks at 3.5° 2θ indicate pore and void formation. In contrast for the b2 PTF R sample the (0 0 2) indexed peak is centred at 21.5° 2θ. The difference between the peaks at 26° and 21.5° 2θ may be considered a result of different stacking configurations, perhaps one from the amorphous polymer stacking and the other from a more ordered hexagonal arrangement. From the CHN analysis, which suggests the PTF P b2 is more likely in the hexagonal form, it may be construed that the peak at 26° 2θ relates to the hexagonal arrangement and 21.5° 2θ to a more amorphous aromatic stacking arrangement.

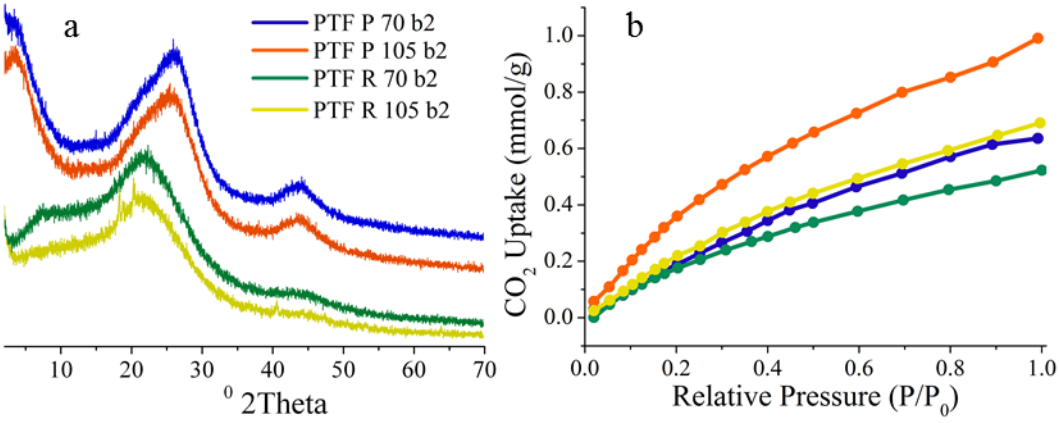

Figure 7.17. (a) XRD analysis and (b) CO_2 adsorption isotherms (0-1 bar) for the b2 PTFs.

Volumetric CO_2 analysis was carried out to determine the PTF b2 materials capability for CO_2 capture (Figure 7.17(b)). The PTF R 105 b2 has the greatest uptake capacity, 0.95 mmol/g at 298 K and 1 bar. Such uptake values are similar, if not slightly less than those found for the other PTF polymers synthesised, indicating that pore blocking by Al species is not hindering uptake.

The chemical structure of PTF P 75 b2 was also analysed using solid-state NMR (SSNMR) analysis (Figure 7.18). From the ^{13}C cross-polarization magic-angle spinning (CP/MAS) spectrum (Figure 7.18(a)) the NMR features observed in the ^{13}C NMR of tris(2,4,6-trihydroxyphenyl)-1,3,5-trizaine can be seen. Carbon atoms bound to polar groups (Figure 7.3(b)), carbons atoms a, c and e, are present in the chemical shift range 150-180 ppm and show several merged peaks. The convoluted nature of these peaks can be ascribed to residual dipolar coupling which gives rise to 2 peaks when one may be expected, also nitrogen is quadrupolar so 2 peaks cannot be expected for 2 types of environment. Furthermore with the apparent semi-

crystalline nature of the polymer structure from the XRD, different crystalline phases may also give rise to different environments.

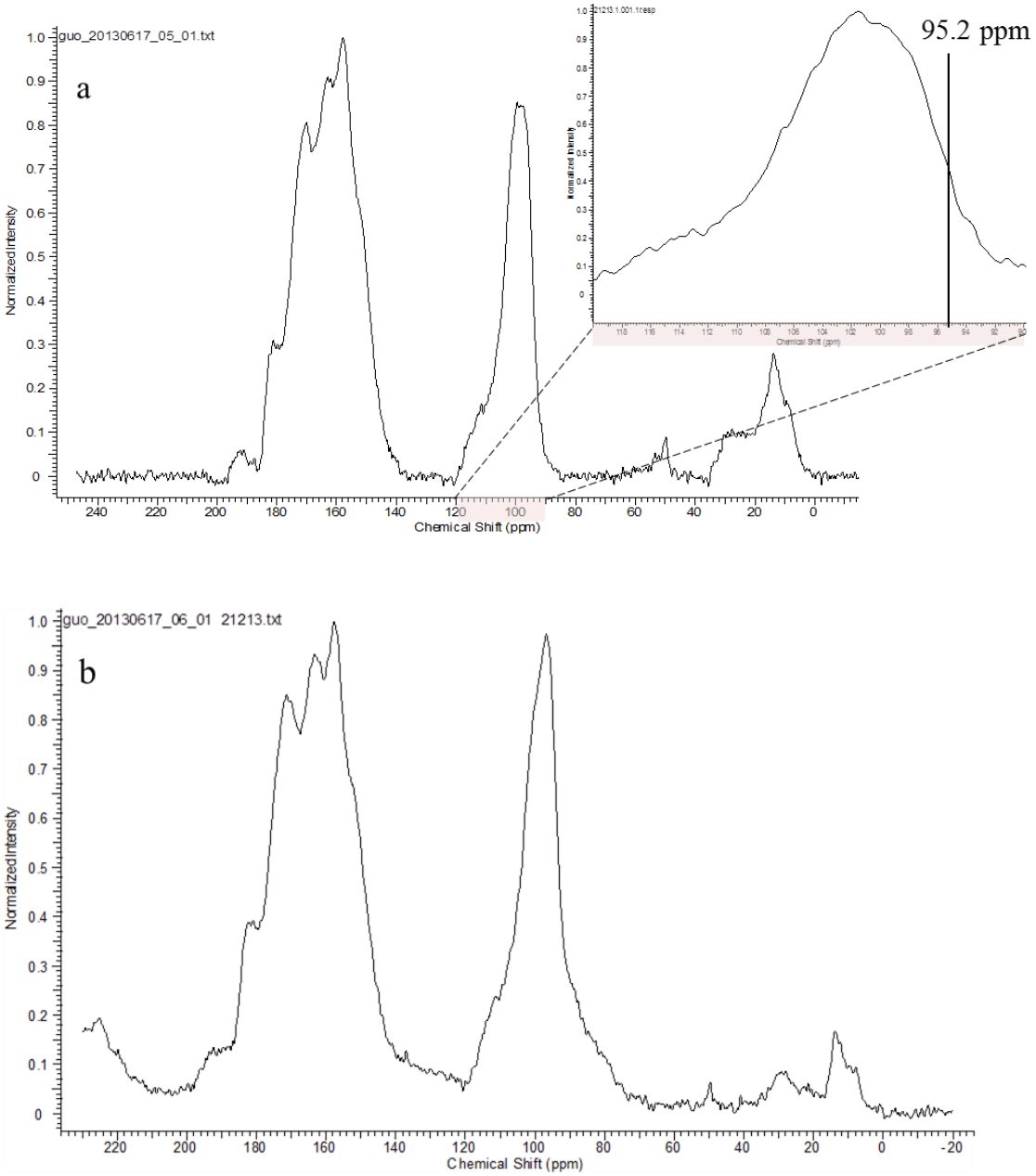

Figure 7.18. Solid-state NMR spectra for the phenolic triazine framework, PTF P 75 b2. (a) ^{13}C cross-polarization magic-angle spinning (CP/MAS) spectrum recorded at a MAS rate of 12 kHz and reported relative to tetramethylsilane, using total sideband suppression (TOSS), with inset highlighting chemical shift range 90-120 ppm. (b) Non-quaternary suppression (NQS) ^{13}C experiment recorded without using TOSS.

For the other carbon environments, carbons b and d in Figure 7.3(b) corresponding to the aryl-aryl carbon and the protonated aryl carbon respectively, a merged peak in the chemical shift range of 95-120 ppm can be observed. From the analysis of the tris(2,4,6-trihydroxyphenyl)-1,3,5-trizaine (Figure 7.4) it is understood that the protonated aryl carbon (carbon d) has a chemical shift of 95.2 ppm and the aryl-aryl carbon (carbon b) has a chemical shift of 98.5 ppm.

In Figure 7.18(a) the chemical shift range 90-120 ppm has been enlarged, showing that at 95.2 ppm little of the protonated aryl carbon environment remains, an indication that the phloroglucinol may reacting at the 2,4 and 6-positions and the theoretical chemical structure (Figure 7.5) is obtained. From the non-quaternary suppression (NQS) ^{13}C spectrum of the PTF P 75 b2 (Figure 7.18(b)), little change is observable in the 150-180 ppm chemical range, however a narrowing of the merged peaks in the chemical shift range 90-120 ppm suggests that some protonated aryl carbon environments may be retained.

To better understand the effect of the PTF polymer functional groups on the sorption of CO_2, volumetric CO_2 uptake analysis was carried out for the PTF P 105 b2 at 273, 298 and 323 K (Figure 7.19(a)). BET surface area analysis using N_2 isotherms at 77 K suggests that these structures have no apparent porosity. That CO_2 sorption is an ultramicropore directed physisorption process can be shown through calculation of the adsorbate-adsorbent binding enthalpy from the CO_2 isotherms at 273, 298 and 323 K. The Q_{st} at near zero loading was 24.12 kJ/mol, typical of a physisorption process, therefore indicating that the triazine and phenol functional groups are not enhancing the adsorbate-adsorbent interaction (Figure 7.19(b)). The CO_2/N_2 selectivity was calculated at 273, 298 and 323 K, using the IAST method giving CO_2/N_2 selectivity at 298 K and 273 K of 31.43 and 20.68 respectively.

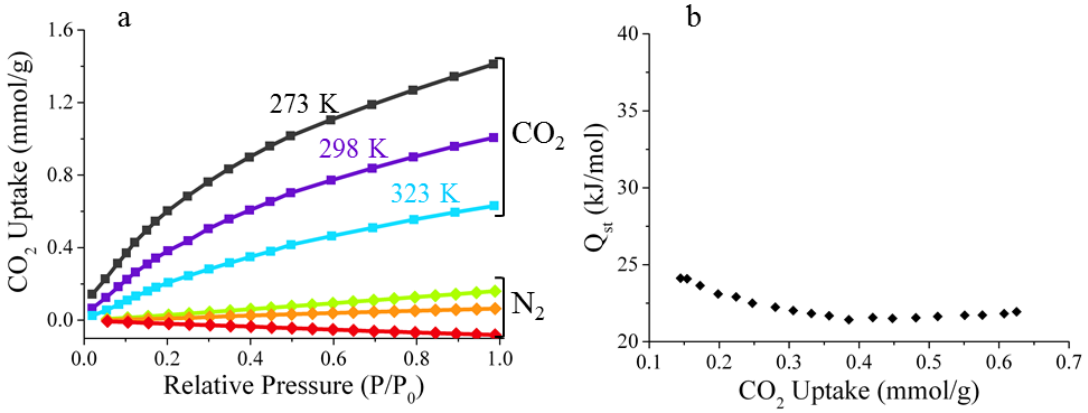

Figure 7.19. Gas sorption analysis for PTF P 105 b2, (a) CO_2 and N_2 adsorption isotherms up to 1 bar at 273, 298 and 323 K. (b) Isosteric heats of adsorption (Q_{st}) calculated from CO_2 adsorption isotherms up to 1 bar at 273, 298 and 323 K.

.

8. Comparison of Materials

In this chapter the materials so far synthesised and characterised will be compared to better understand the key factors that govern an adsorbent's success as CO_2 capture material.

Table 8.1. Summary of materials synthesised in this work detailing pore characteristics

Material	SSA_{BET} (m^2/g)	V_M (cm^3/g)	Volume in pores of size (cm^3/g)			CO_2 Uptake 298 K, 1 bar (mmol/g)
			1	1.5	2	
DCA:DBA 3:7	1.0	-	-	-	-	1.99
DCA:DBA 1:9	10.3	-	-	-	-	2.06
DBA 100 %	4.9	-	-	-	-	1.64
CB 700	450.8	0.161	0.146	0.115	0.150	2.19
CB 700 KOH	892.0	0.494	0.491	0.494	0.494	3.78
CB 900	403.2	0.124	0.048	0.049	0.057	2.31
CB 900 KOH	892.1	0.320	0.319	0.319	0.320	3.57
GLUCOSE 700	443.5	0.157	0.099	0.099	0.101	1.99
GLUCOSE 900	114.1	0.039	0.037	0.039	0.039	2.27
GLUCOSE 700 KOH	1643.5	0.601	0.591	0.601	0.601	4.37
GLUCOSE 900 KOH	1011.2	0.365	0.364	0.365	0.365	3.74
STP 700	468.9	0.131	0.103	0.128	0.133	1.50
STP 700 KOH	1289.7	0.439	0.421	0.434	0.439	3.75
STP 900	385.7	0.098	0.079	0.093	0.099	1.59
STP 900 KOH	864.4	0.287	0.268	0.282	0.287	2.30
CG 900 KOH	1526.6	0.550	0.496	0.553	0.554	4.49
CG 400 2-1	2073.2	0.731	0.619	0.731	0.731	4.21
CG 400 4-1	2785.5	0.716	0.440	0.669	0.716	2.81
CG 700 2-1	1624.7	0.585	0.528	0.589	0.589	4.66
CG 700 4-1	2620.9	0.793	0.528	0.781	0.793	4.00
MFR	327.1	0.015	-	0.015	0.015	0.99
MFRDC 600	142.8	0.026	0.024	0.026	0.023	1.35
MFRDC 700	48.2	0.012	0.011	0.012	0.012	1.58
MFRDC 700 C30	177.7	0.072	0.065	0.071	0.072	1.76
MFRDC 700 C60	388.4	0.117	0.102	0.116	0.117	1.79
PAN 700 KOH	1691.0	0.541	-	0.512	0.541	3.64
PAN 900 KOH	1311.2	0.465	0.441	0.464	0.465	3.59
PVP 700 KOH	1599.6	0.563	-	0.553	0.563	3.43
PVP 900 KOH	1052.4	0.377	0.342	0.376	0.377	3.22
MPNG	505.1	0.008	0.008	0.080	0.008	1.21
PTF P 700	321.5	0.154	0.146	0.149	0.149	2.14
PTF R 700	68.6	0.039	0.039	0.039	0.039	2.14
PTF P 800	158.2	0.083	0.078	0.078	0.078	2.13
PTF R 800	26.4	0.014	0.008	0.008	0.009	2.28
PTF R 105 b2	-	-	-	-	-	0.95

In the introduction the influence of porosity and N-dopants were highlighted as of pertinent interest in the improvement of carbon-based CO_2 sorbents. Synthetic methods enabling the controlled synthesis of microporous structures are therefore of interest, with CO_2 sorption at 1

bar and 298 K being understood to be a micropore dominated process [Presser *et al*. (2011)]. Indeed, to help further technological understanding within the field of porous carbon materials this thesis has investigated various methods of developing microporosity through the use of: aerogels, rigid polymeric linkages, exfoliation of graphene sheets to create crumples and folds, and the use of chemical and physical activation on carbonaceous materials and carbon nitride.

Table 8.2. Summary of materials synthesised in this work detailing N-dopants and CO_2 uptake characteristics

Material	CO_2 Uptake 298 K, 1 bar (mmol/g)	CO_2/N_2	Q_{st} (kJ/mol)	N (at.%)
DCA:DBA 3:7	1.99	-	-	16.0
DCA:DBA 1:9	2.06	18.86	34.7	10.0
DBA 100 %	1.64	21.49	33.4	10.5
CB 700	2.19	26.20	-	-
CB 700 KOH	3.78	15.28	-	-
CB 900	2.31	17.56	-	-
CB 900 KOH	3.57	16.19	-	-
GLUCOSE 700	1.99	23.99	-	-
GLUCOSE 900	2.27	21.93	-	-
GLUCOSE 700 KOH	4.37	15.34	-	-
GLUCOSE 900 KOH	3.74	16.53	-	-
STP 700	1.50	18.76	-	-
STP 700 KOH	3.75	19.96	-	-
STP 900	1.59	9.73	-	-
STP 900 KOH	2.30	16.29	-	-
CG 900 KOH	4.49	16.05	-	-
CG 400 2-1	4.21	-	26.3	-
CG 400 4-1	2.81	-	25.8	-
CG 700 2-1	4.66	13.61	25.7	-
CG 700 4-1	4.00	-	22.7	-
MFR	0.99	-	28.7	44.9
MFRDC 600	1.35	-	48.4	28.9
MFRDC 700	1.58	-	49.8	30.1
MFRDC 700 C30	1.76	14.46	47.3	10.5
MFRDC 700 C60	1.79	23.00	51.0	23.1
PAN 700 KOH	3.64	14.55	26.4	15.1
PAN 900 KOH	3.59	17.33	27.9	1.6
PVP 700 KOH	3.43	14.11	26.0	0.8
PVP 900 KOH	3.22	15.18	29.5	1.8
MPNG	1.21	-	23.5	24.7
PTF P 700	2.14	18.91	30.2	5.2
PTF R 700	2.14	23.20	32.7	4.4
PTF P 800	2.13	23.74	31.0	5.4
PTF R 800	2.28	21.68	28.9	3.8
PTF R 105 b2	0.95	31.43	24.12	10.9

8.1 The Influence of Pore Size

The influence of micropore volume and surface area for the materials synthesised (Table 8.1) can be seen in Figure 8.1. CO_2 uptake capacity at 298 K and 1 bar can be seen to increase with both BET surface area and micropore volume. Adsorption at 1 bar is believed to be a micropore dominated process and this is supported by the Pearson's R value for surface area of 0.781 increasing to 0.886 for micropore volume when the two are plotted against CO_2 capacity. The deviation from 0.99 for the Pearson's R value for micropore volume vs. CO_2 uptake (Figure 8.1(b)) can be explained by studies stating that micropores of <0.8 nm are particularly critical for sorption at 298 K and 1 bar. Furthermore, micropore volume is calculated from N_2 isotherms at 77 K and at these temperature conditions the nitrogen probe molecules are too large to access such pores, reducing the apparent micropore volume for ultramicroporous materials. Conversely, in broader supermicropores (>0.7 nm), a number of the N_2 molecules fill the centre of the pores and do not touch the surface, leading to an overestimate of the surface area.

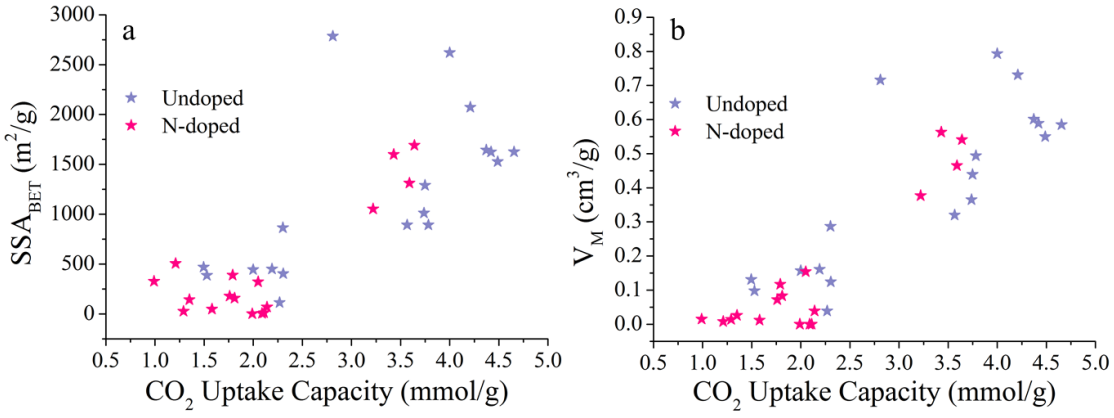

Figure 8.1 Graphs showing BET surface area (a) and micropore volume (V_M) (b) vs. CO_2 uptake capacities at 298 K and 1 bar for the materials in Table 8.1 and 8.2, highlighting the N-doped materials. Pearson's R values are 0.78062 and 0.88598 for (a) and (b) respectively.

By using QSDFT pore size analysis to calculate the pore volume in pores of width ≤1.5 nm (Figure 8.2(a)) and ≤1.0 nm (Figure 8.2(b)) for the materials synthesised in this work (Table 8.1), further support is given to the critical role that small micropores play in CO_2 adsorption at 1 bar and 298 K. The Pearson's R value for the correlation between pore volume and CO_2 capacity increases to 0.895 when capacity is fitted against pore volume within pores of width ≤1.5 nm, relative to 0.886 for overall micropore volume. The R values increases again when fitting capacity against pore volume within pores of width ≤1.0 nm to 0.943, the highest positive correlation. Due to the size of the nitrogen probe molecule the pore volumes in smaller pores were not calculated.

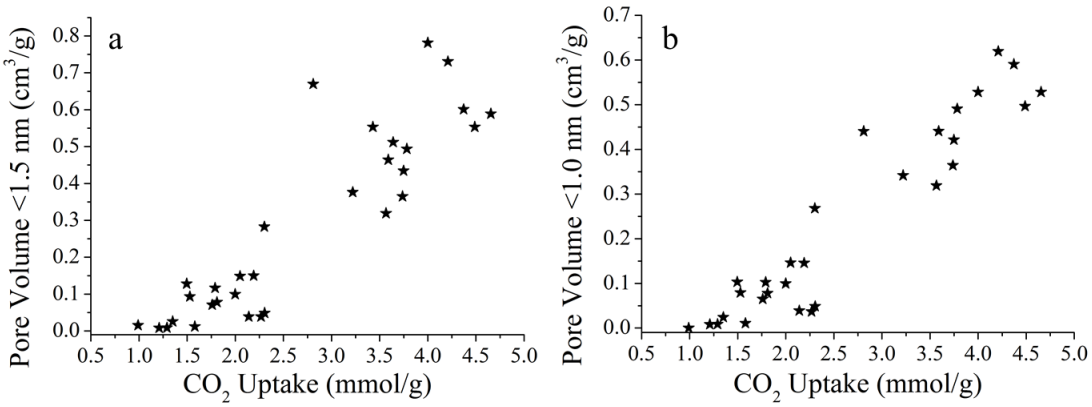

Figure 8.2. CO_2 uptake values at 298 K and 1 bar for the materials in Table 8.1 vs. pore volume in pores smaller than (a) 1.5 nm and (b) 1.0 nm. The Pearson's R values are 0.89491 and 0.94307 for (a) and (b) respectively.

In turn, the controlled synthesis of N-dopants within carbon structures is also of interest with correlations between N-dopants and increases in CO_2 capacity, CO_2/N_2 selectivity, and adsorbate-adsorbent interaction energy being cited in recent studies [Wang *et al*. (2012b), Zhong *et al*. (2012), Rabbani *et al.* (2012)]. However, from the discussions in the introduction, these correlations are not yet fully understood. From Figure 8.1(a) and (b) the N-doped materials are highlighted, with no observable correlation between presence of N-dopants and a straightforward increase in CO_2 capacity. To determine if the quantity of nitrogen plays a key role, Figure 8.3 shows a colour map of micropore volume vs. CO_2 uptake for the materials synthesised in this work (Table 8.1 and 8.2) and from literature (Table 1.1 and 1.2), with nitrogen rich materials in dark blue to purple. Again here no correlation between nitrogen content and an increase in CO_2 uptake can be observed.

8.2 The Influence of N-doping

While it appears that the CO_2 capacity of porous carbon materials at 298 K and 1 bar is very much a micropore dominated process, it is expected that N-doping may be used to increase CO_2/N_2 selectivity and adsorbate-adsorbent interaction [Rabbani *et al.* (2012), Zhao *et al.* (2012b)]. For the tuning of potential sorbents a mechanistic understanding of the adsorbent-adsorbate interaction within doped carbon based sorbents is therefore vital, however this mechanism is still unclear. Nitrogen groups such as pyridine are proposed to act as Lewis-base active sites that attract the Lewis-acidic CO_2 molecules [Vogiatzis *et al.* (2009)]. Alternatively, hydrogen bonding interactions may also be important. Nitrogen atoms in the carbon lattice have been proposed to alter the electronic structure of graphitic layers and edge hydrogen atoms, which may in turn influence the interactions between the carbon surface and CO_2 molecules

[Xing *et al.* (2012)]. To better understand this interaction, materials containing a variety of nitrogen functionality within different carbon matrices: organic polymers, graphene and defective carbon have been synthesised and characterised as discussed so far in this work.

By plotting the isosteric heats of adsorption (Q_{st}) against nitrogen content, for materials from literature and this work (Figure 8.4(a) and (b)), it can be observed that no materials without N-dopant achieve Q_{sr} values >30 kJ/mol. Therefore suggesting that the elevated binding enthalpies (>30 kJ/mol) reported in literature and discussed in this work, result from action of the N-dopants. It may also be noted that nitrogen content does not always correlate to elevated Q_{st} values.

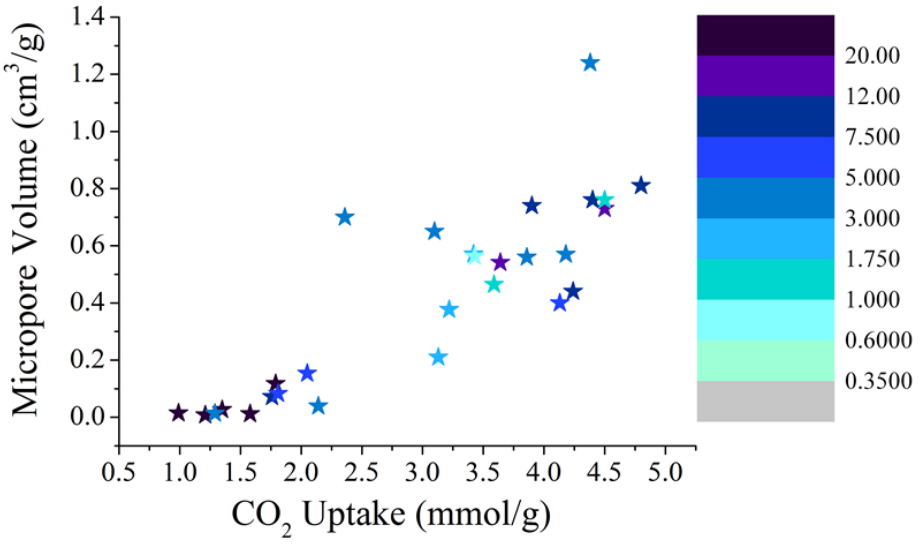

Figure 8.3. Colour mapped scatter graph of micropore volume vs. CO_2 uptake at 298 K and 1 bar. Highlighting the influence of nitrogen content (calculated form XPS elemental analysis at sample surface in at.%) for the N-doped as synthesised materials (Table 8.1 and 8.2) and from literature (Table 1.1 and 1.2).

From the postulated mechanisms of adsorbate-adsorbent interaction the Lewis basicity of N-dopants is of clear interest and within the N-doped carbon materials obtained through carbonisation/activation it is the pyridine groups that are the strongest Lewis bases. The Q_{st} values for materials from literature and this work are therefore plotted against nitrogen content, highlighting those that contain pyridinic content (Figure 8.4(b)). It can be seen that many pyridine containing materials, even some with nitrogen content of > 20 wt%, do not display elevated binding enthalpies and this is true for materials from our work and from literature. As the analysis of nitrogen content throughout this work is carried out using XPS and this is mirrored in the literature, the pyridine content can be expected to exist on the surface of the materials. Being on the surface, it should be in a suitable position to act as an active site for Lewis acid-base interactions with the Lewis acidic CO_2 molecules, so consistently elevated binding enthalpies in the presence of pyridine may be expected. However, as this is not always

the case, it may be deduced that other properties of the carbon matrix are paramount to the elevation in binding enthalpies.

For this deduction it was assumed that "binding enthalpies (>30 kJ/mol) reported in literature and discussed in this work, result from action of the N-dopants". To further support this assumption the influence of oxygen functional groups must also be considered, potentially playing an active cooperative role, enhancing the nitrogen groups. From the XPS analysis throughout the thesis (Figure 4.4(c), 4.9(b), 5.8(b), 6.5 and 7.11(b) and (e)) the core level O 1s peaks for the N-doped carbon materials are broad at 530-534 eV and there is no observable difference between the samples that exhibit elevated binding enthalpies and those that do not. Figure 8.5(a) shows a scatter graph of oxygen content against Q_{st} for the materials in Table 8.1 and 8.2 (this work) and shows no correlation. No correlation is also observable in Figure 8.5(b) where the N/O ratio is plotted against Q_{st}.

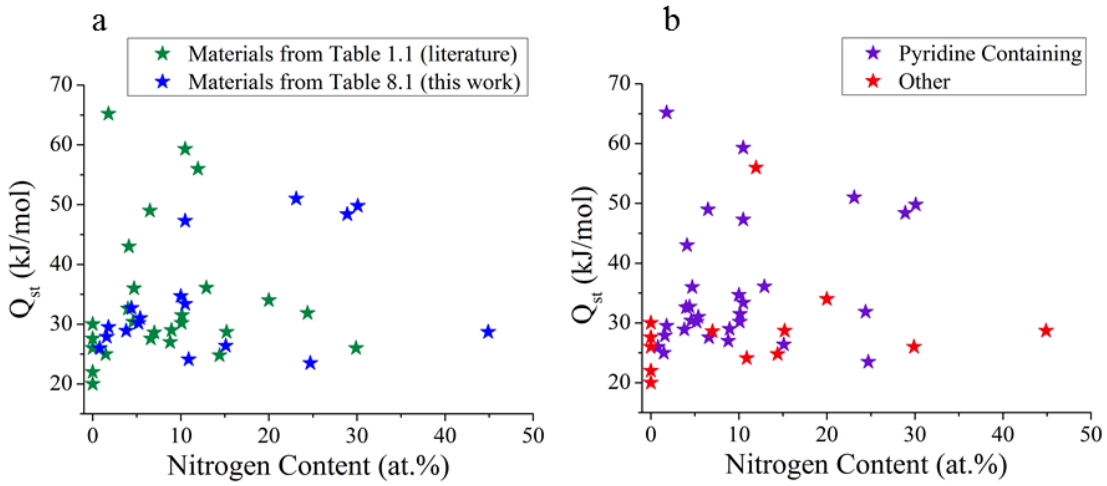

Figure 8.4. Isosteric heats of adsorption plotted vs. nitrogen content (calculated from XPS elemental analysis at sample surface) for materials from literature and this work (a), highlighting materials containing pyridinic-type nitrogen functionality (b).

The increase in binding enthalpy between CO_2 and N-doped adsorbents is therefore likely due to the postulated mechanism whereby nitrogen atoms in the carbon lattice alter the electronic structure of graphitic layers and edge hydrogen atoms, which may in turn influence the interactions between the carbon surface and CO_2 molecules. Using this information it is possible to explain the variation in binding enthalpies for the materials in this work.

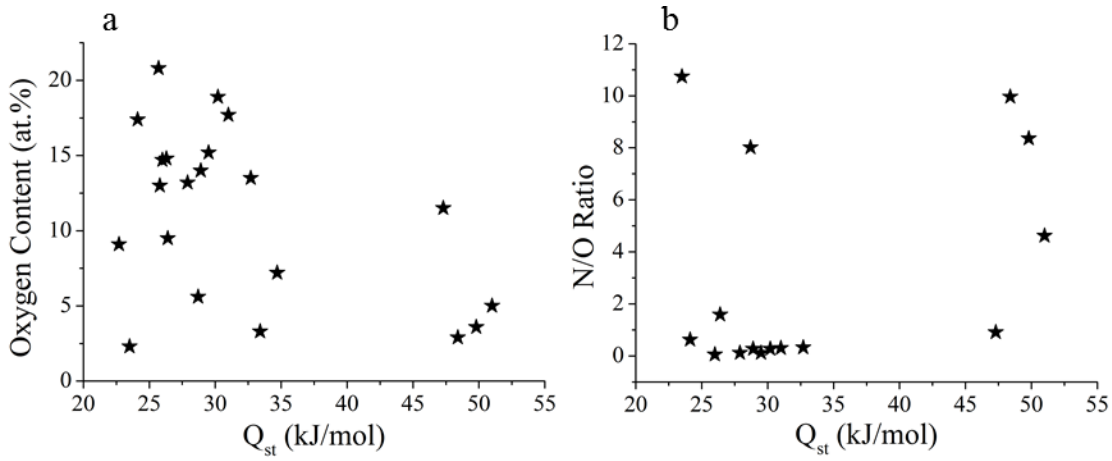

Figure 8.5. The influence of oxygen groups on the isosteric heat of adsorption for the samples prepared in this work (Table 8.1 and 8.2). Showing oxygen content vs. isosteric heat of adsorption (a) and the nitrogen/oxygen ratio vs. isosteric heat of adsorption (Q_{st}) (b).

For the MFRDCs the Q_{st} values are among the highest reported so far for N-doped carbon [Zhong *et al.* (2012), Zhao *et al.* (2012b), Wang *et al.* (2013)], between 47.3-51.0 kJ/mol for the 4 samples. These materials are nitrogen-rich, possessing between 10.5-30.1 atomic % nitrogen, with a disordered structure resulting from the decomposition of a triazine based amorphous polymer into a pyridine and quaternary N-doped amorphous carbon. Such a material will then have many defect and edge hydrogen atoms that when polarised by the N-dopants within the carbon matrix may attract CO_2 molecules. Conversely, the PVP and PAN activated carbons, although also N-doped carbon derived from amorphous polymers, do not have elevated Q_{st} values. It is worth noting that they are not as nitrogen-rich, but as discussed this is not of apparent import (Figure 8.4). From the core level XPS N 1s analysis (Figure 4.4(c)) the peaks are all cenertered around 400.2 eV for the PAN and PCP activated carbons, indicating the N-dopants are in a quaternary form, not pyridinic. It can therefore be argued that pyridine N-dopants are required for suitable polarisation of the edge hydrogen atoms, likely due to the available lone pair that is not part of the pyridine aromatic π-system. Indeed the low Q_{st} values for the MFR and the PTF R 105 b2 can be attributed to the triazine nitrogen form lacking suitable Lewis basicity. In turn, following carbonisation the PTF derived carbons show increased binding enthalpies, relative to the PTF polymer, likely due to the conversion of the triazine rings into pyridinic and quaternary forms. While slightly elevated (at most 32.7 kJ/mol) the Q_{st} values for the PTF derived carbons are likely curbed by the ordered structure evident from the XRD patterns (Figure 7.12) and resulting lack of hydrogen and defective edge sites. This may also be why the pyridinic nitrogen-rich MPNG does not show an elevated Q_{st}, with hydrogen and defective edge sites being sparse in the planar graphene structure. The amorphous carbons DBA 100 % and DCA:DBA 1:9 both contain pyridine groups and show corresponding elevated Q_{st} values of 33.4 and 34.7 respectively.

9. Conclusions and Future Work

9.1 Conclusions

The materials studied in this work utilise factors instrumental in the synthesis of successful porous carbon based solids for CO_2 separation. A combination of new, expanded and existing solid carbon-based CO_2 capture materials have been designed, synthesised and characterised to better understand their mechanism of operation. From the results and analysis the following conclusions are obtained:

Research and analyse existing methods utilised and factors instrumental in the synthesis of successful porous carbon based solids for CO_2 separation

- A range of interesting activated carbons were synthesized using KOH activation regimes. These were synthesized using different precursors to generate N-doped and undoped materials. Of these precursors the dense lignocellulosic coffee grounds yielded the best performing CO_2 sorbent with CO_2 uptake at 323 K and 1 bar of 2.8 mmol/g. Such performance is in line with the practical requirements for a solid sorbent to be competitive with current liquid amine technology in post-combustion flue gas conditions.

- The use of KOH activation on a range of precursors was used to produce highly microporous materials capable of CO_2 uptake capacities >4 mmol/g at 1 bar and 298 K, making them among the best performing CO_2 sorbents so far reported. Pore size can be tailored using controlled activation regimes, with an increase in KOH concentration leading to a greater pore etching and therefore wider pores. Due to greater pore-filling as gas pressure increases the resultant activated carbons can be tailored to maximize CO_2 capacity over a range of pressures.

- It was shown that hierarchical carbon with good CO_2 uptake capacity can be synthesized from phenol-formaldehyde polymers using soft template methods. The hierarchical porous structure is retained following controlled KOH activation which acts to exclusively enhance pores in the micropore region.

- Novel phenolic triazine framework microporous organic polymers were synthesized using Friedel-Crafts aryl-aryl coupling chemistry between simple aromatic molecules to generate a nitrogen-rich exclusively microporous material. The polymer was thermally stable over 300 °C, with changes in reactant concentration and reaction temperature

having little understood effect on the CO_2 uptake. The ultramicroporous structure lead to an apparent elevated CO_2/N_2 selectivity compared to other polymer and carbon-based materials synthesized in this work.

- From the synthesis of a range of microporous and N-doped materials consisting of a range of nitrogen functionality: pyridine, triazine, quaternary and pyrrole groups within different porous carbon matrices: graphene, adventitious carbon, amorphous defective carbon and aromatic layered arrays, the role of the N-dopants in the materials synthesised has been studied, primarily focussing on materials enthalpy of adsorption and CO_2/N_2 selectivity. Having identified that a Q_{st} of 40 kJ/mol is suitable for the industrial capture of CO_2 by solid sorbents, pyridine N-doping within porous solids was utilised to achieve Q_{st} values ranging 25-50 kJ/mol. The controlled carbonisation of selected amine-rich precursors yielded porous carbons with an optimised Q_{st} of 35 kJ/mol. Cumulative evidence in this thesis stresses the importance of pyridine functional groups and their proximity with edge hydrogen atoms and defects for the control of Q_{st}. The inability of undoped porous carbon materials to achieve Q_{st} values of >29 kJ/mol is emphasised.

- The CO_2/N_2 selectivity of the porous materials synthesised has also been well characterised at 298 K, using the ideal adsorbed solution theory, with N-doping of the type used here: pyridinic, triazine, quaternary and pyrrolic showing little effect on the CO_2/N_2 selectivity. Rather, pore size effects appear important for the tuning of selectivity, with the ultramicroporous PTF polymer showing the highest selectivity. This is likely due to the smaller molecular kinetic diameter of N_2 than CO_2.

- CO_2 storage in an N-doped exfoliated graphene was reported, likely possible through physisorption within pores created by conjugation and folds of the graphene sheets.

- The synthesis of a microporous polymer has been achieved through aerogel formation from a simple melamine-formaldehyde resin through freeze-drying, without the need for rigid binding between linker molecules or bulky constituents.

- Triazine-rich carbon precursors were shown to be highly suitable for the synthesis of pyridine-doped porous carbon materials with high nitrogen content. This was shown possible due to the high thermal stability of the triazine group, with decomposition into pyridine forms occurring between 600-700 °C. From the carbonisation of the highly stable phenolic triazine framework, controlled decomposition of the triazine forms resulted in the synthesis of exclusively microporous N-doped carbon.

- We have demonstrated that g-C_3N_4 is soluble in water, although sparingly. The possible intercalation of metallic species such as potassium within the g-C_3N_4 structure has also been discussed.

9.2 Future Work

This thesis has largely considered the properties of porous carbons as obtained from carbonisation and through activation. From this is has been observed that the high thermal stability of triazine makes it highly suitable for use as a carbon precursor. Future work developing N-doped porous carbon materials should therefore use triazine-rich materials as carbon precursors.

The ultramicroporous phenolic triazine frameworks have so far been prepared by combination of two simple aromatic molecules, cyanuric chloride and a phenol: either phloroglucinol or resorcinol. Use of a wider variety of rigid monomeric precursors, e.g. 2,6-naphthalenediol as phenolic equivalent, may lead to materials with increased pore diameter. Use of a wide array of precursors could ultimately lead to a range of PTFs with excellent control of pore widths.

The low angle scatter in the XRD patterns of the PTF structures likely contains detailed structural information that may be interpreted using higher resolution X-ray diffraction beamlines, such as those available at the Diamond Light Source.

Of the materials synthesised the activated carbon derived from spent coffee grounds appears to show the greatest potential as an industrial CO_2 sorbent. The further investigation of this material is therefore of great interest. Useful further assays may be the use of more realistic flue gasses, i.e. gas streams that contain N_2, H_2O and particulates. Cyclic testing to determine sorbent and capacity life time are also greatly interesting, as too are fluidised bed experiments to determine suitability.

Adsorption capacity at 1 bar is a very useful measure of an adsorbents performance. However, some post combustions systems may operate using pressure swings at elevated pressure. To therefore determine the practicality of all the adsorbents synthesised in this thesis, isotherms recorded in the pressure range of 0-10 bar may be used to identify an adsorbent that can achieve an uptake capacity of 3 mmol/g at 323 K within the lowest pressure range.

The layered structure of the PTF materials is of course interesting, as too is that this layered form appears to be retained after carbonisation, as determine from XRD analysis. Such layered carbons forms may hold great promise for intercalation of various metallic species and ions. For

example of pertinent interest may be the synthesis of Li intercalated materials for electrode devices.

References

Aaron D and Tsouris C (2005) Seperation of CO_2 from Flue Gas: A Review. *Separation Science and Technology*; **40**, 321-348 (2005)

Adams L B, Hall C H, Holmes R J and Newton R A (1988) An Examination of How Exposure to Humid Air Can Result in Changes in the Adsorption Properties of Activated Carbons. *Carbon*; **26**, 451-459 (1988)

Ahmadpour A and Do D D (1996) The Preparation of Active carbons from Coal by Chemical and Physical Activation. *Carbon*; **34**, 471-479 (1996)

An H, Feng B and Su S (2009) CO_2 Capture Capacities of Activated Carbon Fibre-Phenolic Resin Composites. *Carbon*; **47**, 2396-2405 (2009)

An J and Rosi N (2010) Tuning MOF CO_2 Adsorption Properties via Cation Exchange. *Journal of the American Chemical Society*; **132**, 5578-5579 (2010)

Arenillas A, Smith K M, Drage T C and Snape C E (2005) CO_2 Capture Using Some Fly Ash-Derived Carbon Materials. *Fuel*; 84, 2204-2210 (2005)

Aroonwilas A and Veawab A (2004) Characterisation and Comparison of the CO_2 Absorption Performance into Single and Blended Alkanolamines in a Packed Column. *Industrial & Engineering Chemistry Research*; **43**, 2228-2237 (2004)

Arstad B, Fjellvåg H, Kongshaug K, Swang O and Blom R (2008) Amine Functionalised Metal Organic Frameworks (MOFs) as Adsorbents for Carbon Dioxide. *Adsorption*; **14**, 755-762 (2008)

Baker R W (2002) Future Directions of Membrane Gas Seperation Technology. *Industrial & Engineering Chemistry Research*; **41**, 1393-1411 (2002)

Bauer D R and Dickie R A (1980) Crosslinking Chemistry and Network Structure in Organic Coatings. Cure of Melamine Formaldehyde/Acrylic Copolymer Films. *Journal of Polymer Science: Polymer Physics Edition*; **18**, 1997-2014 (1980)

Ben T, Ren H, Ma S, Cao D, Lan J, Jing X, Wang W, Xu J, Deng F, Simmons J M, Qiu S and Zhu G (2009) Targeted Synthesis of a Porous Aromatic Framework with High Stability and Exceptionally High Surface Area. *Angewandte Chemie International Edition*; **48**, 9457-9460 (2009)

Barton Cole E, Lakkaraju P S, Rampulla D M, Morris A J, Abelev E and Bocarsly A B (2010) Using a One-Electron Shuttle for the Multielectron Reduction of CO_2 to Methanol; Kinetic, Mechanistic and Structural Insights. *Journal of the American Chemical Society*; **132**, 11539-11551 (2010)

Barroso-Bujans F, Cerveny S, Alegría A and Colmenero J (2010) Sorption and Desorption Behaviour of Water and Organic Solvents from Graphite Oxide. *Carbon*; **48**, 3277-3286 (2010)

Berger C, Song Z, Li T, Li X, Ogbazghi A, Feng R, Dai Z, Marchenkov A, Conrad E and Phillip N (2004) Ultrathin Epitaxial Graphite: 2D Electron Gas Properties and a Route toward Graphene-based Nanoelectronics. *Journal of Physical Chemistry B*; **108**, 19912–19916 (2004)

Bertsch L and Habgood H W (1963) An Infrared Sprectoscopic Study of the Adsorption of Water and Carbon Dioxide by Linde Molecular Sieve X1. *The Journal of Physical Chemistry*; **67**, 1621-1628 (1963)

Bojdys M, Muller J, Antonietti M, Thomas A (2008) Ionothermal Synthesis of Crystalline, Condensed, Graphitic Carbon Nitride. *Chemistry – A European Journal*; **14**. 8177-8182 (2008)

Bojdys M, Severin N, Rabe J, Cooper Thomas A, Antonietti (2013) Exfoliation of Crystalline 2D Carbon Nitride: Thin Sheets, Scrolls and Bundles via Mechanical and Chemical Routes. *Macromolecular Rapid Communications*; **34**, 850-854 (2013)

Boukhvalov D, Katsnelson M (2008) Chemical Functionalization of Graphene with Defects. *Nano Letters*; **8**, 4373-4379 (2008)

Bourrelly S, Llewellyn P L, Serre C, Millange F, Loiseau T and Férey G (2005) Different Adsorption Behaviours of Methane and Carbon Dioxide in the Isotypic Nanoporous Metal Terephthalates MIL-53 and MIL-47. *Journal of the American Chemical Society*; **127**, 13519-13521 (2005)

Bradbury A, Sakai Y and Shafizadeh F (1979) A Kinetic Model for Pyrolysis of Cellulose. *Journal of Applied Polymer Science*; **23**, 3271-3280 (1979)

Brunauer S, Emmett P, Teller E (1938) Adsorption of Gases in Multimolecular Layers. *Journal of the American Chemical Society*; **60**, 309-319 (1938)

Budd P, McKeown N and Fritsch D (2005) Free Volume and Intrinsic Microporosity in Polymers. *Journal of Materials Chemistry*; **15**, 1977-1986 (2005)

Burchell T D and Judkins R R (1996) Passive CO_2 Removal Using a Carbon Fiber Composite Molecular Sieve. *Energy Conversion and Management*; **37**, 947-954 (1996)

Burress J W, Gadipelli S, Ford J, Simmons J, Zhou W and Yildirim T (2010) Graphene Oxide Framework Materials: Theoretical Predictions and Experimental Results. *Angewandte Chemie*; **49**, 8902-8904 (2010)

Cabassud C and Wirth D (2003) Membrane Distillation for Water Desalintation: How to Choose an Appropriate Membrane? *Desalination*; **157**, 307-314 (2003)

Caplow M (1968) Kinetics of Carbamate Formulation and Breakdown. *Journal of the American Chemical Society*; **90**, 6795-6803 (1968)

Cazorla C, Shevlin S A and Guo Z X (2010) First-Principle Study of the Stability of Calcium-Decorated Carbon Nanostructures. *Physical Review B*; **82**, 155454 (2010)

Chapel D G, Ernst J and Mariz C L (1999) *Recovery of CO_2 from Flue Gases: Commercial Trends*. US Department of Energy, Washington, United States of America (2001) pp. 17

Choi S, Drese J H and Jones C W (2009) Adsorbent Materials for Carbon Capture from Large Anthropogenic Point Sources. *ChemSusChem*; **2**, 796-854 (2009)

Choi Y J, Choi J H, Choi K M and Kang J K (2011) Covalent Organic Frameworks for Extremely High Reversible CO_2 Uptake Capacity: A Theoretical Approach. *Journal of Materials Chemistry*; **21**.1073-1078 (2011)

Chue K T, Kim J N, Yoo Y J, Cho S H and Yang R T (1995) Comparison of Activated Carbon and Zeolite 13X for CO_2 Recovery from Flue Gas by Pressure Swing Adsorption. *Industrial & Engineering Chemistry Research*; **34**, 591-598 (1995)

Cohen M (1985) Calculation of Bulk Moduli of Diamond and Zinc-blende Solids. *Physical Review B*; **32**, 7988-7991 (1985)

Conn G and Eisler S (2011) Synthesis and Interamolecular Hydrogen Bonding Networks of 2,4,6-Tri(o-hydroxyaryl)-1,3,5-Traiazines. *Organic Letters*; **13**, 5080-5083 (2011)

Cooper A I (2011) Nanoporous Organics Enter the Cage Age. *Angewandte Chemie International Edition*; **50**, 996-998 (2011)

Côté A P, El-Kaderi H M, Furukawa H, Hunt J R and Yaghi O M (2007) Reticular Synthesis of Microporous and Mesoporous 2D Covalent Organic Frameworks. *Journal of the American Chemical Society*; **129**, 12914-12915 (2007)

Coullerez G, Leonard D, Lundmark S and Mathieu H (2000) XPS and ToF-SIMS Study of Freeze-dried and Thermally Cured Melamine-formaldehyde Resins of Different Molar Ratios. *Surface and Interface Analysis*; **29**, 431-443 (2000)

D'Alessandro D M, Smit B, and Long J R (2009) Carbon Dioxide Capture: Prospects for New Materials. *Angewandte Chemie*; **49**, 6058-6082 (2010)

Davidson R M (2009) *Post-Combustion Carbon Capture: Solid Sorbents and Membrane.* IEA Clean Coal Centre, London United Kingdom (2009)

Davis S J, Caldeira K and Matthews H D (2010) Future CO_2 Emissions and Climate Change from Existing Energy Infrastructure. *Science*; **329**, 1330-1333 (2010)

Dawson R, Stockel E, Holst J, Adams D and Cooper A (2011) Microporous Organic Polymers for Carbon Dioxide Capture. *Energy and Environmental Science*; **4**, 4239-4245 (2011)

Dawson R, Cooper A and Adams D (2012a) Nanoporous Organic Polymer Networks. *Progress in Polymer Science*; **37**, 530–563 (2012)

Dawson R, Ratvijitvech T, Corker M, Laybourn A, Khimyak Y Z, Cooper A I and Adams D J (2012b) Microporous Copolymer for Increased Gas Selectivity. *Polymer Chemistry*; **3**, 2034-2038 (2012)

Demessence A, D'Alessandro D M, Foo M L and Long J R (2009) Strong CO_2 Binding in a Water-Stable, Triazolate-Bridged Metal-Organic Framework Functionalised with Ethylenediamine. *Journal of the American Chemical Society*; **131**, 8784-8786 (2009)

Díaz-Terán J, Nevskaia D M, Fierro J L G, López-Peinado A J, Jerez A (2003) Study of Chemical Activation Process of a Lignocellulosic Material with KOH by XPS and XRD. *Microporous and Mesoporous Materials*; **60**, 173-181 (2003)

Dierker G, Ugolotti J, Kehr G, Fröhlich R and Erker G (2009) Reaction of Bis(alkynyl)silanes with Tris(pentafluorophenyl)borane: Synthesis of Bulky Silole Derivatives by Means of 1,1-Carboboration under Mild Reaction Conditions. *Advanced Synthesis & Catalysis*; **351**, 1080-1088 (2009)

Diringer E (2011) Climate Policy: Letting go of Kyoto. *Nature*; **479**, 291-292 (2011)

Doll G, Speck J, Dresselhaus G, Dresselhaus M, Nakamura K, and Tanuma S (1989) Intercalation of Hexagonal Boron Nitride with Potassium. *Journal of Applied Physics*; **66**, 2554-2558 (1989)

Du N, Robertson G, Song J, Pinnau I and Guiver M (2009) High-Performance Carboxylated Polymers of Intrinsic Microporosity (PIMs) with Tunable Gas Transport Properties. *Macromolecules*; **42**, 6038–6043 (2009)

Drage T, Snape C, Stevens L, Wood J, Wang J, Cooper A, Dawson R, Guo X, Satterley C, Irons R (2012) Materials Challenges for the Development of Solid Sorbents for Post-combustion Carbon Capture. *Journal of Materials Chemistry*; **22**, 2815-2823 (2012)

Dreisbach F, Staudt R and Keller J (1999) High Pressure Adsorption Data of Methane, Nitrogen, Carbon Dioxide and their Binary and Ternary Mixtures on Activated Carbon. *Adsorption*; **5**, 215-227 (1999)

Eddaoudi M, Kim J, Rosi N, Vodak D, Wachter J, O'Keeffe M and Yaghi O M (2002) Systematic Design of Pore Size and Functionality in Isorecticular MOFs and Their Application in Methane Storage. *Science*; **295**, 469-472 (2002)

Ehrburger P, Addoun A, Addoun F and Donnet J B (1986) Carbonisation of Coal in the Presence of Alkaline Hydroxides and Carbonates: Formation of Activated Carbons. *Fuel*; **65**, 1447-1449 (1986)

El-Kaderi H M, Hunt J R, Mendoza-Cortés J L, Côté A P, Taylor R E, O'Keeffe M and Yaghi O M (2007) Designed Synthesis of 3D Covalent Organic Frameworks. *Science*; **316**, 268-272 (2007)

Eric F (2007) Carbon Dioxide Recovery from Post-combustion Processess: Can Gas Permeation Membranes Compete with Absorption. *Journal of Membrane Science*; **294**, 50-59 (2007)

Fan X, Zhang L, Zhang G, Shu Z and Shi J (2013) Chitosan Derived Nitrogen-doped Microporous Carbons for High Performance CO_2 Capture. *Carbon*; **61**, 423-430 (2013)

Farha O, Yazaydin A, Eryazici I, Malliaka C, Hauser B, Kanatzidis M, Nguyen S, Snurr R and Hupp J (2010) De-novo Synthesis of a Metal–organic Framework Material Featuring Ultrahigh Surface Area and Gas Storage Capacities. *Nature Chemistry*; **2**, 944-948 (2010)

Ferrari A, Rodil S, Robertson J (2003) Interpretation of Infrared and Raman Spectra of Amorphous Carbon Nitrides. *Physical review B*; **67**, 155306-20 (2003)

Figueroa J, Fout T, Plasyski S, McIlvried H and Srivatava R (2008) Advances in CO_2 Capture Technology-The U.S. Department of Energy's Carbon Sequestration Program. *International Journal of Greenhouse Gas Control*; **2**, 9-20 (2008)

Fletcher A J, Cussen E J, Prior T J, Rosseinsky M J, Kepert C J and Thomas K M (2001) Adsorption Dynamics of Gases and Vapours on the Nanoporous Metal Organic Framework Material Ni2(4,4'-Bipyridine)$_3$(NO_3)$_4$: Guest Modification of Host Sorption Behaviour. *Journal of the American Chemical Society*; **123**, 10001-10011 (2001)

Florin N H, Blamey J and Fennell P S (2010) Synthesitic CaO-Based Sorbent for CO_2 Capture from Large Point Sources. *Energy & Fuels*; **24**, 4598-4604 (2010)

Fujimoto H (2003) Theoretical X-ray Scattering Intensity of Carbons with Turbostratic Stacking and AB-stacking Structures. *Carbon*; **41**, 1585-1592 (2003)

Furukawa H and Yaghi O M (2009) Storage of Hydrogen, Methane and Carbon Dioxide in Highly Porous Covalent Organic Frameworks for Clean Energy Applications. *Journal of the American Chemical Society*; **131**, 8875-8883 (2009)

Furukawa H, Ko N, Go Y, Aratani N, Choi S, Choi E, Yazaydin O, Snurr R, O'Keeffe M, Kim J and Yaghi O (2010) Ultrahigh Porosity in Metal-Organic Frameworks. *Science*. **329**; 424-428 (2010)

Gale J, Kaya Y (2003) *Greenhouse Gas Control Technologies: 6th International Conference on Greenhouse gas Control Technoligies.* Elsevier Science, Oxford, United Kingdom (2003) pp. 1879

Gallei E and Stumpf G (1976) Infrared Spectroscopic Studies of the Adsorption of Carbon Dioxide and the Coadsorption of Carbon Dioxide and Water on CaY- and NiY-Zeolites. *Journal of Colloid and Interface Science*; **55**, 415-420 (1976)

Gallet G, Carroccio S, Rizzarelli P and Karlsson S (2002) Thermal Degradation of Poly(ethylene Oxide-propylene Oxide-ethylene Oxide) Triblock Copolymer: Comparative Study by SEC/NMR, SEC/MALDI-TOF-MS and SPME/GC-MS. *Polymer*; **43**, 1081-1094 (2002)

Gammon W, Kraft O, Reilly A and Holloway B (2003) Experimental Comparison of N(1s) X-ray Photoelectron Spectroscopy Binding Energies of Hard and Elastic Amorphous Carbon Nitride Films with Reference Organic Compounds. *Carbon*; **41**, 1917-1923 (2003)

Gao W, Alemany L, Ci L and Ajayan P (2009) New Insights into the Structure and Reduction of Graphite Oxide. *Nature Chemistry*; **1**, 403-408 (2009)

Gao H, Yan S, Wang J, Huang Y, Wang P, Li Z, Zou Z (2013) Towards Efficient Solar Hydrogen Production by Intercalated Carbon Nitride Photocatalyst. *Physical Chemistry Chemical Physics*; **5**, 10877-18084 (2013)

Garrido J, Linares-Solano A, Martin-Martinez J, Molina-Sabio M, Rodriguez-Reinoso R and Torregrosa R (1987) Use of Nitrogen vs. Carbon Dioxide in the Characterization of Activated Carbons. *Langmuir*; **3**, 76–81 (1987)

Geim A K (2009) Graphene: Status and Prospects. *Science*; **324**, 1530-1534 (2009)

Geng D, Yang S, Zhang Y, Yang J, Liu J, Li R, Sham T, Sun X, Ye S and Knights S (2011) Nitrogen Doping Effects on the Structure of Graphene. *Applied Surface Science*; **257**, 9193-9198 (2011)

Germain J, Fréchet J and Svec F (2009) Nanoporous Polymers for Hydrogen Storage. *Small*; **5**, 1098-1111 (2009)

Global CCS Institute (2014) see website for latest listing and analysis of CCS projects around the world: http://www.globalccsinstitute.com/projects/browse. Also; *Global Status of Large-Scale Integrated CCS Projects. December 2011 Update*. (2011) pp. 6

González A, Plaza M, Pis J, Rubiera F and Pevida C (2013) Post-combustion CO_2 Capture Adsorbents from Spent Coffee Grounds. *Energy Procedia*; **37**, 134-141 (2013)

Göttlicher G and Pruschek R (1997) *Comparison of CO_2 Removal Systems for Fossil-Fuelled Power Plant Processes.* Energy Conversion and Management; **38,** 173-178 (1997)

Grasa G, González B, Alonso M and Abanades C J (2007) Comparision of CaO-Based Synthetic CO_2 Sorbents Under Realistic Calcination Conditions. *Energy & Fuels*; **21**, 3560-3562 (2007)

Gray M, Soong Y, Champagne K, Pennline H, Baltrus J, Stevens R, Khatri R, Chuang S and Filburn T (2005) Improved Immobilized Carbon Dioxide Capture Sorbents. *Fuel Processing Technology*; **86**, 1449-1455 (2005)

Gray M, Champagne K, Fauth D, Baltrus J, Pennline H (2008) Performance of Immobilized Tertiary Amine Solid Sorbents for the Capture of Carbon Dioxide. *International Journal of Greenhouse Gas Control*; **2**, 3-8 (2008)

Guardia L, Fernandez-Merino M, Paredes J, Soli-Fernandez P, Villar-Rodil S, Martinez-Alonso A and Tascon J (2011) High-throughput Production of Pristine Graphene in an Aqueous Dispersion Assisted by Non-ionic Surfactants. *Carbon*; **49**, 1653-1662 (2011)

Gudim L I and Klimenko P L (1972) Infrared Spectra of Polyurethanes in the Near Infrared Region. *Journal of Applied Spectroscopy*; **16**, 685-686 (1972)

Guo B, Chang L, Xie K (2006) Adsorption of Carbon Dioxide on Activated Carbon. *Journal of Natural Gas Chemistry*; **15**, 223-229 (2006)

Guo D, Kondo T, Machida T, Iwatake K, Okada S and Nakamura J (2012) Observation of Landau Levels in Potassium-intercalated Graphite under a Zero Magnetic Field. *Nature Communications*; **3**, 1068 (2012)

Han S S, Furukawa H, Yaghi O M and Goddard W A (2008) Covalent Organic Frameworks as Exceptional Hydrogen Storage Materials. *Journal of the American Chemical Society*; **130**, 11580-11581 (2008)

Han S L, Xue X, Nie X C, Zhai H, Wang F, Sun Q, Jia Y, Li S F and Guo X Z (2010) First-Principles Calculations on the Role of Ni-Doping in Cun Clusters: From Geometric and Electronic Structures to Chemical Activities Towards CO_2. *Physics Letters A*; **374**, 4324-4330 (2010)

Hansen J, Sato M, Ruedy R, Lo K, Lea D W and Medina-Elizade M (2006) Global Temperature Change. *Proceedings of the National Academy of Sciences*; **103**, 14288-14293 (2006)

Hao G P, Li W C, Qian D and Lu A H (2010) Rapid Synthesis of Nitrogen-Doped Porous Carbon Monolith for CO_2 Capture. *Advanced Materials*; **22**, 853-857 (2010)

Harlick P J E and Tezel F H (2004) An Experimental Adsorbent Screening Study for CO_2 Removal from N_2. *Microporous and Mesoporous Materials*; **76**, 71-79 (2004)

Haszeldine R S (2009) Carbon Capture and Storage: How Green Can Black Be? *Science*; **325**, 1647-1652 (2009)

Hernández-Huesca R, Díaz L and Aguilar-Armenta G (1999) Adsorption Equilibria and Kinetics of CO_2, CH_4 and N_2 in Natural Zeolites. *Separation and Purification Technology*; **15**, 163-173 (1999)

Herzog H, Meldon J and Hatton A (2009) *Advanced Post-Combustion CO_2 Capture*. Clean Air task Force, Boston, United States of America (2009) pp. 39

Himeno S, Komatsu T and Fujita S (2005) High-Pressure Adsorption Equilibria of Methane and Carbon Dioxide on Several Activated Carbons. *Journal of Chemical and Engineering Data*; **50**, 369-376 (2005)

Holst J R, Trewin A and Cooper A I (2010a) Porous Organic Molecules. *Nature Chemistry*; **2**, 915-920 (2010)

Holst J R, Stöckel E, Adams D J and Cooper A I (2010b) High Surface Area Networks From Tetrahedral Monomers: Metal-Catalysed Coupling, Thermal Polymerisation, and "Click" Chemistry. *Macromolecules*; **43**, 8531-8538 (2010)

Hu Z, Srinivasan M and Ni Y (2001) Novel Activation Process for Preparing Highly Microporous and Mesoporous Activated Carbons. *Carbon*; **39**, 877-886 (2001)

Hu X, Radosz M, Cychosz k and Thommes M (2011a) CO_2-Filling Capacity and Selectivity of Carbon Nanopores: Synthesis, Texture, and Pore-Size Distribution from Quenched-Solid Density Functional Theory (QSDFT). *Environmental Science and Technology*; **45**, 7068-7074 (2011)

Hu M, Reboul J, Furukawa S, Radhakrishnan L, Zhang Y, Srinivasu P, Iwai H, Wang H, Nemoto Y, Suzuki N, Kitagawa S and Yamauchi Y (2011b) Direct Synthesis of Nanoporous Carbon Nitride Fibers using Al-based Porous Coordination Polymers (Al-PCPs). *Chemical Communications*; **47**, 8124-8126 (2011)

Huang J, Zou J and Ho W S (2008) Carbon Dioxide Capture Using a CO_2-Selective Facilitated Transport Membrane. *Industrial & Engineering Chemistry Research*; **47**, 1261-1267 (2008)

Hummers W and Offeman R (1958) Preparation of Graphitic Oxide. *Journal of the American Chemical Society*; **80**, 1339 (1958)

Ibrahim M, Alaam M, El-Haes, Jalbout A and Leon A (2006) Analysis of the Structure and Vibrational Spectra of Glucose and Fructose. *Ecletica Quimica*; **31**, 15-21 (2006)

IEA (2008) *CO_2 Capture and Storage: A key Abatement Option.* IEA Publications, Paris, France (2008)

IEA (2013) *Technology Roadmap: Carbon Capture and Storage*. IEA Publications, Paris, France (2013) pp. 19

IPCC (2001) *Climate Change 2001: The Scientific Basis. Contribution of the Working Group I to the Third Assessment Report of the Intergovernmental Panel on Climate Change*. Houghton J T, Ding Y, Griggs D J, Noguer M, van der Linden P J, Dai X, Maskell K and Johnson C A (eds.) Cambridge University Press, Cambridge, United Kingdom and New York, NY, United States of America (2001)

IPCC (2005) *Special Report on Carbon dioxide Capture and Storage. Working Group III of the Intergovernmental Panel on Climate Change.* Metz B, Davidson O, de Coninck H, Loos M, Meyer L (eds.) Cambridge University Press, Cambridge, United Kingdom and New York, NY, United States of America, (2005)

IPCC (2007) *Climate Change 2007: The Physical Science Basis. Contribution of Working Group I to the Fourth Assessment Report of the Intergovernmental Panel on Climate Change.* Solomon S, Qin D, Manning M, Chen Z, Marquis M, Averyt K B, Tignor M and Miller H L (eds.) Cambridge University Press, Cambridge, United Kingdom and New York, NY, United States of America (2007)

IPCC (2011) *IPCC Special Report on Renewable Energy Sources and Climate Change Mitigation. Prepared by Working Group III of the Intergovernmental Panel on Climate Change*. Edenhofer O, Pichs-Madruga Y, Sokona Y, Seyboth K, Matschoss P, Kadner S, Zwickel T, Eickemeier P, Hansen G, Schlomer S, von Stechow C (eds.) Cambridge University Press, Cambridge, United Kingdom and New York, NY, United States of America (2011)

IPCC (2013) *Summary for Policymakers. In: Climate Change 2013: The Physical Science Basis. Contribution of Working Group I to the Fifth Assessment Report of the Intergovernmental Panel on Climate Change* Stocker, T.F., D. Qin, G.-K. Plattner, M. Tignor, S.K. Allen, J. Boschung, A. Nauels, Y. Xia, V. Bex and P.M. Midgley (eds.). Cambridge University Press, Cambridge, United Kingdom and New York, United States of America (2013)

Jansen J C, Stocker M, Karge H G, and Weitkamp J (1994) *Studies in Surface Science and Catalysis: Advanced Zeolite Science and Applications*; Elsevier Science, Amsterdam, Netherlands (1994) pp. 698

Jiang J and Cooper A (2010) Microporous Organic Polymers: Design, Synthesis, and Function. Functional Metal-Organic Frameworks: Gas Storage, Separation and Catalysis. Topics in Current Chemistry. Springer Berlin, Heidelberg, Germany. Volume 293 (2010) pp. 1-33

Jin Y, Hawkins S, Huynh C and Su S (2013) Carbon Nanotube Modified Carbon Composite Monoliths as Superior Adsorbents for Carbon Dioxide Capture. *Energy and Environmental Science*; **6**, 2591-2596 (2013)

Kalderis D, Bethanis S, Paraskeva P and Diamadopoulos E (2008) Production of Activated Carbon from Bagasse and Rice Husk by a Single-stage Chemical Activation Method at Low Retention Times. *Bioresource Technology*; **99**, 6809-6816 (2008)

Kaneko K, Ishii C, Ruike M, Kuwabara H (1992) Origin of Superhigh Surface Area and Microcrystalline Graphitic Structures of Activated Carbons. *Carbon*; **30**, 1075-1088 (1992)

Karl T R and Trenberth K E (2003) Modern Global Climate Change. *Science*; **302**, 1719-1723 (2003)

Katekomol P, Roeser J, Bojdys M, Weber J, and Thomas A (2013) Covalent Triazine Frameworks Prepared from 1,3,5-Tricyanobenzene. *Chemistry of Materials*; **25**, 1542−1548 (2013)

Katz D L and Rasin Tek M (1981) Overview on Underground Storage of Natural Gas. *Journal of Petroleum Technology*; **33**, 943-951 (1981)

Kelkar A A, Patil N M and Chaudhari R V (2002) Copper-Catalysed Amination of Aryl Halides: Single Step Synthesis of Triarylamines. *Tetrahedron Letters*; **43**, 7143-7146 (2002)

Kerr K A (2010) Do We Have the Energy for the Next Transition? *Science*; **329**, 780-781 (2010)

Keskin S, van Heest T M, Sholl D S (2010) Can Metal-organic Framework Materials Play a Useful Role in Large-scale Carbon Dioxide Separations? *ChemSusChem*; **3**, 879-891 (2010)

Khodakov A Y and Rees L V C (1995) Effect of Propane on the Kinetics of Carbon Dioxide Adsorption in NaA Zeolites. *Gas Separation and Purification*; **9**, 253-257 (1995)

Kikkinides E S, Yang R T and Cho S H (1993) Concentration and Recovery of Carbon Dioxide from Flue Gas by Pressure Swing Adsorption. *Industrial & Engineering Chemistry Research*; **32**, 2714-2720 (1993)

Krewitt W, Teske S, Simon S, Pregger T, Graus W, Blomen E, Schmid S and Schäfer O (2009) Energy Revolution 2008: A Sustainable World Energy Perspective. *Energy Policy*; **37**, 5764-5775 (2009)

Kuhn P, Antonietti M and Thomas A (2008) Porous, Covalent Triazine-Based Frameworks Prepared by Ionothermal Synthesis. *Angewandte Chemie International Edition*; **47**, 3450-3453 (2008)

Kumar N, Choi H, Shin Y, Chang D, Dai L, and Baek J (2012) Polyaniline-Grafted Reduced Graphene Oxide for Efficient Electrochemical Supercapacitors. *ACS Nano*; **6**, 1715-1723 (2012)

Lackner K S (2003) A Guide to CO_2 Sequestration. *Science*; **300**, 1677-1678 (2003)

Larciprete R, Fabris S, Sun T, Lacovig P, Baraldi A, Lizzit S (2011) Dual Path Mechanism in the Thermal Reduction of Graphene Oxide. *Journal of the American Chemical Society*; **133**, 17315-17321 (2011)

Lashof D A (1989) The Dynamic Greenhouse: Feedback Processes that may Influence Future Concentrations of Atmospheric Trace Gases and Climate Change. *Journal of Climatic Change*; **14**, 213-242 (1989)

Lee E, Jun Y, Hong W, Thomas A, and Jin M (2010) Cubic Mesoporous Graphitic Carbon(IV) Nitride: An All-in-One Chemosensor for Selective Optical Sensing of Metal Ions. *Angewandte Chemie*; **49**, 9706-9710 (2010)

Lee D, Zhang C, Wei C, Ashfeld B and Gao H (2013) Hierarchically Porous Materials via assembly of Nitrogen-rich Polymer Nanoparticles for Efficient and Selective CO_2 Capture. *Journal of Materials Chemistry A*; **1**, 14862-14867 (2013)

Leidl M and Schwarzinger C (2005) Pyrolysis and THM Reactions of Melamine and it's Resins. *Journal of Analytical and Applied Pyrolysis*; **74**, 200-203 (2005)

León M, Díaz E, Bennici S, Vega A, Ordóñez S and Auroux A (2010) Adsorption of CO_2 on Hydrotalcite-Derived Mixed Oxides: Sorption Mechanisms and Consequences for Adsorption Irreversibility. *Industrial & Engineering Chemistry Research*; **49**, 3663-3671 (2010)

Lewis I C (1982) Chemistry of Carbonization. *Carbon*; **20**, 519-529 (1982)

Li D and Kaneko K (2001) Hydrogen Bond-Regulated Microporous Nature of Copper Complex-assembled Microcrystals. *Chemical Physics Letters*; **335**, 50-56 (2001)

Li X, Wang H, Robinson J, Sanchez, Diankov G and Dai H (2009a) Simultaneous Nitrogen Doping and Reduction of Graphene Oxide. *Journal of the American Chemical Society*; **131**, 15939-15944 (2009)

Li X, Zhang J, Shen L, Ma Y, Lei W, Cui Q, Zou G (2009b) Preparation and Characterization of Graphitic Carbon Nitride through Pyrolysis of Melamine. *Applied Physics A*; **94**, 387-392 (2009)

Li Q, Yang J, Feng D, Wu Z, Wu Q, Park S, Ha C S and Zhao D (2010) Facile Synthesis of Porous Carbon Nitride Spheres with Hierarchical Three-Dimensional Mesostructures for CO_2 Capture. *Nano Research*; **3**, 632-642 (2010)

Li B, Gong R, Wang W, Huang X, Zhang W Li H, Hu C and Tan B (2011a) A New Strategy to Microporous Polymers: Knitting Rigid Aromatic Building Blocks by External Cross-Linker. *Macromolecules*; **44**, 2410-2414 (2011)

Li B, Gong R, Luo Y and Tan B (2011b) Tailoring the Pore Size of Hypercrosslinked Polymers. *Soft Matter*; **7**, 10910-10916 (2011)

Li X, Kurasch S, Kaiser U, Antonietti M (2012a) Synthesis of Monolayer-Patched Graphene from Glucose. *Angewandte Chemie International Edition*; **51**, 9689-9692 (2012)

Li C and Shi G (2012b) Three-dimensional Graphene Architectures. *Nanoscale*; **4**, 5549-5563 (2012)

Li Y, Ben T, Zhang B, Fu Y and Qiu S (2013) Ultrahigh Gas Storage both at Low and High Pressures in KOH-Activated Carbonized Porous Aromatic Frameworks. *Scientific Reports*; **3**, 2420 (2013)

Liang C and Dai S (2006) Synthesis of Mesoporous Carbon Materials via Enhanced Hydrogen-Bonding Interaction. *Journal of the American Chemical Society*; **128**, 5316-5317 (2006)

Liebig J (1834) Uber Einige Stickstoff-Verbindungen. *Annalen der Pharmacie*; **10**, 1-47 (1834)

Lin Z, Waller G, Liu Y, Liu M, Wong C (2012) Facile Synthesis of Nitrogen-Doped Graphene via Pyrolysis of Graphene Oxide and Urea, and its Electrocatalytic Activity toward the Oxygen-Reduction Reaction. *Advanced Energy Materials*; **2**, 884-888 (2012)

Liu L, Deng Q, Ma T, Lin X, Hou X, Liu Y and Yuan Z (2011a) Ordered Mesoporous Carbons: Citric Acid-catalyzed Synthesis, Nitrogen Doping and CO_2 Capture. *Journal of Materials Chemistry*; **21**, 16001-16009 (2011)

Liu J, Zhang T, Wang Z, Dawson G and Chen W (2011b) Simple Pyrolysis of Urea into Graphitic Carbon Nitride with Recyclable Adsorption and Photocatalytic Activity. *Journal of Materials Chemistry*; **21**, 14398-14401 (2011)

Llewellyn P, Bourrelly S, Serre C, Vimont A, Daturi M, Hmaon L, Weirled G, Chang J, Hong D, Hwang Y, Jhung S and Ferey G (2008) High Uptakes of CO_2 and CH_4 in Mesoporous Metal-Organic Frameworks MIL-100 and MIL-101. *Langmuir*; **24**, 7245-7250 (2008)

Lillo-Ródenas M A, Carzola-Amorós D, Linares-Solano A (2003) Understanding Chemical Reactions between Carbons and NaOH and KOH: An Insight into the Chemical Activation Mechanism. *Carbon*; **41**, 267-275 (2003)

Lillo-Ródenas M A, Juan-Juan J, Cazorla-Amorós D, Linares-Solano A (2004) About Reactions Occuring during Chemical Activation with Hydroxides. *Carbon*; **42**, 1371-1375 (2004)

Liu L, Ma D, Zheng H, Li X, Cheng M and Bao X (2008) Synthesis and Characterisation of Microporous Carbon Nitride. *Microporous and Mesoporous Materials*; **110**, 216-222 (2008)

Lotsch B, Doblinger M, Sehnert J, Seyfarth L, Senker J, Oeckler O and Schnick W (2007) Unmasking Melon by a Complementary Approach Employing Electron Diffraction, Solid-State NMR Spectroscopy, and Theoretical Calculations-Structural Characterization of a Carbon Nitride Polymer. *Chemistry a European journal*; **13**, 4969-4980 (2007)

Lu C, Xu S, Gan Y, Liu S and Liu C (2005) Effect of Pre-carbonization of Petroleum Cokes on Chemical Activation Process with KOH. *Carbon*; **43**, 2295-2301 (2005)

Lu W, Sculley J, Yuan D, Krishna R, Wei Z, and Zhou H (2012) Polyamine-Tethered Porous Polymer Networks for Carbon Dioxide Capture from Flue Gas. *Angewandte Chemie*; **51**, 7480 –7484 (2012)

Lua A C and Yang T (2004) Effect of Activation Temperature on the Textual and Chemical Properties of Potassium Hydroxide Activated Carbon Prepared from Pistachio-Nut Shell. *Journal of Colloid and Interface Science*; **274**, 594-601 (2004)

Lv R, Li Q, Botello-Mendez A, Hayashi T, Wang B, Berkdemir A, Hao Q, Elias A, Cruz-Silva R, Gutierrez H, Kim Y, Muramatsu H, Zhu J, Endo M, Terrones H, Charlier J, Pan

Maciá-Agulló J A, Moore B C, Cazorla-Amorós D and Linares-Solano A (2004) Activation of Coal Tar Pitch carbon Fibres: Physical Activation vs. Chemical Activation. *Carbon*; **42**, 1367-1370 (2004)

Marsh H and Rodriguez-Reinoso F (2006) *Activated carbon*. Elsevier Limited, Oxford, United Kingdom (2006)

Mart C, Stöckel E, Clowes R, Adams D, Cooper A, Pis J, Rubiera F and Pevida C (2011) Hypercrosslinked Organic Polymer Networks as Potential Adsorbents for Pre-combustion CO_2 Capture. *Journal of Materials Chemistry*; **21**, 5475-5483 (2011)

Martín C F, Plaza M G, Garcia S, Pis J J, Rubiera F, Pevida C (2011a) Microporous Phenol-Formaldehyde Resin-Based Adsorbents for Pre-Combustion CO_2 Capture. *Fuel*; **90**, 2064-2072 (2011)

Martín C F, Stockel E, Clowes R, Adams D J, Cooper A I, Pis J J, Rubiera F and Pevida C (2011b) Hypercrosslinked Organic Polymer Networks as Potential Adsorbents for Pre-Combustion CO_2 Capture. *Journal of Materials Chemistry*; **21**, 5475-5483 (2011)

McAllister M, Je-Luen L, Adamson D, Schniepp H, Abdala A, Liu J, Herrera-Alsono M, Milius D, Car R, Prud'Homme R and Aksay I (2007) Single Sheet Functionalized Graphene by Oxidation and Thermal Expansion of Graphite. *Chemistry of Materials*; **19**, 4396-4404 (2007)

McGann J, Zhong M, Kim E, Natesakhawat S, Jaroniec M, Whitacre J, Matyjaszewski K, Kowalewski T (2012) Block Copolymer Templating as a Path to Porous Nanostructured Carbons with Highly Accessible Nitrogens for Enhanced (Electro) chemical Performance. *Macromolecular Chemistry and Physics*; **213**, 1078−1090 (2012)

McKeown N and Budd P (2010) Exploitation of Intrinsic Microporosity in Polymer-Based Materials. *Macromolecules*; **43**, 5163-5176 (2010)

Meadowcroft J and Langhelle O (2009) *Catching the Carbon: The Politics and Policy of Carbon Capture and Storage.* Edward Elger Publishing Limited, Cheltenham, United Kingdom and Northampton United States of America (2009) pp. 300

de Meijere A and Diederich F (2004) *Metal-Catalysed Cross-Coupling reactions, 2nd Completely Revised and Enlarged Edition*. Wiley-VCH, Weinheim, Germany (2004) pp. 916

Menéndez J A, Phillips J, Xia B and Radovic L R (1996) On the Modification and Characterisation of Chemical Surface Properties of Activated Carbon: In the Search of Carbons with Stable Basic Properties. *Langmuir*; **12**, 4404-4410 (1996)

Meratla Z (1997) *Combining Cyrogenic Flue gas Emission Remediation with a CO_2/O_2 Combustion Cycle.* Energy Conversion and Management; **38**, 147-152 (1997)

Merline D, Vukusic S and Abdala A (2013) Melamine Formaldehyde: Curing Studies and Reaction Mechanism. *Polymer Journal*; **45**, 413-419 (2013)

Michelena J A, Peeters G, Vansant E F and de Bièvre P (1977) The Adsorption of Carbon Monoxide and Carbon Dioxide in Calcium-Exchanged Zeolite Y. *Recueil des Travaux Chimiques des Pays-Bas*; **96**, 121-124 (1977)

Millward A R and Yaghi O M (2005) Metal-Organic Frameworks with Expeptionally High Capacity for Storage of Carbon Dioxide at Room Temperature. *Journal of the American Chemical Society*; **127**, 17998-17999 (2005)

Mitsunaga T, Conner A and Hill C (2000) Reaction of Formaldehyde with Phenols: A Computational Chemistry Study. *Wood Adhesives*; **7**, 147-153 (2000)

Mohanty P, Kull L and Landskron K (2011) Porous Covalent Electron-rich Organonitridic Frameworks as Highly Selective Sorbents for Methane and Carbon Dioxide. *Nature Communications*; **2**, 401. (2011)

Mou Z, Chen X, Du Y, Wang X, Yang P and Wang S (2011) Forming Mechanism of Nitrogen Doped Graphene Prepared by Thermal Solid-state Reaction of Graphite Oxide and Urea. *Applied Surface Science*; **258**, 1704-1710 (2011)

Myers A and Prausnitz J (1965) Thermodynamics of Mixed-gas Adsorption. *American Institute of Chemical Engineers*; **11**, 121-127 (1965)

Na B K, Koo K K, Eum H M, Lee H and Song H (2001) CO_2 Recovery from Flue Gas by PSA Process using Activated Carbon. *Korean Journal of Chemical Engineering*; **18**, 220-227 (2001)

Niu C, Lu Y, Lieber C (1993) Experimental Realization of the Covalent Solid Carbon Nitride. *Science*; **261**, 334-337 (1993)

Niu P, Zhang L, Liu G and Cheng H (2012) Graphene-like Carbon Nitride Nanosheets for Improved Photocatalytic Activities. *Advanced Functional Materials*; **22**, 4763-4770 (2012)

Nandi M, Okada K, Dutta A, Bhaumik A, Maruyama J, Derks D and Uyama H (2012) Unprecedented CO_2 Uptake over Highly Porous N-doped Activated Carbon Monoliths Prepared by Physical Activation. *Chemical Communications*; **48**, 10283-10285 (2012)

Noriega R, Rivnay J, Vandewa K, Koch F, Stingelin N, Smith P, Toney M and Salleo A (2013) A General Relationship Between Disorder, Aggregation and Charge Transport in Conjugated Polymers. *Nature Materials*; **12**, 1038-1044 (2013)

Novoselov K, Jiang D, Schedin F, Booth T, Khotkevich V, Morozov S, and Geim A (2005) Two-Dimensional Atomic Crystals. *Proceedings of the National Academy of Sciences* of the United States of America; **102**, 10451–10453 (2005)

Oh S, Yoo D, Shin Y and Seo G (2005) FTIR Analysis of Cellulose Treated with Sodium Hydroxide and Carbon Dioxide. *Carbohydrate Research*; **340**, 417-428 (2005)

Oliveira E L G, Grande C A and Rodrigues A E (2008) CO_2 Sorption on Hydrotalcite and Alkali-Modified (K and Cs) Hydrotalcites at High-Temperatures. *Separation and Purification Technology*; **62**, 137-147 (2008)

Oreskes N (2004) The Scientific Concensus on Climate Change. *Science*; **306**, 1686 (2004)

OECD/IEA (2011) *World Energy Outlook: Executive Summary*. Bernan Assoc, Paris, France (2011) pp. 740

Őrsi F (1973) Kinetic Studies on the Thermal Decomposition of Glucose and Fructose. *Journal of Thermal Analysis*; **5**, 329-335 (1973)

Otowa T, Nojima Y and Miyazaki T (1997) Development of KOH Activated High Surface Area Carbon and its Application to Drinking Water Purification. C*arbon*; **35**, 1315-1319 (1997)

Pan L, Adams K M, Hernandez H E, Wang X, Zheng C, Hattori Y and Kaneko K (2003) Porous Lanthanide-Organic Frameworks: Synthesis Characterisation and Unprecedented Gas Adsorption Properties. *Journal of the American Chemical Society*; **125**, 3062-3067 (2003)

Panda T, Pachfule P, Chen Y, Jiangb J and Banerjee R (2011) Amino Functionalized Zeolitic Tetrazolate Framework (ZTF) with High Capacity for Storage of Carbon Dioxide. *Chemical Communication;* **47**, 2011-2013. 2011

Paolo D (2002) Flue Gas Treatment by Activated carbon Obtained from Oil-Fired Fly Ash. *Carbon*; **40**, 1973-1979 (2002)

Park K, Ni Z, Cote A, Choi J, Huang R, Uribe-Romo F, Chae H, O'Keeffe M and Yaghi O (2006) Exceptional Chemical and Thermal Stability of Zeolithic Imidazolate Frameworks. *Proceedings of the National Academy of Sciences of the United States of America*; **103**, 10186-10191 (2006)

Park S, Ruoff R (2009) Chemical Methods for the Production of Graphenes. *Nature Nanotechnology*; **4**, 217-224 (2009)

Patel H and Yavuz C (2012) Noninvasive Functionalization of Polymers of Intrinsic Microporosity for Enhanced CO_2 Capture. *Chemistry Communications*; **48**, 9989-9991 (2012)

Patel H, Je S, Park J, Chen D, Jung Y, Yavuz C and Coskun A (2013) Unprecedented High-temperature CO_2 Selectivity in N_2-phobic Nanoporous Covalent Organic Polymers. *Nature Communications*; **4**, 1357-1365 (2013)

Pauling L, Sturdivant J (1937) The Structure of Cyameluric Acid, Hydromelonic Acid and Related Substances. *Proceedings of the National Academy of Sciences of the United States of America*; **23**, 615-620 (1937)

Pearce J M, Holloway S, Wacker H, Nelis M K, Rochelle C and Bateman K (1996) Natural Occurrences as Analogous for the Geological Disposal of Carbon Dioxide. *Energy Conversion and Management*; **37**, 1123-1128 (1996)

Pei S and Cheng H M (2012) Reduction of Graphene Oxide. *Carbon*; **50**, 3210-3228 (2012)

Pekala R, Alviso R, Kong F and Hulsey S (1992) Aerogels Derived from Multifunctional Organic Monomers. *Journal of Non-Crystalline Solids*; **145**, 90-98 (1992)

Pels J, Kapteijn F, Moulijn J, Zhu Q and Thomas K (1995) Evolution of Nitrogen Functionalities in Carbonaceous Materials During Pyrolysis. *Carbon;* **33**, 1641-1653 (1995)

Pennline H W, Luebke D R, Jones K L, Myers C R, Morsi B I, Heintz Y J and Ilconich J B (2008) Progress in Carbon Dioxide Capture and Separation Research for Gasification-based Power Generation Point Sources. *Fuel Processing Technology*; **89**, 897-907 (2008)

Peters G P, Marland G, Le Quere C, Boden T, Canadell J G and Raupach M R (2012) Rapid growth in CO_2 emissions after the 2008-2009 global financial crisis. *Nature Climate Change*; **2**, 2-4 (2012)

Pevida C, Plaza M G, Arias B, Fermoso J, Rubiera F and Pis J J (2008a) Surface Modification of Activated Carbons for CO_2 Capture. *Applied Surface Science*; **254**, 7165-7172 (2008)

Pevida C, Drage T C and Snape C E (2008b) Silica-Templated Melamine-Formaldehyde Resin Derived Adsorbents for CO_2 Capture. *Carbon*; **46**, 1464-1474 (2008)

Pierre A, Pajonk G (2002) Chemistry of Aerogels and Their Applications. *Chemical Reviews*; **102**, 4243-4265 (2002)

Plaza M, Gonzalez A, Pevida C, Pis J and Rubiera F (2012) Valorisation of Spent Coffee Grounds as CO_2 Adsorbents for Post-combustion Capture Applications. *Applied Energy*; **99**, 272–279 (2012)

Powell C E and Qiao G G (2006) Polymeric CO_2/N_2 Gas Seperation Membranes for the Capture of Carbon Dioxide from Power Plant Flue Gases. *Journal of Membrane Science*; **279**, 1-49 (2006)

Presser V, McDonough J, Yeon S and Gogotsi Y (2011) Effect of Pore Size on Carbon Dioxide Sorption by Carbide Derived Carbon. *Energy and Environmental Science*; **4**, 3059–3066 (2011)

Przepiórski J, Skrodzewicz M and Morawski A W (2004) High-Temperature Ammonia Treatment of Activated Carbon for Enhancement of CO_2 Adsorption. *Applied Surface Science*; **225**, 235-242 (2004)

Rabbani M and El-Kaderi H (2012) Synthesis and Characterization of Porous Benzimidazole-Linked Polymers and Their Performance in Small Gas Storage and Selective Uptake. *Chemistry of Materials*; **24**, 1511−1517 (2012)

Ram Reddy M K, Xu Z P and Diniz da Costa J C (2008) Influence of Water on high-Temperature CO_2 Capture Using Layered Double Hydroxide Derivatives. *Industrial & Engineering Chemistry Research*; **47**, 2630-2635 (2008)

Ramsahye N A, Maurin G, Bourrelly S, Llewellyn P L, Serre C, Loiseau T, Devic T and Ferey G (2007) Probing the Adsorption Sites for CO_2 in Metal Organic Framework Materials MIL-53 (Al, Cr) and MIL-47 (V) by Density Functional Theory. *Journal of Physical Chemistry C*; **112**, 514-520 (2007)

Redemann C E, Lucas H J (1940) Some Derivatives of Cyameluric Acid and Probable Structures of Malam, Melem and Melon. *Journal of the American Chemical Society*; **62**, 842-946 (1940)

Ruben G, Pekala R (1995) High-resolution Transmission Electron Microscopy of the Nanostructure of Melamine-formaldehyde Aerogels. *Journal of Non-crysralline Solids*; **186**, 219-231 (1995)

Rubin E S, Rao A B and Chen C (2005) *Comparative Assessments of Fossil Fuel Power Plants with CO_2 Capture and Storage. Proceedings of 7th International Conference on Greenhouse Gas Control Technologies*. Elsevier Science, Oxford, United Kindgdom (2005) pp. 285-294

Saleh M, Jitendra N. Tiwari K. Kemp C, Yousuf M, and Kim K (2013) Highly Selective and Stable Carbon Dioxide Uptake in Polyindole-Derived Microporous Carbon Materials. *Environmental Science and technology*; **47**, 5467−5473 (2013)

Savage N (2011) Algae: The Scum Solution. *Nature*; **474**, S15-S16 (2011)

Sevilla M, Valle-Vigón P, and Fuertes A (2011a) N-Doped Polypyrrole-Based Porous Carbons for CO_2 Capture. *Advanced Functional Materials*; **21**, 2781-2787 (2011)

Sevilla M and Fuertes A (2011b) Sustainable Porous Carbons with a Superior Performance for CO_2 Capture. *Energy and Environmental Science*; **4**, 1765-1771 (2011)

Sevilla M and Fuertes A (2012a) CO_2 Adsorption by Activated Templated Carbons. *Journal of Colloid and Interface Science*; **366**, 147-154 (2012)

Sevilla M, Falco C, Titirici M and Fuertes A (2012b) High-performance CO_2 Sorbents from Algae. *Royal Society of Chemistry Advances*; **2**, 12792-12797 (2012)

Sevilla M, Parra J B and Fuertes A B (2013) Assessment of the Role of Micropore Size and N-doping in CO_2 Capture by Porous Carbons. *ACS Applied Materials and Interfaces*; **5**, 6360-6368 (2013)

Shen W, Zhang S, He Y, Li J and Fan W (2011) Hierarchical Polyacrylonitrile-Based Activated Carbon Fibers for CO_2 Capture. *Journal of Materials Chemistry*; **21**, 14036-14040 (2011)

da Silva E F and Svendsen H F (2004) Ab Initio Study of the Reaction of the Carbamate Formation from CO_2 and Alkanolamines. *Industrial & Engineering Chemistry Research*; **43**, 3413-3418 (2004)

Sing K, Everett D, Haul R, Moscou L, Pierotti R, Rouquerol J, Siemieniewska T (1985) Reporting Physisorption Data for Gas/Solid Systems-with Special Refencence to the Determination of Surface Area and Porosity. *Pure and Applied Chemistry*; **57**, 603–19 (1985)

Sircar S, Golden T C and Rao M B (1996) Activated Carbon for Gas Seperation and Storage. *Carbon*; **34**, 1-12 (1996)

Siriwardane R V, Shen M S, Fisher E P and Poston J A (2001) Adsorption of CO_2 on Molecular Sieves and Activated Carbon. *Energy & Fuels*; **15**, 279-284 (2001)

Siriwardane R V, Shen M S and Fisher E P (2003) Adsorption of CO_2, N_2 and O_2 on Natural Zeolites. *Energy & Fuels*; **17**, 571-576 (2003)

Siriwardane R V, Shen M S, Fisher E P and Losch J (2005) Adsorption of CO_2 on Zeolites at Moderate Temperatures. *Energy & Fuels*; **19**, 1153-1159 (2005)

Scheepers M, Gelan J, Carleer R, Adriaensens P and Vanderzande D (1993) Investigation of Melamine-formaldehyde Cure by Fourier Transform Raman spectroscopy. *Vibrational Spectroscopy*; **6**, 55-69 (1993)

Shen W, Zhang S, He Y, Li J and Fan W (2011) Hierarchical Porous Polyacrylonitrile-based Activated Carbon Fibers for CO_2 Capture. *Journal of Materials Chemistry*; **21**, 14036-14040 (2011)

Sheng Z, Shao L, Chen J, Bao W, Wang F, Xia X (2011) Catalyst-free Synthesis of Nitrogen-doped Graphene via Thermal Annealing Graphite Oxide with Melamine and Its Excellent Electrocatalysis. *ACS Nano*; **6**, 4350-4358 (2011)

Smith M, March J (2007) *Advanced Organic Chemistry: Reactions, Mechanisms and Structure, 6th Edition*. Wiley-Interscience, New York, United States of America (2007) pp. 722

Socrates G (1980) *Infrared Characteristic Group Frequencies*. Wiley-Interscience, Chichester, United Kingdom (1980)

Solomons T W G (1980) *Organic Chemistry: Second Edition*. John Wiley and Sons, New York, United States of America (1980)

Song J, Shen W, Wang J and Fan W (2012) Superior Carbon-based CO_2 Adsorbents Prepared from Poplar Anthers. *Carbon*; **69**, 255-263 (2012)

de Souza L, Wickramaratne N, Ello A, Costa M, da Costa C, Jaroniec M (2013) Enhancement of CO_2 Adsorption on Phenolic Resin-based Mesoporous Carbons by KOH Activation. *Carbon*; **65**, 334-340 (2013)

Srinivas G, Burress J and Yildrem T (2012) Graphene Oxide Derived Carbons (GODCs); Synthesis and Gas Adsorption Properties. *Energy and Environmental Science*; **5**, 6453-6459 (2012)

Srinivas G, Krungleviciute V, Guo Z and Yildirim T (2014) Exceptional CO_2 Capture in a Hierarchically Porous Carbon with Simultaneous High Surface Area and Pore Volume. *Energy and Environmental Science*; **7**, 335-342 (2014)

Stankovich S, Dikin D, Piner R, Kohlhaas K, Kleinhammes A, Jia Y, Wu Y, Nguyen and Ruoff R (2007) Synthesis of Graphene-based Nanosheets via Chemical Reduction of Exfoliated Graphite Oxide. *Carbon*; **45**, 1558-1565 (2007)

Stefan B (2008) CO_2 Storage in Geological Media: Role, Means, Status in Barriers to Deployment. *Progress in Energy and Combustion Science*; **34**, 254-273 (2008)

Styring P and Jansen D (2011) *Carbon Capture and Utilisation in the Green Economy 2011*. The Center for Low Carbon Futures, York, United Kingdom (2011) pp. 68

Sun L, Wang L, Tian C, Tan T, Xie Y, Shi K, Li M, Fu H (2012) Nitrogen-doped Graphene with High Nitrogen Level via a One-step Hydrothermal Reaction of Graphene Oxide with Urea for Superior Capacitive Energy Storage. *Royal Society of Chemistry Advances*; **2**, 4498-4506 (2012)

Tennison S (1998) Phenolic-resin-derived Activated Carbons. *Applied Catalysis A*; **173**, 289-311 (1998)

Terrones M (2012) Nitrogen-doped Graphene: Beyond Single Substitution and Enhanced Molecular Sensing. *Scientific Reports*; **2**, 586 (2012)

Teter D, Hemley R (1996) Low-Compressibility Carbon Nitrides. *Science*; **271**, 53-55 (1996)

Thomas A, Fischer A, Goettmann F, Antonietti M, Muller J, Schlogl R, Carlsson J (2008) Graphitic Carbon Nitride Materials: Variation of Structure and Morphology and their use as Metal-free Catalysts. *Journal of Materials Chemistry*; **18**, 4893-4908 (2008)

Trans P, Conway T (1959-current) National Oceanic and Atmospheric Administration/Earth System Research Laboratory. *Trends in Atmospheric Carbon Dioxide*. Available from: www.esrl.noaa.gov/gmd/ccgg/trends

Tomita B (1977) Melamine-formaldehyde Resins: Molecular Species Distributions of Methylolmelamines and Some Kinetics of Methylolation. *Journal of Polymer Science*; **15**, 2347-2365 (1977)

Torrisi A, Mellot-Draznieks C and Bell R G (2010) Impact of Ligands on CO_2 adsorption in metal-organic frameworks: First Priniciple Study of the Interaction of CO_2 with Functionalised benzenes. The Effect of Polar and Acidic Substituents. *The Journal of Chemical Physics*; **132**, 044705 (2010)

Tozawa T, Jones J T A, Swamy S I, Jiang S, Adams D J, Shakespeare S, Clowes R, Bradshaw D, Hasell T, Chong S Y, Tang C, Thompson S, Parker J, Trewin A, Bacsa J, Slawin A M Z, Steiner A and Cooper A I (2009) Porous Organic Cages. *Nature Materials*; **8**, 973-978 (2009)

Tyndall J (1860) On the Absorption and Radiation of Heat by Gaseous Matter. *Proceedings of the Royal Society of London*; **11**, 558-561 (1860)

United Nations (1998) *Kyoto Protocol to the United Nations Framework Convention on Climate Change* (1998) pp. 20. Available from: http://unfccc.int

United Nations Framework Convention on Climate Change (2009) *Report of the Conference of the Parties on its Fifteenth Session, Held in Copenhagen from 7 to 19 December 2009. Part Two: Action Taken by the Conference of the Parties at its Fifteenth Session* (2009) pp. 43. Available from: http://unfccc.int

Vaidhyanathan R, Iremonger S S, Shimizu G K H, Boyd P G, Alavi S and Woo T K (2010) Direct Observation and Quantification of CO_2 Binding Within an Amine-Functionalized Nanoporous Solid. *Science*; **330**, 650-653 (2010)

Van der Sluijs J P, Hendriks C A, Blok K (1992) Feasability of Polymer Membranes for Carbon Dioxide Recovery from Flue Gases. *Energy Coversion and Management*; **33**, 429-436 (1992)

Veawab A, Tontiwachwuthikul P and Chakma A (1999) Corrosion Behaviour of Carbon Steel in the CO_2 Absorption Process Using Aqueous Amine Solutions. *Industrial & Engineering Chemistry Research*; **38**, 3917-3924 (1999)

Vogiatzis K D, Mavandonakis A, Klopper W and Froudakis G E (2009) Ab initio Study of the Interactions Between CO_2 and N-containing Organic Heterocycles. *ChemPhysChem*; **10**, 374-383 (2009)

de Vries B J M, van Vuuren D P and Hoogwijk M M (2007) Renewable Energy Sources: Their Global Potential for the First-half of the 21st Century at a Global Level: An Integrated Approach. *Energy Policy*; **35**, 2590-2610 (2007)

Wang X P, Yu J J, Cheng J, Hao Z P and Xu Z P (2007) High-Temperature Adsorption of Carbon Dioxide on Mixed Oxides Derived from Hydrotalcite-Like Compounds. *Environmental Science & Technology*; **42**, 614-618 (2007)

Wang Y, Zhou Y, Liu C and Zhou L (2008) Comparative Studies of CO_2 and CH_4 Sorption on Activated Carbon in Presence of Water. *Colloids and Surfaces A: Physicochemical and Engineering Aspects*; **322**, 14-18 (2008)

Wang G Q, Huang C C, Xing W and Zhuo S P (2011) Hierarchical Porous Carbon Counter Electrode for Dye-Sensitive Solar Cells. *Chinese Physical Letters*; **28**, 038801 (2011)

Wang R, Wang P, Yan X, Lang J, Peng C, and Xue Q (2012a) Promising Porous Carbon Derived from Celtuce Leaves with Outstanding Supercapacitance and CO_2 Capture Performance. *ACS Applied Material and Interfaces*; **4**, 5800-5806 (2012)

Wang L and Yang R T (2012b) Significantly Increased CO_2 Adsorption Performance of Nanostructured Templated Carbon by Tuning Surface Area and Nitrogen Doping. *Journal of Physical Chemistry C*; **116**, 1099-1106 (2012)

Wang J, Senkovska I, Oschatz M, Lohe M, Borchardt L, Heerwig A, Liu Q and Kaskel S (2013) Highly Porous Nitrogen-doped Polyimine-based Carbons with Adjustable Microstructures for CO_2 Capture. *Journal of Materials Chemistry A*; **1**, 10951-10961 (2013)

Ward J W and Habgood H W (1966) The Infrared Spectra of Carbon Dioxide Adsorbed on Zeolite X. *The Journal of Physical Chemistry*; **70**, 1178-1182 (1966)

Wickramaratne N and Jaroniec M (2013) Activated Carbon Spheres for CO_2 Adsorption. *Applied Materials and Interfaces*; **5**, 1849-1855 (2013)

Wilke A and Weber J (2011) Hierarchical Nanoporous Melamine Resin Sponges with Tunable Porosity-Porosity Analysis and CO_2 Sorption Properties. *Journal of Materials Chemistry*; **21**, 5226-5229

Wilson L M and Griffin A C (1993) Synthesis of Molecular 'Jacks': Rigid Tetrahedral Molecules with p-Phenylene arms. *Journal of Materials Chemistry*; **3**. 991-994 (1993)

Wilson R C and Pfohl W F (2000) Study of Cross-Linking Reactions of Melamine/Formaldehyde Resin with Hydroxyl Functional Polyester by Generalised 2D Infrared Spectroscopy. *Vibrational Spectroscopy*; **23**, 13-22 (2000)

Witze A (2012) Climate Change Confirmed… Again. *Nature Geoscience*; **5**, 4-4 (2012)

Wood C, Tan B, Trewin A, Niu H, Bradshaw D, Rosseinsky M, Khimyak Y, Campbell N, Kirk R, Stöckel E and Cooper A (2007) Hydrogen Storage in Microporous Hypercrosslinked Organic Polymer Networks. *Chemistry of Materials*; **19**, 2034-2048 (2007)

Wu P, Qian Y, Du P, Zhang H, Cai C (2012) Facile Synthesis of Nitrogen-doped Graphene for Measuring the Releasing Process of Hydrogen Peroxide from Living Cells. *Journal of Materials Chemistry*; **22**, 6402-6412 (2012)

Xia Y, Mokaya R, Walker G, and Zhu Y (2011) Superior CO_2 Adsorption Capacity on N-Doped, High-Surface-Area, Microporous Carbons Templated from Zeolite. *Advanced Energy Materials*; 1, 678-683 (2011)

Xing W, Liu C, Zhou Z, Zhang L, Zhou J, Zhuo S, Yan Z, Gao H, Wang G and Qiao S (2012) Superior CO_2 Uptake of N-doped Activated Carbon Through Hydrogen-bonding Interaction. *Energy and Environmental Science*; **5**, 7323-7327 (2012)

Xu X, Song C, Andresen J, Miller B and Scaroni A (2002) Novel Polyethylenimine-modified Mesoporous Molecular Sieve of MCM-41 Type as High-Capacity Adsorbent for CO_2 Capture. *Energy and Fuels*; **16**, 1463-1469 (2002)

Xu X, Song C, Andresen J, Miller B and Scaroni A (2003) CO_2 Capture via Mesoporous Spherical Particles. Microporous and Mesoporous Materials; **62**, 29-45 (2003)

Xu Y, Bai H, Lu G, Li C and Shi G (2008) Flexible Graphene Films via the Filtration of Water-Soluble Noncovalent Functionalized Graphene Sheets. *Journal of the American Chemical Society*; **130**, 5856-5857 (2008)

Xu S, Yan X, Wang X, Yang S and Xue (2010) Synthesis of Carbon Nanospheres from Carbon-based Network Polymers. *Journal of Materials Science*; **45**, 2619-2624 (2010)

Yan S, Li Z, Zou Z (2009) Photodegradation Performance of g-C_3N_4 Fabricated by Directly Heating Melamine. *Langmuir*; **25**, 10397-10401 (2009)

Yang D, Velamakanni A, Bozoklu G, Park S, Stoller M, Piner R, Stankovich S, Jung I, Field D, Ventrice C, Ruoff R (2009) Chemical Analysis of Graphene Oxide Films after Heat and Chemical Treatments by X-ray Photoelectron and Micro-Raman Spectroscopy. *Carbon*; **47**, 145-152 (2009)

Yang S, Zhan L, Xu X, Wang Y, Ling L, and Feng X (2013) Graphene-Based Porous Silica Sheets Impregnated with Polyethyleneimine for Superior CO2 Capture. *Advanced Functional Materials*; **5**, 2130–2134 (2013)

Yazaydin O, Snurr R, Park T, Koh K, Liu J, LeVan D, Benin A, Jakubczak P, Lanuza M, Galloway D, Low J, and Willis R (2009a) Screening of Metal-Organic Frameworks for Carbon Dioxide Capture from Flue Gas Using a Combined Experimental and Modeling Approach. *Journal of the American Chemical Society*; **131**, 18198-18199 (2009)

Yazaydın O, Benin A, Faheem S, Jakubczak P, Low J, Willis R and Snurr R (2009b) Enhanced CO_2 Adsorption in Metal-Organic Frameworks via Occupation of Open-Metal Sites by Coordinated Water Molecules. *Chemistry of Materials*; **21**, 1425-1430 (2009)

Yong Z, Mata and Rodrigues A E (2000) Adsorption of carbon Dioxide onto Hydrotalcite-Like Compounds at High-Temperatures. *Industrial & Engineering Chemistry Research*; **40**, 204-209 (2000)

Yong Z and Rodrigues A E (2002) Hydrotalcite-like Compounds as Adsorbents for Carbon Dioxide. *Energy Conversion and Management*; **43**, 1865-1876 (2002)

Youn H, Kim J, Chandrasekar G, Jin H and Ahn W (2011) High Pressure Carbon Dioxide Adsorption on Nanoporous Carbons Prepared by Zeolite Y Templating. *Materials Letters*; **65**, 1772-1774 (2011)

Yu C, Huang C, Tan C (2012) A Review of CO_2 Capture by Absorption and Adsorption. *Aerosol and Air Quality Research*; **12**, 745-769 (2012)

Zhang J, Tan Z, Meng S, Li S, Zhang L (1997) Heat Capacity and Thermal Decomposition of Dicyandiamide. *Thermochimica Acta*; **307**, 11-15 (1997)

Zhang F, Meng Y, Gu D, Yan, Yu C, Tu B and Zhao D (2005) A Facile Aqueous Route to Synthesize Highly Ordered Mesoporous Polymers and Carbon Freameworks with la3d Bicontinuous Cubic Structure. *Journal of the American Chemical Society*; **127**, 13508-13509 (2005)

Zhang X, Xie X, Wang H, Zhang J, Pan B and Xie Y (2012) Enhanced Photoresponsive Ultrathin Graphitic-Phase C3N4 Nanosheets for Bioimaging. *Journal of the American Chemical Society*; **135**, 18−21 (2012)

Zhang Z, Zhou J, Xing W, Xue Q, Yan Z, Zhuo S and Qiao S (2013) Critical Role of Small Micropores in High CO_2 Uptake. *Physical Chemistry Chemical Physics*; **15**, 2523-2529 (2013)

Zhao Z, Cui X, Ma J and Li R (2007) Adsorbtion of Carbon Dioxide on Alkali-Modified Zeolite 13X Adsorbents. *International Journal of Greenhouse Gas Control*; **1**, 355-359 (2007)

Zhao Y, Zhao L, Yao K, Yang Y, Zhang Q and Han Y (2012a) Novel Porous Carbon Materials with Ultrahigh Nitrogen Contents for Selective CO_2 Capture. *Journal of Materials Chemistry*; **22**, 19726-19731 (2012)

Zhao Y, Liu X, Yao K, Zhao L, and Han Y (2012b) Superior Capture of CO_2 Achieved by Introducing Extra-framework Cations into N‑doped Microporous Carbon. *Chemistry of Materials*; **24**, 4725-4734 (2012)

Zheng Y, Liu J, Liang Ji, Jaroniec M, Qiao S (2012) Graphitic Carbon Nitride Materials: Controllable Synthesis and Applications in Fuel Cells and Photocatalysis. *Energy and Environmental Science*; **5**, 6717-6731 (2012)

Zhou J, Li W, Zhang Z, Xing W and Zhuo S (2012) Carbon Dioxide Adsorption Performance of N-doped Zeolite Y Templated Carbons. *Royal Society of Chemistry Advances*; **2**. 161-167 (2012)

Zhou H, Yu W, Liu L, Cheng R, Chen Y, Huang X, Liu Y, Wang Y, Huang U and Duan X (2013) Chemical Vapour Deposition Growth of Large Single Crystals of Monolayer and Bilayer Graphene. *Nature Communications*; **4**, 2096 (2013)

Zou J and Ho W S (2006) CO_2-Selective Polymeric Membranes Containing Amines in Crosslinked Poly(vinyl alcohol). *Journal of Membrane Science*; **286**, 310-321 (2006)

Zhu Y, Murali S, Cai W, Li X, Suk J, Potts J and Ruoff R (2010) Graphene and Graphene Oxide: Synthesis, Properties, and Applications. *Advanced Materials*; **22**, 3906-3924. 2010

Zhu Y, Murali S, Stoller M, Ganesh K, Cai W, Ferreira P J, Pirkle A, Wallace R M, Cychosz K A, Thommes M, Su D, Stach E A, Ruoff R S (2011) Carbon-Based Supercapacitors Produced by Activation of Graphene. *Science*; **332**, 1537-1541 (2011)

Zhu X, Tian C, Mahurin S, Chai S, Wang C, Brown S, Veith G, Luo H, Liu H and Dai S (2012) A Superacid-Catalyzed Synthesis of Porous Membranes Based on Triazine Frameworks for CO_2 Separation. *Journal of the American Chemical Society*; **134**, 10478-10484 (2012)

Zhong M, Natesakhawat S, Baltrus J, Luebke D, Nulwala H, Matyjaszewski K and Kowalewski T (2012) Copolymer-templated Nitrogen-enriched Porous Nanocarbons for CO_2 Capture. *Chemistry Communications*; **48**, 11516-11518 (2012)